Scattering of Elastic Waves using Non-Orthogonal Expansions

by

Matthias Georg Imhof

Submitted to the Department of
Earth, Atmospheric, and Planetary Sciences
in partial fulfillment of the requirements
for the degree of
Doctor of Philosophy in Geophysics

at the

MASSACHUSETTS INSTITUTE OF TECHNOLOGY

September, 1996

Signature of Author .....
Department of Earth, Atmospheric, and Planetary Sciences
July 29, 1996

Certified by .....
Professor M. Nafi Toksöz
Director, Earth Resources Laboratory
Thesis Advisor

Accepted by .....
Professor Thomas H. Jordan
Department Chair

Scattering of Elastic Waves using Non-Orthogonal Expansions

by

Matthias Georg Imhof

Submitted to the Department of Earth, Atmospheric, and Planetary Sciences
on July 29, 1996 in partial fulfillment of the requirements
for the degree of Doctor of Philosophy in Geophysics

ABSTRACT

This thesis is concerned with scattering of acoustic and elastic waves from scatterers embedded in a homogeneous background. The scatterers and the background can be a mixture of fluid and solid domains, e.g. solid scatterers submerged in water. The background will always be a homogeneous half- or fullspace.

Commonly, wavefields are expanded into an orthogonal set of basis functions, e.g. planar or cylindrical waves. Unfortunately, these expansions converge rather slowly for complex geometries. The new approach enhances convergence by summing multipole solutions to the wave equation with different centers of expansions. For this reason, the method is also called Multiple MultiPole expansions (MMP) or Generalized Matching Technique (GMT). The non-orthogonal expansion functions allow irregularities of the wavefields (e.g. due to a rough boundary) to be resolved locally from a nearby center of expansion. This means that the wavefields are expanded into a non-orthogonal set of basis functions. The incident wavefield and the fields induced by the scatterers are matched by evaluating the boundary conditions at discrete matching points along the domain boundaries. Due to the non-orthogonal expansions, no unique answer can be found. Instead, more matching points than actually needed are used. The resulting overdetermined system is solved in the least-squares sense.

Since there are free parameters such as location and number of expansion centers as well as kind and orders of expansion functions used, numerical experiments are performed to measure the performance of different discretizations. An empirical set of rules governing the choice of these parameters is found from these numerical experiments. The resulting scheme is thoroughly tested against numerical experiments performed by finite differences and physical experiments in an ultrasonic watertank. As an application, the method is used to study the effects of shallow-subsurface cavities on reflection seismic data.

To account for heterogeneous scatterers, a hybrid scheme with finite elements is devised. Multiple multipole expansions are used to expand the scattered fields in homogeneous scatterers and in the background. Contrarily, the wavefields inside heterogeneous scatterers are modelled by the finite element method. By condensation, the finite element regions are then collapsed into superelements directly coupling the MMP expansions.

Thesis supervisor: M. Nafi Toksöz

Title: Professor of Geophysics

ACKNOWLEDGMENT

There is no dark side of the moon really. Matter of fact it's all dark!

or: *Per Ardua ad Astra*

I would like to thank my advisor M. Nafi Toksöz for providing an environment such as the Earth Resources Laboratory. Also, I am very grateful that I had the complete freedom to study or work on whatever I wanted to. It allowed me to explore many different things and to get acquainted with a large range of topics.

Also, I wish to thank a few other people for contributing to the present thesis: Lars Bomholt, Rick Gibson, Christian Hafner, Rong-Song Jih, John Queen, Bill Rodi, Henrik Schmidt, and Zhenya Zhu.

Likewise, I need to mention my officemates David Cist, Matthijs Haartsen and Chengbin Peng. For nearly five years, I shared the office with Matthijs. Not enough, he turned into a roommate and became a dear friend!

Finally, I want to express my admiration for my wife, Nancy Imhof-Romero. She gave up her life in Switzerland to share with me the misery of graduate student life and the hardships of winter in New England. Thank you, Nancy - I love you very much!

This thesis was partly supported by the Reservoir Delineation Consortium at ERL and the Air Force Office of Scientific Research under Grant No. F49620-94-1-0282 and the Air Force Technical Applications Center / Phillips Laboratory under Contract No. F19628-95-C-0091. The seismic data used in this thesis was provided by Conoco. The author also held the nCUBE fellowship for two years.

Contents

Chapter 1

Introduction

1.1 Objective

The propagation of elastic waves in inhomogeneous media leads to mode-conversion and a deflection of wave-energy relative to a hypothetical fiducial background homogeneous medium. The inhomogeneity may take the form of a sharp discontinuity in the material properties of the medium (e.g. cavity or inclusion). These obstacles or scatterers change the path of the primary wave and act as a source of secondary waves. The irregular and diffuse deflection of energy of the incident wave by the obstacle is called scattering. The scattered field is composed basically of reflected, refracted and diffracted waves. According to Rayleigh's definition, the scattered wave is the difference of the total wavefield as observed in the presence of the obstacle and the incident field.

Scattering not only degrades the coherence of the propagating wave, e.g. by generating the coda (Aki and Wu, 1988), but can also be a major cause of attenuation (Aki, 1982). Studying the response of one or more scatterers reveals valuable information about the internal structure of the medium. An important tool in understanding these responses is the forward modelling approach. Forward modelling consists of analytical, numerical, or even experimental simulations of waves propagating through the structures of interest.

Identifying the origin of simulated wave arrivals allows using them as indicators of the model's internal features. Correlations between simulated events and real seismic data can later be used to infer the real internal structure.

In the course of the present thesis, we derive a framework to solve scattering problems in the frequency domain. In order to obtain full waveform solutions, the equations of motion are discretized reducing the original integro-differential equation into a set of linear equations and thus into a matrix problem. Specifically, we derive numerical schemes to model acoustic and elastic waves scattering from inclusions embedded in a homogeneous space. We will consider various kinds of scatterers: fluids, elastics, or cavities. While the scatterers might be heterogeneous, the background will always be a homogeneous half- or fullspace. All these problems will be solved with Multiple MultiPole expansions (MMP).

1.2 Numerical Modelling

The calculation of synthetic seismograms has been of interest for many years. Various methods have been proposed for modeling waves in 2 dimensional, heterogeneous media. Each of them has its own range of validity and interest. Fully numerical techniques in the space-time domain, either in the finite difference formulation (Kelly *et al.*, 1976; Virieux, 1986; Cheng *et al.*, 1994) or in the finite element formulation (Smith, 1974; Marfurt, 1984; Murphy and Chin-Bing, 1989), handle any kind of waves in complex media. But for either method, an area containing the source, the receiver and the scatterers plus some neighborhood around them has to be discretized, which limits the distances between scatterers, sources and receivers. Computer runtime and memory requirements are functions of the total volume contained in the model.

The (generalized) ray theory (Červený *et al.*, 1977; Červený and Pšenčík, 1984) can be used when the scatterers and their radii of curvature are large compared to the wavelength. For small or weak scatterers, the (extended) Born approximation (Miles, 1960; Aki and Richards, 1980; Habashy *et al.*, 1993) allows an efficient calculation of the seismogram. In

other cases, the problem can be simplified by assuming the medium consists of homogeneous regions with sharp boundaries in between. Then, reflectivity (Kennett, 1983; Müller, 1985) and global matrix methods (Chin *et al.*, 1984; Schmidt and Tango, 1986) are routinely used for planarly or cylindrically layered media. For laterally heterogeneous media, discrete wave-number integration can be used (Bouchon and Aki, 1977; Haartsen *et al.*, 1994).

In another class of problems, waves scatter from inclusions embedded in a homogeneous medium. The classical eigenfunction expansion (Morse and Feshbach, 1953) allows the analysis of simple shapes only, such as circular or elliptical cylinders, where the eigenfunctions are known (Bowman *et al.*, 1969; Pao and Mow, 1973). Methods based on the perturbation of a prescribed geometry, such as the T-matrix method (Waterman, 1976; Boström, 1980a) work extremely well for certain geometries but are harder to apply efficiently in general situations such as slender scattering objects (Lakhtakia *et al.*, 1984).

Alternatively, integral equation methods can be used. Examples thereof are the boundary element method (Rokhlin, 1983; Schuster and Smith, 1985; Brebbia and Dominguez, 1989; Bouchon, 1993; Dong *et al.*, 1995) or the method of moments (Harrington, 1968; Lakhtakia and Mulholland, 1993; Thompson *et al.*, 1994). Whenever these schemes require numerical integrations, they tend be computationally intensive. Furthermore, the matrices resulting from integral equation discretizations are almost always full. Rokhlin (1990), Coifman (1993), Boag (1994), and Rosen (1995) independently developed schemes which lead to sparse systems.

Based on the work of Mie (1900) and Vekua (1967), Hafner (1983) presented another method. Instead of making the matrix sparse, he tried to reduce the size of the matrix system by using fewer, but better suited, basis functions. In contrast to other approaches, the scattered wavefields are expanded into a set of basis functions which do not necessarily satisfy orthogonality conditions. Any solution to the wave equation in a homogeneous medium could be used as a basis function. Different kinds of solutions can be mixed, e.g. plane waves and cylindrical waves can be used simultaneously as expansion functions. Because one commonly chooses multipole solutions with different origins, the method is

accordingly named the 'Multiple MultiPole' method (MMP). Hafner and Bomholt (1993) provide an extensive bibliography about MMP expansions for electromagnetic scattering problems.

As mentioned previously, the classical eigenfunction method (Morse and Feshbach, 1953) expands the wavefield into multipole sources of various orders but with the same origin. Contrarily, the multifilament source model (Boag *et al.*, 1988; Murphy *et al.*, 1996) uses many monopole sources with different origins as expansion functions. Extreme cases thereof are the discrete wave-number integration method (Bouchon and Aki, 1977; Campillo, 1987) or the boundary element method (Dong *et al.*, 1995; Kessel, 1996). All these techniques are limiting cases of the MMP method. In fact, the MMP technique is a generalization which allows to scale continuously between the classical eigenfunction method, multifilament source model, and the boundary element methods.

A matrix system for the complex weighting coefficients can be found by enforcing boundary conditions along the inclusions. Because the basis functions are not-orthogonal, the resulting matrix system will commonly be ill-conditioned if not numerically singular. To stabilize the solution, an overdetermined matrix system is employed (Hafner, 1993). A similar idea has also been used in combination with the finite element method (Chang, 1990) or with the boundary element method (Wong, 1982; Kessel, 1996). Different techniques exist to obtain equations for the complex weighting coefficients (Appendix A.4). Since the matrix system will be overdetermined, the point matching technique (Harrington, 1968; Hafner, 1980) is optimally suited to construct the individual equations. The advantage of the point matching technique is that it does not need to evaluate numerical integrals. Hence, it is computationally efficient to build the equations. Kessel (1996) suggested an interesting extension. The exact solution obeys not only the continuity equations along boundaries but also the extinction theorem (Born and Wolf, 1980; Chew, 1990). At discrete points, the extinction theorem could also be enforced to yield additional equations which stabilize the matrix equation even further.

An advantage of the MMP scheme is that the same algorithm can be used to model scatter-

ing from a single inclusion, multiple inclusions or layered ones. Scattering between multiple inclusions is just a straight extension of the single scatterer problem (Imhof, 1995). It can be solved without complicated bookkeeping or involving the translation theorems (Peterson and Ström, 1974; Chew, 1989; Wang and Chew, 1993).

Many frequency domain methods are closely related as demonstrated in Appendix A. This makes it relatively easy to couple MMP expansions with, e.g., the method of moments (Hafner *et al.*, 1994), or the finite element method (Sroka *et al.*, 1990; Bomholt, 1994).

The MMP method allows to incorporate prior knowledge or expectations into the modelling. First, special solution to the wave equation can be used as expansion functions. For example, fractional multipoles (Engheta, 1996) describe wavefields in wedge-shaped regions (Elsherbeni *et al.*, 1991). Another generalization of multipoles are beams obtained by assigning the origin to a location in complex space (Deschamps, 1971; Shin and Felsen, 1977). Second, the complete solution of a particular problem can be used as one expansion function for a perturbed problem. Hopefully, only a few additional expansion functions are needed to account for the perturbation (Hafner, 1990). This feature allows to split problems into substructures. Each piece is then solved independently and the complete problem is reassembled recursively (Zienkiewicz, 1977; Schwarz, 1988; Marfurt and Shin, 1989; Hafner, 1990). Finally, since the problems are solved in the frequency domain, the solution at a different frequency can be used as initial solution for an iterative solver scheme (Hafner, 1994).

The MMP scheme can be used to decompose the numerical solution which helps to understand the solution. For example, the scheme might decompose propagating body waves into their P- and S-modes. It can also be used to test a hypothesis. For example, the wavefield due to an incident beam scattering from an inclusion might contain a strong, specularly reflected beam. What is the importance of the specular reflected beam component? Expanding the scattered field into the specularly reflected beam as well as a MMP expansion allows to estimate the specular beam contribution.

To name the scheme 'Multiple MultiPole expansions' (MMP) is in fact misleading. The set of possible expansion functions is not limited to multipole solutions of the wave equation. Any solution which seems to make sense for the problem at hand can be used as an expansion function. The least-squares scheme yields then the set of weighting coefficients which solve the scattering problem best for the given set of expansion functions. Plane waves, multipole solutions, beams, and previous solutions can all be used together to expand the solution to a particular scattering problem.

Moreover, hybrid schemes with other matrix methods are very simple to derive. Thus, a better name would be 'Generalized Multipole Technique' (GMT) as nowadays suggested by Hafner (1990). Even more accurate would be 'Generalized Matching Technique'. Additionally, the scheme is also known as the method of discrete sources (Eremin and Sveshnikov, 1993). Although GMT would be more accurate, the scheme is named MMP throughout this present thesis for consistency with published work. Also, we expand the wavefields predominantly into multipole functions in the course of this thesis.

1.3 Outline

In this thesis, we develop the application of the MMP method to 2-dimensional acoustic and elastic wave propagation.

In Chapter 2, the multiple multipole method (MMP) is introduced in the context of 2D acoustic scattering where homogeneous, bounded scatterers are embedded in a homogeneous fullspace. Numerical experiments are used to deduce a set of rules about the locations, orders, and numbers of multipoles and their relation to the matching points.

Chapter 3 expands the MMP to 2D elastic media where homogeneous scatterers are embedded in a homogeneous fullspace. In the elastic case, separate expansions are used for P- and S-waves. As a welcome bonus, scattered wavefields are automatically decomposed into P- and S-waves for each individual scatterer. Further numerical experiments and a

comparison with finite difference results are used to validate the set of rules found in the acoustic case.

To solve scattering problems where heterogeneous scatterers are embedded in a homogeneous fullspace, a hybrid scheme is derived in Chapter 4 combining the MMP with finite elements (FE). Heterogeneous scatterers are modelled by FE, while the wavefields in the homogeneous fullspace or homogeneous scatterers are expressed by MMP expansions. The different methods are coupled by the boundary conditions along the interfaces of the various scatterers. Each finite-element region is ultimately condensed into one 'super-element' which contains all the coupling between the MMP expansion functions for the background domain. The hybrid scheme is first derived for acoustic waves and later extended for the elastic case.

An ultrasonic watertank experiment in Chapter 5 shows that the wavefield scattered from a few solid objects submerged in water is very complex. The interpretation of the scattered wavefields becomes especially tedious when waves reverberate between the scatterers and the water surface. To aid the interpretation, the experiment is numerically modelled with an acousto-elastic MMP scheme which automatically decomposes the scattered wavefields by scatterer.

In Chapter 6, a reflection seismic dataset acquired in West Texas is presented. The quality of the data shot over limestone mesas is badly degraded by scattered energy. Two different scattering mechanisms are proposed: surface topography and near surface cavities. First, a finite difference method is used to study the effect of surface topography on the propagating waves. Second, a scheme is derived to study the scattering from cavities close to the surface. Because many backscattered events appear to be Rayleigh waves, the effect of a free surface is incorporated into the MMP expansion functions. The contribution of the Rayleigh pole and the saddle point contributions of the reflected and converted wavefields are directly added to the MMP expansion functions. The projection method (Harrington, 1968) is then used to approximate the scattering from cavities being too large for Rayleigh scatterers but too small to justify a full treatment. For a variety of models, energy flux density (Poynting

vector) and energy density function are used as interpretative tools.

Finally, Chapter 7 summarizes the results obtained in this thesis and points out future work.

Various appendices complement the present work. Appendix A demonstrates the relations between different matrix methods commonly used to solve scattering problems. The two main differences are how they expand the wavefields and how they evaluate the unavoidable errors due to discretization and truncation. Also, Appendix A presents the solver scheme used for the hybrid cases. Appendix B develops asymptotic expansion functions for waves propagating in an elastic halfspace with a free surface. Each expansion function contains direct wave, reflections, conversions, and the surface wave. Appendix C derives a scheme to model inclusions with dimensions smaller than the dominant wavelength. Finally, Appendix D contains the relations between the Helmholtz potentials, displacements, stresses, and strains both in Cartesian and cylindrical coordinate frames.

Chapter 2

Multiple Multipole Expansions for Acoustic Scattering

Abstract

The paper presents a new approach to solve multiple scattering of acoustic waves in 2 dimensions. Traditionally, wavefields are expanded into an orthogonal set of basis functions. Often these functions build a multipole. Unfortunately, these multipoles converge rather slowly for complex geometries. The new approach enhances convergence by including multiple multipoles into each region, allowing irregularities of the boundary to be resolved locally. The wavefields are expanded into a set of non-orthogonal basis functions. The incident wavefield and the fields induced by the scatterers are matched in the least-squares sense by evaluating the boundary conditions at discrete matching points along the domain boundaries. Due to the non-orthogonal expansions, we choose more matching points than actually needed resulting in an overdetermined system which is solved in the least-squares sense. This allows an estimate of how well the expansion converges and can help to tune the scheme to enhance accuracy or reduce runtime. The idea of the multiple multipole can be extended by using more complicated basis functions which are closer to the solution

sought. The resulting algorithm is a very general tool to solve relatively large and complex two dimensional scattering problems.

Introduction

Several methods are routinely employed for the solution of acoustic scattering problems. The ray theory or the generalized ray theory (Červený *et al.*, 1977; Hong and Helmberger, 1978; Červený and Pšenčík, 1984) are used when the scatterers and their radii of curvature are large compared to the wavelength. The Born approximation (Miles, 1960; Aki and Richards, 1980; Habashy *et al.*, 1993) is often used for small or weak scatterers. Methods based on the perturbation of a prescribed geometry, such as the T-matrix method (Waterman, 1969; Varadan and Varadan, 1980) as well as the classical multipole expansions (Morse and Feshbach, 1953), work extremely well for certain geometries but cannot be efficiently applied in general situations. Thus, there exists a wide class of problems in which the scatterers are too small for the ray theory, the velocity contrasts too strong for the Born approximation, and their geometry unsuitable for the T-matrix method.

Attempts to apply the finite difference (Kelly *et al.*, 1976; Virieux, 1985; Cheng *et al.*, 1994) or finite element methods (Smith, 1974; Marfurt, 1984; Murphy and Chin-Bing, 1989) to such problems tend to meet with serious difficulties. For example, in many scattering problems the distances between the source, the receivers, and the scatterers are very large compared to the size of the scatterer itself. In order to solve a scattering problem by means of finite elements or finite differences, an area containing the source, the receiver and the scatterers plus a substantial neighborhood around them has to be discretized, resulting in prohibitive computation times.

Thus it becomes attractive to apply a boundary or integral method. Unfortunately, the traditional boundary integral methods (Rokhlin, 1983; Brebbia and Dominguez, 1989; Schuster and Smith, 1985; Dong *et al.*, 1995) are computationally very intensive. A faster version thereof was described by Rokhlin (1990) and Coifman (1993). Alternatively, we will apply a

method which Hafner presented as a more general approach first for electrostatic problems (Hafner and Ballisti, 1983) and later to electromagnetic scattering (Hafner, 1990). In contrast to the traditional approaches, he employed an expansion of the scattered fields into a non-orthogonal and non-complete set of basis-functions. For that reason, the wavefield is evaluated by choosing more matching points along the domain boundaries than unknown coefficients for the expansion functions, yielding an overdetermined system of equations.

An advantage of the technique is that it allows a quick overview of the solution to a particular problem. On the other hand, it also allows the calculation of very precise solutions. Furthermore, the accuracy can be tuned: regions of special interest can be modelled more accurately than others. Due to the overdetermined system, one also gets a very good estimate of the absolute and relative errors of the solutions.

The method is well suited to solve scattering between multiple scatterers. Due to its close relationship with other integral methods, hybrid schemes involving the generalized matching technique (Ballisti and Hafner, 1983; Hafner, 1990), the method of moments (Harrington, 1968), boundary element methods (Rokhlin, 1983; Schuster and Smith, 1985; Dong *et al.*, 1995; Kessel, 1996), or finite elements (Smith, 1974; Marfurt, 1984; Murphy and Chin-Bing, 1989) can be devised easily.

The paper will be structured as follows: first we will present the method for an incident wavefield being scattered by one object. Then we adapt the method to multiple scatterers or scatterers embedded within scatterers. We also generalize the method to take advantage of more complicated expansion functions. Finally we discuss some details of the implementation of the technique on a parallel computer and present numerical results for different models.

2.1 Theoretical Background

We would like to model how an incident wavefield described by its Helmholtz potential $\Phi^{inc}(\mathbf{x},\omega)e^{i\omega t}$ scatters from one object. Figure 2-1 depicts the configuration. For the sake of clarity, we will suppress the time factor $e^{i\omega t}$ in all following expressions. Superscripts denote the region to which a material property or field belongs to, and, to distinguish different regions or domains, we use the symbol Γ^d. The boundary between two regions Γ^x and Γ^y will be denoted by $\partial\Gamma_{xy}$. We call the region Γ^0 the background and define the other regions Γ^d $(d \neq 0)$ to be scatterers. As is well known, in the frequency domain the displacement due to a travelling wave in a homogeneous fluid can be described by a displacement potential $\Phi(\mathbf{x},\omega)$ satisfying the Helmholtz equation

$$(\nabla^2 + k^2)\,\Phi(\mathbf{x},\omega) = 0\,, \tag{2.1}$$

where we defined the wave number $k = \omega/\alpha$ for a particular frequency ω and the propagation velocity $\alpha = \sqrt{\lambda/\rho}$ as a function of the Lamé parameter λ and density ρ. The displacement $\mathbf{u}(\mathbf{x})$ and the pressure $p(\mathbf{x})$ at an arbitrary point $\mathbf{x}$ are then defined by the formulas

$$\mathbf{u}(\mathbf{x}) = \nabla\Phi\big|_{\mathbf{x}} \tag{2.2}$$

$$p(\mathbf{x}) = \lambda\nabla^2\Phi\big|_{\mathbf{x}} = -\lambda k^2\Phi\big|_{\mathbf{x}} = -\omega^2\rho\Phi\big|_{\mathbf{x}}\,. \tag{2.3}$$

A field Φ^{inc} incident on the scatterer will induce two scattered fields: $\Phi^0(\mathbf{x},\omega)$ outside the scattering object and $\Phi^1(\mathbf{x},\omega)$ on the inside. The total fields inside and outside of the scatterer are related by the boundary conditions. For the problem posed, these conditions are continuity of normal displacement and continuity of pressure:

$$\hat{\mathbf{n}}\cdot\nabla\left(\Phi^{inc}(\mathbf{x},\omega) + \Phi^0(\mathbf{x},\omega)\right) = \hat{\mathbf{n}}\cdot\nabla\Phi^1(\mathbf{x},\omega) \tag{2.4}$$

$$\lambda^0\nabla^2\left(\Phi^{inc}(\mathbf{x},\omega) + \Phi^0(\mathbf{x},\omega)\right) = \lambda^1\nabla^2\Phi^1(\mathbf{x},\omega)\,, \tag{2.5}$$

where we used λ^0 and λ^1 to denote the Lamé parameters in the different media. The boundary $\partial\Gamma_{01}$ is described by its normal direction $\hat{\mathbf{n}} = \hat{\mathbf{n}}(\mathbf{x})$. Anticipating multiple scattering

objects, we define the normal $\hat{\mathbf{n}}$ to point from the medium with the lower index to the one with the higher index. The normal approach is to expand the unknown fields Φ^0 and Φ^1 into a series of complete and orthogonal basis functions $\vartheta_n^d(\mathbf{x}, \mathbf{x}_p, \omega)$ where each of them is a solution to the Helmholtz equation (2.1). For some expansion functions, e.g. cylindrical solutions, we need a center of expansion denoted by $\mathbf{x}_0^d$. Thus we could express the field in the domain d by

$$\Phi^d(\mathbf{x}, \omega) = \sum_{n=-\infty}^{\infty} a_n^d \vartheta_n^d(\mathbf{x}, \mathbf{x}_0^d, k^d, \omega)\,. \tag{2.6}$$

In potential theory, expansions of this form are called multipole expansions (Morse and Feshbach, 1953). Deviating from the normal approach, we expand the fields not only from one single expansion point $\mathbf{x}_0^d$ but choose multiple expansion points $\mathbf{x}_p^d$ where $p \in \{1, \ldots, P\}$. Thus instead of using a single multipole as in (2.6), we use multiple multipoles (Ballisti and Hafner, 1983; Hafner, 1990) where the multiple multipoles governing the same region differ in their expansion point $\mathbf{x}_p^d$:

$$\Phi^d(\mathbf{x}, \omega) = \sum_{p=1}^{P} \sum_{n=-\infty}^{+\infty} a_{pn}^d \vartheta_{pn}^d(\mathbf{x}, \mathbf{x}_p^d, k^d, \omega)\,. \tag{2.7}$$

At first glance, adding several multipoles to an expansion which is theoretically complete does not seem very reasonable. But numerical experiments show that the convergence is enhanced dramatically if we use multiple expansion points. For practical reasons we also have to truncate the expansion of Φ^d after only $\pm N$ terms. To account for the neglected terms we introduce an additional error term $\epsilon^d(\mathbf{x}, \omega)$ into our expansions (2.7), leading to the following expansions for the scattered field Φ^1 (inside) and Φ^0 (outside):

$$\Phi^d(\mathbf{x}, \omega) = \sum_{p=1}^{P} \sum_{n=-N}^{+N} a_{pn}^d \vartheta_{pn}^d(\mathbf{x}, \mathbf{x}_p^d, k^d, \omega) \; + \; \epsilon^d(\mathbf{x}, \omega)\,. \tag{2.8}$$

Taking the radiation condition into account, we could choose the actual expansions (Morse and Feshbach, 1953) to be:

$$\Phi^0(\mathbf{x},\omega) = \sum_{p=1}^{P}\sum_{n=-N}^{N} a_{pn}^0 e^{in\theta} H_{|n|}^{(1)}\left(k^0\,|\mathbf{x}-\mathbf{x}_p^0|\right) + \epsilon^0(\mathbf{x},\omega) \tag{2.9}$$

$$\Phi^1(\mathbf{x},\omega) = \sum_{p=1}^{P}\sum_{n=-N}^{N} a_{pn}^1 e^{in\theta} J_{|n|}\left(k^1\,|\mathbf{x}-\mathbf{x}_p^1|\right) + \epsilon^1(\mathbf{x},\omega)\,, \tag{2.10}$$

where $J_{|n|}$ is the Bessel function and $H_{|n|}^{(1)}$ is the Hankel function of the first kind radiating outward. We solve for the unknown coefficients a_{pn}^d by enforcing the boundary conditions (2.4) and (2.5) on discrete matching points $\mathbf{x}_m$ along the domain boundary $\partial\Gamma_{01}$. Altogether, we have $2L = 2P\cdot(2N+1)$ unknown coefficients a_{pn}^d. In order to eliminate an index, we renumber the expansion functions $\vartheta_{pn}^d(\mathbf{x},\mathbf{x}_p^d,k^d,\omega)$ and their coefficients a_{pn}^d resulting in $\vartheta_l^d(\mathbf{x},\mathbf{x}_l^d,k^d,\omega)$ and a_l^d. Each matching point provides two rows to a linear system, one for each boundary condition. Choosing M discrete matching points along the boundary $\partial\Gamma^{01}$, we have to solve a linear system of the form

$$\begin{pmatrix} -\mathbf{W}^0 & \mathbf{W}^1 \\ -\mathbf{T}^0 & \mathbf{T}^1 \end{pmatrix}_{2M\times 2L} \cdot \begin{pmatrix} \mathbf{a}^0 \\ \mathbf{a}^1 \end{pmatrix}_{2L} = \begin{pmatrix} \mathbf{w} \\ \mathbf{t} \end{pmatrix}_{2M} + \begin{pmatrix} \mathbf{e} \\ \mathbf{f} \end{pmatrix}_{2M} \tag{2.11}$$

where we used the submatrices $\mathbf{W}^d$ and $\mathbf{T}^d$ respectively to denote the normal displacement and pressure at the matching points. The vectors $\mathbf{a}^0$ and $\mathbf{a}^1$ contain the unknown coefficients a_l^0 and a_l^1 for the fields Φ^0 and Φ^1. The vectors $\mathbf{w}$ and $\mathbf{t}$ hold the normal displacement and the pressure at the M matching points due to the incident field Φ^{inc}. Finally, we have the residual vectors $\mathbf{e}$ and $\mathbf{f}$ with the misfit of the boundary conditions at the individual matching points. Defining the matching points by their location $\mathbf{x}_m$ and their normal direction $\hat{\mathbf{n}}_m = \hat{\mathbf{n}}(\mathbf{x}_m)$ with respect to the domain boundary $\partial\Gamma_{01}$, we can write the submatrices

and vectors as

$$W^d_{ml} = \hat{\mathbf{n}}_m \cdot \nabla \vartheta^d_l(k^d|\mathbf{x}_m - \mathbf{x}^d_l|) \tag{2.12}$$

$$T^d_{ml} = -\lambda^d \, (k^d)^2 \, \vartheta^d_l(k^d|\mathbf{x}_m - \mathbf{x}^d_l|) \tag{2.13}$$

$$w_m = \hat{\mathbf{n}}_m \cdot \nabla \Phi^{inc}(\mathbf{x}_m, \omega) \tag{2.14}$$

$$t_m = -\lambda^d \, (k^d)^2 \, \nabla \Phi^{inc}(\mathbf{x}_m, \omega) \tag{2.15}$$

where we used the index $m \in \{1, \ldots, M\}$ to denote the matching points $\mathbf{x}_m$, the index $l \in \{1, \ldots, L\}$ for the expansion function ϑ^d_l and the index $d \in \{0, 1\}$ for the domain.

Often we choose the same number of matching points (M) as we have unknowns (L), but this is not necessarily the best choice. It does have the 'advantage' that the resulting matrix system is of square form and therefore can be solved omitting the error vectors $\mathbf{e}$ and $\mathbf{f}$. Unfortunately this does not mean that we really obtain an exact solution without any error. In fact, this method has the drawback that the error vector is suppressed. Thus we have no control over the real misfit of our solution. The error at the matching points will be very small, but the solution might have a very poor behavior in between matching points (e.g. oscillations).

A better way is to use more matching points than needed ($M \gg L$). This yields an overdetermined system which can be solved in the minimal least-squares sense using the Givens or Householder transformation (Wilkinson, 1988; Schwarz, 1989). On the matching points the approximations will not satisfy the boundary conditions anymore - but the overall error in the boundary conditions will be minimal and the solution is 'smoother' in between matching points.

A problem arising now is the question of weighting. The least-squares solver tends to numerically equal errors for each boundary condition and each matching point. Since boundary conditions must be satisfied for both the displacement and the pressure, their numerical values must be normalized to common physical units. Otherwise one boundary condition dominates the resulting solution. Thus we convert the equations for the pressure to the

same physical units as the displacement by scaling them with $1/(\lambda^0 k^0)$. It would also be possible to non-dimensionalize both pressure and displacement. Furthermore, we choose an individual weighting factor s_m for each matching point to allow a better control of the errors:

- Spatial weighting depends on the spatial properties of the fields. Assuming a numerically equal absolute error $e = f = \epsilon_m$ at each boundary point $\mathbf{x}_m$, we see that the relative error $\epsilon_m/\Phi^d(\mathbf{x}_m)$ depends on the numerical values of the field at that matching point (Leuchtmann and Bomholt, 1993). Without special measures, the simulation will yield an almost arbitrary field $\Phi^d(\mathbf{x}_m)$ where the field values are small, since the numerical values may be smaller than ϵ_m. Thus small field values are lost in the range of error. The numerical result will be determined by spatial properties of the field rather than by the boundary condition. To eliminate this effect, rows should also be weighted with the reciprocal of the respective field $\Phi^d(\mathbf{x}_m)$. Since this is exactly the quantity we are seeking, these weighting functions are a priori unknown. We have to estimate them or to apply an iterative scheme where we use the reciprocal of the prior solution as weights.

- Geometrical weighting depends on the geometry of the model, mainly the locations of the expansion and matching points. An appropriate weight is $s_m = \sqrt{r_m \cdot d_m}$ where $r_m = \min(|\mathbf{x}_m - \mathbf{x}_l^d|)$ for a particular matching point m and multipoles located at $\mathbf{x}_l^d$. The factor r_m compensates for the decay of amplitude with distance due to spreading. The factor $d_m = \frac{1}{2}\left(|\mathbf{x}_m - \mathbf{x}_{m-1}| + |\mathbf{x}_m - \mathbf{x}_{m+1}|\right)$ is the average distance between adjacent matching points. The matching point is weighted by the 'area' of the boundary it controls. Thus, a higher density of matching points in a particular part of the boundary will not automatically reduce the error in that area. Other choices allow to make the method numerically equal to other methods presented in Appendix A.4.

- Additional weighting which is problem dependent. As an example, we can enhance the accuracy of the solution in regions of special interest or decrease it in others. We can also weight displacement and pressure differently. Choosing a scaling factor

$s < 1$ decreases the importance of the boundary condition and its matching point. On the other hand, a scaling factor $s > 1$ makes the boundary condition at that particular matching point more important and thus the boundary condition will be better satisfied.

Consequently, the weighting coefficients s_m should be chosen considering all these aspects.

The number P of the matching points and the orders N of the multipoles are not completely arbitrary (Hafner, 1990; Hafner and Bomholt, 1993). No multipole should be within the region of greatest influence of any other multipole. For a multipole located at $\mathbf{x}_l^d$, the region of greatest influence is a circle centered at $\mathbf{x}_l^d$ and radius $\sqrt{2} \cdot \min(|\mathbf{x}_m - \mathbf{x}_l^d|)$, where $\mathbf{x}_m$ are the matching points. The maximum order N^{max} of a multipole $\sum_{-N}^{+N} a_n \vartheta_n$ is limited by the sampling theorem. N^{max} is given by the largest angle φ^{max} between two adjacent matching points $\mathbf{x}_m$ and $\mathbf{x}_{m+1}$ and the location $\mathbf{x}_l^d$ of the multipole (Figure 2-2):

$$N^{max} < \frac{\pi}{\varphi^{max}} . \tag{2.16}$$

2.2 External Multiple Scattering

So far, we have only considered one scattering object. The extension to multiple scattering objects is straight forward. We assume that the scatterers don't intersect each other (Figure 2-3). For each additional scatterer, we use another expansion of the form of (2.9) with at least one multipole. Vekua (1967) proved that the field in the background region Γ^0 can be expanded as described if each scatterer Γ^d contains one multipole. The theorem also holds for multiple multipoles expansions because a multipole can be expanded into a multiple multipole and vice versa by using the addition theorems for Bessel functions (Abramowitz and Stegun, 1964). Thus for D scatterers, we write the field in the background as:

$$\Phi^0(\mathbf{x},\omega) = \sum_{d=1}^{D} \sum_{p=1}^{P} \sum_{n=-N}^{N} a_{pn}^{0d} e^{in\theta} H_{|n|}^{(1)} \left(k^0 \, |\mathbf{x} - \mathbf{x}_p^d|\right) + \epsilon^0(\mathbf{x},\omega) . \tag{2.17}$$

The fields in the scatterers we write as in equation (2.10):

$$\Phi^d(\mathbf{x},\omega) = \sum_{p=1}^{P} \sum_{n=-N}^{N} a_{pn}^{dd} e^{in\theta}\, J_{|n|}\left(k^d\,|\mathbf{x}-\mathbf{x}_p^d|\right) \;+\; \epsilon^d(\mathbf{x},\omega)\,. \tag{2.18}$$

In order to eliminate an index, we renumber the expansion functions ϑ_{pn}^s and their coefficients a_{pn}^{ds} resulting in ϑ_l^s and a_l^{ds}. Expanding our previous notation slightly, we can write the resulting matrix equation in a similar form as (2.11):

$$\begin{pmatrix} -\mathbf{W}^{01}_{\partial\Gamma_{01}} & \cdots & -\mathbf{W}^{0D}_{\partial\Gamma_{01}} & \mathbf{W}^{11}_{\partial\Gamma_{01}} & \cdots & \mathbf{0} \\ \vdots & & \vdots & \vdots & \ddots & \vdots \\ -\mathbf{W}^{0D}_{\partial\Gamma_{0D}} & \cdots & -\mathbf{W}^{DD}_{\partial\Gamma_{0D}} & \mathbf{0} & \cdots & \mathbf{W}^{DD}_{\partial\Gamma_{0D}} \\ -\mathbf{T}^{01}_{\partial\Gamma_{01}} & \cdots & -\mathbf{T}^{0D}_{\partial\Gamma_{01}} & \mathbf{T}^{11}_{\partial\Gamma_{01}} & \cdots & \mathbf{0} \\ \vdots & & \vdots & \vdots & \ddots & \vdots \\ -\mathbf{T}^{0D}_{\partial\Gamma_{0D}} & \cdots & -\mathbf{T}^{DD}_{\partial\Gamma_{0D}} & \mathbf{0} & \cdots & \mathbf{T}^{DD}_{\partial\Gamma_{0D}} \end{pmatrix} \cdot \begin{pmatrix} \mathbf{a}^{01} \\ \vdots \\ \mathbf{a}^{0D} \\ \mathbf{a}^{11} \\ \vdots \\ \mathbf{a}^{DD} \end{pmatrix} \backsimeq \begin{pmatrix} \mathbf{w}_{\partial\Gamma_{01}} \\ \vdots \\ \mathbf{w}_{\partial\Gamma_{0D}} \\ \mathbf{t}_{\partial\Gamma_{01}} \\ \vdots \\ \mathbf{t}_{\partial\Gamma_{0D}} \end{pmatrix}. \tag{2.19}$$

As before, each row evaluates the boundary condition of continuity of either normal displacement or pressure at one particular matching point. The symbols $\mathbf{W}^{ds}_{\partial\Gamma_{kl}}$ and $\mathbf{T}^{ds}_{\partial\Gamma_{kl}}$ denote submatrices for normal displacement and pressure at the matching points. Specifically, we use the index d to indicate in which domain Γ^d the field is evaluated. The index s indicates the scatterer which induces this field in the domain Γ^d. Finally the symbol $\partial\Gamma_{xy}$ denotes the boundary the matching point belongs to. All scatterers contribute to the scattered field Φ^0 in the background domain Γ^0. Therefore, we have submatrices $\mathbf{W}^{0s}_{\Gamma_{0s}}$ and $\mathbf{T}^{0s}_{\Gamma_{0s}}$ for each scatterer and each boundary. But because scatterer Γ^x has no common boundary with scatterer Γ^y, the fields Φ^x and Φ^y in the scatterers do not interact with each other. Thus for $s \neq d$ and $d \neq 0$ the submatrices $\mathbf{W}^{sd}_{\Gamma_{0s}}$ and $\mathbf{T}^{sd}_{\Gamma_{0s}}$ vanish. The individual scatterers are only coupled by the field Φ^0 in the background domain Γ^0. All multiple scattering is automatically accounted for by the boundary conditions. The only contribution for the fields within a scatterer are due to the self interactions $\mathbf{W}^{ss}_{\Gamma_{0s}}$ and $\mathbf{T}^{ss}_{\Gamma_{0s}}$ where $s = d$. Again, we define the matching points by their location $\mathbf{x}_m$ and their normal direction $\hat{\mathbf{n}}_m = \hat{\mathbf{n}}(\mathbf{x}_m)$

with respect to the domain boundary $\partial\Gamma_{kl}$. Then we can write the submatrices and vectors as

$$W_{ml}^{ds} = \hat{\mathbf{n}}_m \cdot \nabla \vartheta_l^s(k^d|\mathbf{x}_m - \mathbf{x}_l^s|)\,, \tag{2.20}$$

$$T_{ml}^{ds} = -\lambda^d\,(k^d)^2\,\vartheta_l^s(k^d|\mathbf{x}_m - \mathbf{x}_l^s|)\,, \tag{2.21}$$

$$w_m = \hat{\mathbf{n}}_m \cdot \nabla \Phi^{inc}(\mathbf{x}_m, \omega)\,, \tag{2.22}$$

$$t_m = -\lambda^d\,(k^d)^2\,\nabla\Phi^{inc}(\mathbf{x}_m, \omega)\,. \tag{2.23}$$

2.3 Internal Multiple Scattering

Placing a scatterer within another scatterer yields a slightly different form for the matrix system. We want to have D scatterers recursively within each other such that they don't intersect or touch. We also assume that there is only one such scattering object in the background domain Γ^0 (see Figure 2-4). Then again we can use expansion (2.9) for the potential field in the background domain Γ^0:

$$\Phi^0(\mathbf{x},\omega) = \sum_{p=1}^{P}\sum_{n=-N}^{N} a_{pn}^{01} e^{in\theta}\, H_{|n|}^{(1)}\left(k^0\,|\mathbf{x} - \mathbf{x}_p^d|\right) + \epsilon^0(\mathbf{x},\omega)\,. \tag{2.24}$$

To enhance the convergence for the fields $\Phi^d(\mathbf{x},\omega)$ $(0 < d < D)$, we should add an additional expansion to the fields within each scatterer (2.18) which takes care of the scattering from the enclosed object Γ^{d+1}. This is again a consequence of the theorem of Vekua (1967) which is here used recursively. In analogy to the boundary value problem for an annular geometry, we choose solutions involving the Neumann functions (Morse and Feshbach, 1953). Notice that a multiple multipole expansion built by either Bessel functions or Hankel functions would yield a solution due to the non-orthogonal and overdetermined nature of the expansion. But the better the expansion functions approximate the behavior of the

solution sought, the faster the series will converge.

$$\Phi^d(\mathbf{x},\omega) = \sum_{p=1}^{P}\sum_{n=-N}^{N}\left\{a_{pn}^{dd}e^{in\theta}\,J_{|n|}\left(k^d\,|\mathbf{x}-\mathbf{x}_p^d|\right) + a_{pn}^{d(d+1)}e^{in\theta}\,Y_{|n|}\left(k^d\,|\mathbf{x}-\mathbf{x}_p^{(d+1)}|\right)\right\} + \epsilon^d(\mathbf{x},\omega) \qquad \text{for } 0<d<D \tag{2.25}$$

The field inside scatterer Γ^D we model as (2.18):

$$\Phi^D(\mathbf{x},\omega) = \sum_{p=1}^{P}\sum_{n=-N}^{N} a_{pn}^{DD}e^{in\theta}\,J_{|n|}\left(k^D\,|\mathbf{x}-\mathbf{x}_p^d|\right) + \epsilon^D(\mathbf{x},\omega)\,. \tag{2.26}$$

Thus we can again set up a matrix system similar to (2.19). To simplify the notation we use $C = D-1$ and $B = D-2$. The submatrices and vectors are the same as defined in equations (2.20) to (2.23):

$$\begin{pmatrix}
-\mathbf{W}^{01}_{\partial\Gamma_{01}} & \mathbf{W}^{11}_{\partial\Gamma_{01}} & \mathbf{W}^{12}_{\partial\Gamma_{01}} & & \\
 & -\mathbf{W}^{11}_{\partial\Gamma_{12}} & -\mathbf{W}^{12}_{\partial\Gamma_{12}} & \mathbf{W}^{22}_{\partial\Gamma_{12}} & \mathbf{W}^{23}_{\partial\Gamma_{12}} \\
 & \ddots & \ddots & \ddots & \ddots \\
 & -\mathbf{W}^{BB}_{\partial\Gamma_{BC}} & -\mathbf{W}^{BC}_{\partial\Gamma_{BC}} & \mathbf{W}^{CC}_{\partial\Gamma_{BC}} & \mathbf{W}^{CD}_{\partial\Gamma_{BC}} \\
 & & -\mathbf{W}^{CC}_{\partial\Gamma_{CD}} & -\mathbf{W}^{CD}_{\partial\Gamma_{CD}} & \mathbf{W}^{DD}_{\partial\Gamma_{CD}} \\
-\mathbf{T}^{01}_{\partial\Gamma_{01}} & \mathbf{T}^{11}_{\partial\Gamma_{01}} & \mathbf{T}^{12}_{\partial\Gamma_{01}} & & \\
 & -\mathbf{T}^{11}_{\partial\Gamma_{12}} & -\mathbf{T}^{12}_{\partial\Gamma_{12}} & \mathbf{T}^{22}_{\partial\Gamma_{12}} & \mathbf{T}^{23}_{\partial\Gamma_{12}} \\
 & \ddots & \ddots & \ddots & \ddots \\
 & -\mathbf{T}^{BB}_{\partial\Gamma_{BC}} & -\mathbf{T}^{BC}_{\partial\Gamma_{BC}} & \mathbf{T}^{CC}_{\partial\Gamma_{BC}} & \mathbf{T}^{CD}_{\partial\Gamma_{BC}} \\
 & & -\mathbf{T}^{CC}_{\partial\Gamma_{CD}} & -\mathbf{T}^{CD}_{\partial\Gamma_{CD}} & \mathbf{T}^{DD}_{\partial\Gamma_{CD}}
\end{pmatrix} \cdot \begin{pmatrix} \mathbf{a}^{01} \\ \mathbf{a}^{11} \\ \mathbf{a}^{12} \\ \vdots \\ \mathbf{a}^{CC} \\ \mathbf{a}^{CD} \\ \mathbf{a}^{DD} \end{pmatrix} \backsimeq \begin{pmatrix} \mathbf{w}_{\partial\Gamma_{01}} \\ \vdots \\ \mathbf{w}_{\partial\Gamma_{CD}} \\ \mathbf{t}_{\partial\Gamma_{01}} \\ \vdots \\ \mathbf{t}_{\partial\Gamma_{CD}} \end{pmatrix} \tag{2.27}$$

where $\mathbf{w}_{\partial\Gamma_{12}}, \ldots, \mathbf{w}_{\partial\Gamma_{CD}}$, $\mathbf{t}_{\partial\Gamma_{12}}, \ldots, \mathbf{t}_{\partial\Gamma_{CD}}$ are zero because the incident wavefield Φ^{inc} is located in Γ^0.

2.4 Generalizations of the technique

So far we only used expansion functions such as $e^{in\theta}\, J_{|n|}(kr)$, $e^{in\theta}\, Y_{|n|}(kr)$ and $e^{in\theta}\, H^{(1)}_{|n|}(kr)$. It is obvious that we could also use $e^{in\theta}\, H^{(2)}_{|n|}\,(kr)$ or any linear combination of Bessel functions for an expansion. All these functions are solutions to the Helmholtz equation (2.1) in cylindrical coordinates. In fact, any function which satisfies the wave equation (2.1) in any coordinate system is a potential basis function because the property of satisfying the wave equation is independent of the coordinate system chosen. Of course, the actual representation of a particular solution might be easier in one coordinate system than in another one. But nothing prevents us from using a different local coordinate system for each basis function. We are already making use of this by using multiple expansion points $\mathbf{x}^d_p$ which corresponds to a different local coordinate system for each multipole.

Best known among additional coordinate systems is the Cartesian one with the plane wave solution $e^{i\mathbf{k}\cdot\mathbf{r}}$. We can also use these plane waves in discrete directions $\mathbf{k}_l$ as additional basis functions. Other choices are, e.g., solutions in elliptic or parabolic coordinates (Morse and Feshbach, 1953) or beams (Deschamps, 1971; Shin and Felsen, 1977). Eventually the choice of the expansions depends on prior knowledge or expectations. The better a basis function approximates the real solution, the faster the expansion converges.

In some cases, it is useful to choose a linear combination of basis functions as one basis function. An example of this is the perturbation of a previously solved problem. Then we can use the prior solution to the unperturbed system as one basis function which can be rather complex. But this one expansion function will yield nearly the correct fields. Thus, we add a few additional basis functions as corrections for the perturbation. The resulting matrix system will be much smaller than the one solving the perturbed problem without using the prior solution.

We are also not limited to either external or internal multiple scattering. We can mix all these cases in any way we desire, leading to a general system of the form

$$\begin{pmatrix} \mathbf{W} \\ \mathbf{T} \end{pmatrix} \cdot \mathbf{a} = \begin{pmatrix} \mathbf{w} \\ \mathbf{t} \end{pmatrix} + \begin{pmatrix} \mathbf{e} \\ \mathbf{f} \end{pmatrix}, \tag{2.28}$$

where the rows contain one of the boundary conditions evaluated at a particular matching point, while the columns contain the contributions of that particular expansion function at the matching points. Expansions governing a domain which does not contribute at that particular boundary simply yield a zero entry. It is also obvious that we can choose different maximal orders for different multipoles. We may even skip certain orders, e.g. use only the even ones. For every scatterer Γ^d, we can choose different expansion points $\mathbf{x}_p^d$ and a different number of multipoles expanding the fields Φ^0 and Φ^d induced by scatterer Γ^d. For the sake of simplicity, we will not exploit these possibilities in this paper. We will use all orders between $-N$ and $+N$ and use the same expansion points for both Φ^0 and Φ^d.

For other problems, we might want to adjust our simple set of basis functions. As an example, for scatterers on top of a layered halfspace (Figure 2-5), we add the reflections from the layers to each expansion function governing the field in the background, so that all interactions with the halfspace are implicitly included in the expansion. We make use of the raising operator (Chew, 1990) which relates a solution of order n of the Helmholtz equation (2.1) to a solution of order $n+1$:

$$e^{i(n+1)\theta}\, Z_{n+1}(kr) = -k \left[\frac{\partial}{\partial x} + i \frac{\partial}{\partial z} \right] e^{in\theta}\, Z_n(kr)\,. \tag{2.29}$$

This holds for $Z_n(kr)$ being any linear combination of $J_n(kr)$, $Y_n(kr)$, $H_n^{(1)}(kr)$ and $H_n^{(2)}(kr)$. Using the integral form for the Hankel functions of the first kind

$$H_0(kr) = e^{i0\theta}\, H_0(kr) = \frac{1}{\pi} \int_{-\infty}^{+\infty} \frac{e^{ik_x x + ik_z |z|}}{k_z}\, dk_x\,, \tag{2.30}$$

we can write any higher order solution involving Hankel functions of the first kind as

$$e^{in\theta}\, H_n(kr) = \frac{1}{\pi}\int_{-\infty}^{+\infty} \frac{e^{ik_x x + ik_z|z|}}{k_z}\left(\frac{ik_x \mp k_z}{-k}\right)^n dk_x\,. \tag{2.31}$$

Similar expressions result for $J_n(kr)$, $Y_n(kr)$, and $H_n^{(2)}(kr)$ by using the real or imaginary part or the conjugate complex in the expressions (2.30) and (2.31). The wavefield Φ due to a generalized interface $\tilde{R}$ at a depth $z = -d$ can then be written as

$$\Phi = \frac{1}{\pi}\int_{-\infty}^{+\infty} \tilde{R}(k_z)\frac{e^{ik_x x}}{k_z} e^{ik_z(z+2d)}\left(\frac{ik_x \mp k_z}{-k}\right)^n dk_x\,, \tag{2.32}$$

where we used the generalized reflection coefficient $\tilde{R}(k_z)$ (Kennett, 1983; Chew, 1990; Kong, 1990). This reflection coefficient contains all reflections from the layered halfspace. For a simple halfspace, it reduces to the familiar $\tilde{R}(k_z) = (1-p)/(1+p)$ where $p = k_z^0\lambda^0/k_z^1\lambda^1$. We evaluate expression (2.32) using the stationary phase approximation (Chew, 1988). The stationary phase point yields

$$k_x^s = \frac{kx}{\sqrt{x^2+(z+2d)^2}}\,, \tag{2.33}$$

$$k_z^s = \frac{k(z+2d)}{\sqrt{x^2+(z+2d)^2}}\,. \tag{2.34}$$

Combining the stationary phase point with equation (2.32) yields the expected result

$$\Phi = \tilde{R}(k_z^s)\, e^{in\psi}\, Z_n(k\sqrt{x^2+(z+2d)^2})\,. \tag{2.35}$$

We easily recognize this expression as the wave generated by the mirror source, weighted by the generalized reflection coefficient evaluated at the stationary phase point. Adding direct and reflected wave yields:

$$\vartheta_n = e^{in\theta}\, Z_n(kr) + \tilde{R}(k_z^s)\, e^{in\psi}\, Z_n(k\sqrt{x^2+(z+2d)^2})\,. \tag{2.36}$$

Thus for the case of the more complex system involving a stack of flat layers, we simply adapted the basis functions to contain the reflected field as well.

2.5 Implementation

The objective in seismic forward modelling is normally to obtain a synthetic seismogram. Because we formulated the problem in the frequency domain, we have to solve the problem for a range of frequencies such that we can apply a Fourier transformation to obtain the seismogram. All these problems can be solved independently of each other. Hence we can use a parallel computer to speed up the calculation. Each processor will only calculate a few frequencies.

The matrix computed in this procedure can become large. Different numerical schemes were developed to obtain the least-squares solution for a general linear systems. There exist mainly two techniques for solving the system without using the classical normal equations: Householder and Givens transformation (Wilkinson, 1988; Schwarz, 1989). The faster one is the Householder transformation. Unfortunately, it requires the storage of the complete matrix in the core memory of the computer. Even for medium sized problems the amount of memory needed becomes too large for small computers. Better suited, but slower, is the Givens transformation which processes the matrix system one row at a time. Thus we can calculate a row, corresponding to one boundary condition at one matching point, one at a time and update the coefficient matrix accordingly (George and Heath, 1980).

In the general case (2.28), it is no longer important what a particular expansion $\vartheta_l(\mathbf{x}, \omega)$ represents. All we need to know is its contribution towards either boundary condition evaluated at a matching or receiver point. The same holds for the matching points. We do not care what boundary condition they represent as long as we can build the rows for the matrix system governed by that matching point. For these reasons, the scheme is perfectly suited for an object oriented implementation where the expansion functions for source and scattered fields as well as the matching points with their boundary conditions are represented by independent objects. All the objects for the fields have to know is how to evaluate the displacements or the pressure at some place $\mathbf{x}$. All the objects for the matching points have to know is how to build the rows of the matrix system for at a particular matching point. Despite being slower than a direct implementation, the object

oriented approach has the advantage of allowing any geometric configuration and any kind of expansions we desire without changing the program. New boundary conditions, e.g. hard or soft boundaries, or new expansion functions, e.g. plane waves, are simply incorporated by defining the necessary objects. Even a future expansion into 3 dimensions or an application to fully elastic media will merely require the definition of additional objects. The main driver will always stay the same.

Consequently, we implemented this method on a nCUBE2 parallel computer using the computer language C++ for the main program and the FORTRAN version of the LINPACK library (Dongarra *et al.*, 1979) to solve the linear matrix. To reduce numerical noise, we make the materials lossy by adding a small imaginary component ω_I to the frequency (Bouchon and Aki, 1977). Thus we have to evaluate Bessel functions with a complex argument (Amos, 1986). After the transformation from the frequency domain into the time domain, we recover the true amplitude by a multiplication with $e^{\omega_I t}$.

2.6 Numerical Results

As a first example, we want to examine how different discretizations affect the solutions obtained. We have to choose the number and orders of the expansion functions, the number of multipoles, and the number of equations or matching points. Thus, for the first example depicted in Figure 2-6, we will vary the MMP discretizations and compare the results to a reference solution obtained by finite differences. The scatterer is roughly 240 m in length and 50 m in thickness. The density and velocity in the background are $\rho^0 = 2000\,\mathrm{kg/m^3}$ and $\alpha^0 = 2000\,\mathrm{m/s}$, respectively. In the scatterer, the density and velocity are $\rho^1 = 2000\,\mathrm{kg/m^3}$ and $\alpha^1 = 3000\,\mathrm{m/s}$. Thus, the density $\rho^{0,1}$ is the same for both regions.

For the sake of simplicity, the incident field p^{inc} is an explosive line source modulated with a Ricker pulse (Hosken, 1988; Paillet and Cheng, 1991) of 50 Hz center frequency. Altogether, 64 receivers will measure the pressure of the scattered field $p^0(\mathbf{x}, t)$. The center frequency of 50 Hz yields an incident wavelength of 40 m which roughly equals the thickness of the

scatterer.

To measure how well the MMP seismogram $p^{MMP}(r,t)$ correlates with the FD reference seismogram $p^{FD}(r,t)$ shown in Figure 2-7, we define the root mean square error (RMSE) as the squared difference between the two seismograms over all timesamples t and all receivers r:

$$\text{RMSE} = \frac{1}{\sqrt{RT}} \sqrt{\sum_{r=1}^{R} \sum_{t=1}^{T} \left\{ p^{MMP}(r,t) - p^{FD}(r,t) \right\}^2}, \tag{2.37}$$

where $R = 64$ is the number of recorders and $T = 256$ is the total number of time samples.

As a first numerical experiment, we study how the number of expansion functions (2.9),(2.10) affects the solution. To accomplish this, we start with either 2 expansion functions and one expansion center for the classical SMP case, or 16 expansion functions and eight expansion centers for the MMP case. Thus, at each expansion center, we placed a monopole for each field $\Phi^0(\mathbf{x},\omega)$ and $\Phi^1(\mathbf{x},\omega)$. For each case, we calculate the solution and estimate the RMSE. Then, we add dipole fields to each expansion center, recalculate the solution and estimate the RMSE. We double the number of expansion functions while keeping the number of expansion centers constant ($P = 1$ for SMP, $P = 8$ for MMP), recalculate the solution, estimate the RMSE and so on. The resulting RMSE curve as a function of the number of expansion functions is presented in Figure 2-9. The SMP expansion never converges! For more than 256 expansion functions, the matrix system becomes numerically singular due to the high order Bessel- and Hankel solutions. The classical SMP is not able to solve the problem posed in Figure 2-6. Conversely, the MMP expansions converge for more than 128 expansion functions. Thus, using 8 multipoles and maximal orders $N = \pm 4$ was enough to converge to the correct result. Increasing the maximal order even further yields a slightly better result by attenuating spurious but minute events. The seismogram obtained with 8 multipoles and orders $N = \pm 8$ is shown in Figure 2-8.

The second numerical experiment is to study how the number of multipoles affects the solution. While the total number of expansion functions is kept constant at 128, the number

of expansion centers is varied between 1 and 23. Also, the number of matching points is kept constant at 256. Thus, the computational effort to calculate each seismogram is the same. The resulting RMSE as a function of the number of expansion centers is shown in Figure 2-10. The whole range from 7 to 13 expansion centers converges with an optimum for 9 or 10 multipoles. The optimal ones are only slightly better than any other discretization employing 7 to 13 centers. MMP expansions are insensitive to the discretization used! The pathological case with 23 expansion centers shows that the errors increase dramatically when too many expansion centers are used. In this particular case, the expansion centers are separated by only a quarter of the dominant wavelength. The different expansion functions begin to interact by approximating higher order solutions to the wave equation. It is well-known that two monopoles of opposite sign placed closely together are equivalent to a dipole (Morse and Feshbach, 1953). Thus, the matrix system becomes badly conditioned since each expansion center could be replaced by the adjacent ones. Moreover, we add more similar equations to the matrix system which renders it more ill-conditioned. As a comparison, we also simulate a simple boundary element (BEM) discretization where all the multipoles are placed on the boundary using only the monopole terms. The large RMSE indicates that this expansion does not converge.

The next experiment is to study the tradeoff between the number of expansion centers and the orders of the multipoles. Figure 2-11 presents the RMSE as a function of the number of expansion centers P and the maximal orders $\pm N$ of the multipoles. The solution has converged for a RMSE of 0.05 or smaller. Clearly, the MMP expansion converges for $N = 2$ and $P = 13$, or for $N = 8$ and $P = 7$. Incidentally, the best result is obtained for $N = 8$ and $P = 8$. But there is also a tradeoff between RMSE and the computational effort, i.e., the total number of expansion functions $2(2N + 1)P$. Taking the computational effort into account, the optimal result is obtained by using 7 to 9 expansion centers and a maximal order of multipole of 3 to 5. Using the addition theorem for the Bessel functions (Abramowitz and Stegun, 1964)

$$H_0(k\,|\mathbf{x} - \mathbf{x}_m|) = \sum_{n=-\infty}^{+\infty} J_n(k\,|\mathbf{x}_m|)\; H_n(k\,|\mathbf{x}|)\; e^{in(\theta-\theta_m)}\,, \tag{2.38}$$

we transform a virtual monopole source located on the boundary $\mathbf{x}_m$ into a multipole at the origin. The present form of the addition theorem assumes the receiver $\mathbf{x}$ to be outside the scatterer. The Bessel function $J_n(k\,|\mathbf{x}_m|) = J_n(kx_m)$ can be asymptotically expanded for large orders as (Abramowitz and Stegun, 1964)

$$J_n(kx_m) \approx \frac{1}{\sqrt{2\pi n}}\Big(\frac{ekx_m}{2n}\Big)^n, \tag{2.39}$$

which vanishes for $kx < n$ as $n \to \infty$. For the model used, kx_m is around 6 for the dominant wavelength. For $n > 3$, the Hankel terms have less effect because the Bessel terms begin to vanish. This is consistent with Figure 2-11. For 4 to 10 expansion centers, increasing the order of the multipoles beyond $N = 4$ hardly effects the RMSE.

Finally, we study the effect of the number of equations per unknown. The fields are expanded with 9 multipoles and 128 expansion functions in accordance with the prior experiment. The boundary is discretized with 64 to 2048 matching points which corresponds to 1 to 32 equations per expansion function. The resulting RMSE is shown in Figure 2-12. As expected, one equation per unknown does not perform well for the non-orthogonal MMP expansion. The optimum is 2 equations per unknown. Increasing the number of equations further increases the RMSE because the matrix system becomes more ill-conditioned with each additional equation we add. The result is a larger error due to roundoff and other numerical effects.

As a second example, we compare the multiple multipole expansion against finite differences. As model, we use two elliptical scatterers which are illuminated by an explosion source. The configuration is shown in Figure 2-13. Both scatterers are elliptical cylinders with a semi-major axis of 40 m and a semi-minor axis of 30 m. The velocity α^0 in the background is 2000 m/s. The velocities $\alpha^1 = \alpha^2$ in both scatterers are 3000 m/s. The density ρ in the background and scatterers is kept constant at 2000 kg/m^3. The source function is a line source with a Ricker wavelet of 50 Hz.

For the finite difference case, we used a grid spacing of 1 m and a grid of 600 by 600 points.

The timestep was 0.125 ms. The runtime on a nCUBE2 using 64 nodes was 300 seconds. For the multiple multipole expansion, we used a total of 120 expansion functions, 200 matching points and 64 frequencies. The scattered fields are described by two multipoles per scatterer. The resulting runtime on a nCUBE2 using again 64 nodes was 150 seconds. The two methods yield very similar results. Figure 2-14 shows the seismogram calculated using the multiple multipole expansion. The seismogram calculated by finite differences is presented in Figure 2-15. As can be seen, they agree very well in both traveltimes and phases.

As a third example, we calculate the scattered fields due to the elliptical scatterer depicted in Figure 2-16. For the sake of simplicity, we use a monochromatic planar field modulated with a Ricker wavelet (Hosken, 1988; Paillet and Cheng, 1991) of 50 Hz center frequency as source field Φ^{inc}. The angle of incidence is 5°. The scatterer is an elliptical cylinder with a semi-major axis of 80 m and a semi-minor axis of 30 m. The velocity α^0 and density ρ^0 in the background are 2000 m/s and 2000 kg/m^3. The velocity α^1 and density ρ^1 in the scatterer are 3000 m/s and 2500 kg/m^3. Assuming a frequency of 50 Hz for the monochromatic incident field yields a wavelength of essentially of same size as the scatterer. We expand each of the two wavefields Φ^0 and Φ^1 with five multipoles and choose the orders to yield altogether 80 expansion functions and thus 80 unknown coefficients. We choose 100 matching points which results in an equation system of size 80×200. Thus, we have 2.5 times more equations than unknowns. Using 64 frequencies and 64 nodes we obtain a runtime of 65 seconds on the nCUBE2 parallel computer. Figure 2-18 shows the resulting seismogram. Both reflections from the top of the scatterer as well as from the bottom can clearly be seen.

As an extension of the third example, we want to show the effect of a halfspace on the model in example 3 (Figure 2-16). We change the previous model to include a simple halfspace below the depth of 200 m. For simplicity, we choose the same material parameters for the halfspace as for the scatterers. The extended model is shown in Figure 2-17. Again, we choose the incident field Φ^{inc} to be a planar Ricker wavelet with a center frequency of 50 Hz and angle of incidence of 5°. The only differences from the computations for model 3

(Figure 2-16) are the basis functions. As shown before, we use the modified basis functions (2.36) also containing the wavefields from the mirror sources located at $\mathbf{x}_{m_p}$. Thus, the form of the resulting matrix system is the same as (2.11). After a runtime of about 80 seconds we obtain the seismogram (Figure 2-19).

Additionally to the seismogram in Figure 2-18, we have reflections from the halfspace as well as interactions between scatterer and halfspace. On both the left and the right side of the scatterer, the undisturbed reflection from the halfspace can be observed. Underneath the scatterer, the halfspace reflection is lifted upwards due to the fast scatterer. These reflections coming from underneath are much weaker because the halfspace is in the shadow of the scatterer. Below the halfspace reflection, we find some weak interactions between halfspace and scatterer.

Theoretical considerations yield a linear dependence of the runtime on the number M of matching points used. For the models discussed, we also found a roughly linear dependence of the runtime on the number L of unknown coefficients. Thus setting up the equation system dominates the runtime. For larger systems, the least-squares procedure becomes dominant and the runtime will be of order $O(L^3)$.

2.7 Summary

We presented a new expansion technique where the basis functions are *non-orthogonal.* For that reason we *overdetermine* the resulting matrix system. Thus, we also get an estimate of the absolute and relative misfits using the residuals of the least-squares procedure. Numerical experiments show that the expansion converges faster than a traditional, orthogonal scheme. In one example involving an elongated scattering object, orthogonal expansions did not even converge. Instead, the resulting matrix system became numerically singular.

For another example involving two scatterers, we found the new expansion to be twice as fast as finite difference modelling with approximately the same degree of accuracy. In the

example, source, receivers and scatterers were located close to each other. For problems with larger distances between them, we expect an even greater decrease in computation time compared to finite differences.

The formalism is very general and allows the incorporation of multiple scattering in a very natural way. Furthermore, we can choose expansion functions which satisfy certain properties from the beginning. We presented a problem where a scatterer was underlain by an infinite halfspace. The complete effect of the halfspace was incorporated in the expansion functions by adding mirror sources. Thus the method is very general, we can calculate different problems without changing the formalism.

Due to its spectral nature, the method is well suited to be used on a parallel computer. The formalism suggests that an object oriented programming language be used. This has the advantage that additional expansion functions, additional boundary conditions, or a future expansion into 3 dimensional applications or fully elastic media merely means to define the new objects for the expansion functions and boundary conditions.

The method is well suited to solve multiple scattering in two dimensions for a large range of problems and many different applications.

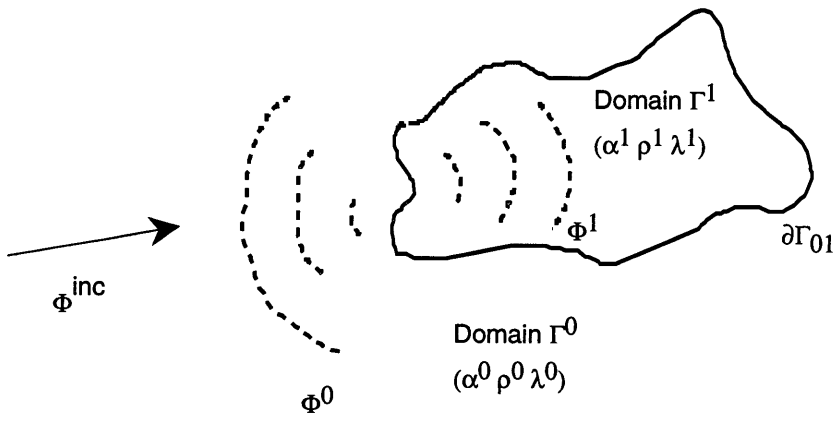

Figure 2-1: Schematic representation of the scattering experiment. An incident field $\Phi^{inc}(\mathbf{x},\omega)$ illuminates a bounded, two-dimensional inhomogeneity which induces a scattered field $\Phi^0(\mathbf{x},\omega)$ in the background medium $(\alpha^0,\lambda^0,\rho^0)$ as well as a field $\Phi^1(\mathbf{x},\omega)$ in the scatterer itself $(\alpha^1,\lambda^1,\rho^1)$.

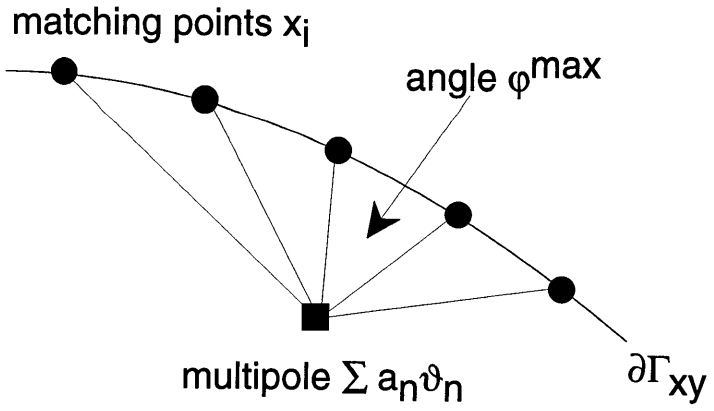

Figure 2-2: The maximum order N^{max} of a multipole $\sum_{-N}^{N} a_n\vartheta_n$ is given by the largest angle φ^{max} between two adjacent matching points and the multipole.

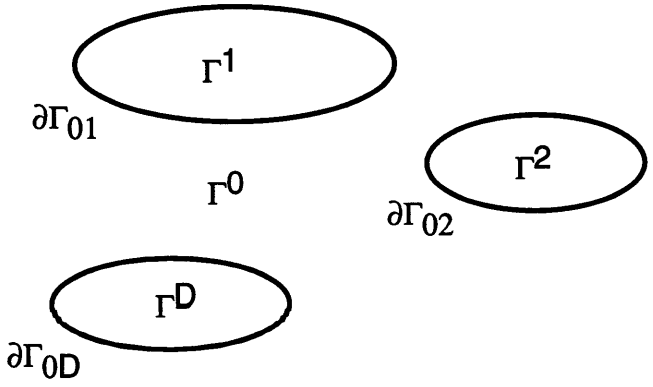

Figure 2-3: Definition of external multiple scattering. The background domain Γ^0 contains multiple scatterers which don't intersect or touch. No scatterer is part of any other scatterer.

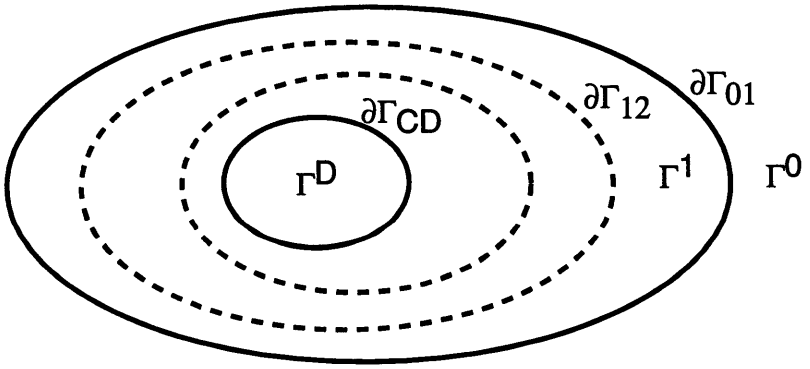

Figure 2-4: Definition of internal multiple scattering. The background domain Γ^0 contains one scatterer which is build up recursively by adding one scatterer into the other. The different scatterers don't intersect or touch.

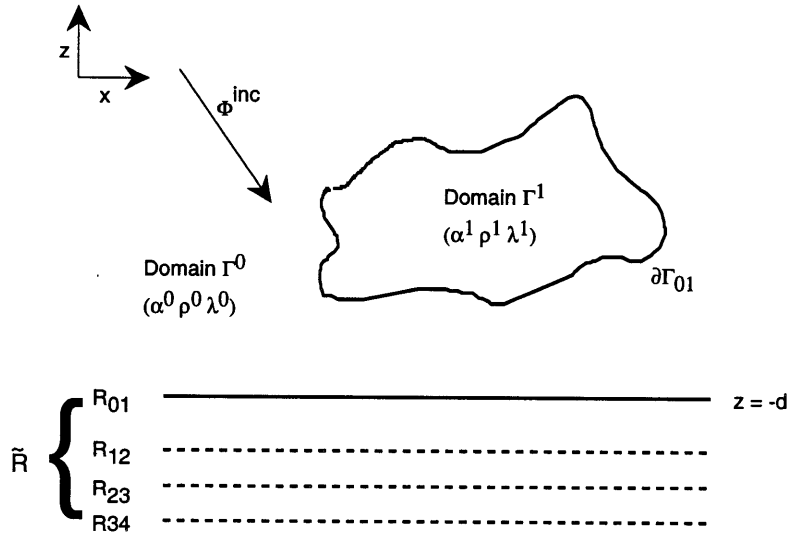

Figure 2-5: Schematic representation of a single scatterer underlain by a stack of flat layers. All the reflections from that stack can be expressed by a generalized reflection coefficient $\tilde{R}(k_z^0)$.

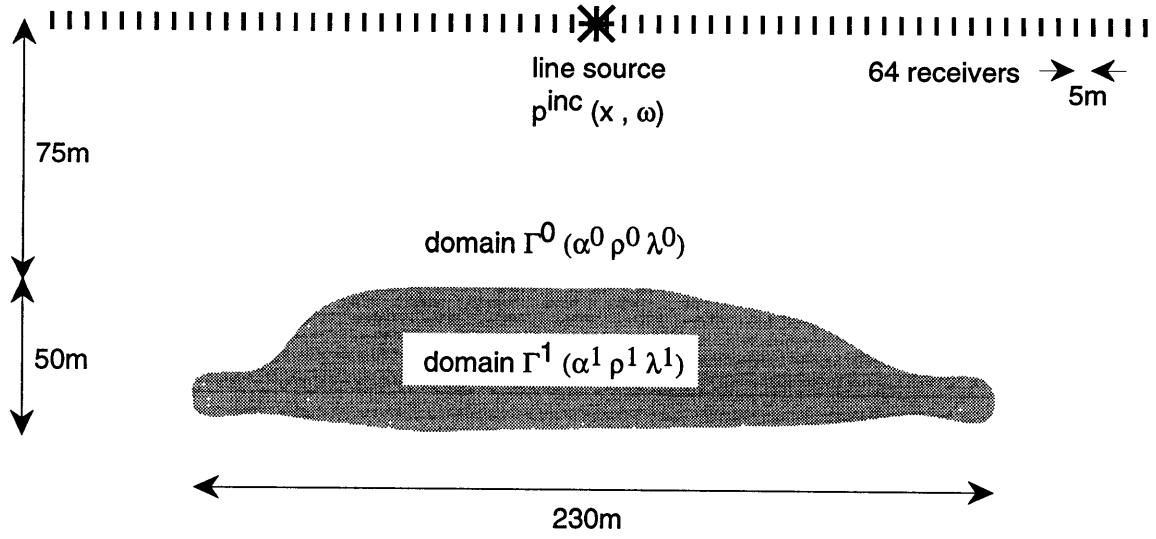

Figure 2-6: Generic scatterer used for numerical experiments. The scatterer is illuminated by an explosive line source modulated by a Ricker pulse of 50 Hz center frequency. The velocity in the background domain Γ^0 is $\alpha^0 = 2000\,\mathrm{m/s}$. The velocity in the scatterer Γ^1 is $\alpha^1 = 3000\,\mathrm{m/s}$. The density $\rho^{0,1} = 2000\,\mathrm{kg/m^3}$ is the same in both regions.

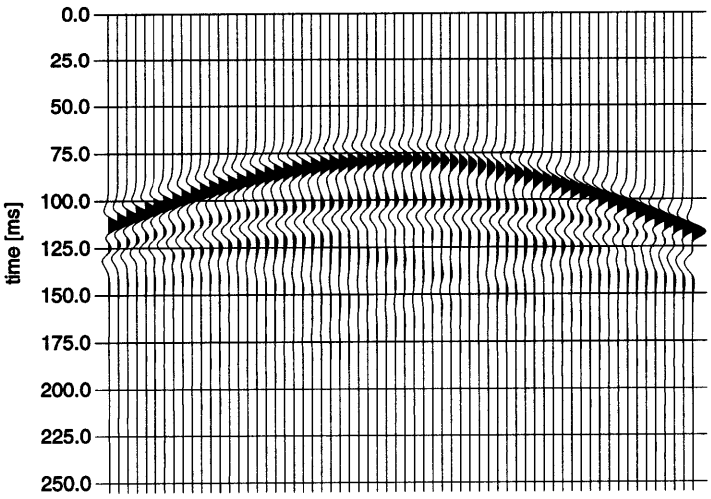

Figure 2-7: The seismogram for the model shown in Figure 2-6 as produced by an acoustic finite difference code. The source function is a line source with a Ricker wavelet of 50 Hz. This seismogram is used as a reference to compare the outcome of different MMP discretizations against. The incident field is suppressed.

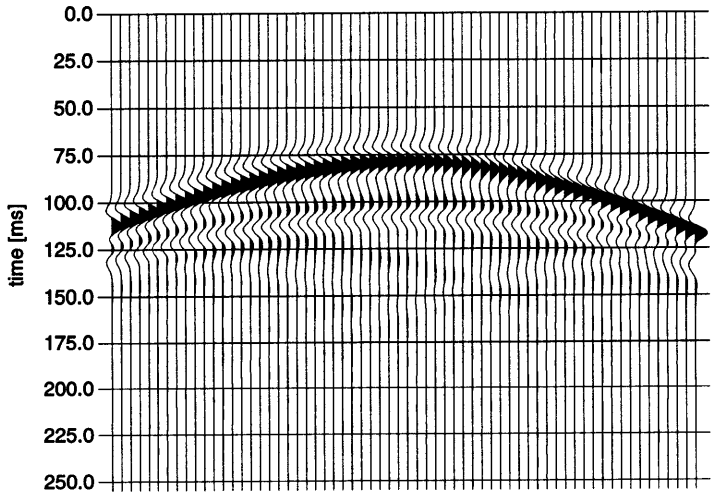

Figure 2-8: The seismogram for the model shown in Figure 2-6 as produced by the MMP method. The source function is a line source with a Ricker wavelet of 50 Hz. In total, 128 expansion functions located at 8 expansion centers were used. The incident field is suppressed.

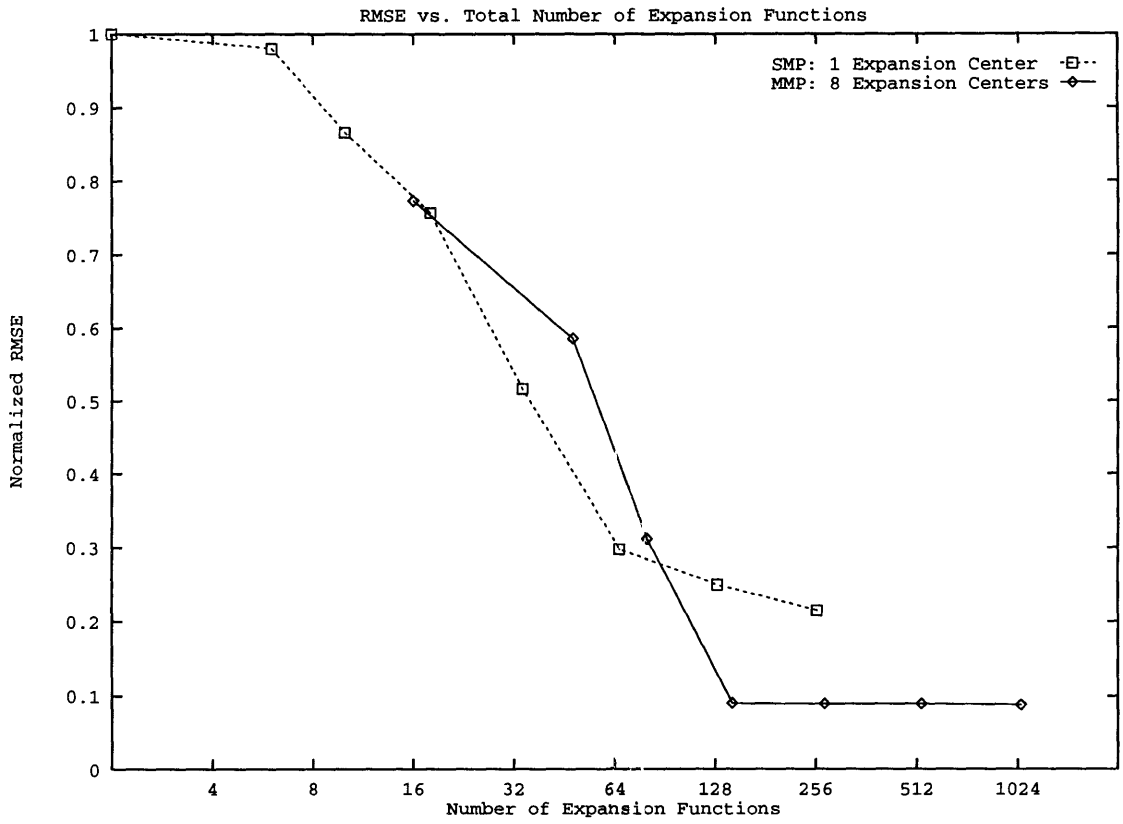

Figure 2-9: Comparison between the traditional eigenfunction expansion SMP (boxes, dashed) and the MMP expansion (diamonds, solid). Shown is how the total number of expansion functions affects the RMSE as obtained from the FD reference solution. For 128 and more expansion functions, the MMP expansions converge. The SMP actually never converges. Even the solutions obtained with 128 or 256 expansion functions contain spurious events while missing real ones. Moreover, the SMP matrix system becomes numerically singular for more than 256 expansion functions.

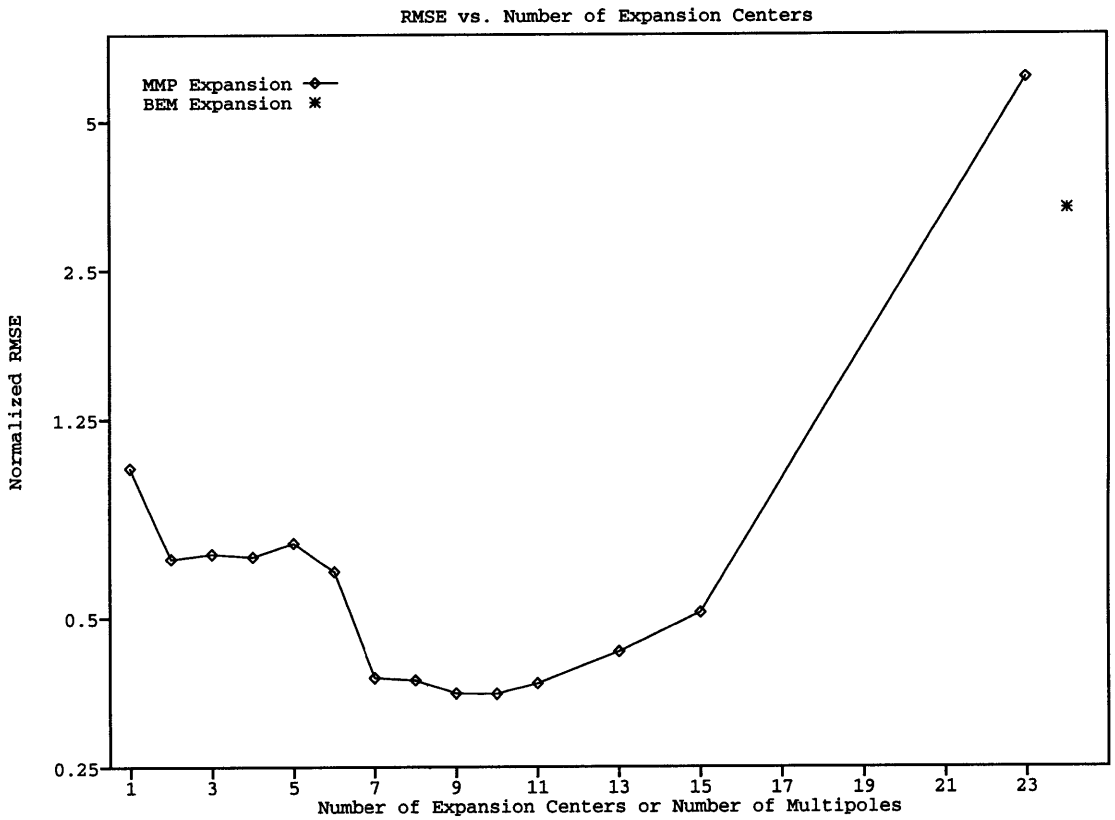

Figure 2-10: Effect of the number of expansion centers. The total number of expansion functions is kept constant at 128, while the number of expansion centers is varied from 1 up to 23. Keeping the number of matching points constant at 256 yields a constant computational effort for each case tested. The whole range between 7 and 13 centers converges with a only slightly better optimum for 9 or 10 centers. MMP expansions are rather insensitive to the actual discretization used. Placing all expansion centers onto the boundary and using only the terms of 0^{th} order, corresponding to a simple boundary element expansion (BEM), fails surprisingly.

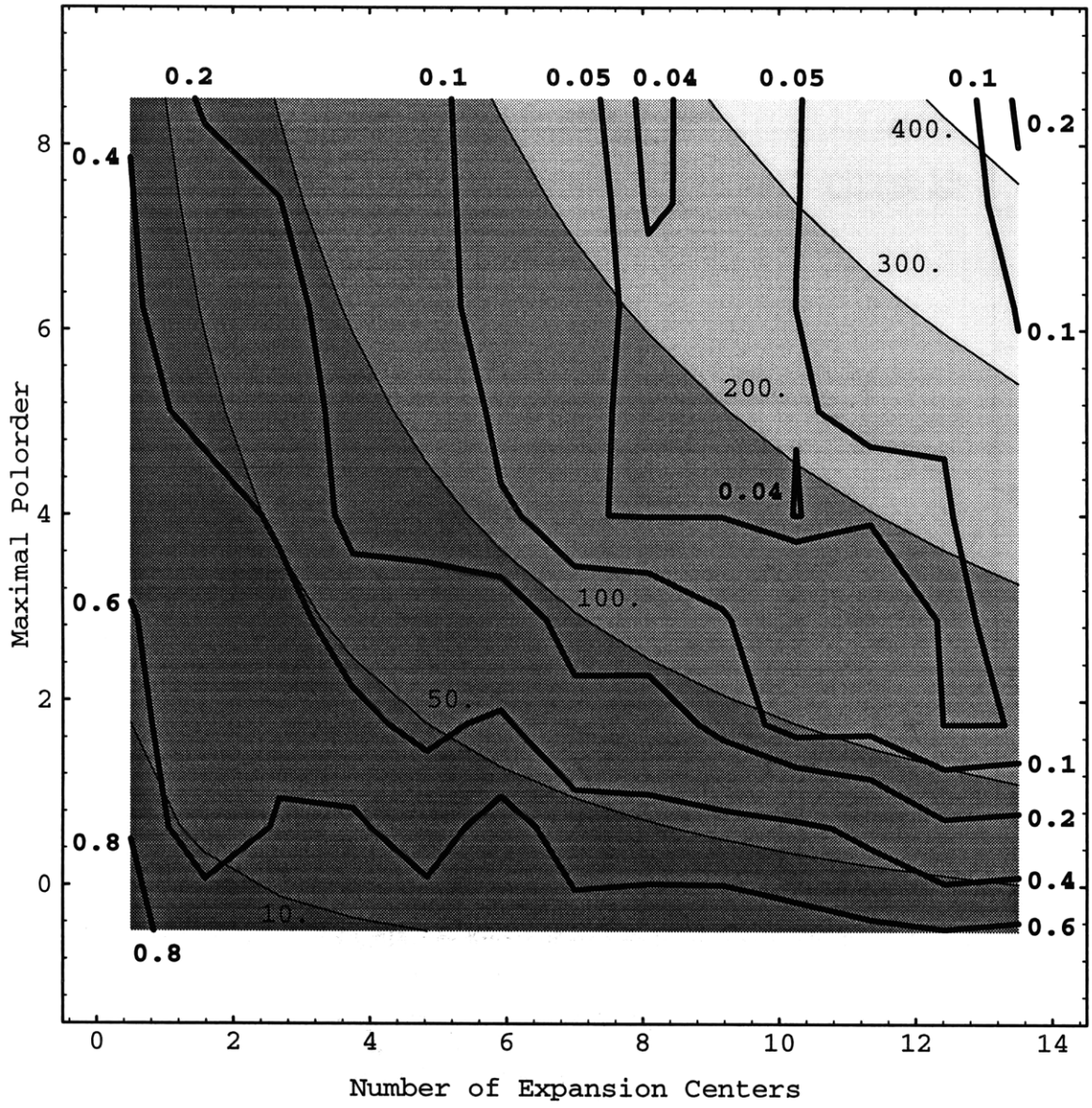

Figure 2-11: RMSE and the number of expansion functions versus the maximal polorder $\pm N$ and the number of expansion centers P. The bold lines contour the RMSE while the shading and the fine contour lines denote the total number of expansion functions $2(2N+1)P$. The minimal RMSE is obtained for $N = 8$ and $P = 8$.

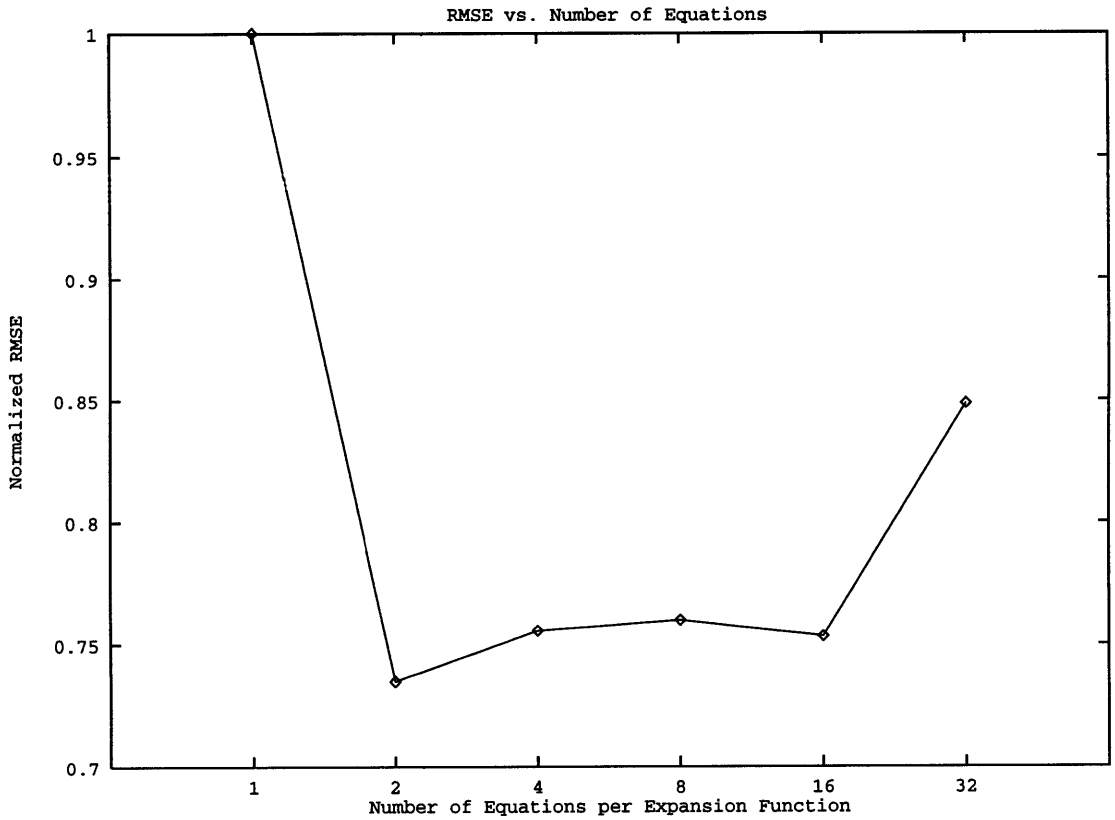

Figure 2-12: Influence of the number of matching points or the number of equations. The fields are expressed with 128 expansion functions located at 9 centers of expansion. Each matching point provides 2 equations. Since the expansion is non-orthogonal, using as many equations as unknowns to be resolved does not yield a correct result. The optimum is reached for twice as many equations as unknowns. Adding more equations to the system increases the condition number and thus the RMSE.

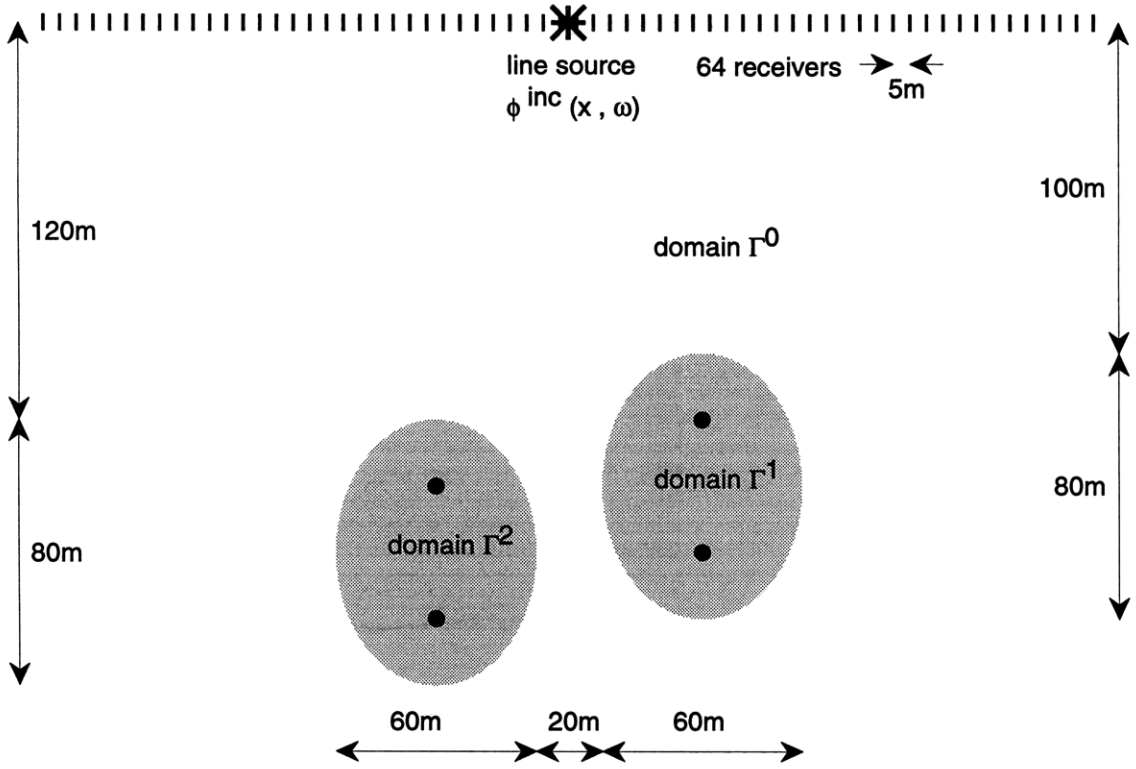

Figure 2-13: Model 2: a multiple scattering experiment. Two elliptical scatterers are illuminated by an explosion source. The velocity in the background domain Γ^0 is $\alpha^0 = 2000\,\mathrm{m/s}$. The velocity in the domains Γ^1 and Γ^2 (scatterers) is $\alpha^{1,2} = 3000\,\mathrm{m/s}$. The density ρ is kept constant at $2000\,\mathrm{kg/m^3}$ for all domains. At each black dot $\mathbf{x}_p$, we set up an expansion $\Phi^0(\mathbf{x},\omega) = \sum_{n=-5}^{5} a_{pn}^0 e^{in\theta}\, H_{|n|}^{(1)}\,(k^0\,|\mathbf{x}-\mathbf{x}_p|)$ for the field induced in the background and an expansion $\Phi^d(\mathbf{x},\omega) \sum_{n=-5}^{5} a_{pn}^d e^{in\theta}\, J_{|n|}\,(k^d\,|\mathbf{x}-\mathbf{x}_p|)$ for the fields in the scatterers Γ^1 and Γ^2.

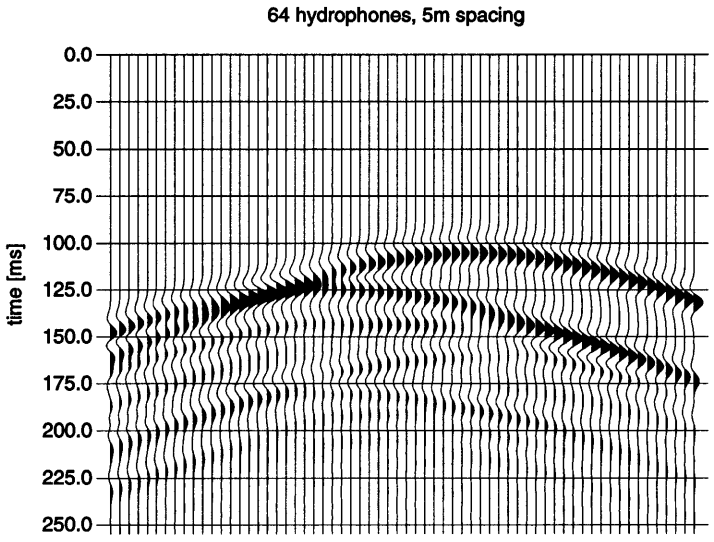

Figure 2-14: The seismogram for the model shown in Figure 2-13 as calculated using a multiple multipole expansion. The source function is a line source with a Ricker wavelet of 50 Hz. The incident field is suppressed.

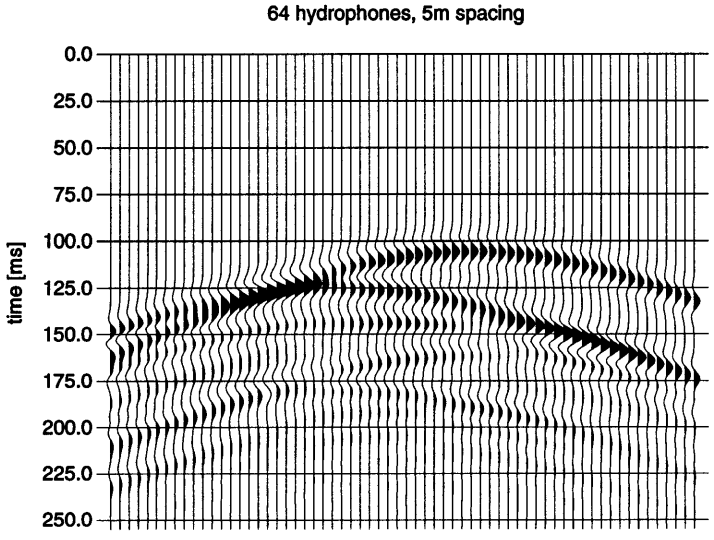

Figure 2-15: The seismogram for the model shown in Figure 2-13 as produced by an acoustic finite difference code. The source function is a line source with a Ricker wavelet of 50 Hz. The incident field is suppressed.

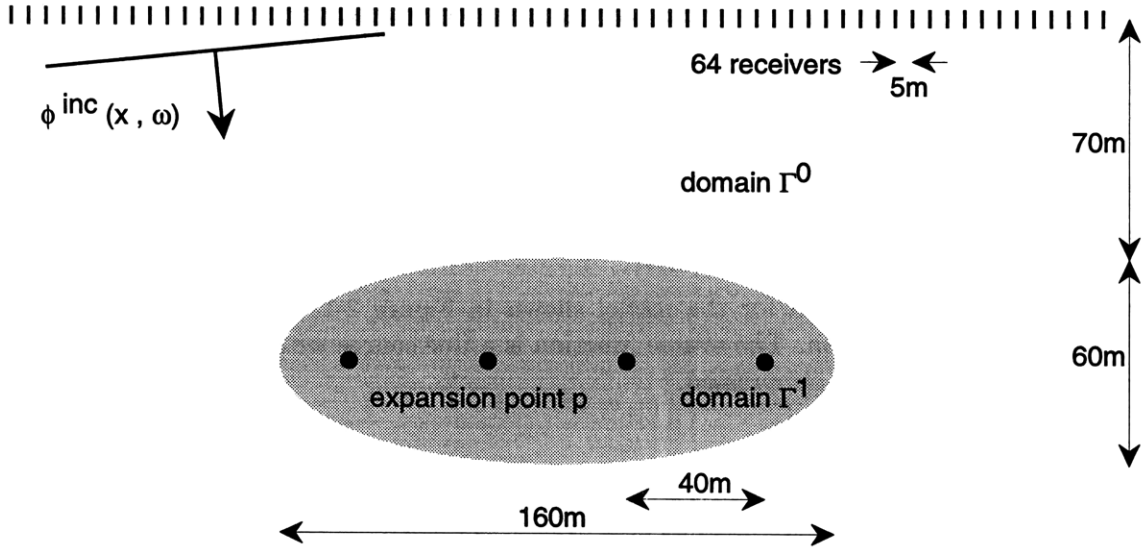

Figure 2-16: Model 3: An elliptical scatterer is illuminated by a planar wavefield with an angle of incidence of 5°. The material parameters in the background domain Γ^0 are velocity $\alpha^0 = 2000\,\mathrm{m/s}$ and density $\rho^0 = 2000\,\mathrm{kg/m^3}$. The material parameters in domain Γ^1 (scatterer) are velocity $\alpha^1 = 3000\,\mathrm{m/s}$ and density $\rho^1 = 2500\,\mathrm{kg/m^3}$. Shown is the situation with 4 multipoles. At each expansion center (black dots), we set up an expansion $\Phi^0(\mathbf{x},\omega) = \sum_{n=-5}^{5} a^0_{pn} e^{in\theta}\, H^{(1)}_{|n|}\left(k^0\,|\mathbf{x}-\mathbf{x}_p|\right)$ for the field induced in the background and an expansion $\Phi^1(\mathbf{x},\omega) = \sum_{n=-5}^{5} a^1_{pn} e^{in\theta}\, J_{|n|}\left(k^1\,|\mathbf{x}-\mathbf{x}_p|\right)$ for the field in the scatterer.

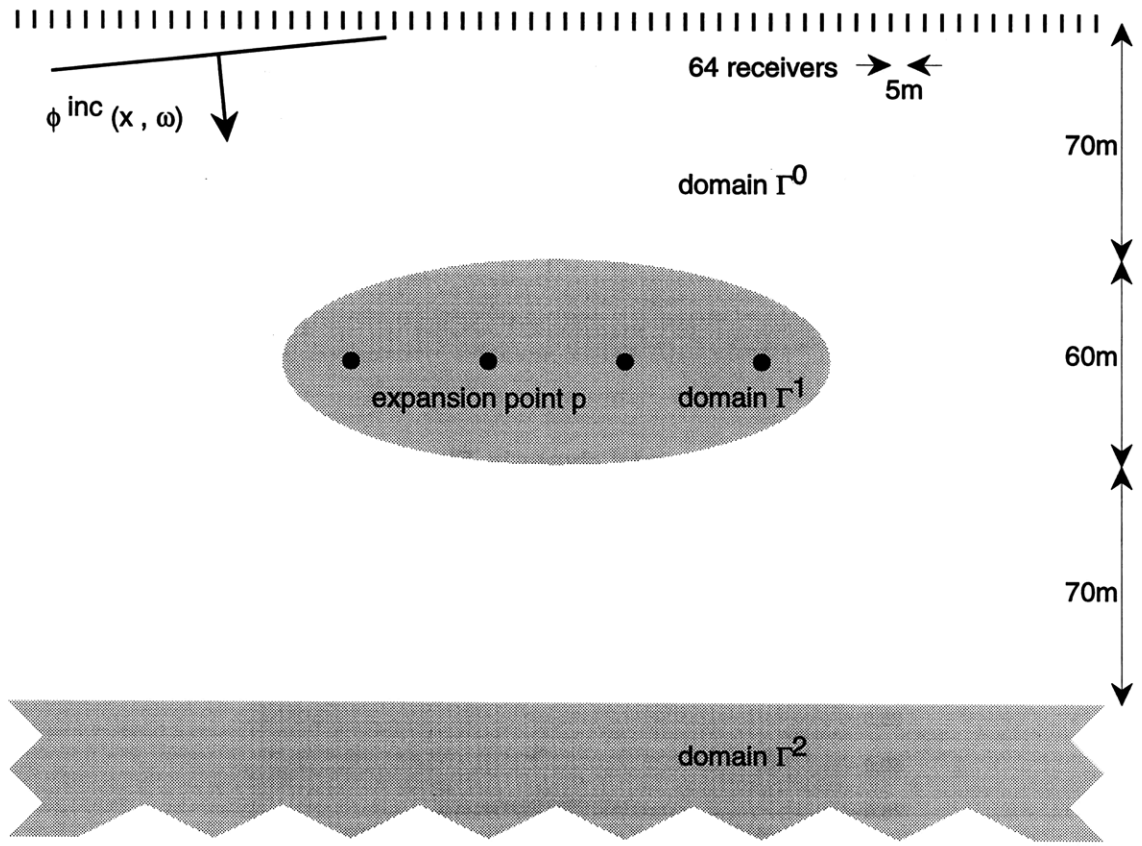

Figure 2-17: The same elliptical scatterer as shown in Figure 2-16, but over a halfspace, is illuminated by a planar wavefield with an angle of incidence of 5°. The reflection of the incident planar wavefield is included in the incident field. The material parameters in the background domain Γ^0 are velocity $\alpha^0 = 2000\,\mathrm{m/s}$ and density $\rho^0 = 2000\,\mathrm{kg/m^3}$. The material parameters in domain Γ^1 (scatterer) and Γ^2 (halfspace) are velocity $\alpha^{1,2} = 3000\,\mathrm{m/s}$ and density $\rho^{1,2} = 2500\,\mathrm{kg/m^3}$. At each black dot, we set up an expansion $\Phi^0(\mathbf{x},\omega) = \sum_{n=-5}^{5} a^0_{pn}\{e^{in\theta}\, H^{(1)}_{|n|}\,(k^0\,|\mathbf{x}-\mathbf{x}_p|) + \tilde{R}(k^s_z)\, e^{in\psi}\, H^{(1)}_{|n|}(k^0\,|\mathbf{x}-\mathbf{x}_{m_p}|)$ for the field induced in the background and an expansion $\Phi^1(\mathbf{x},\omega) = \sum_{n=-5}^{5} a^1_{pn} e^{in\theta}\, J_{|n|}\,(k^1\,|\mathbf{x}-\mathbf{x}_p|)$ for the field in the scatterer. The mirror sources are located at $\mathbf{x}_{m_p}$.

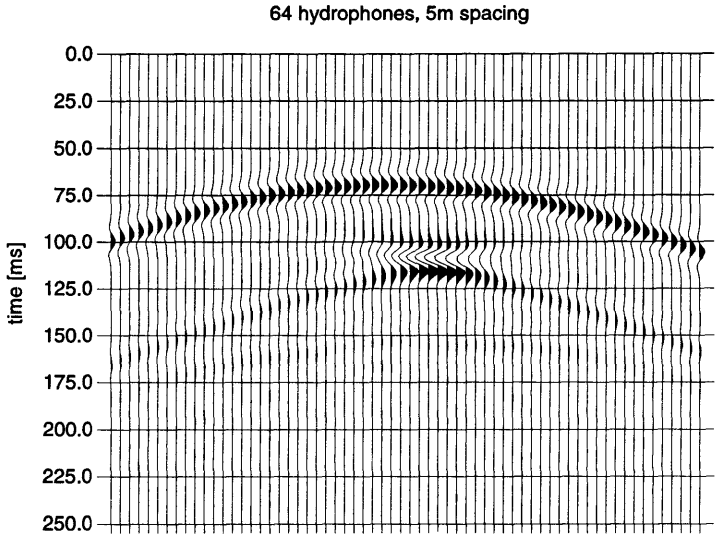

Figure 2-18: The seismogram for the model shown in Figure 2-16. The source is a planar wave with an angle of incidence of 5°. The reflections from both the top and the bottom of the scatterer can clearly be seen. The incident field is suppressed.

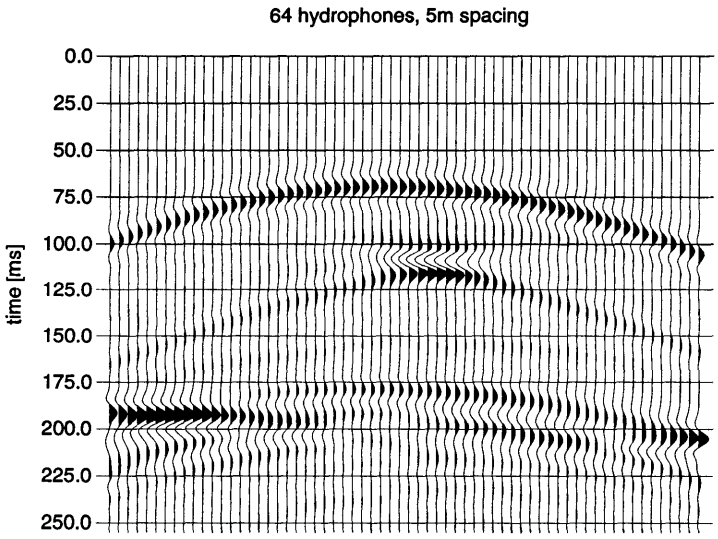

Figure 2-19: The seismogram due to a single scatterer on top of a halfspace. The model is shown in Figure 2-17. On the left and on the right side of the scatterer, the undisturbed reflection from the halfspace can be observed. Underneath the scatterer, the halfspace reflection is lifted upwards due to the fast scatterer. Below the halfspace reflection, we find some weak interactions between halfspace and scatterer.

Chapter 3

Multiple Multipole Expansions for Elastic Scattering

Abstract

The paper presents a new approach to solving scattering of elastic waves in two dimensions. Often, wavefields are expanded into an orthogonal set of basis functions. Unfortunately, these expansions converge rather slowly for complex geometries. The new approach enhances convergence by summing multiple expansions with different centers of expansions. This allows irregularities of the boundary to be resolved locally from a nearby center of expansion. Mathematically, the wavefields are expanded into a set of non-orthogonal basis functions. The incident wavefield and the fields induced by the scatterers are matched by evaluating the boundary conditions at discrete matching points along the domain boundaries. Due to the non-orthogonal expansions, more matching points are used than actually needed, resulting in an overdetermined system which is solved in the least-squares sense.

Since there are free parameters such as location and number of expansion centers as well as kind and orders of expansion functions used, numerical experiments are performed to measure the performance of different discretizations. An empirical set of rules governing

the choice of these parameters is found from these experiments. The resulting algorithm is a general tool to solve relatively large and complex two-dimensional scattering problems.

Introduction

The calculation of synthetic seismograms has been of interest for many years. Various methods have been proposed for modeling waves in heterogeneous media. Each of them has its own range of validity and interest. Fully numerical techniques in the space-time domain, either in the finite difference formulation (FD) (Kelly *et al.*, 1976; Virieux, 1986; Cheng *et al.*, 1994) or in the finite element formulation (FE) (Smith, 1974; Murphy and Chin-Bing, 1991), handle any kind of waves in complex media. For either method, an area containing the source, the receivers, the scatterers plus some neighborhood around them has to be discretized, which limits the distances between scatterers, sources and receivers. Computer runtime and memory requirements are functions of the total volume contained in the model.

The (generalized) ray theory (Červený *et al.*, 1977; Červený and Pšenčík, 1984) can be used when the scatterers and their radii of curvature are large compared to the wavelength. For small or weak scatterers, the (extended) Born approximation (Miles, 1960; Aki and Richards, 1980; Habashy *et al.*, 1993) allows an efficient calculation of the seismogram.

In other cases, the problem can be simplified by assuming the medium consists of homogeneous regions with sharp boundaries in between. Then, reflectivity (Müller, 1985; Kennett, 1983) and global matrix methods (Chin *et al.*, 1984; Schmidt and Tango, 1986) are routinely used for planarly or cylindrically layered media. For laterally heterogeneous media, numerical integration over wave number can be used (Bouchon and Aki, 1977; Haartsen *et al.*, 1994).

The classical eigenfunction expansion (SMP) (Morse and Feshbach, 1953) allows the analysis of simple shapes only, such as circular or elliptical cylinders where the eigenfunctions are

known (Bowman *et al.*, 1969; Pao and Mow, 1973). Methods based on the perturbation of a prescribed geometry, such as the T-matrix method (Waterman, 1976; Boström, 1980a) work extremely well for certain geometries but are harder to apply efficiently in general situations such as slender scattering objects (Lakhtakia *et al.*, 1984).

The method we use is a derivative of the boundary element methods (BEM) (Brebbia and Dominguez, 1989; Bouchon, 1993; Dong *et al.*, 1995; Kessel, 1996). It was first presented as a more general approach for electromagnetic scattering (Hafner and Ballisti, 1983; Hafner, 1990) and later adapted to acoustic scattering problems (Imhof, 1995). In contrast to more traditional approaches, the wavefields are expanded into a set of *non-orthogonal* and *non-complete* basis functions. Actually, non-complete basis functions are not a new concept, since for numerical and computational reasons, we can never use an infinite number of basis functions. But, the simultaneous use of a non-orthogonal expansion allows us to reduce the truncation errors (Hafner, 1993). To solve for the unknown weighting coefficients of the basis functions, discrete matching points are chosen along the boundary of the scattering object. In the elastic case, each matching point provides four boundary conditions and thus four equations involving the unknowns. Because the expansion is non-orthogonal, we need more equations than unknowns, thus building an overdetermined matrix system and solving for it in the *least-squares sense.* Mathematically speaking, we search for the set of weighting coefficients which solves the problem at hand "best" employing the chosen expansions. In fact, we build a model for the wavefields and invert for the "optimal" set of parameters. There will always be an error in the boundary conditions at each matching point, although on average these errors are small. Furthermore, the fields in between matching points are forced to be smooth, such that no wild jumps or oscillations can occur. Thus, as an added bonus, we control the behavior of the expansions in between matching points where we have no control using traditional methods. Also, this allows us to see in which parts of the boundary the chosen expansions can solve the problem and where they need further refinement.

The method is well-suited for solving scattering from either one scatterer alone or between multiple scatterers. Each scatterer consists of a homogeneous and bounded region embedded

in a homogeneous and unbounded background. Applications of the problems posed can be found in geophysical exploration or earthquake engineering, ultrasonic nondestructive testing, medial imaging, or underwater acoustics. The computer runtime and the memory requirements are functions of the interface area of the embedded scatterers. Due to its close relationship with other matrix methods, e.g. the finite element method, a hybridized scheme can be devised easily, which allows one to embed heterogeneous scatterers in a homogeneous background.

This paper is structured as follows: First, we adapt the method from acoustical (Imhof, 1995) to elastic scattering. Then, we present results from several calculations and compare them to solutions obtained by the finite difference method and the classical eigenfunction expansion. We show how different discretizations affect the resulting solutions. Finally, we compile these findings into an empirical set of rules which allows us to set up a problem in a fashion which yields satisfactory results without having to resort to a trial and error approach.

3.1 Theoretical Background

We would like to model how an incident wavefield $\mathbf{u}^{inc}(\mathbf{x},\omega)e^{i\omega t}$ scatters from an object. The situation is depicted in Figure 3-1. For the sake of simplicity, we will suppress the harmonic time factor $e^{i\omega t}$ in all the following expressions. Superscripts will denote the region to which a material property or field belongs to, and, to distinguish different regions or domains, we will use the symbol Γ^d. The boundary between the two regions Γ^0 and Γ^1 will be denoted by $\partial\Gamma_{01}$. Also, the homogeneous and unbounded region Γ^0 will often be called the 'background'. All other regions Γ^d, where $d \neq 0$, are homogeneous but bounded. They will be called 'scatterers'.

In the frequency domain, the displacement $\mathbf{u}(\mathbf{x},\omega)$ of an elastic P-SV wave travelling in a

two dimensional, homogeneous medium is described by (Pao and Mow, 1973)

$$\frac{1}{k^2}\nabla\nabla\cdot\mathbf{u}-\frac{1}{l^2}\nabla\times\nabla\times\mathbf{u}+\mathbf{u}=0\,, \tag{3.1}$$

where we defined the wave numbers $k=\omega/\alpha$ and $l=\omega/\beta$ for a particular frequency ω and the propagation velocities $\alpha=\sqrt{\lambda+2\mu/\rho}$ and $\beta=\sqrt{\mu/\rho}$. The parameters ρ, λ and μ denote respectively the density and the Lamé parameters of the medium. In a local cylindrical coordinate system (r,θ,y) centered at a point $\mathbf{x}_p$ (Figure 3-2), the strains due to a displacement $\mathbf{u}$ are expressed as (Pao and Mow, 1973)

$$\epsilon_{rr} = \frac{\partial u_r}{\partial r} \tag{3.2a}$$

$$\epsilon_{\theta\theta} = \frac{\partial u_\theta}{\partial\theta}+\frac{\partial u_r}{\partial r} \tag{3.2b}$$

$$\epsilon_{r\theta}=\epsilon_{\theta r} = \frac{1}{2}\left(\frac{1}{r}\frac{\partial u_r}{\partial\theta}+\frac{\partial u_\theta}{\partial r}-\frac{u_\theta}{r}\right)\,. \tag{3.2c}$$

All other components are zero since they involve the u_y component or cross-derivatives with respect to y. The stresses are linearly related to the strains by (Pao and Mow, 1973)

$$\sigma_{pq}=\lambda\delta_{pq}\sum_k\epsilon_{kk}+2\mu\epsilon_{pq}\qquad\text{where}\qquad p,q\in\{r,\theta\}\,. \tag{3.3}$$

A displacement field $\mathbf{u}^{inc}(\mathbf{x})$ incident on the scatterer will induce two scattered fields: $\mathbf{u}^0(\mathbf{x},\omega)$ outside the scattering object and $\mathbf{u}^1(\mathbf{x},\omega)$ on the inside. The displacements and stresses inside and outside the scatterer are related by the boundary conditions. For the problem posed, these conditions are continuity of displacement and stresses in both normal and tangential directions. We define the normal $\hat{\mathbf{n}}$ to point from medium Γ^0 into medium Γ^1, as depicted in Figure 3-2. Using the subscripts n and t to denote the normal and

tangential direction, we write

$$u_n^0 + u_n^{inc} = u_n^1 , \tag{3.4a}$$

$$u_t^0 + u_t^{inc} = u_t^1 , \tag{3.4b}$$

$$\sigma_{nn}^0 + \sigma_{nn}^{inc} = \sigma_{nn}^1 , \tag{3.4c}$$

$$\sigma_{nt}^0 + \sigma_{nt}^{inc} = \sigma_{nt}^1 . \tag{3.4d}$$

Since we express the displacements and stresses in a local cylindrical coordinate system (r, θ, y), but want to specify the boundary in a local Cartesian system (n, t, y), we have to use the rotation matrix $\mathbf{M}$ to transform the individual components

$$\mathbf{u}_{nty} = \mathbf{M} \cdot \mathbf{u}_{r\theta y} \tag{3.5}$$

$$\boldsymbol{\sigma}_{nty} = \mathbf{M} \cdot \boldsymbol{\sigma}_{r\theta y} \cdot \mathbf{M}^T , \tag{3.6}$$

where the rotation matrix $\mathbf{M}$ is defined by the unit vectors $\hat{\mathbf{r}}$, $\hat{\boldsymbol{\theta}}$, $\hat{\mathbf{n}}$ and $\hat{\mathbf{t}}$:

$$\mathbf{M} = \begin{pmatrix} \hat{\mathbf{n}} \cdot \hat{\mathbf{r}} & \hat{\mathbf{n}} \cdot \hat{\boldsymbol{\theta}} & 0 \\ \hat{\mathbf{t}} \cdot \hat{\mathbf{r}} & \hat{\mathbf{t}} \cdot \hat{\boldsymbol{\theta}} & 0 \\ 0 & 0 & 1 \end{pmatrix} . \tag{3.7}$$

Instead of using the displacement $\mathbf{u}(\mathbf{x}, \omega)$ directly, we break it into two parts

$$\mathbf{u}(\mathbf{x}, \omega) = \nabla \Phi(\mathbf{x}, \omega) + \nabla \times \left\{ \Psi(\mathbf{x}, \omega) \hat{\mathbf{y}} \right\} \tag{3.8}$$

using the scalar potentials $\Phi(\mathbf{x}, \omega)$ and $\Psi(\mathbf{x}, \omega)$. Then, equation (3.1) separates into two independent Helmholtz equations:

$$\left(\nabla^2 + k^2\right) \Phi(\mathbf{x}, \omega) = 0 , \tag{3.9a}$$

$$\left(\nabla^2 + l^2\right) \Psi(\mathbf{x}, \omega) = 0 . \tag{3.9b}$$

Therefore, we replace the induced displacement fields $\mathbf{u}^0(\mathbf{x}, \omega)$ and $\mathbf{u}^1(\mathbf{x}, \omega)$ by the potentials

$\Phi^0(\mathbf{x},\omega)$, $\Psi^0(\mathbf{x},\omega)$, $\Phi^1(\mathbf{x},\omega)$, and $\Psi^1(\mathbf{x},\omega)$. Similar to the acoustic case (Imhof, 1995), we expand the potential fields as:

$$\Phi^d(\mathbf{x},\omega) = \sum_{p=1}^{P}\sum_{n=-N}^{+N} a_{pn}^d \phi_{pn}^d(\mathbf{x},\mathbf{x}_p^d,k^d,\omega) + e_\Phi^d \tag{3.10a}$$

$$\Psi^d(\mathbf{x},\omega) = \sum_{p=1}^{P}\sum_{n=-N}^{+N} b_{pn}^d \psi_{pn}^d(\mathbf{x},\mathbf{x}_p^d,l^d,\omega) + e_\Psi^d \tag{3.10b}$$

where $\phi_{pn}^d(\mathbf{x},\mathbf{x}_p^d,k^d,\omega)$ and $\psi_{pn}^d(\mathbf{x},\mathbf{x}_p^d,l^d,\omega)$ are solutions to either Helmholtz equation (3.9a) or (3.9b), respectively. The error terms e_Φ^d and e_Ψ^d are included not only because the series are truncated after $\pm N$ terms, but also because an expansion of this form is mathematically *non-orthogonal.*

An expansion of the form (3.10a) or (3.10b) is known as a multiple multipole (MMP) expansion (Ballisti and Hafner, 1983; Hafner, 1990). Setting P to one yields the classical eigenfunction (SMP) expansion (Morse and Feshbach, 1953). In the background region Γ^0, we choose propagating waves (Morse and Feshbach, 1953) involving the Hankel solutions $H_{|n|}^{(1)}\, e^{in\theta}$ as expansion functions ϕ_{pn}^0 and ψ_{pn}^0:

$$\phi_{pn}^0(\mathbf{x},\mathbf{x}_p^0,k^0,\omega) = H_{|n|}^{(1)}\left(k^0\,|\mathbf{x}-\mathbf{x}_p^0|\right) e^{in\theta} \tag{3.11a}$$

$$\psi_{pn}^0(\mathbf{x},\mathbf{x}_p^0,l^0,\omega) = H_{|n|}^{(1)}\left(l^0\,|\mathbf{x}-\mathbf{x}_p^0|\right) e^{in\theta} \tag{3.11b}$$

where the expression $\mathbf{x}_p^0$ denotes the p^{th} center of expansion for $\Phi^0(\mathbf{x},\omega)$ and $\Psi^0(\mathbf{x},\omega)$. The expansion centers $\mathbf{x}_p^0$ have to be positioned *inside the scatterer* Γ^1 to avoid the singularity of the Hankel functions (Morse and Feshbach, 1953; Imhof, 1995).

However, there are two possible choices for the expansions of the fields $\Phi^1(\mathbf{x},\omega)$ and $\Psi^1(\mathbf{x},\omega)$ inside the finite scatterer Γ^1. First, we can place the expansion centers $\mathbf{x}_p^1$ *inside the scatterer* ($\mathbf{x}_p^1 \in \Gamma^1$) and use expansions involving the Bessel solutions $J_{|n|}\, e^{in\theta}$ which correspond to

standing waves (Morse and Feshbach, 1953):

$$\phi^1_{pn}(\mathbf{x}, \mathbf{x}^1_p, k^1, \omega) = J_{|n|}\left(k^1 \left|\mathbf{x} - \mathbf{x}^1_p\right|\right) e^{in\theta} \qquad \text{if } \mathbf{x}^1_p \in \Gamma^1 \tag{3.12a}$$

$$\psi^1_{pn}(\mathbf{x}, \mathbf{x}^1_p, k^1, \omega) = J_{|n|}\left(l^1 \left|\mathbf{x} - \mathbf{x}^1_p\right|\right) e^{in\theta} \qquad \text{if } \mathbf{x}^1_p \in \Gamma^1\,. \tag{3.12b}$$

Second, we can place the expansion centers $\mathbf{x}^1_p$ *into the background* ($\mathbf{x}^1_p \in \Gamma^0$) and use propagating waves $H^{(1)}_{|n|}\, e^{in\theta}$ involving the Hankel functions of the first kind:

$$\phi^1_{pn}(\mathbf{x}, \mathbf{x}^1_p, k^1, \omega) = H^{(1)}_{|n|}\left(k^1 \left|\mathbf{x} - \mathbf{x}^1_p\right|\right) e^{in\theta} \qquad \text{if } \mathbf{x}^1_p \in \Gamma^0 \tag{3.13a}$$

$$\psi^1_{pn}(\mathbf{x}, \mathbf{x}^1_p, k^1, \omega) = H^{(1)}_{|n|}\left(l^1 \left|\mathbf{x} - \mathbf{x}^1_p\right|\right) e^{in\theta} \qquad \text{if } \mathbf{x}^1_p \in \Gamma^0\,. \tag{3.13b}$$

These expansions represent waves propagating from the expansion center toward the scatterer (Morse and Feshbach, 1953). Inside the scatterer, we need waves propagating in all directions. Thus, expansion centers have to be placed all around the scatterer to "illuminate" the region Γ^1 from all sides.

To emphasize the difference between the expansions (3.12) and (3.13); if the expansion center $\mathbf{x}^1_p$ is placed *inside* the scatterer Γ^1, we have to use the expansions (3.12) by superposing Bessel solutions $J_{|n|}\, e^{in\theta}$ corresponding to standing waves. Contrary to the propagatory Hankel solutions $H^{(1)}_{|n|}\, e^{in\theta}$, the Bessel solutions do not have a singularity and may therefore be evaluated at their origins. Because the singularities of the Hankel solutions represent sources, the Hankel solutions may never be used to expand wavefields in a domain in which their expansion center $\mathbf{x}_p$, and thus their singularity, is located. By definition, the only source in the problem posed is the incident field $\mathbf{u}^{inc}$.

However, if the expansion center $\mathbf{x}^1_p$ is located *outside* the scatterer, then we should use the expansions (3.13) with the Hankel solutions $H^{(1)}_{|n|}\, e^{in\theta}$ representing wavefields emanating from expansion center $\mathbf{x}^1_p$ propagating through the scatterer. The singularities pose no problem anymore since they are not located in the domain Γ^1 and therefore never contribute. Figure 3-3 illustrates this subtlety.

We solve for the unknown coefficients a_{pn}^d and b_{pn}^d by enforcing the boundary conditions (3.4a) - (3.4d) on M discrete matching points $\mathbf{x}_m$ along the domain boundary $\partial\Gamma_{01}$. Since we have four boundary conditions, each matching point also provides four rows of the resulting linear matrix system. Altogether, we have $4J = 2 \cdot 2 \cdot P \cdot (2N+1)$ unknown coefficients a_{pn}^d, b_{pn}^d. To simplify the notation, we eliminate an index by sequentially renumbering the double-indexed expansion functions $\phi_{pn}^d(\mathbf{x}, \mathbf{x}_p^d, k^d, \omega)$ and the coefficients a_{pn}^d, which results in $\phi_j^d(\mathbf{x}, \mathbf{x}_j^d, k^d, \omega)$ and a_j^d. Similarly, $\psi_{pn}^d(\mathbf{x}, \mathbf{x}_p^d, l^d, \omega)$ and b_{pn}^d reduce to $\psi_j^d(\mathbf{x}, \mathbf{x}_j^d, l^d, \omega)$ and b_j^d. Combining all together, we have to solve a matrix system of the form

$$\begin{pmatrix} -\Phi_n^0 & -\Psi_n^0 & \Phi_n^1 & \Psi_n^1 \\ -\Phi_t^0 & -\Psi_t^0 & \Phi_t^1 & \Psi_t^1 \\ -\Phi_{nn}^0 & -\Psi_{nn}^0 & \Phi_{nn}^1 & \Psi_{nn}^1 \\ -\Phi_{nt}^0 & -\Psi_{nt}^0 & \Phi_{nt}^1 & \Psi_{nt}^1 \end{pmatrix}_{4M \times 4J} \cdot \begin{pmatrix} \mathbf{a}^0 \\ \mathbf{b}^0 \\ \mathbf{a}^1 \\ \mathbf{b}^1 \end{pmatrix}_{4J} = \begin{pmatrix} \mathbf{u}_n \\ \mathbf{u}_t \\ \sigma_{nn} \\ \sigma_{nt} \end{pmatrix}_{4M} + \begin{pmatrix} \mathbf{e}_n \\ \mathbf{e}_t \\ \mathbf{e}_{nn} \\ \mathbf{e}_{nt} \end{pmatrix}_{4M} \tag{3.14}$$

where the submatrices Φ_n^d and Ψ_n^d denote the normal displacements u_n at the matching points due to ϕ_j^d and ψ_j^d, respectively. The submatrices Φ_t^d and Ψ_t^d are the same except for the tangential component u_t of the displacement. The submatrices Φ_{nn}^d and Ψ_{nn}^d contain the normal stresses σ_{nn}, while Φ_{nt}^d and Ψ_{nt}^d contain the tangential stresses σ_{nt}. Defining the matching points by their location $\mathbf{x}_m$, we evaluate these submatrices as

$$\left[\Phi_{n,mj}^d\right] = u_n\left(\phi_j^d(\mathbf{x}_m)\right) \qquad \left[\Psi_{n,mj}^d\right] = u_n\left(\psi_j^d(\mathbf{x}_m)\right) \tag{3.15a}$$

$$\left[\Phi_{t,mj}^d\right] = u_t\left(\phi_j^d(\mathbf{x}_m)\right) \qquad \left[\Psi_{t,mj}^d\right] = u_t\left(\psi_j^d(\mathbf{x}_m)\right) \tag{3.15b}$$

$$\left[\Phi_{nn,mj}^d\right] = \sigma_{nn}\left(\phi_j^d(\mathbf{x}_m)\right) \qquad \left[\Psi_{nn,mj}^d\right] = \sigma_{nn}\left(\psi_j^d(\mathbf{x}_m)\right) \tag{3.15c}$$

$$\left[\Phi_{nt,mj}^d\right] = \sigma_{nt}\left(\phi_j^d(\mathbf{x}_m)\right) \qquad \left[\Psi_{nt,mj}^d\right] = \sigma_{nt}\left(\psi_j^d(\mathbf{x}_m)\right) \tag{3.15d}$$

where we used the index $m \in \{1, \ldots, M\}$ to denote the matching points $\mathbf{x}_m$, the index $j \in \{1, \ldots, J\}$ for the expansion functions ϕ_j^d, ψ_j^d and the index $d \in \{0, 1\}$ for the domain. The expression $u_n\left(\phi_j^d(\mathbf{x}_m)\right)$ represents the normal displacement due to the expansion function ϕ_j^d evaluated at the matching point $\mathbf{x}_m$. The other ones are to be interpreted similarly. The

vectors $\mathbf{a}^0$, $\mathbf{b}^0$, $\mathbf{a}^1$, and $\mathbf{b}^1$ in equation (3.14) contain the unknown coefficients a_j^0, b_j^1, a_j^1, b_j^1 for the respective expansion functions ϕ_j^0, ψ_j^0, ϕ_j^1, and ψ_j^1. The vectors $\mathbf{u}_n$, $\mathbf{u}_t$, $\boldsymbol{\sigma}_{nn}$, and $\boldsymbol{\sigma}_{nt}$ hold the normal and tangential displacements as well as normal and tangential stresses at the M matching points due to the incident field $\mathbf{u}^{inc}$.

$$\left[u_{n,m}\right] = u_n^{inc}(\mathbf{x}_m) \qquad \left[u_{t,m}\right] = u_t^{inc}(\mathbf{x}_m) \tag{3.16a}$$

$$\left[\sigma_{nn,m}\right] = \sigma_{nn}^{inc}(\mathbf{x}_m) \qquad \left[\sigma_{nt,m}\right] = \sigma_{nt}^{inc}(\mathbf{x}_m)\,. \tag{3.16b}$$

Finally, the matrix equation (3.14) contains the residual vectors $\mathbf{e}_n$, $\mathbf{e}_t$, $\mathbf{e}_{nn}$, $\mathbf{e}_{nt}$ with the misfit of the boundary conditions at the individual matching points.

The extension to multiple scattering objects is straightforward and follows exactly the acoustic case (Imhof, 1995). Assuming that the scatterers do not intersect, a MMP expansion has to be set up from each scatterer $d \in \{1, \ldots, D\}$. Thus for the fields in the background domain Γ^0, we obtain

$$\Phi^0(\mathbf{x},\omega) = \sum_d^D \sum_p^P \sum_n^N a_{pn}^d \phi_{pn}^d(\mathbf{x}, \boldsymbol{x}_p^d, k^0, \omega) + e_\Phi^0 \tag{3.17a}$$

$$\Psi^0(\mathbf{x},\omega) = \sum_d^D \sum_p^P \sum_n^N b_{pn}^d \psi_{pn}^d(\mathbf{x}, \boldsymbol{x}_p^d, l^0, \omega) + e_\Psi^0 \tag{3.17b}$$

where $\boldsymbol{x}_p^d$ denotes the centers for the expansions of $\Phi^0(\mathbf{x},\omega)$ and $\Psi^0(\mathbf{x},\omega)$. The expansion centers $\boldsymbol{x}_p^d$ have to be positioned *inside the scatterer* Γ^d to avoid the effect of the singularity of the Hankel functions. The fields inside the scatterers Γ^d can still be expressed by (3.10).

3.2 Numerical Results

To obtain a seismogram in the domain $d \in \{0, 1\}$, we must evaluate the Fourier integral

$$\mathbf{u}^d(\mathbf{x},t) = \int_{-\infty}^{+\infty} \mathbf{U}^d(\mathbf{x},\omega) e^{i\omega t}\, d\omega \tag{3.18}$$

where

$$\mathbf{U}^d(\mathbf{x},\omega) = \delta_{0d}\ \mathbf{u}^{inc}(\mathbf{x},\omega) + \sum_{p}^{}\sum_{n}^{} a_{pn}^d \cdot \nabla\phi_{pn}^d(\mathbf{x},\mathbf{x}_p^d,k^d,\omega) + b_{pn}^d \cdot \nabla \times \left\{\psi_{pn}^d(\mathbf{x},\mathbf{x}_p^d,l^d,\omega)\hat{\mathbf{y}}\right\}. \quad (3.19)$$

To perform the operation, one needs to move the singularities of $\mathbf{U}^d(\mathbf{x},\omega)$ off the real ω axis. This may be done by adding a small imaginary component ω_I to the frequency (Bouchon and Aki, 1977):

$$\omega = \omega_R + i\omega_I \qquad \text{where} \quad \omega_I > 0\,. \quad (3.20)$$

The singularities in $\mathbf{U}^d(\mathbf{x},\omega)$ correspond to resonances, surface modes, and creeping waves induced by the scatterers. The use of the complex frequency has the effect of smoothing the spectrum and enhancing the first motions relative to later arrivals. This attenuating effect of the imaginary frequency component can be removed from the final time domain solution by a multiplication with $e^{\omega_I t}$:

$$\mathbf{u}^d(\mathbf{x},t) = e^{\omega_I t}\int_{-\infty}^{+\infty} \mathbf{U}^d(\mathbf{x},\omega)e^{i\omega_R t}\,d\omega_R\,. \quad (3.21)$$

Due to the complex frequency, the Bessel and Hankel functions have to be evaluated with a complex argument (Abramowitz and Stegun, 1964; Amos, 1986). In practice, the integral is approximated by a discrete Fourier transformation (DFT). Its use will result in aliasing in the time-domain due to the periodicity in time and frequency as implied by the DFT (Brigham, 1988). Again, this effect can be reduced by the small imaginary part ω_I which attenuates disturbances not belonging to the time window of interest.

The matrix system is solved by QR decomposition using Givens rotations (Wilkinson, 1988) which allows one to build the matrix system row by row while storing only a triangular matrix with dimensions of the number of unknowns in the computer memory (George and Heath, 1980). Since we want to calculate synthetic seismograms using a frequency domain method, we have to solve the scattering problem for a range of frequencies and later apply

a Fourier transformation to obtain the seismograms. All these problems can be solved independently of each other. Consequently, the algorithm is implemented on a nCUBE2 parallel computer where each processor will calculate a few frequencies.

We now show how the method performs solving a simple problem using different ways to discretize it. For the sake of simplicity, the incident field $\mathbf{u}^{inc}$ is an explosive line source modulated with a Ricker pulse (Hosken, 1988; Paillet and Cheng, 1991) of 50 Hz center frequency. Altogether, 64 receivers will measure the u_z component of the total field $\mathbf{u}^0(\mathbf{x}, t)$ in the background. The rather generic scatterer is shown in Figure 3-4. Its size is roughly 240 m in length and 50 m in thickness. The density and velocities in the background are respectively $\rho^0 = 2000\,\mathrm{kg/m^3}$, $\alpha^0 = 2000\,\mathrm{m/s}$ and $\beta^0 = 1155\,\mathrm{m/s}$. In the scatterer, the density and velocities are $\rho^1 = 2500\,\mathrm{kg/m^3}$, $\alpha^1 = 3000\,\mathrm{m/s}$ and $\beta^1 = 1732\,\mathrm{m/s}$. Thus, the Poisson's ratio is the same for both regions ($\sigma = 0.25$). The center frequency of 50 Hz yields an incident wavelength of 40 m which roughly equals the thickness of the scatterer.

In order to have a reference seismogram to compare the different MMP solutions, we calculate the solution using a finite difference (FD) method (Kelly *et al.*, 1976; Peng and Toksöz, 1994). The resulting reference seismogram is shown in Figure 3-5. As a measure of how well the MMP seismogram $u_z^{MMP}(r,t)$ correlates with the FD reference seismogram $u_z^{FD}(r,t)$, we define the root mean square error (RMSE) and the relative root mean square error (RRMSE). The RMSE is defined by the squared difference between the two seismograms

$$\mathrm{RMSE} = \frac{1}{\sqrt{RT}} \sqrt{\sum_{r=1}^{R} \sum_{t=1}^{T} \left\{ u_z^{MMP}(r,t) - u_z^{FD}(r,t) \right\}^2} \tag{3.22a}$$

where $u_z(r,t)$ denotes the vertical displacement measured at recorder r at time sample t. $R = 64$ is the number of recorders and $T = 256$ is the total number of time samples. The RRMSE is defined by the squared relative difference between the two seismograms

$$\mathrm{RRMSE} = \frac{1}{\sqrt{N'}} \sqrt{\sum_{r'} \sum_{t'} \left\{ \frac{u_z^{MMP}(r',t') - u_z^{FD}(r',t')}{u_z^{MMP}(r',t') + u_z^{FD}(r',t')} \right\}^2} \tag{3.22b}$$

where we drop terms for which $\frac{1}{2}|u_z^{MMP}(r',t')| + \frac{1}{2}|u_z^{FD}(r',t')|$ is below 50 dB relative to its maximum value. N' is simply the number of terms above the threshold. The use of the threshold prevents the RRMSE from being dominated by minute amplitudes while still accounting for smaller, yet visible features in the seismograms.

3.2.1 MMP versus the Finite Difference Reference Solution

As a first example, we present both a solution obtained by MMP expansions and the reference solution as obtained by finite differences. For the finite difference case, we used a grid spacing of 1 m and a grid of 750 by 750 points. The grid dimensions are larger than needed to prevent reflections from imperfectly absorbing boundaries to reach the receivers. The timestep used is 0.05 ms. The runtime on a nCUBE2 using 64 nodes was 23 minutes. The seismogram calculated by finite differences is shown in Figure 3-5.

For the MMP expansion, we used a total of 256 expansion functions, 128 matching points, 8 expansion centers, and 64 frequencies. The resulting runtime on a nCUBE2, again using 64 nodes, was 12 minutes. Figure 3-6 shows the seismogram calculated using the MMP expansion. The two methods yield the same result. As can be seen, they agree very well in both traveltimes and phases.

To facilitate the comparison, we placed 5 receivers inside the scatterer and positioned 9 additional receivers around the scatterer. The exact geometry is presented in Table 3.1 and depicted in Figure 3-7. The normalized traces for both the FD and MMP solutions are overlaid in Figure 3-8. For all receiver positions, the two solutions match perfectly even for small amplitudes.

3.2.2 Effect of the Number of Expansion Functions

As a second experiment, we study how the number of expansion functions affects the solutions obtained. We start with totally 32 expansion functions located at 8 expansion centers.

Thus, we have one monopole for each potential and each region at every expansion center. We calculate the seismogram and estimate the resulting RMSE and RRMSE. Then, we double the number of expansion functions per expansion center, calculate the seismograms anew, estimate the RMSE, estimate the RRMSE, and so on, until a total of 4048 expansion functions are used. The number of matching points is kept constant at $M = 2048$ while the number of expansion centers is kept constant at $P = 8$. Figure 3-9 shows the resulting RMSE and RRMSE as functions of the total number of expansion functions used. A first observation is that 256 expansion functions seem to be the critical amount. Fewer expansion functions yield solutions that cannot capture important features of the true seismogram; hence, the solutions do not converge. Figure 3-10 shows a seismogram which is typical for a not converged solution. The seismogram was obtained with only 64 expansion functions. For more than 256 expansion functions, we have convergence where both RMSE and RRMSE decrease slowly with an increasing number of expansion functions. As a reminder, the well-converged MMP solution presented in Figures 3-6 and 3-8 was also calculated with 256 expansion functions and 8 expansion centers.

3.2.3 MMP versus SMP Expansion

The next numerical experiment shows the enhanced convergence of the MMP expansion compared to the classical eigenfunction expansion (SMP). As mentioned previously, the SMP expansion corresponds to using only one expansion center in (3.10a) or (3.10b). We perform the same experiment as before but use only one expansion center. Again, we start with one expansion function per domain and scalar potentials Φ and Ψ, which yield 4 expansion functions altogether. We calculate the seismogram and estimate the RMSE and RRMSE. The seismogram is shown in Figure 3-11. It is clean enough to be mistaken as correct but has no resemblance with the correct solution shown in Figure 3-5. Then we double the number of expansion functions per expansion center, calculate the seismograms, estimate the RMSE, the RRMSE, and so on. The number of matching points is again kept constant at $M = 2048$. Figure 3-9 shows the resulting RMSE and RRMSE as functions of the total number of expansion functions used. We notice that the MMP expansion using 8

expansion centers always performs better than the classical SMP. Also, using more than 256 expansion functions in the SMP expansion yields no useful results. The solutions obtained begin to diverge rapidly. This is an effect due to the expansion functions of higher-order violating the sampling condition (Hafner, 1990; Imhof, 1995). The maximum order N^{max} of a multipole is given by the largest angle φ^{max} between any two adjacent matching points and the location of the multipole:

$$N^{max} < \frac{\pi}{\varphi^{max}} . \tag{3.23}$$

The increased error in the SMP expansion between 16 and 64 expansion functions is an effect of the error measures (3.22) which are strongly affected by phase shifts. Contrary to the MMP expansion, an SMP expansion cannot solve the problem posed in Figure 3-5.

3.2.4 Effect of Number and Location of Expansion Centers

The next numerical experiment is to examine the importance and effect of the number, location and distribution of the expansion centers. As mentioned above, we have the choice of placing the expansion centers for the $\Phi^1(\mathbf{x},\omega)$ and $\Psi^1(\mathbf{x},\omega)$ fields either in or outside the scatterer, and thus expanding either into standing waves $J_{|n|}(kr)\, e^{in\theta}$ or into propagating waves $H^{(1)}_{|n|}(kr)e^{in\theta}$. We will use both to study the difference. We calculate the solutions for a range of expansion centers while keeping the total number of expansion functions constant at 256. Also, the number of matching points is kept constant at 256. Thus, the overall computational effort to calculate one seismogram is kept constant. The resulting RMSE and RRMSE are shown in Figure 3-12. It is surprising how broad the 'U'-shaped, minimal-error region is. The whole range from 5 to 15 expansion centers seems to converge. Indeed, the minimal RMSE and RRMSE obtained by 11 expansion centers are only slightly better than any other discretization employing 5 to 15 centers. Remarkably, MMP expansions are very insensitive to the actual discretization used! Neither the number of expansion centers nor the kind of expansions changes the RMSE or RRMSE by much, although the use of $H^{(1)}_{|n|}(kr)\ e^{in\theta}$ produces smoother RMSE and RRMSE curves. The pathological

case with 23 expansion centers shows that the errors increase dramatically when too many expansion centers are used. In this particular case, the expansion centers are separated by only a quarter of the dominant wavelength. The different expansion functions begin to interact by approximating higher order solutions to the wave equation. It is well-known that two monopoles of opposite sign placed closely together are equivalent to a dipole (Morse and Feshbach, 1953). Thus, the matrix system becomes badly conditioned since each expansion center could be replaced by the adjacent ones. Moreover, we add more similar equations to the matrix system which renders it more ill-conditioned. For comparison, we also use a simple boundary element (BEM) discretization with the same number of matching points and expansion functions. Along the boundary in between matching points, we place rotational and compressional monopole sources. As in the MMP cases, we use point matching and solve the system in the least-squares sense. The resulting large RMSE and RRMSE indicate that the seismogram obtained is not correct. Indeed, it contains mainly the reflections from the top of the scatterer. Reflections from the bottom as well as internal multiple scattered phases are mostly missing.

3.2.5 Number of Expansion Centers versus their Order of Poles

The next experiment is to study the tradeoff between the number of expansion centers and the orders of the multipoles. Figure 3-13 presents the RMSE as a function of the number of expansion centers P and the maximal orders $\pm N$ of the multipoles. The solution has converged for a RMSE of 0.15 or smaller. Clearly, the MMP expansion converges for $N = 2$ and $P = 13$, or for $N = 8$ and $P = 8$. Incidentally, the best result is obtained for $N = 8$ and $P = 12$. But there is also a tradeoff between RMSE and the computational effort, i.e., the total number of expansion functions $4(2N + 1)P$. Taking the computational effort into account, the optimal result is obtained by using 8 to 12 expansion centers and a maximal order of multipole of 4 to 2.

Using the addition theorem for the Bessel functions (Abramowitz and Stegun, 1964)

$$H_0(k\,|\mathbf{x}-\mathbf{x}_m|) = \sum_{n=-\infty}^{+\infty} J_n(k\,|\mathbf{x}_m|)\, H_n(k\,|\mathbf{x}|)\, e^{in(\theta-\theta_m)}, \tag{3.24}$$

we transform a virtual monopole source located on the boundary $\mathbf{x}_m$ into a multipole at the origin. The present form of the addition theorem assumes the receiver $\mathbf{x}$ to be outside the scatterer. The Bessel function $J_n(k\,|\mathbf{x}_m|) = J_n(kx_m)$ can be asymptotically expanded for large orders as (Abramowitz and Stegun, 1964)

$$J_n(kx_m) \approx \frac{1}{\sqrt{2\pi n}}\left(\frac{ekx_m}{2n}\right)^n \tag{3.25}$$

which vanishes for $kx < n$ as $n \to \infty$. For the model used, kx_m is around 6 for the dominant wavelength. For $n > 3$, the Hankel terms have less effect because the Bessel terms begin to vanish. This is consistent with Figure 3-13 where increasing the order of the multipoles beyond $N = 3$ hardly effects the RMSE in the optimal region of 8 to 12 expansion centers.

3.2.6 Effect of the Number of Matching Points

The final numerical experiment examines how the number of matching points affects the solutions. Actually, the ratio between the total number of equations in the matrix system and the number of expansion functions used – not the number of matching points – is the important parameter. In accordance with the earlier experiments, we choose 11 expansion centers and keep the number of expansion functions constant at 256. Since each matching point provides 4 equations (one for each boundary condition), we start out with 64 matching points along the boundary which provide 256 equations altogether. We calculate the resulting seismogram, estimate the RMSE and RRMSE, double the number of matching points, and so on. Figure 3-14 shows the resulting errors against the number of equations per expansion function. Since the expansion is non-orthogonal, it is not surprising that we get large errors when we use as many equations as we have unknowns. Using twice as many equations as unknowns provides the optimal result. Afterwards, the more equations

we add, the more the RMSE and RRMSE increase because the matrix system becomes more ill-conditioned with each additional equation we add. The result is more errors due to roundoff and other numerical effects.

Using twice as many equations as unknowns yields a distance of 4 m between matching points. This spacing corresponds to 10 matching points per dominant wavelength of 40 m. Assuming that the highest frequency in the propagating seismic Ricker pulse is 3 times the center frequency of 50 Hz (Hosken, 1988), the boundary is sampled with 3 matching points per wavelength for the highest frequency. The sampling theorem which states that the boundary has to be sampled at least twice per wavelength to prevent aliasing (Bouchon and Aki, 1977), is just satisfied. Thus, it is also theoretically justified to use about 10 matching points per dominant wavelength.

3.3 Discussion and Conclusions

Combining these numerical experiments with prior experiences with electromagnetic (Hafner, 1990) and acoustical MMP methods (Imhof, 1995), we obtain a set of empirical rules on how to discretize elastic scattering problems. A very important parameter is the radius of greatest influence of a multipole which is $\sqrt{2}$ times the distance between the center of expansion and the closest matching point.

- The radius of greatest influence should be on the order of the dominant wavelength.
- No expansion center should be within the radius of greatest influence of any other expansion center.
- There should be ≈ 10 matching points per dominant wavelength
- There has to be at least half a matching point per expansion function or similarly two equations per expansion function.
- The maximum order N of a multipole is given by the sampling theorem: $N < \pi/\varphi^{max}$ where φ^{max} is the maximal angle φ under which two adjacent matching points located

within the radius of greatest influence are seen by the respective multipole.

- The addition theorem for Bessel functions determines a reasonable order N of a multipole. For a dominant wavelength λ and a radius of greatest influence r, the maximum order N should be comparable to $3r/\lambda$.

- Expansions of the form $H_{|n|}^{(1)}(kr)\, e^{in\theta}$ should not be used for the region where their expansion center $\mathbf{x}_p$ is located.

  Expansions of the form $J_{|n|}(kr)\, e^{in\theta}$ should only be used for bounded domains. The expansion center $\mathbf{x}_p$ has to be located inside this region.

The above rules, except the last one, are general guidelines, but adhering to them generally yields satisfactory results. As the numerical experiments show, all parameters can be varied by large amounts while only perturbing the resulting solution. The MMP method is not very sensitive to the actual discretization used.

We showed that the MMP expansion converges faster than the classical multipole or simple boundary element expansions for complex scattering geometries. The method can solve scattering problems involving either harmonic or impulsive sources. Seismograms in the time-domain are obtained by Fourier synthesis.

For a homogeneous scatterer embedded in a homogeneous background, we found that the MMP expansions yield the same degree of accuracy as the finite difference method. For the MMP method, the computational effort is related to the interface area of the embedded scatterers and thus to the number of expansion functions and matching points needed. For the FD method, the computational effort relates to the volume containing the sources, receivers and scatterers. For problems where the distances between sources, receivers and scatterers are large, MMP expansions are competitive. Also, due to its spectral nature, attenuation can easily be accounted for. For problems where heterogeneous scatterers are embedded in a homogeneous background, hybridized schemes with finite elements can be devised.

In conclusion, the MMP method is well-suited for a large range of scattering problems since both acoustic and elastic media with different boundary conditions (fluid-fluid, fluid-elastic, elastic-elastic and others) can be treated exactly the same way in this algorithm.

Receiver	x	z	Comments
1	-70.0	0.0	incident field does not contribute
2	70.0	0.0	incident field does not contribute
3	70.0	-200.0	
4	0.0	-200.0	
5	-70.0	-200.0	
6	-110.0	-110.0	inside scatterer
7	-50.0	-100.0	inside scatterer
8	0.0	-100.0	inside scatterer
9	50.0	-100.0	inside scatterer
10	105.0	-110.0	inside scatterer
11	-150.0	-200.0	
12	150.0	-200.0	
13	-150.0	200.0	
14	150.0	200.0	

Table 3.1: Locations of the receivers used in the comparison of the MMP solution to the FD solution. The source location is the origin of the coordinate system used.

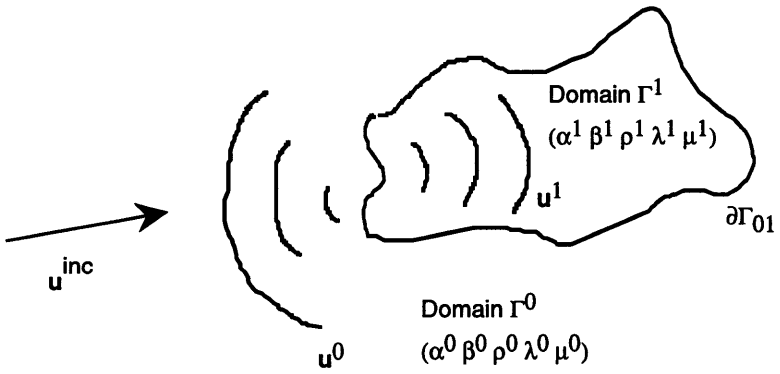

Figure 3-1: Schematic representation of the scattering experiment. An incident field $\mathbf{u}^{inc}(\mathbf{x},\omega)$ illuminates a bounded two-dimensional inhomogeneity which induces a scattered field $\mathbf{u}^0(\mathbf{x},\omega)$ in the background medium $(\alpha^0,\beta^0,\rho^0)$ as well as a field $\mathbf{u}^1(\mathbf{x},\omega)$ in the scatterer itself $(\alpha^1,\beta^1,\rho^1)$.

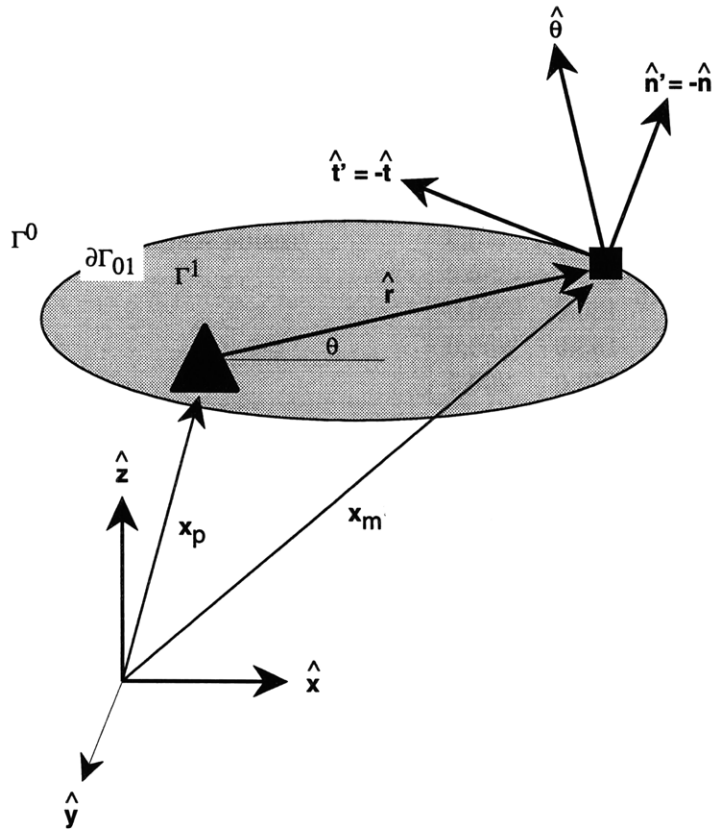

Figure 3-2: Schematic of the coordinate systems used. In addition to the global Cartesian coordinate frame (x, z, y), local cylindrical systems (r, θ, y), and local Cartesian systems (n, t, y) are used. The cylindrical coordinate systems (r, θ, y) have their origins at the expansion centers $\mathbf{x}_p$ (triangles) and are used to express the expansion functions ϕ^d_{pn} and ψ^d_{pn}. The boundary Γ_{01} between the scatterer and the background is defined by discrete matching points (squares) located at $\mathbf{x}_m$, where the normal $\hat{\mathbf{n}}$ and the tangential $\hat{\mathbf{t}}$ directions are specified. The normal direction $\hat{\mathbf{n}}$ is defined to point from the background Γ^0 into the scatterer Γ^1. The boundary conditions are expressed in the local systems (n, t, y).

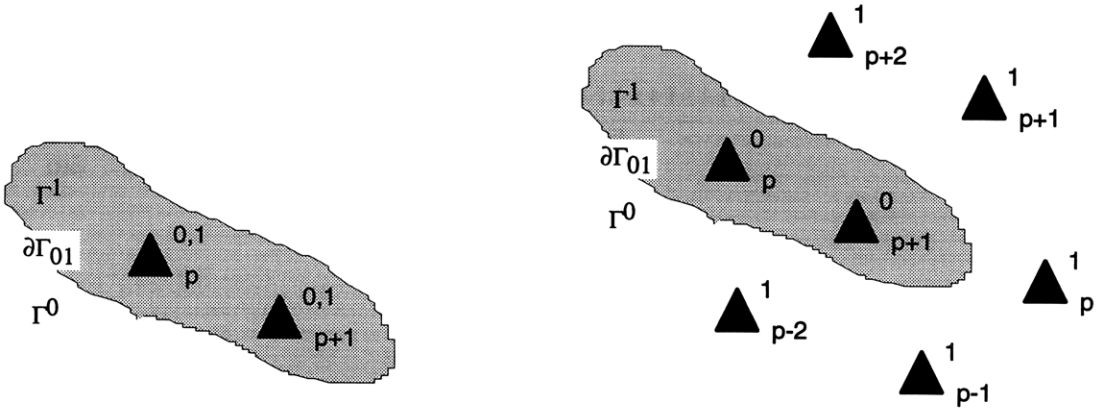

$$\Phi^0 = \sum\sum a^0_{pn} H^{(0)}_{|n|}(k^0 r^0_p) e^{in\theta} \qquad \Phi^0 = \sum\sum a^0_{pn} H^{(0)}_{|n|}(k^0 r^0_p) e^{in\theta}$$

$$\Psi^0 = \sum\sum b^0_{pn} H^{(0)}_{|n|}(l^0 r^0_p) e^{in\theta} \qquad \Psi^0 = \sum\sum b^0_{pn} H^{(0)}_{|n|}(l^0 r^0_p) e^{in\theta}$$

$$\Phi^1 = \sum\sum a^1_{pn} J_{|n|}(k^1 r^1_p) e^{in\theta} \qquad \Phi^1 = \sum\sum a^1_{pn} H^{(0)}_{|n|}(k^1 r^1_p) e^{in\theta}$$

$$\Psi^1 = \sum\sum b^1_{pn} J_{|n|}(l^1 r^1_p) e^{in\theta} \qquad \Psi^1 = \sum\sum b^1_{pn} H^{(0)}_{|n|}(l^1 r^1_p) e^{in\theta}$$

Figure 3-3: Basis functions can either contain Hankel solutions $H_n\, e^{in\theta}$ or Bessel solutions $J_n\, e^{in\theta}$. If the same expansion center $\mathbf{x}^0_p = \mathbf{x}^1_p$ is to be used for both ϕ^0_p and ϕ^1_p, the inside field Φ^0 has to be expanded using the Bessel solutions $J_n\, e^{in\theta}$ representing standing waves. If the inside and the outside scattered field are represented by Hankel solutions $H_n\, e^{in\theta}$, different expansion centers $\mathbf{x}^0_p$ and $\mathbf{x}^1_p$ have to be used. Expansion centers are depicted by a triangle.

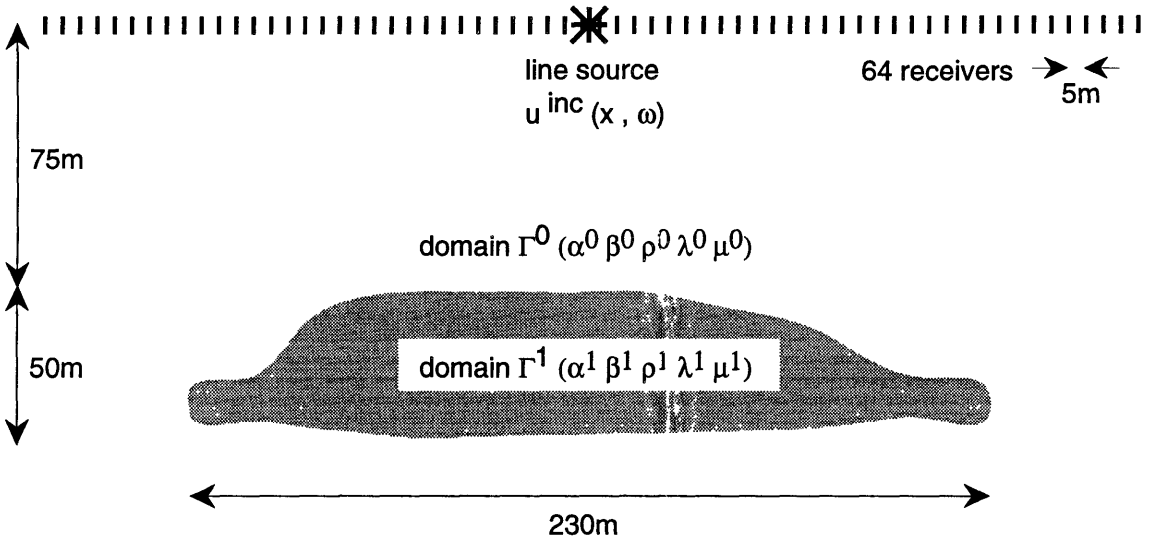

Figure 3-4: Generic scatterer used for numerical experiments. The scatterer is illuminated by an explosive line source modulated by a Ricker pulse of 50Hz center frequency. The density and the velocities in the background domain Γ^0 are $\rho = 2000\,\mathrm{kg/m^3}$, $\alpha^0 = 2000\,\mathrm{m/s}$, and $\beta^0 = 1155\,\mathrm{m/s}$. Density and velocities in the scatterer Γ^1 are $\rho = 2500\,\mathrm{kg/m^3}$, $\alpha^1 = 3000\,\mathrm{m/s}$, and $\beta^1 = 1732\,\mathrm{m/s}$. The Poisson's ratio is the same for both regions ($\sigma = 0.25$).

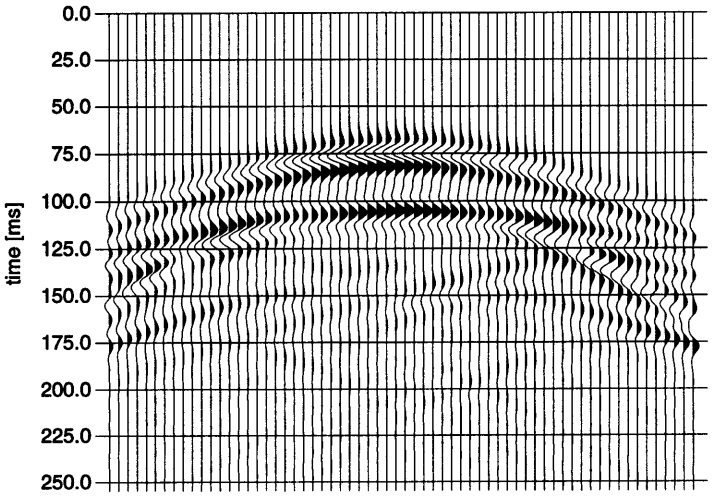

Figure 3-5: The seismogram (vertical displacement) of the model shown in Figure 3-4 calculated with a finite-difference program. This seismogram is used as a reference to compare those calculated with different MMP discretizations.

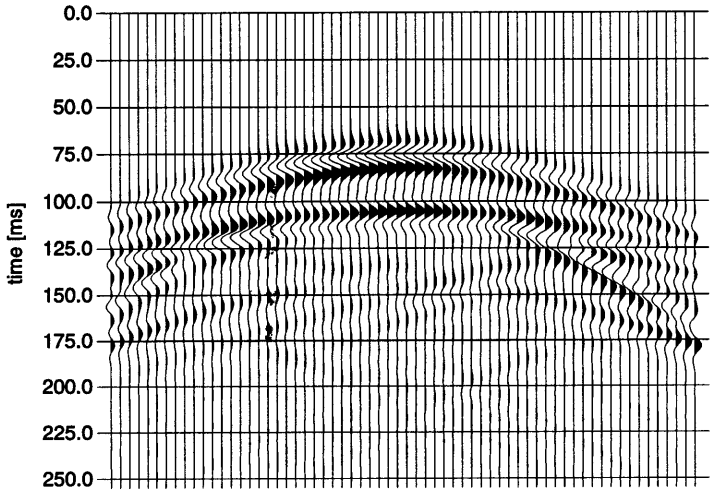

Figure 3-6: The seismogram of the model shown in Figure 3-4 calculated using the MMP algorithm. Altogether, 256 expansion functions, 8 expansion centers, 128 matching points and 64 frequencies were used. As can be seen, the MMP solution agrees very well with the finite difference reference seismogram shown in Figure 3-5.

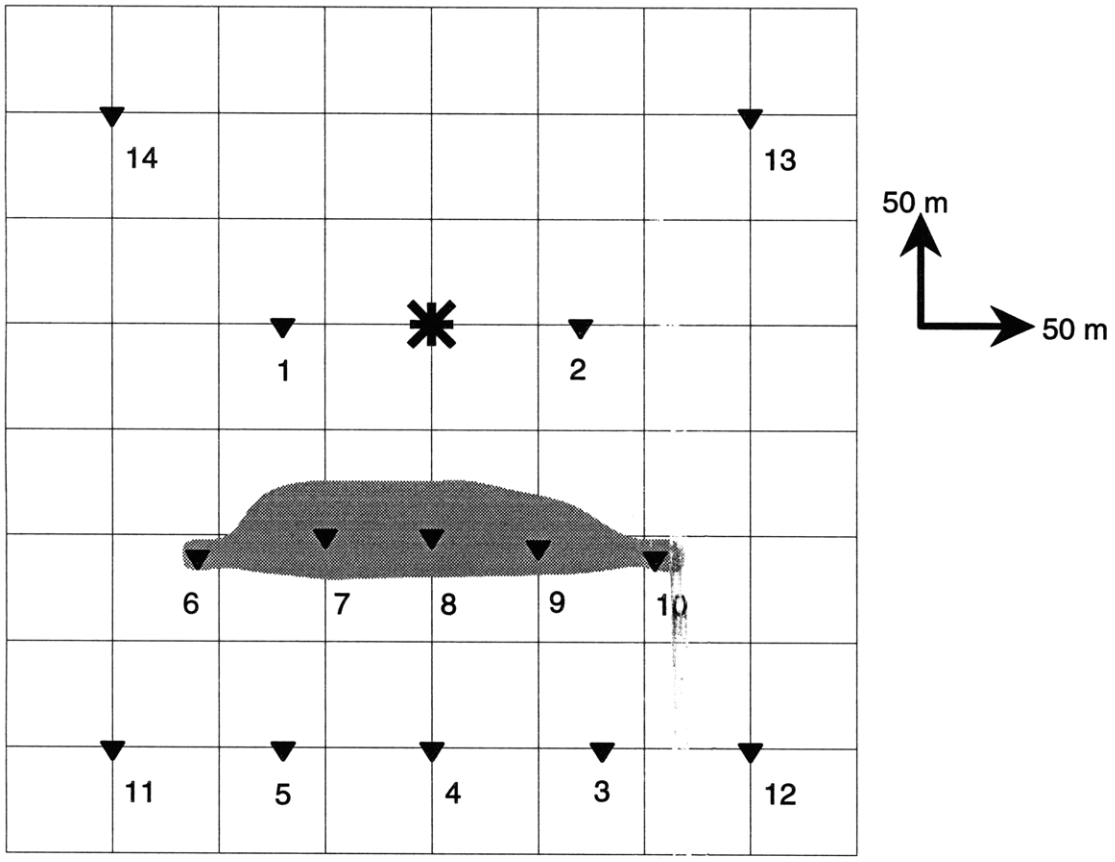

Figure 3-7: Locations of the source (star) and the receivers (triangles) used for comparison between the MMP and FD solutions as presented in Figure 3-8.

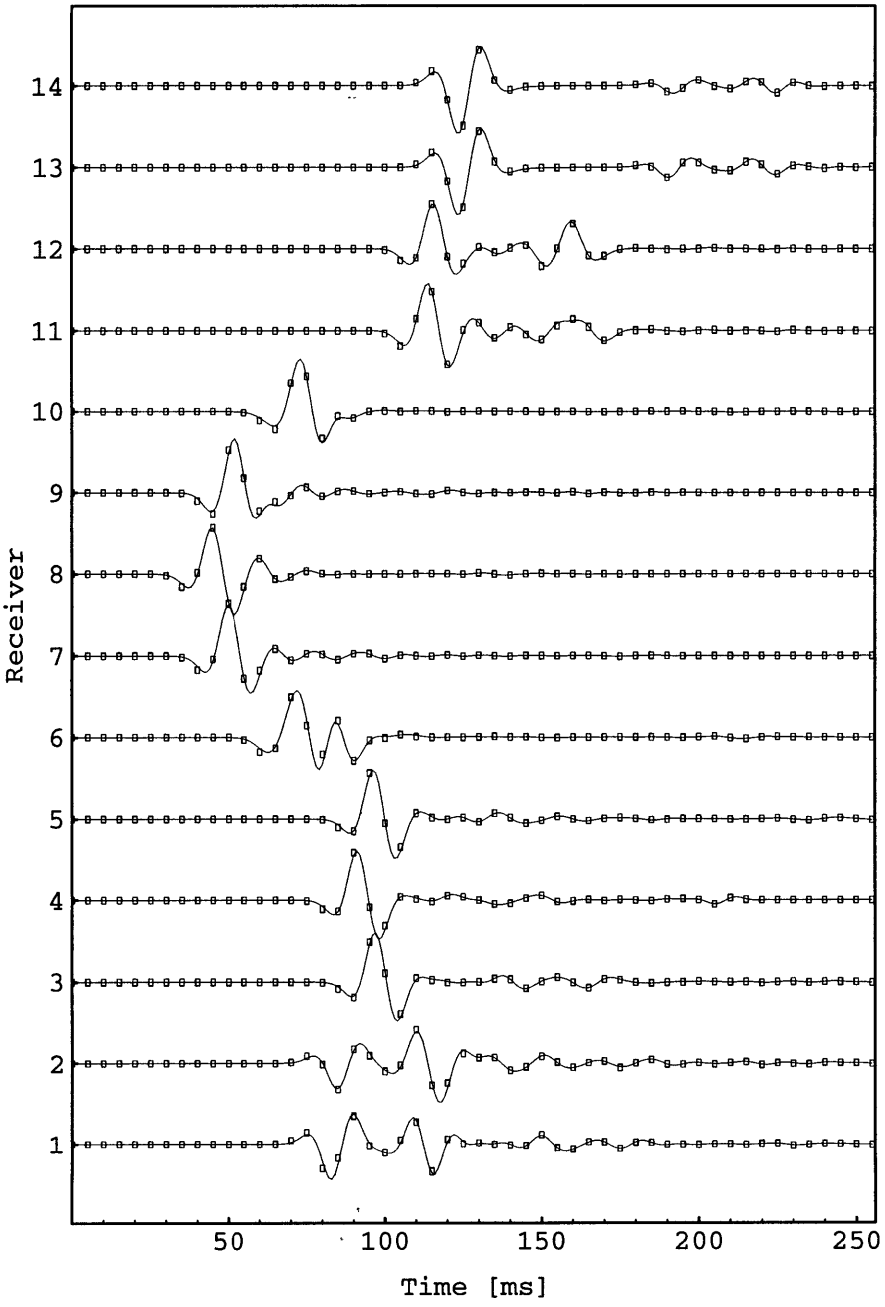

Figure 3-8: Comparison of the MMP solution (solid line) with the FD solution (boxed). The exact location of the receivers is given in Table 3.1 and Figure 3-7. Receivers 1, 2, 13, and 14 are above the scatterer; 6, 7, 8, 9, and 10 are in the scatterer; and 3, 4, 5, 11, and 12 are below the scatterer.

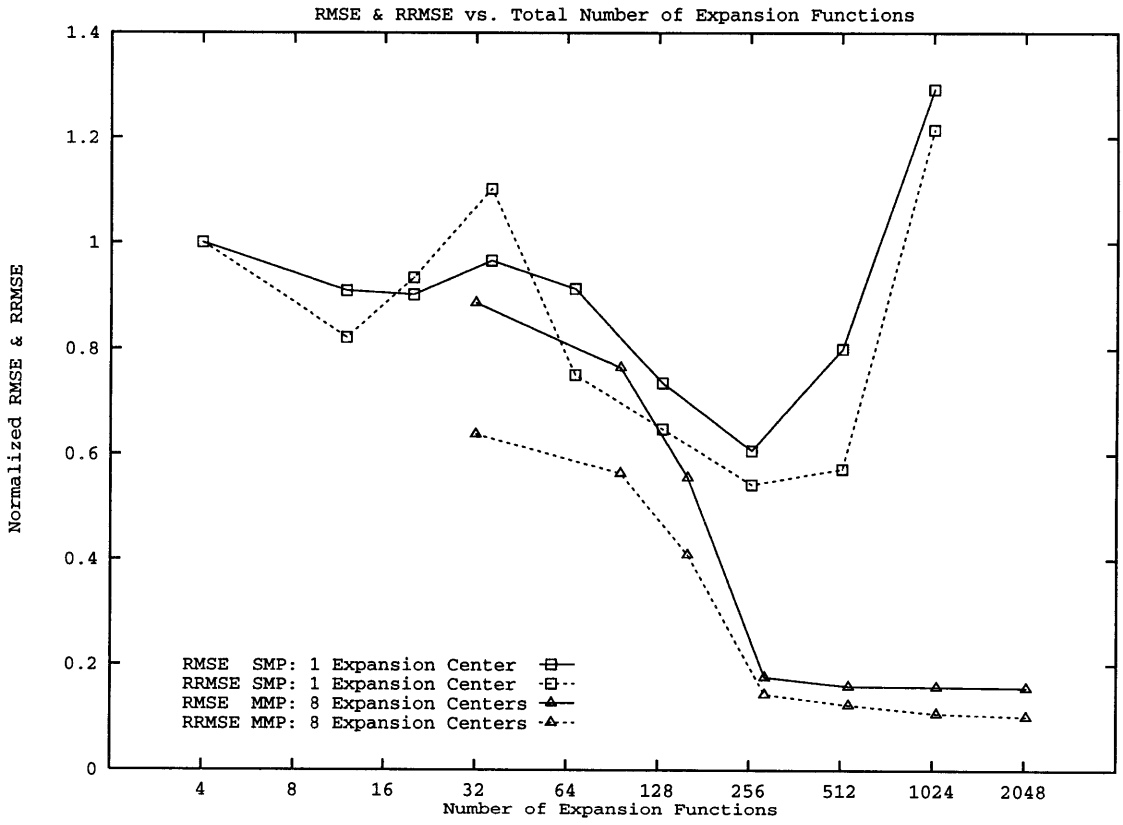

Figure 3-9: Comparison between the traditional eigenfunction expansion SMP (boxes) and the MMP expansion (triangles). Shown is how the total number of expansion functions affects the RMSE (solid) and RRMSE (dashed) compared to the FD reference solution. For 256 and more expansion functions, the MMP expansion converge. The SMP actually never converges since it violates the sampling condition for more than 256 expansion functions.

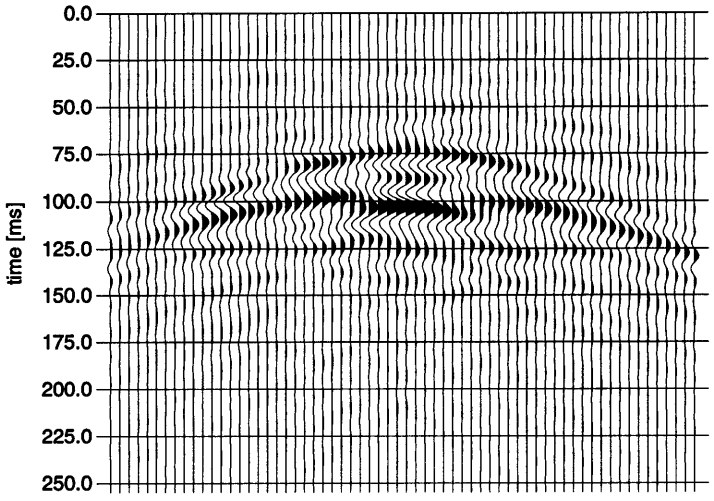

Figure 3-10: The seismogram for the case where 64 expansion functions are used. The seismogram is very noisy. Some of the prominent features in Figure 3-5 begin to show up, but the expansions have not yet converged. More terms have to be used to obtain convergence.

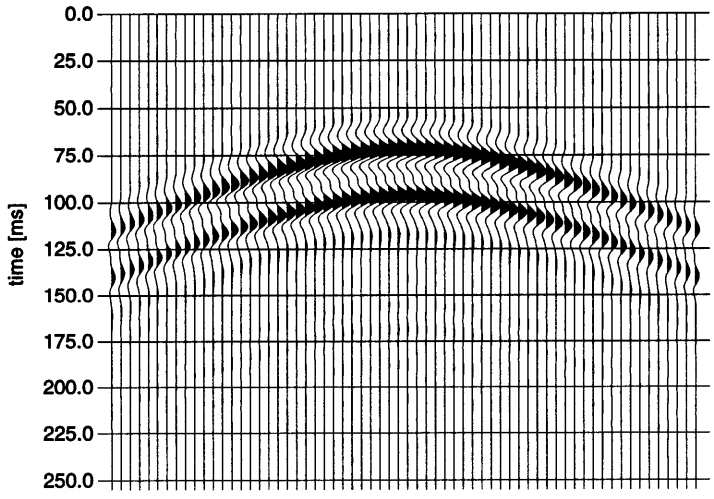

Figure 3-11: The seismogram for the case where only 4 expansion functions are used. Clearly, no self-interaction of the scattered wavefields is possible. Unfortunately, the seismogram is clean enough to be mistaken as correct.

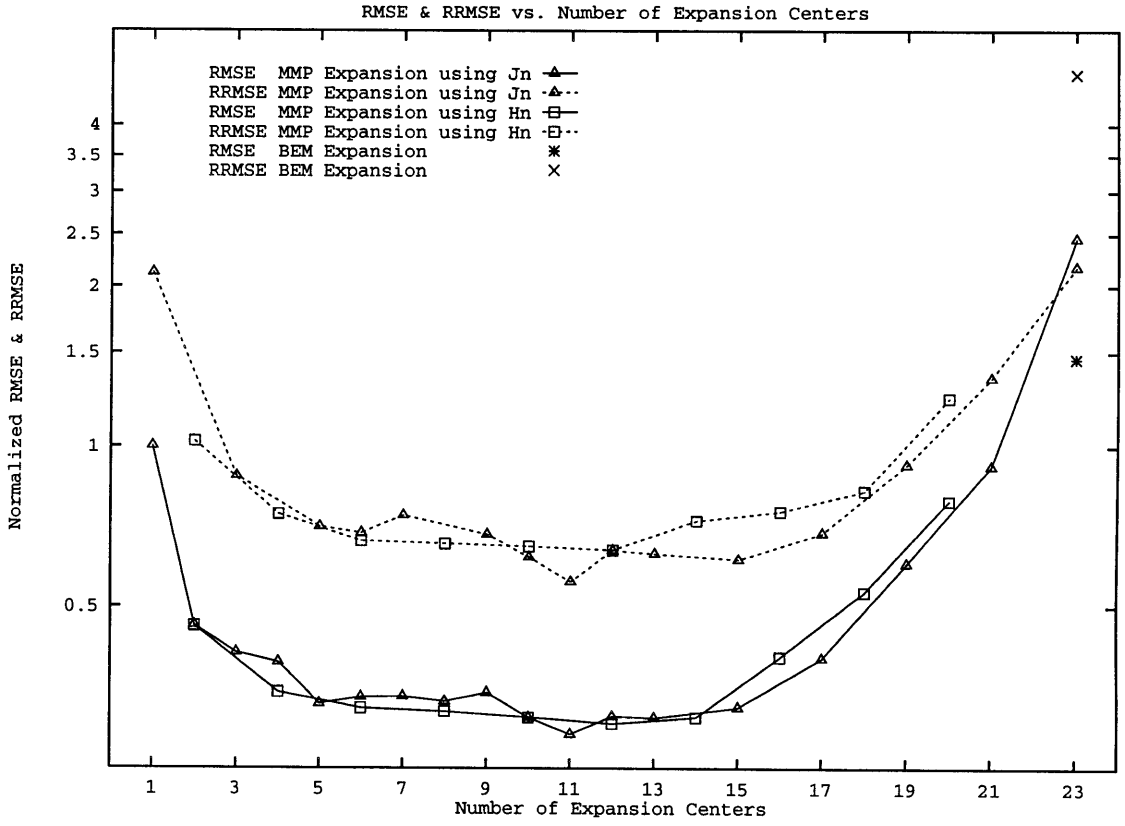

Figure 3-12: Effect of the number and location of expansion centers. The total number of expansion functions is kept constant at 256 while the number of expansion centers is varied from 1 up to 23. Expansions using the same expansion centers $\mathbf{x}_p^d \in \Gamma^1$ for $\phi^0, \psi^0, \phi^1, \psi^1$, and thus Bessel functions J_n, as well as expansions using expansion centers $\mathbf{x}_p^0 \in \Gamma^1$ for ϕ^0, ψ^0 and $\mathbf{x}_p^1 \in \Gamma^0$ for ϕ^1, ψ^1, and thus Hankel functions H_n, are tested. The difference between these two kinds of expansions is rather small. Placing all expansion centers onto the boundary and using only the terms of 0^{th} order corresponding to a simple boundary element expansions fails surprisingly.

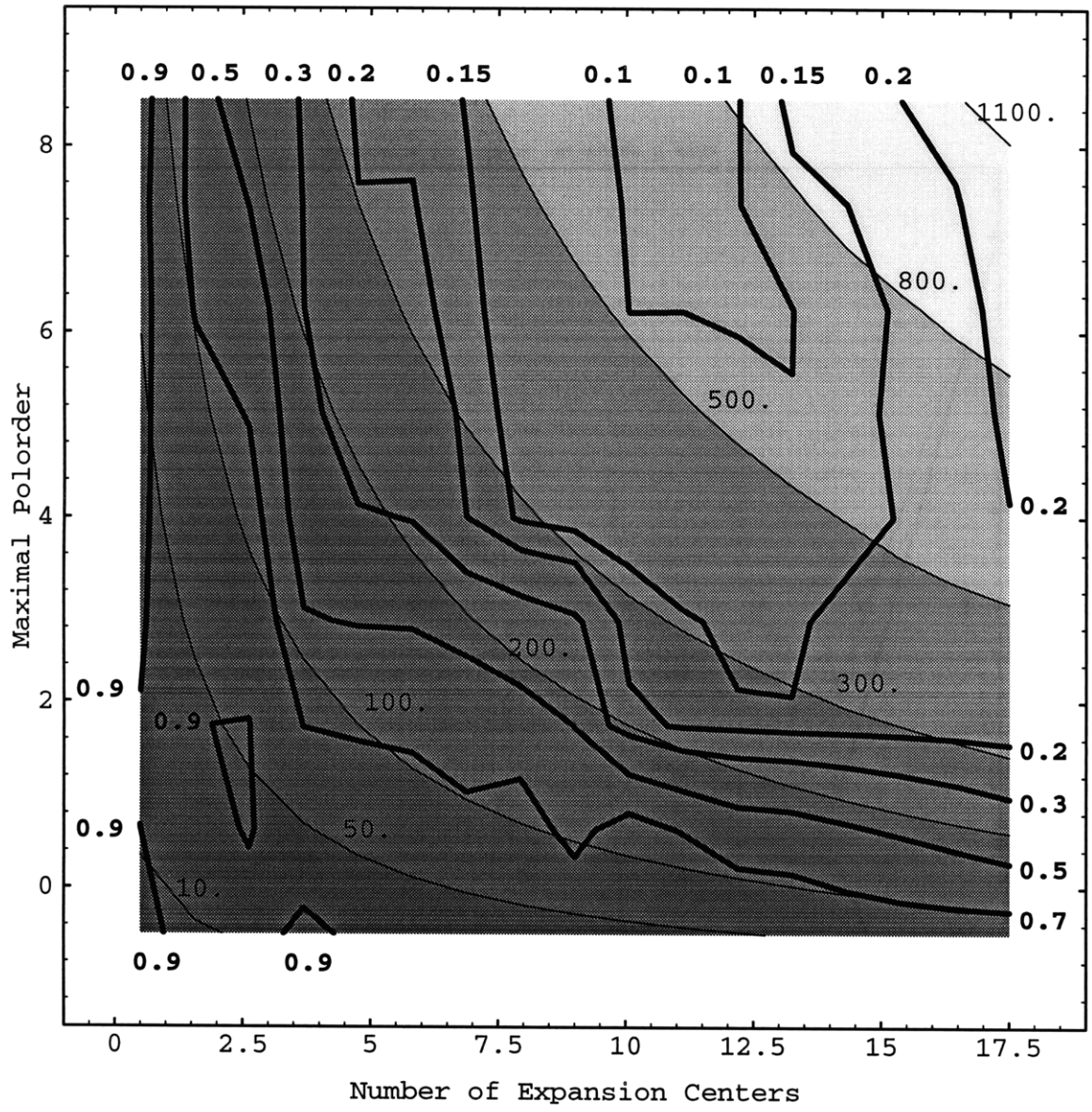

Figure 3-13: RMSE and the number of expansion functions versus the maximal polorder $\pm N$ and the number of expansion centers P. The bold lines contour the RMSE while the shading and the fine contour lines denote the total number of expansion functions $4(2N+1)P$. The minimal RMSE is obtained for $N = 8$ and $P = 12$.

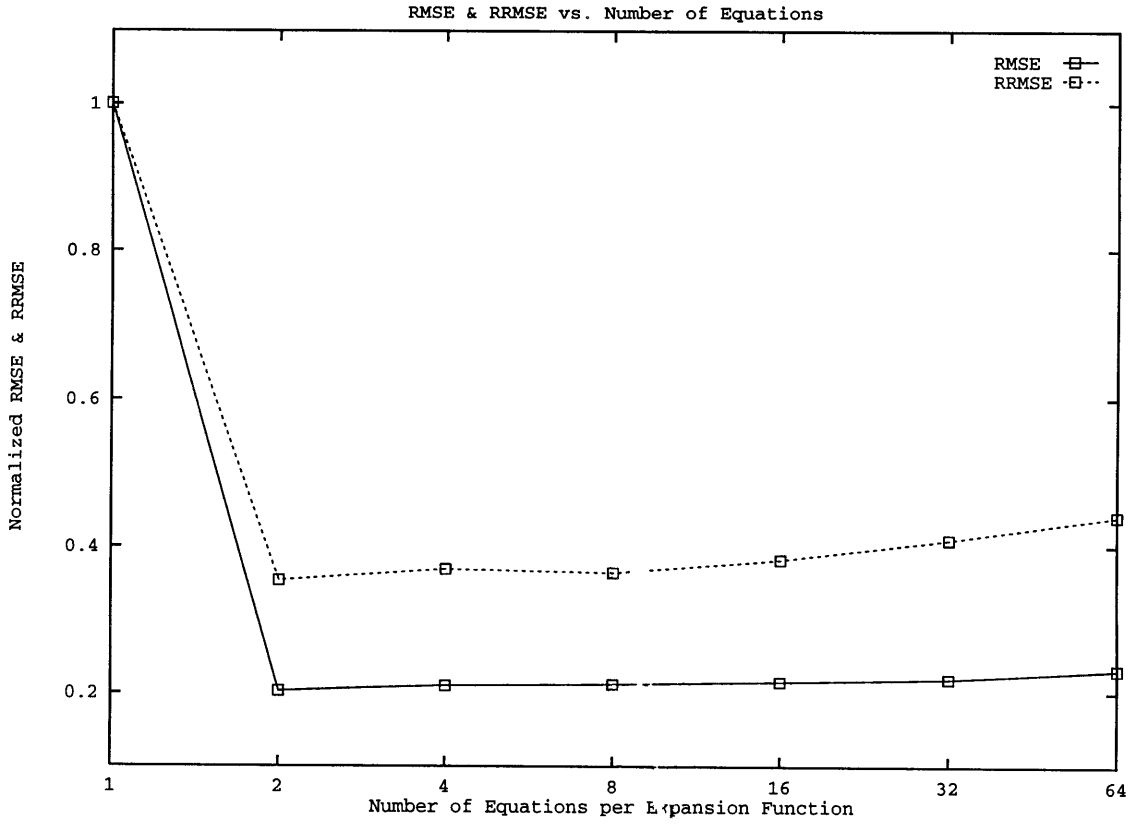

Figure 3-14: Influence of the number of matching points on the expansion with 256 expansion functions and 8 centers of expansion. Each matching point provides 4 equations. Since the expansion is non-orthogonal, using as many equations as unknowns to be resolved does not yield a correct result. Adding more and more equations to the system increases the condition number and thus the RMSE (solid) and RRMSE (dashed) are increased due to numerical errors.

Chapter 4

Scattering of Acoustic and Elastic Waves using a Hybrid Multiple Multipole Expansions - Finite Element Technique

Abstract

In this paper, two different methods to solve scattering problems in acoustic or elastic media are coupled to enhance their usefulness. The multiple multipole (MMP) expansions are used to solve for the scattered fields in unbounded homogeneous regions. The finite element (FE) method is used to calculate the scattered fields in bounded, heterogeneous regions. Applying the boundary conditions, the different regions and methods are coupled together in the least-squares sense as the MMP method requires. By construction, the scattered field in the homogeneous regions is decomposed into P- and S-modes for the elastic case. In some examples, the scattered fields are calculated and compared to the analytical solutions. Additionally, the seismograms are calculated for a few scattering problems with one or

several heterogeneous scatterers of complex geometries. The hybrid MMP-FEM technique proves to be a rather general and useful tool to solve complex, two-dimensional scattering problems.

Introduction

Wave scattering problems have been investigated by different techniques. Analytical solutions to the integral equations do not generally exist, except for some very simple geometries. Analytical mode expansion is limited to geometries such as circular cylinders, where the modes decouple (Pao and Mow, 1973). Therefore, numerical schemes seem to be the most direct procedure for arbitrary geometries. Numerical boundary integral techniques (Schuster and Smith, 1985; Bouchon, 1993; Dong *et al.*, 1995), the T-matrix method (Waterman, 1969, 1976) and MMP expansions (Hafner, 1990; Imhof, 1995) are examples thereof. Unfortunately, they all depend on either Green's functions or other solutions to the wave equation, which tend to be hard or impossible to find for heterogeneous or anisotropic media. These methods are normally limited to scattering between homogeneous scatterers embedded in a homogeneous background. On the other hand, these methods do not encounter problems with unbounded domains. No artificial radiating boundary conditions have to be enforced. In fact, the scattered fields can be evaluated anywhere.

In cases where the medium is heterogeneous, finite element (FE) (Zienkiewicz, 1977; Marfurt, 1984; Schwarz, 1988; Murphy and Chin-Bing, 1989, 1991) or finite differences (FD) (Marfurt, 1984; Kelly *et al.*, 1976; Virieux, 1986; Cheng *et al.*, 1994) techniques are routinely used to calculate the scattered wavefields. In contrast to the boundary methods mentioned above, FE and FD do encounter serious problems with unbounded domains. The domain has to be truncated and radiating boundary conditions have to be enforced (Gan *et al.*, 1993). In addition, they are limited by computer memory and runtime considerations. For many problems the distances between inhomogeneities, source, and receivers are rather large and thus might result in prohibitive computation times and memory requirements.

Many scattering problems exist which fall in between these two classes. These problems involve heterogeneous regions which are bounded and embedded in a homogeneous background. Applications of this can be found in geophysical exploration, earthquake engineering, ultrasonic nondestructive testing and medical imaging, and underwater acoustics. There is an interest in combining methods (Zienkiewicz *et al.*, 1977; Shah *et al.*, 1983; Su *et al.*, 1983; Dubus, 1994) for unbounded, homogeneous domains with methods which can handle heterogeneous regions of limited extent. In the present paper, such a combination is made between MMP expansions and the FE method (FEM). A similar combination has already been presented for electromagnetic scattering problems (Sroka *et al.*, 1990; Bomholt, 1994). As a bonus in the elastic case, the scattered fields in the homogeneous domain are, by construction, decomposed into P- and S-waves.

We will apply the hybrid technique to both acoustic and elastic in-plane scattering problems where one or multiple heterogeneities are embedded in a homogeneous medium. Both source and receiver are in the homogeneous region, although all the ideas presented here will also hold if the source and/or the receiver are located in the heterogeneity. Furthermore, we could use the combined MMP-FEM technique to construct radiating boundary conditions. But in this work, we will not investigate this usage of the technique. Also, we will not present the case of anti-plane wave motion (SH) because it can be derived easily from the acoustic case.

The present paper is structured as follows: First, we review both MMP expansions and the finite element method for the acoustic case. Next, we combine the methods for the acoustic case. Then, we extend MMP and FEM to the elastic case and present the combination. Finally, we discuss a few details of the implementation on a digital computer, present solutions to some scattering problems, and compare them to analytical solutions where available.

4.1 Acoustic Theory

We would like to model how an incident wavefield $P^{inc}(\mathbf{x},\omega)e^{i\omega t}$ of angular frequency ω scatters from an object. The situation is depicted in Figure 4-1. The scatterer Ω^I is heterogeneous and embedded in a homogeneous background Ω^O. For the sake of simplicity, we will suppress the time factor $e^{i\omega t}$ in all following expressions. Where necessary, the superscripts ^{O}, ^{B}, and ^{I} will respectively denote quantities which belong to the homogeneous region on the outside, lie on the boundary between the domains, or are inside the heterogeneous region. Quantities marked with a tilde are either transformed quantities (e.g., LU or QR decomposed) or local quantities for a particular little region $\tilde{\Omega}$, e.g., a finite element. The context normally allows one to infer the correct meaning.

4.1.1 Homogeneous Regions: Multiple Multipole Expansions (MMP)

In a homogeneous region Ω^O, expansions for the scattered pressure fields are made with exact solutions to the homogeneous wave equation

$$P^O(\mathbf{x}) = \sum_{j=1}^{J^O} p_j^O P_j^O(\mathbf{x}), \tag{4.1}$$

where all $P_j^O(\mathbf{x})$ satisfy the homogeneous Helmholtz equation

$$(\nabla^2 + k_O^2)P_j^O(\mathbf{x}) = 0 \tag{4.2}$$

with the wave number $k_O = \omega/\alpha_O$ and the wave velocity α_O in the homogeneous region. The factors p_j^O are complex valued weighting coefficients for the different expansion functions P_j^O. As the name of the method implies, several multipole solutions centered at different locations are often used as expansion functions. These functions have a local behavior and thus are able to model wavefields scattered from complex geometries (Imhof, 1995). In general, MMP expansions have a smaller number of unknowns than comparable methods. Hence, using M multipoles with their respective origins located at $\mathbf{x}_m$, we commonly write

the scattered wavefields in the homogeneous region as

$$P^O(\mathbf{x}) = \sum_{m=1}^{M} \sum_{n=-N}^{N} p_{mn}^O e^{in\theta} H_{|n|}^{(1)} \left(k_O \left|\mathbf{x} - \mathbf{x}_m\right|\right). \tag{4.3}$$

The functions $H_{|n|}^{(1)}$ are the Hankel functions of the first kind and order n radiating outward. Each summation over the index n builds up one multipole. Since the Hankel functions have a singularity at their origin, the centers of expansions $\mathbf{x}_m$ may not be located in the homogeneous region Ω^O. For each multipole, all orders between $-N \leq n \leq +N$ are normally used as basis functions.

Additional expansion functions such as plane waves, beams, or other special modes can be included. Although we will not make use of these additional expansion functions in the present work, we prefer the notation (4.1) to (4.3) for its generality and simplicity. Equations for the weighting coefficients p_j^O are obtained by enforcing boundary conditions for the pressure and the normal displacement on discrete matching points $\mathbf{m}_i$ on the boundaries between domains. The normal direction pointing outward from $\mathbf{m}_i$ is denoted by $\hat{\mathbf{n}}_i$. Then, the boundary conditions between two domains Ω^O and Ω^X are

$$\sum_{j=1}^{J^O} p_j^O P_j^O(\mathbf{m}_i) + P^{inc}(\mathbf{m}_i) = P^X(\mathbf{m}_i), \tag{4.4}$$

$$\frac{-1}{k_O^2 \lambda^O} \hat{\mathbf{n}}_i \cdot \sum_{j=1}^{J^O} p_j^O \nabla P_j^O(\mathbf{m}_i) + \frac{-1}{k_O^2 \lambda^O} \hat{\mathbf{n}}_i \cdot \nabla P^{inc}(\mathbf{m}_i) = \frac{-1}{k_X^2 \lambda^X} \hat{\mathbf{n}}_i \cdot \nabla P^X(\mathbf{m}_i), \tag{4.5}$$

where it is assumed that the only source is the incident field P^{inc} propagating in the homogeneous domain Ω^O. The parameter $\lambda = \alpha^2 \rho$ is the Lamé constant for a region with density ρ and velocity α. Hence, we can construct a linear equation system

$$\begin{pmatrix} \mathbf{P}^O \\ \mathbf{U}^O \end{pmatrix} \cdot \mathbf{p}^O = \begin{pmatrix} \mathbf{P}^X - \mathbf{P}^{inc} \\ \mathbf{U}^X - \mathbf{U}^{inc} \end{pmatrix}, \tag{4.6}$$

where the submatrices P_{ij}^O and U_{ij}^O contain P_j^O and $\frac{-1}{k_O^2 \lambda^O} \hat{\mathbf{n}}_i \cdot \nabla P_j^O$ evaluated at the matching points $\mathbf{m}_i$. In general, expansions of the form (4.1) are *not orthogonal.* Thus, more matching

points than expansion functions have to be used and the resulting overdetermined linear system (4.6) has to be solved in the *least-squares sense* minimizing the overall error in the boundary conditions. Thus, by construction, the matrices $\mathbf{P}^O$ and $\mathbf{U}^O$ are rectangular and dense.

4.1.2 Heterogeneous Regions: Finite Elements (FE)

Neglecting source terms, waves propagating in a heterogeneous region Ω^I are governed by the general Helmholtz equation

$$\nabla \cdot \{\rho^{-1} \nabla P\} + \rho^{-1} k^2 P = 0\,, \tag{4.7}$$

where $\rho = \rho(\mathbf{x})$ and $k = k(\mathbf{x})$ respectively denote spatially varying density and wave number.

To solve this equation, we partition the heterogeneous domain Ω^I into small and nonoverlapping elements $\tilde{\Omega}$ (Zienkiewicz, 1977; Schwarz, 1988; Murphy and Chin-Bing, 1989) as depicted in Figure 4-1. The complex valued weighting coefficients $\tilde{p}_j$ are the pressure values at the element's corners $\tilde{\mathbf{x}}_j$. They are also known as node points and thus the coefficients $\tilde{p}_j$ are called node variables. Commonly, one chooses triangular or quadrangular elements. In each element, the pressure field $\tilde{P}$ is approximated by an interpolation function. For a quadrangular element, the simplest interpolation function to use is the bilinear one:

$$\tilde{P}(\mathbf{x}) = \tilde{a}_0 + \tilde{a}_1 x + \tilde{a}_2 z + \tilde{a}_3 xz\,. \tag{4.8}$$

Instead of directly using the coefficients $\tilde{a}_j$, the polynomial (4.8) is transformed into the sum of simple shape functions $\tilde{N}_j(\mathbf{x})$ having local support only.

$$\tilde{P}(\mathbf{x}) = \sum_{j=1}^{4} \tilde{p}_j \tilde{N}_j(\mathbf{x}) \tag{4.9}$$

For example, in a rectangular element of unit size, $\tilde{N}_3(\mathbf{x}) = xz$. This particular shape function is visualized in Figure 4-2. The other ones are obtained by rotations of $-180°$,

$-90°$ and $90°$, respectively. The complex valued weighting coefficients $\tilde{p}_j$ are the pressure values at the element's corners $\tilde{\mathbf{x}}_j$. They are also known as node points and thus the coefficients $\tilde{p}_j$ are called node variables. Also, the interpolation functions have to satisfy the following orthogonalization and normalization conditions:

$$\tilde{N}_j(\tilde{\mathbf{x}}_i) = \delta_{ij} \tag{4.10}$$

$$\sum_{j=1}^{4} \tilde{N}_j(\mathbf{x}) = 1 \quad \text{for} \quad \mathbf{x} \in \tilde{\Omega} \tag{4.11}$$

where δ_{ij} is the Kronecker delta function.

Consequently, the continuous pressure in the Helmholtz equation (4.7) is replaced by the interpolation (4.9). Applying Galerkin's method, we multiply the resulting expression by the test function $\tilde{N}_i(\mathbf{x})$ and integrate over the element $\tilde{\Omega}$. We obtain

$$\sum_{j=1}^{4} \left\{ \iint_{\tilde{\Omega}} \rho^{-1} \nabla\tilde{N}_i \cdot \nabla\tilde{N}_j \, dA - \iint_{\tilde{\Omega}} \rho^{-1} k^2 \, \tilde{N}_i \tilde{N}_j \, dA \right\} \tilde{p}_j - \int_{\tilde{\Gamma}} \rho^{-1} \tilde{N}_i \frac{\partial P}{\partial n} \, dl = 0 \,, \tag{4.12}$$

where the divergence theorem has been used to transform the first integral. All integrals are over the surface $\tilde{\Omega}$ or around the boundary $\tilde{\Gamma}$ of the element $\tilde{\Omega}$, respectively. Evaluating (4.12) for all four $\tilde{N}_i(\mathbf{x})$ will yield a set of four equations for the four unknown node variables $\tilde{p}_j$.

These three integrals define the local stiffness matrix $\tilde{\mathbf{S}}$, the local mass matrix $\tilde{\mathbf{M}}$ and the local force vector $\tilde{\mathbf{f}}$.

$$\tilde{S}_{ij} = \iint_{\tilde{\Omega}} \rho^{-1} \nabla\tilde{N}_i \cdot \nabla\tilde{N}_j \, dA \tag{4.13}$$

$$\tilde{M}_{ij} = \iint_{\tilde{\Omega}} \rho^{-1} k^2 \, \tilde{N}_i \tilde{N}_j \, dA \tag{4.14}$$

$$\tilde{f}_i = \int_{\tilde{\Gamma}} \rho^{-1} \tilde{N}_i \frac{\partial P}{\partial n} \, dl \tag{4.15}$$

For interior elements, the boundary integral (4.15) is not zero, but its contributions will exactly cancel with like terms coming from neighboring elements. One only need recall

that the term $\rho^{-1}\frac{\partial P}{\partial n}$ is proportional to the normal displacement. But, both the normal displacement and the pressure are continuous across boundaries. Therefore, the line integral has to be taken into account only on the domain boundary since it is not cancelled by a like term from a neighboring element.

If the element $\tilde{\Omega}$ is adjacent to a void domain, the boundary integral (4.15) will vanish, since $\tilde{N}_i = 0$. If the element is adjacent to a rigid domain, the integral (4.15) also vanishes because $\frac{\partial P}{\partial n} = 0$. In all other cases, the boundary integral (4.15) has to be included. Assuming that $\frac{\partial P}{\partial n}$ can be approximated by a function similar to $\tilde{N}_i$ along the boundary, we replace (4.15) by

$$\tilde{f}_i = \sum_{j=1}^{4} \tilde{F}_{ij} \frac{\partial P(\mathbf{x}_j)}{\partial n} \qquad \text{where} \qquad \tilde{F}_{ij} = \int_{\tilde{\Gamma}} \rho^{-1} \tilde{N}_i \tilde{N}_j \, dl \,. \tag{4.16}$$

If the density ρ and the wave number k are treated as constants within each element, $\tilde{\mathbf{S}}$, $\tilde{\mathbf{M}}$ and $\tilde{\mathbf{F}}$ can be evaluated exactly. Once the contributions of the various elements are determined, the global system of equations is formed by mapping the local node numbers onto the global node numbers, giving rise to the global pressure vector $\mathbf{p}$, and combining all of the subsystems $\tilde{\mathbf{S}}$, $\tilde{\mathbf{M}}$ and $\tilde{\mathbf{f}}$ into their global counterparts $\mathbf{S}$, $\mathbf{M}$ and $\mathbf{f}$ (Schwarz, 1988). Both matrices $\mathbf{S}$ and $\mathbf{M}$ are sparse, banded and symmetric. Each row of the global matrix system can then be reduced to

$$\sum_{j=1}^{J} \left\{ (S_{ij} - M_{ij}) p_j - F_{ij} \frac{\partial P(\mathbf{x}_j)}{\partial n} \right\} = 0 \,, \tag{4.17}$$

where J is the total number of node variables or in the simpler matrix form

$$\mathbf{K} \cdot \mathbf{p} - \mathbf{f} = 0 \,, \tag{4.18}$$

where $\mathbf{K} = \mathbf{S} - \mathbf{M}$ and the vector $\mathbf{p}$ contains all the unknown, global nodal values p_j.

4.1.3 Coupling the Regions

By reordering equations and unknowns, the vector $\mathbf{p}$ obtained from the finite elements containing the node variables can be split into two subvectors $\mathbf{p}^I$ and $\mathbf{p}^B$. The node variables from inside the domain Ω^I are collected in the vector $\mathbf{p}^I$. The subvector $\mathbf{p}^B$ accommodates the node variables whose node points $\mathbf{x}_j$ lie on the boundary $\partial\Omega^B$. Since the boundary $\partial\Omega^B$ belongs to both domains, the scattered wavefield P^O expanded into (4.1), P^{inc}, and P^B have to match across the boundary. Hence, we replace the node variables p_j^B by

$$p_j^B = \sum_{k=1}^{J^O} p_k^O P_k(\mathbf{x}_j) + P^{inc}(\mathbf{x}_j)\,. \tag{4.19}$$

Furthermore, we can also find $\frac{\partial P(\mathbf{x}_j)}{\partial n}$ by evaluating

$$\frac{\partial P(\mathbf{x}_j)}{\partial n} = \sum_{k=1}^{J^O} p_k^O \hat{\mathbf{n}}_j \cdot \nabla P_k(\mathbf{x}_j) + \hat{\mathbf{n}}_j \cdot \nabla P^{inc}(\mathbf{x}_j)\,. \tag{4.20}$$

Combining (4.17), (4.19) and (4.20) yields the hybrid matrix system

$$\sum_{j=1}^{J^I}\Big\{K_{ij}p_j\Big\} + \sum_{j=J^I+1}^{J}\Big\{K_{ij}\sum_{k=1}^{J^O}p_k^O P_k(\mathbf{x}_j) - F_{ij}\sum_{k=1}^{J^O}p_k^O\hat{\mathbf{n}}_j\cdot\nabla P_k(\mathbf{x}_j)\Big\} = \sum_{j=J^I+1}^{J}\Big\{F_{ij}\hat{\mathbf{n}}_j\cdot\nabla P^{inc}(\mathbf{x}_j) - K_{ij}P^{inc}(\mathbf{x}_j)\Big\}, \tag{4.21}$$

where the node points $\mathbf{x}_j$ lie in the interior of the heterogeneous FE domain Ω^I for $1 \le j \le J^I$. The node points $\mathbf{x}_j$ are located on the boundary $\partial\Omega^B$ for $J^I + 1 \le j \le J$. As before, J is the total number of node points. Finally, J^O is the total number of functions used for the MMP expansion of the outside field. The complete hybrid system can be written in a

more compact form as

$$\begin{pmatrix} \mathbf{A}^{II} & \mathbf{A}^{IO} \\ \mathbf{A}^{OI} & \mathbf{A}^{OO} \end{pmatrix} \cdot \begin{pmatrix} \mathbf{p}^{I} \\ \mathbf{p}^{O} \end{pmatrix} = \begin{pmatrix} \mathbf{f}^{I} \\ \mathbf{f}^{O} \end{pmatrix}, \tag{4.22}$$

where the first term of (4.21) maps into $\mathbf{A}^{II}$ or $\mathbf{A}^{OI}$ depending on whether the node point of the corresponding test function N_i lies inside the heterogeneity ($\mathbf{A}^{II}$) or on the boundary ($\mathbf{A}^{OI}$). Similarly, the second term and the right hand side map into $\mathbf{A}^{IO}$ or $\mathbf{A}^{OO}$ and $\mathbf{f}^{I}$ or $\mathbf{f}^{O}$, respectively.

It is important to distinguish between the submatrices $\mathbf{A}^{II}, \ldots, \mathbf{A}^{OO}$ which have different physical interpretations, mathematical forms and numerical properties. The submatrix $\mathbf{A}^{II}$ is a sparse, diagonally dominant and symmetric matrix which stems from the heterogeneous region where wavefields are modelled by FE. Thus, the wavefields inside only approximate the wave equation (4.7). The residuals between the true wavefield and the approximate solution are going to be spread over all node variables $\mathbf{p}^{I}$.

Contrarily, the submatrix $\mathbf{A}^{OO}$ is dense and rectangular. Each column stems from a MMP expansion function while each row originates from the boundary conditions to be satisfied at a particular node point on the boundary. Since the MMP expansions are non orthogonal, the coefficients $\mathbf{p}^{O}$ have to be solved for in the least-squares sense.

The submatrices $\mathbf{A}^{IO}$ and $\mathbf{A}^{OI}$ are sparse and rectangular. These submatrices actually couple the wavefield (FE) inside the heterogeneity to the wavefield (MMP) in the homogeneous background.

Altogether, we end up with the rectangular system (4.22) where the upper half has completely different properties than the lower half. Therefore, we solve the system (4.22) in two steps: first, the interior node variables $\mathbf{p}^{I}$ are successively Gaussian eliminated (Schwarz, 1989) reducing the submatrix $\mathbf{A}^{II}$ to the triangular submatrix $\tilde{\mathbf{A}}^{II}$. This replaces the coupling matrix $\mathbf{A}^{OI}$ by a null matrix $\mathbf{0}$. Because $\mathbf{A}^{II}$ is diagonally dominant, the Gaussian elimination can be performed without additional pivoting. The elimination of the interior

node variables $\mathbf{p}^I$ respectively transforms $\mathbf{A}^{IO}$ and $\mathbf{A}^{OO}$ into $\tilde{\mathbf{A}}^{IO}$ and $\tilde{\mathbf{A}}^{OO}$. We obtain a new, transformed linear system:

$$\begin{pmatrix} \tilde{\mathbf{A}}^{II} & \tilde{\mathbf{A}}^{IO} \\ \mathbf{0} & \tilde{\mathbf{A}}^{OO} \end{pmatrix} \cdot \begin{pmatrix} \mathbf{p}^I \\ \mathbf{p}^O \end{pmatrix} = \begin{pmatrix} \tilde{\mathbf{f}}^I \\ \tilde{\mathbf{f}}^O \end{pmatrix} . \tag{4.23}$$

Actually, this step corresponds to a partial LU decomposition or similarly, to a static condensation (Schwarz, 1988) where the node variables p_j for $j \in \{1, J^I\}$ in the heterogeneous domain are successively eliminated. The complete heterogeneous domain collapses into one single 'super-element' coupling the nodal points on the boundary. This 'super-element' directly couples the incident field to the MMP expansion.

Second, the remaining system, $\tilde{\mathbf{A}}^{OO} \cdot \mathbf{p}^O = \tilde{\mathbf{f}}^O$, is solved in the least-squares sense using QR decomposition (Wilkinson, 1988). If desired, the values of the node variables $\mathbf{p}^I$ can later be found by back-substitution.

$$\tilde{\mathbf{A}}^{II} \cdot \mathbf{p}^I = \tilde{\mathbf{f}}^I - \tilde{\mathbf{A}}^{IO} \cdot \mathbf{p}^O . \tag{4.24}$$

In practice, the system (4.22) is solved by a combined, row-oriented LU-QR algorithm. The scheme is similar to traditional Givens updating (Schwarz, 1989). But for each new equation added to update the system, the first J^I Givens rotations are replaced by Gaussian eliminations instead. As a result, the first J^I equations are only LU composed and used to build the triangular submatrix $\tilde{\mathbf{A}}^{II}$ and the transformed $\tilde{\mathbf{A}}^{IO}$. For the remaining equations, the first J^I unknowns can be eliminated using $\tilde{\mathbf{A}}^{II}$ $\tilde{\mathbf{A}}^{IO}$. The rest are used for Givens updating which builds $\tilde{\mathbf{A}}^{OO}$ directly.

4.1.4 Remark: An Alternative Solver Scheme

Alternatively, the system (4.22) can be solved by the iterative scheme:

$$\mathbf{A}^{II} \cdot \mathbf{p}_n^I = \mathbf{f}^I - \mathbf{A}^{IO} \cdot \mathbf{p}_{n-1}^O , \tag{4.25a}$$

$$\mathbf{A}^{OO} \cdot \mathbf{p}_n^O = \mathbf{f}^O - \mathbf{A}^{OI} \cdot \mathbf{p}_{n-1}^I . \tag{4.25b}$$

Optimally, each of (4.25a) and (4.25b) is also solved by an iterative scheme such as the conjugate gradient method (Hestenes and Stiefel, 1952). The first part (4.25a) is square, symmetric and sparse. The second part (4.25b) is rectangular and dense, but relatively small compared to (4.25a). The iterative scheme (4.25) offers an alternative to LU-QR decomposition (4.23), but this has not yet been tried.

4.2 Elastic Theory

4.2.1 Homogeneous Regions: Multiple Multipole Expansions

In a homogeneous region Ω^O, expansions for the scattered displacement fields $\mathbf{w}^O(\mathbf{x}) = \big(u(\mathbf{x}), v(\mathbf{x})\big)$ are made with exact solutions to the homogeneous wave equation:

$$\mathbf{w}^O(\mathbf{x}) = \sum_{j=1}^{J^O} \Big\{ \phi_j \mathbf{w}_j^\Phi(\mathbf{x}) + \psi_j \mathbf{w}_j^\Psi(\mathbf{x}) \Big\} , \tag{4.26}$$

where

$$\mathbf{w}_j^\Phi(\mathbf{x}) = \nabla \Phi_j(\mathbf{x}) , \tag{4.27a}$$

$$\mathbf{w}_j^\Psi(\mathbf{x}) = \nabla \times \big[\hat{\mathbf{y}} \Psi_j(\mathbf{x}) \big] . \tag{4.27b}$$

Each expansion function Φ_j or Ψ_j satisfies a Helmholtz equation.

$$(\nabla^2 + k_O^2)\Phi_j = 0 \tag{4.28a}$$

$$(\nabla^2 + l_O^2)\Psi_j = 0 \tag{4.28b}$$

The constants k_O and l_O are respectively the wave numbers of the P- and the S-wave in the homogeneous region. The factors ϕ_j and ψ_j are complex valued weighting coefficients for the different expansion functions Φ_j and Ψ_j. Similar to the acoustic MMP expansions (4.3), the displacement field $\mathbf{w}^O(\mathbf{x})$ is expanded into multiple multipoles (Chapter 3)

$$\mathbf{w}^O(\mathbf{x}) = \sum_{m=1}^{M} \sum_{n=-N}^{N} \left\{ \phi_{mn} \nabla \Phi_{mn}(\mathbf{x}) + \psi_{mn} \nabla \times \left[\hat{\mathbf{y}} \Psi_{mn}(\mathbf{x}) \right] \right\} \tag{4.29}$$

$$= \sum_{m=1}^{M} \sum_{n=-N}^{N} \left\{ \phi_{mn} \nabla e^{in\theta} H_{|n|}^{(1)} \left(k_O \left| \mathbf{x} - \mathbf{x}_m \right| \right) + \psi_{mn} \nabla \times \left[\hat{\mathbf{y}} e^{in\theta} H_{|n|}^{(1)} \left(l_O \left| \mathbf{x} - \mathbf{x}_m \right| \right) \right] \right\}, \tag{4.30}$$

where $\mathbf{x}_m$ is the location or expansion center of the m^{th} multipole. Although we will not use other expansion functions than applied in (4.29) and (4.30), we prefer the notation (4.26) for its simplicity and generality. To go from (4.29) to (4.26), the double index mn is simply replaced by the single index j and vice versa. Thus, we will use (4.26) but mean (4.29). Equations for the weighting coefficients ϕ_j and ψ_j are obtained by enforcing boundary conditions along discrete matching points $\mathbf{m}_i$ on the boundaries between domains. The boundary conditions between two domains Ω^O and Ω^X are the continuity of displacement

and stresses in normal and tangential directions $\hat{\mathbf{n}}_i$ and $\hat{\mathbf{t}}_i$:

$$\sum_{j=1}^{J^O} \hat{\mathbf{n}}_i \cdot \left\{ \phi_j \mathbf{w}_j^{\Phi}(\mathbf{m}_i) + \psi_j \mathbf{w}_j^{\Psi}(\mathbf{m}_i) \right\} + \hat{\mathbf{n}}_i \cdot \mathbf{w}^{inc}(\mathbf{m}_i) = \hat{\mathbf{n}}_i \cdot \mathbf{w}^{X}(\mathbf{m}_i), \quad (4.31)$$

$$\sum_{j=1}^{J^O} \hat{\mathbf{t}}_i \cdot \left\{ \phi_j \mathbf{w}_j^{\Phi}(\mathbf{m}_i) + \psi_j \mathbf{w}_j^{\Psi}(\mathbf{m}_i) \right\} + \hat{\mathbf{t}}_i \cdot \mathbf{w}^{inc}(\mathbf{m}_i) = \hat{\mathbf{t}}_i \cdot \mathbf{w}^{X}(\mathbf{m}_i), \quad (4.32)$$

$$\sum_{j=1}^{J^O} \hat{\mathbf{n}}_i \cdot \left\{ \phi_j \boldsymbol{\sigma}_j^{\Phi}(\mathbf{m}_i) + \psi_j \boldsymbol{\sigma}_j^{\Psi}(\mathbf{m}_i) \right\} \cdot \hat{\mathbf{n}}_i + \hat{\mathbf{n}}_i \cdot \boldsymbol{\sigma}^{inc}(\mathbf{m}_i) \cdot \hat{\mathbf{n}}_i = \hat{\mathbf{n}}_i \cdot \boldsymbol{\sigma}^{X}(\mathbf{m}_i) \cdot \hat{\mathbf{n}}_i, \quad (4.33)$$

$$\sum_{j=1}^{J^O} \hat{\mathbf{t}}_i \cdot \left\{ \phi_j \boldsymbol{\sigma}_j^{\Phi}(\mathbf{m}_i) + \psi_j \boldsymbol{\sigma}_j^{\Psi}(\mathbf{m}_i) \right\} \cdot \hat{\mathbf{n}}_i + \hat{\mathbf{t}}_i \cdot \boldsymbol{\sigma}^{inc}(\mathbf{m}_i) \cdot \hat{\mathbf{n}}_i = \hat{\mathbf{t}}_i \cdot \boldsymbol{\sigma}^{X}(\mathbf{m}_i) \cdot \hat{\mathbf{n}}_i . \quad (4.34)$$

The quantities $\boldsymbol{\sigma}_j^{\Phi}(\mathbf{m}_i)$, $\boldsymbol{\sigma}_j^{\Psi}(\mathbf{m}_i)$, $\boldsymbol{\sigma}^{inc}(\mathbf{m}_i)$, and $\boldsymbol{\sigma}^{X}(\mathbf{m}_i)$ denote the stress tensors evaluated at $\mathbf{m}_i$ due to the respective displacements $\mathbf{w}_j^{\Phi}(\mathbf{m}_i)$, $\mathbf{w}_j^{\Psi}(\mathbf{m}_i)$, $\mathbf{w}_j^{inc}(\mathbf{m}_i)$, and $\mathbf{w}_j^{X}(\mathbf{m}_i)$. Accordingly, we build a linear equation system for the unknown coefficients ϕ_j and ψ_j,

$$\begin{pmatrix} \mathbf{U}^{\Phi} & \mathbf{U}^{\Psi} \\ \mathbf{V}^{\Phi} & \mathbf{V}^{\Psi} \\ \boldsymbol{\Sigma}_n^{\Phi} & \boldsymbol{\Sigma}_n^{\Psi} \\ \boldsymbol{\Sigma}_t^{\Phi} & \boldsymbol{\Sigma}_t^{\Psi} \end{pmatrix} \cdot \begin{pmatrix} \phi \\ \psi \end{pmatrix} = \begin{pmatrix} \mathbf{U}^{X} - \mathbf{U}^{inc} \\ \mathbf{V}^{X} - \mathbf{V}^{inc} \\ \boldsymbol{\Sigma}_n^{X} - \boldsymbol{\Sigma}_n^{inc} \\ \boldsymbol{\Sigma}_t^{X} - \boldsymbol{\Sigma}_t^{inc} \end{pmatrix}, \quad (4.35)$$

where the submatrices contain equations (4.31)-(4.34) evaluated at all matching points $\mathbf{m}_i$. In general, expansions of the form (4.26) are *not orthogonal.* Thus, more matching points than expansion functions are used and the resulting overdetermined linear system (4.35) is solved in the *least-squares sense* minimizing the overall error in the boundary conditions.

4.2.2 Heterogeneous Regions: Finite Elements

In a Cartesian coordinate frame (x, z) with unit vectors $\hat{\mathbf{x}}$ and $\hat{\mathbf{z}}$, the coupled equations of motion for the displacement $\mathbf{w}(\mathbf{x}) = \big(u(\mathbf{x}), v(\mathbf{x})\big)$ are

$$\omega^2 \rho u(\mathbf{x}) + \big\{c_{11} u(\mathbf{x})_{,x} + c_{12} v(\mathbf{x})_{,z}\big\}_{,x} + c_{33}\big\{u(\mathbf{x})_{,z} + v(\mathbf{x})_{,x}\big\}_{,z} = 0\,, \tag{4.36a}$$

$$\omega^2 \rho v(\mathbf{x}) + c_{33}\big\{u(\mathbf{x})_{,z} + v(\mathbf{x})_{,x}\big\}_{,x} + \big\{c_{12} u(\mathbf{x})_{,x} + c_{22} v(\mathbf{x})_{,z}\big\}_{,z} = 0\,; \tag{4.36b}$$

where we neglected eventual source terms. The density ρ and the elastic constants $c_{11} = c_{22} = \lambda + 2\mu$, $c_{12} = \lambda$ and $c_{33} = \mu$ are all spatially varying. The parameters λ and μ are the spatially varying Lamé constants. The subscripts $_{,x}$ and $_{,z}$ denote partial derivatives with respect to x or z.

Similar to the acoustic case (4.9), the heterogeneous region is partitioned into small elements $\tilde{\Omega}$. The components of the displacement inside the elements $\tilde{\Omega}$ are approximated by bilinear interpolation functions $\tilde{N}_j(\mathbf{x})$ (Zienkiewicz, 1977; Schwarz, 1988; Murphy and Chin-Bing, 1991):

$$\tilde{u}(\mathbf{x}) = \sum_{j=1}^{4} \tilde{u}_j \tilde{N}_j(\mathbf{x})\,, \tag{4.37a}$$

$$\tilde{v}(\mathbf{x}) = \sum_{j=1}^{4} \tilde{v}_j \tilde{N}_j(\mathbf{x})\,. \tag{4.37b}$$

The complex valued weighting coefficients $\tilde{u}_j$ and $\tilde{v}_j$ are the components of the displacements at the element's corners $\tilde{\mathbf{x}}_j$. The shape functions $\tilde{N}_j(\mathbf{x})$ are the same as in the acoustic case, e.g. $\tilde{N}_3(\mathbf{x}) = xz$ (Figure 4-2).

In the equations of motion (4.36), we replace the continuous displacements u and v by their interpolations (4.37). Applying Galerkin's method for each element $\tilde{\Omega}$, we multiply the resulting expression by the test function $\tilde{N}_i(\mathbf{x})$ and integrate over the element $\tilde{\Omega}$. Hence,

we obtain

$$\sum_{j=1}^{4}\left\{\iint_{\tilde{\Omega}}\left(c_{11}\tilde{N}_{i,x}\tilde{N}_{j,x}+c_{33}\tilde{N}_{i,z}\tilde{N}_{j,z}\right)\,dA-\iint_{\tilde{\Omega}}\rho\omega^2\,\tilde{N}_i\tilde{N}_j\,dA\right\}\tilde{u}_j\;+$$
$$\sum_{j=1}^{4}\left\{\iint_{\tilde{\Omega}}\left(c_{12}\tilde{N}_{i,x}\tilde{N}_{j,z}+c_{33}\tilde{N}_{i,z}\tilde{N}_{j,x}\right)\,dA\right\}\tilde{v}_j-$$
$$\int_{\tilde{\Gamma}}\tilde{N}_i\hat{\mathbf{x}}\cdot\boldsymbol{\sigma}\cdot\hat{\mathbf{n}}\,dl=0\,,\quad(4.38a)$$

$$\sum_{j=1}^{4}\left\{\iint_{\tilde{\Omega}}\left(c_{12}\tilde{N}_{i,z}\tilde{N}_{j,x}+c_{33}\tilde{N}_{i,x}\tilde{N}_{j,z}\right)\,dA\right\}\tilde{u}_j\;+$$
$$\sum_{j=1}^{4}\left\{\iint_{\tilde{\Omega}}\left(c_{33}\tilde{N}_{i,x}\tilde{N}_{j,x}+c_{22}\tilde{N}_{i,z}\tilde{N}_{j,z}\right)\,dA-\iint_{\tilde{\Omega}}\rho\omega^2\,\tilde{N}_i\tilde{N}_j\,dA\right\}\tilde{v}_j-$$
$$\int_{\tilde{\Gamma}}\tilde{N}_i\hat{\mathbf{z}}\cdot\boldsymbol{\sigma}\cdot\hat{\mathbf{n}}\,dl=0\,,\quad(4.38b)$$

where we used the divergence theorem to transform some of the volume integrals into line integrals. The quantity $\boldsymbol{\sigma}=\boldsymbol{\sigma}(\mathbf{x})$ denotes the stress tensor along the boundary. Evaluating (4.38) for all $\tilde{N}_i(\mathbf{x})$ yields a set of linear equations for the unknown node variables, $\tilde{u}_j$ and $\tilde{v}_j$. Again, equation (4.38) defines the stiffness matrices $\tilde{\mathbf{S}}^{rs}$, mass matrices $\tilde{\mathbf{M}}^{rs}$ and the force vectors $\tilde{\mathbf{f}}^{r}$ where the superscript $r\in\{1,2\}$ denotes whether the quantity is obtained from equation (4.38a) or (4.38b). The superscript $s\in\{1,2\}$ indicates whether the matrix

governs the respective coefficients $\tilde{u}_j$ or $\tilde{v}_j$:

$$\tilde{M}_{ij}^{11} = \tilde{M}_{ij}^{22} = \iint_{\tilde{\Omega}} \rho\omega^2 \, \tilde{N}_i \tilde{N}_j \, dA \,, \tag{4.39}$$

$$\tilde{M}_{ij}^{12} = \tilde{M}_{ij}^{21} = \mathbf{0} \tag{4.40}$$

$$\tilde{S}_{ij}^{11} = \iint_{\tilde{\Omega}} \left(c_{11} \tilde{N}_{i,x} \tilde{N}_{j,x} + c_{33} \tilde{N}_{i,z} \tilde{N}_{j,z} \right) \, dA \,, \tag{4.41}$$

$$\tilde{S}_{ij}^{22} = \iint_{\tilde{\Omega}} \left(c_{33} \tilde{N}_{i,x} \tilde{N}_{j,x} + c_{22} \tilde{N}_{i,z} \tilde{N}_{j,z} \right) \, dA \,, \tag{4.42}$$

$$\tilde{S}_{ij}^{12} = \tilde{S}_{ji}^{21} = \iint_{\tilde{\Omega}} \left(c_{12} \tilde{N}_{i,x} \tilde{N}_{j,z} + c_{33} \tilde{N}_{i,z} \tilde{N}_{j,x} \right) \, dA \,, \tag{4.43}$$

$$\tilde{f}_i^1 = \int_{\tilde{\Gamma}} \tilde{N}_i \hat{\mathbf{x}} \cdot \boldsymbol{\sigma} \cdot \hat{\mathbf{n}} \, dl \,, \tag{4.44}$$

$$\tilde{f}_i^2 = \int_{\tilde{\Gamma}} \tilde{N}_i \hat{\mathbf{z}} \cdot \boldsymbol{\sigma} \cdot \hat{\mathbf{n}} \, dl \,. \tag{4.45}$$

If the density ρ and the elastic constants c_{11}, c_{22}, c_{12}, and c_{33} are treated as constants within each element $\tilde{\Omega}$, all integrals (4.39)-(4.43) can be evaluated exactly. For elements which are in the interior, the boundary integrals (4.44) and (4.45) are not zero, but their contributions will exactly cancel with like terms coming from neighboring elements because displacements and stresses are continuous across elements. Therefore, the line integrals have to be taken into account only on the domain boundary. Assuming that $\hat{\mathbf{x}} \cdot \boldsymbol{\sigma} \cdot \hat{\mathbf{n}}$ and $\hat{\mathbf{z}} \cdot \boldsymbol{\sigma} \cdot \hat{\mathbf{n}}$ can be approximated by functions similar to $\tilde{N}_i$ along the boundary, we replace (4.44),(4.45) by

$$\tilde{f}_i^1 = \sum_{j=1}^{4} \tilde{F}_{ij} \hat{\mathbf{x}} \cdot \boldsymbol{\sigma}(\mathbf{x}_j) \cdot \hat{\mathbf{n}}_j \,, \tag{4.46}$$

$$\tilde{f}_i^2 = \sum_{j=1}^{4} \tilde{F}_{ij} \hat{\mathbf{z}} \cdot \boldsymbol{\sigma}(\mathbf{x}_j) \cdot \hat{\mathbf{n}}_j \,, \tag{4.47}$$

where

$$\tilde{F}_{ij} = \int_{\tilde{\Gamma}} \tilde{N}_i \tilde{N}_j \, dl \,, \tag{4.48}$$

which can also be evaluated analytically. Finally, mapping the local node numbers into global node numbers yields the global matrices $\mathbf{S}^{rs}$, $\mathbf{M}^{rs}$, $\mathbf{f}^r$ and the global nodal vectors $\mathbf{u}$

and $\mathbf{v}$. Writing $\mathbf{K}^{rs} = \mathbf{S}^{rs} - \mathbf{M}^{rs}$, the global matrix system reduces to the simpler system

$$\mathbf{K}^{11} \cdot \mathbf{u} + \mathbf{K}^{12} \cdot \mathbf{v} - \mathbf{f}^1 = 0\,, \tag{4.49a}$$

$$\mathbf{K}^{21} \cdot \mathbf{u} + \mathbf{K}^{22} \cdot \mathbf{v} - \mathbf{f}^2 = 0\,. \tag{4.49b}$$

4.2.3 Coupling the Regions

After reordering the equations and unknowns, the solution vectors $\mathbf{u}$ and $\mathbf{v}$ obtained from the finite elements can be split into two subvectors, $\mathbf{u}^I$, $\mathbf{u}^B$ and $\mathbf{v}^I$, $\mathbf{v}^B$. The node variables u_i and v_i from inside the domain Ω^I are collected in the respective subvectors $\mathbf{u}^I$ and $\mathbf{v}^I$. The subvectors $\mathbf{u}^B$ and $\mathbf{u}^B$ accommodate the node variables whose node points $\mathbf{x}_j$ lie on the boundary $\partial\Omega^B$. Since the boundary $\partial\Omega^B$ belongs to both domains, the wavefields $\mathbf{w}^O$ expanded into (4.26), the source field $\mathbf{w}^{inc}$, and $\mathbf{w}^B$ have to match along the boundary. Therefore, we replace the node variables u_j^B and v_j^B by

$$u_j^B = \sum_{k=1}^{J^O} \left\{ \phi_k \hat{\mathbf{x}} \cdot \mathbf{w}_k^{\Phi}(\mathbf{x}_j) + \psi_k \hat{\mathbf{x}} \cdot \mathbf{w}_k^{\Psi}(\mathbf{x}_j) \right\} + \hat{\mathbf{x}} \cdot \mathbf{w}^{inc}(\mathbf{x}_j)\,, \tag{4.50a}$$

$$v_j^B = \sum_{k=1}^{J^O} \left\{ \phi_k \hat{\mathbf{z}} \cdot \mathbf{w}_k^{\Phi}(\mathbf{x}_j) + \psi_k \hat{\mathbf{z}} \cdot \mathbf{w}_k^{\Psi}(\mathbf{x}_j) \right\} + \hat{\mathbf{z}} \cdot \mathbf{w}^{inc}(\mathbf{x}_j)\,, \tag{4.50b}$$

where we use the unit vectors $\hat{\mathbf{x}}$ and $\hat{\mathbf{z}}$ to extract the displacement components $u(\mathbf{x})$ and $v(\mathbf{x})$ in the x-, respectively the z-direction. Also, we find the stress tensor $\boldsymbol{\sigma}(\mathbf{x}_j)$ along the boundary by evaluating

$$\boldsymbol{\sigma}(\mathbf{x}_j) = \sum_{k=1}^{J^O} \left\{ \phi_k \boldsymbol{\sigma}_k^{\Phi}(\mathbf{x}_j) + \psi_k \boldsymbol{\sigma}_k^{\Psi}(\mathbf{x}_j) \right\} + \boldsymbol{\sigma}^{inc}(\mathbf{x}_j)\,. \tag{4.51}$$

Combining (4.49), (4.50) and (4.51) yields the coupled MMP-FEM system. For the sake of clarity, we will expand it explicitly:

$$\sum_{j=1}^{J^I}\left\{K_{ij}^{11}u_j\right\}+\sum_{j=1}^{J^I}\left\{K_{ij}^{12}v_j\right\}+$$
$$\sum_{k=1}^{J^O}\sum_{j=J^I+1}^{J}\left\{K_{ij}^{11}\hat{\mathbf{x}}\cdot\mathbf{w}_k^{\Phi}(\mathbf{x}_j)+K_{ij}^{12}\hat{\mathbf{z}}\cdot\mathbf{w}_k^{\Phi}(\mathbf{x}_j)-F_{ij}\hat{\mathbf{x}}\cdot\boldsymbol{\sigma}_k^{\Phi}(\mathbf{x}_j)\cdot\hat{\mathbf{n}}_j\right\}\phi_k+$$
$$\sum_{k=1}^{J^O}\sum_{j=J^I+1}^{J}\left\{K_{ij}^{11}\hat{\mathbf{x}}\cdot\mathbf{w}_k^{\Psi}(\mathbf{x}_j)+K_{ij}^{12}\hat{\mathbf{z}}\cdot\mathbf{w}_k^{\Psi}(\mathbf{x}_j)-F_{ij}\hat{\mathbf{x}}\cdot\boldsymbol{\sigma}_k^{\Psi}(\mathbf{x}_j)\cdot\hat{\mathbf{n}}_j\right\}\psi_k=$$
$$\sum_{j-J^I+1}^{J}\left\{F_{ij}\hat{\mathbf{x}}\cdot\boldsymbol{\sigma}^{inc}(\mathbf{x}_j)\cdot\hat{\mathbf{n}}_j-K_{ij}^{11}\hat{\mathbf{x}}\cdot\mathbf{w}^{inc}(\mathbf{x}_j)-K_{ij}^{12}\hat{\mathbf{z}}\cdot\mathbf{w}^{inc}(\mathbf{x}_j)\right\}, \quad (4.52a)$$

$$\sum_{j=1}^{J^I}\left\{K_{ij}^{21}u_j\right\}+\sum_{j=1}^{J^I}\left\{K_{ij}^{22}v_j\right\}+$$
$$\sum_{k=1}^{J^O}\sum_{j=J^I+1}^{J}\left\{K_{ij}^{21}\hat{\mathbf{x}}\cdot\mathbf{w}_k^{\Phi}(\mathbf{x}_j)+K_{ij}^{22}\hat{\mathbf{z}}\cdot\mathbf{w}_k^{\Phi}(\mathbf{x}_j)-F_{ij}\hat{\mathbf{z}}\cdot\boldsymbol{\sigma}_k^{\Phi}(\mathbf{x}_j)\cdot\hat{\mathbf{n}}_j\right\}\phi_k+$$
$$\sum_{k=1}^{J^O}\sum_{j=J^I+1}^{J}\left\{K_{ij}^{21}\hat{\mathbf{x}}\cdot\mathbf{w}_k^{\Psi}(\mathbf{x}_j)+K_{ij}^{22}\hat{\mathbf{z}}\cdot\mathbf{w}_k^{\Psi}(\mathbf{x}_j)-F_{ij}\hat{\mathbf{z}}\cdot\boldsymbol{\sigma}_k^{\Psi}(\mathbf{x}_j)\cdot\hat{\mathbf{n}}_j\right\}\psi_k=$$
$$\sum_{j=J^I+1}^{J}\left\{F_{ij}\hat{\mathbf{z}}\cdot\boldsymbol{\sigma}^{inc}(\mathbf{x}_j)\cdot\hat{\mathbf{n}}_j-K_{ij}^{21}\hat{\mathbf{x}}\cdot\mathbf{w}^{inc}(\mathbf{x}_j)-K_{ij}^{22}\hat{\mathbf{z}}\cdot\mathbf{w}^{inc}(\mathbf{x}_j)\right\}. \quad (4.52b)$$

Again, $1\leq j\leq J^I$ means that the node point $\mathbf{x}_j$ is in the interior Ω^I of the FE domain. Contrarily, for $J^I+1\leq j\leq J$ the node points $\mathbf{x}_j$ are located on the boundary $\partial\Omega^B$. As before, J is the total number of node points. Finally, J^O is the total number of functions used for the MMP expansion of the outside field. The resulting hybrid system of linear

equations can be written in a more compact form as

$$\begin{pmatrix} \mathbf{K}^{11,I} & \mathbf{K}^{12,I} & \mathbf{\Phi}^{1,I} & \mathbf{\Psi}^{1,I} \\ \mathbf{K}^{21,I} & \mathbf{K}^{22,I} & \mathbf{\Phi}^{2,I} & \mathbf{\Psi}^{2,I} \\ \mathbf{K}^{11,O} & \mathbf{K}^{12,O} & \mathbf{\Phi}^{1,O} & \mathbf{\Psi}^{1,O} \\ \mathbf{K}^{21,O} & \mathbf{K}^{22,O} & \mathbf{\Phi}^{2,O} & \mathbf{\Psi}^{2,O} \end{pmatrix} \cdot \begin{pmatrix} \mathbf{u}^I \\ \mathbf{v}^I \\ \phi \\ \psi \end{pmatrix} = \begin{pmatrix} \mathbf{f}^{1,I} \\ \mathbf{f}^{2,I} \\ \mathbf{f}^{1,O} \\ \mathbf{f}^{2,O} \end{pmatrix} . \tag{4.53}$$

Equation (4.52a) maps into the first or third row of (4.53) depending on whether the node point $(x)_i$ of the corresponding test function N_i lies inside the heterogeneity or on the boundary. Equation (4.52b) maps exactly the same way into the second or the fourth row of (4.53) depending on the location of the corresponding node point. Furthermore, the first term in both (4.52a) and (4.52b) maps into the first column of (4.53). The second terms map into the second column and so on for the other terms and the right hand side of (4.52).

The hybrid system (4.53) is very similar to the acoustic system (4.22). As in the acoustic case, the submatrices $\mathbf{K}^{rs,I}$, where $r, s \in \{1, 2\}$, result from the interior problem. They are sparse and square. All other submatrices are rectangular. Moreover, $\mathbf{\Phi}^{r,O}$ and $\mathbf{\Psi}^{r,O}$ are dense. By construction, $\mathbf{K}^{11,I}$ and $\mathbf{K}^{22,I}$ are diagonally dominant. Therefore, we can eliminate the node variables $\mathbf{u}^I$ and $\mathbf{v}^I$ by LU decomposition or Gaussian elimination without additional pivoting. We obtain a new linear system

$$\begin{pmatrix} \tilde{\mathbf{K}}^{11,I} & \tilde{\mathbf{K}}^{12,I} & \tilde{\mathbf{\Phi}}^{1,I} & \tilde{\mathbf{\Psi}}^{1,I} \\ \mathbf{0} & \tilde{\mathbf{K}}^{22,I} & \tilde{\mathbf{\Phi}}^{2,I} & \tilde{\mathbf{\Psi}}^{2,I} \\ \mathbf{0} & \mathbf{0} & \tilde{\mathbf{\Phi}}^{1,O} & \tilde{\mathbf{\Psi}}^{1,O} \\ \mathbf{0} & \mathbf{0} & \tilde{\mathbf{\Phi}}^{2,O} & \tilde{\mathbf{\Psi}}^{2,O} \end{pmatrix} \cdot \begin{pmatrix} \mathbf{u}^I \\ \mathbf{v}^I \\ \phi \\ \psi \end{pmatrix} = \begin{pmatrix} \tilde{\mathbf{f}}^{1,I} \\ \tilde{\mathbf{f}}^{2,I} \\ \tilde{\mathbf{f}}^{1,O} \\ \tilde{\mathbf{f}}^{2,O} \end{pmatrix} , \tag{4.54}$$

where $\tilde{\mathbf{K}}^{11,I}$ and $\tilde{\mathbf{K}}^{22,I}$ are now triangular matrices. The submatrices $\mathbf{K}^{rs,O}$ where $r, s \in \{1, 2\}$ vanish because we eliminated the node variables $\mathbf{u}^I$ and $\mathbf{v}^I$ from the lower half of the system. In fact, this step corresponds to static condensation of the inner node variables $\mathbf{u}^I$ and $\mathbf{v}^I$. The whole FE domain is collapsed into one 'super-element' coupling the node variables on the boundary. The 'super-element' couples the incident field directly to the MMP expansion. The lower half (4.55) of the transformed system (4.54) is now solved in

the least-squares sense by QR decomposition because $\tilde{\mathbf{\Phi}}^{r,O}$ and $\tilde{\mathbf{\Psi}}^{r,O}$ are still rectangular matrices.

$$\begin{pmatrix} \tilde{\mathbf{\Phi}}^{1,O} & \tilde{\mathbf{\Psi}}^{1,O} \\ \tilde{\mathbf{\Phi}}^{2,O} & \tilde{\mathbf{\Psi}}^{2,O} \end{pmatrix} \cdot \begin{pmatrix} \phi \\ \psi \end{pmatrix} = \begin{pmatrix} \tilde{\mathbf{f}}^{1,O} \\ \tilde{\mathbf{f}}^{2,O} \end{pmatrix} \tag{4.55}$$

If desired, the node variables in the heterogeneous, interior FE region Ω^I are easily recovered by back-substitution into the upper half of (4.54) which is already in triangular form.

$$\begin{pmatrix} \tilde{\mathbf{K}}^{11,I} & \tilde{\mathbf{K}}^{12,I} \\ \mathbf{0} & \tilde{\mathbf{K}}^{22,I} \end{pmatrix} \cdot \begin{pmatrix} \mathbf{u}^I \\ \mathbf{v}^I \end{pmatrix} = \begin{pmatrix} \tilde{\mathbf{f}}^{1,I} - \tilde{\mathbf{\Phi}}^{1,I} \cdot \phi - \tilde{\mathbf{\Psi}}^{1,I} \cdot \psi \\ \tilde{\mathbf{f}}^{2,I} - \tilde{\mathbf{\Phi}}^{2,I} \cdot \phi - \tilde{\mathbf{\Psi}}^{2,I} \cdot \psi \end{pmatrix} \tag{4.56}$$

4.3 Implementation

Because the technique is a mixture of MMP expansions and the FE method, the finite element method is merged into the prior MMP codes. Thus, the method is implemented on a nCUBE2 parallel computer using the programming language C++. The object oriented design has the advantage that the coupling as described in (4.21) and (4.52) is basically hidden in objects for node variables, finite elements and the expansion functions for the exterior. First, the objects for the finite elements calculate the local $\tilde{\mathbf{M}}$, $\tilde{\mathbf{S}}$ and $\tilde{\mathbf{F}}$ matrices. Then, the resulting coefficients are mapped into the global equation system. Objects for internal node variables simply map the coefficients $\tilde{K}_{ij}^{(rs)}$ for the p_j^I into the global system of equations. In contrast, objects for node variables on the boundary automatically evaluate the MMP expansion at the node point as described in equations (4.19), (4.20) or (4.50), (4.51), weight the expansion with the appropriate $\tilde{K}_{ij}^{(rs)}$ or $\tilde{F}_{ij}^{(rs)}$ coefficient and map the resulting coefficients for p_j^O, or ϕ_j and ψ_j into the global system.

To reduce numerical noise, the materials are made slightly lossy by adding a small imaginary component ω_I to the angular frequency. If seismograms are calculated by Fourier synthesis, the true amplitude is later recovered by a multiplication with $e^{\omega_I t}$.

4.4 Numerical Results: Acoustics

As a first test, we simply embed a homogeneous region in a homogeneous fullspace and illuminate it by an incident plane wave. The wavefield in the embedded region is modelled by FE. The scattered wavefields in the fullspace are expanded into a MMP series. The material parameters in both regions are the same. Namely, the velocity α is 2000 m/s and the density ρ is 2000 kg/m^3. Hence, all coefficients of the MMP expansion should be zero, while the FE solution should simply interpolate the incoming field. Clearly, due to the discretization of the field in the interior, the solution in the interior will deviate from the incident field and thus, an additional scattered field will be induced. The strength of this induced field is both a function of the number of elements per wavelength (EPW) and the angle of incidence of the source field with respect to the FE region. The embedded region consists of $18 * 18$ elements, each $4\,\mathrm{m} * 4\,\mathrm{m}$ in size. The MMP expansion used is (4.3) with $M = 4$ and $N = 4$. Altogether, 36 expansion functions are used. Figure 4-3 shows the exact position of node points and expansion centers. The FE region is illuminated by incident plane waves with four frequencies corresponding to 100, 25, 10 and 5 EPW. The resulting relative errors $\langle |P - P^{inc}|/|P^{inc}| \rangle$ along the boundary of the inclusion are shown in Figure 4-4 as a function of angle of incidence and EPW. Clearly, the errors increase with decreasing EPW until the spurious fields are of similar order of magnitude as the source field. Also visible is the apparent anisotropy due to the finite elements. Compared to normal incidence, the relative error for plane waves incident in the diagonal direction is slightly reduced. For 10 EPW, we obtain a maximal relative error of about 5%.

To test the accuracy of the MMP-FE technique, we compare the scattering from an acoustic cylinder with the well-known analytical series solution (Pao and Mow, 1973). The velocity inside the cylinder is 3000 m/s; the velocity outside the cylinder is 2000 m/s. In both regions, the density is kept constant at 2000 kg/m^3. The radius a of the cylinder is 44 m. To simplify the generation of the FE mesh, a square region larger than the actual cylinder is discretized by 24 elements in either direction. Due to the symmetry of the problem, only one multipole (4.3) is used, where $M = 1$ and $N = 20$. It is located at the origin.

The geometry is shown in Figure 4-5. The size of the elements is 4 m. The experiment is performed for two different incident wavelengths. First, the wavelength is 100 m and the corresponding $ka = 2.5$. Second, the wavelength is 25 m and $ka = 10$. Magnitude and phase are presented in Figure 4-6. For the longer wavelength $ka = 2.5$, the analytical and the hybrid solution agree very well. For the shorter wavelength where $ka = 10$, the deviations of the FE-MMP solution from the analytical one are due to the size of the finite elements. Reducing the element size would reduce the deviations. Furthermore, the largest deviations correlate with the smallest magnitudes as can be observed in Figure 4-6. This is an effect of the least-squares solving procedure. The solver uniformly minimizes the misfit at each boundary point. Thus, if the average misfit is ϵ, any true field value smaller than ϵ is lost in the misfit. If better (relative) accuracy is desired, the solution should be calculated again with the equations scaled by the reciprocal of the previously obtained field. Basically, each row of $\mathbf{A}^{OI}$ and $\mathbf{A}^{OO}$ should be scaled by $\frac{1}{p_i}$. Further details on scaling can be found in a prior paper (Imhof, 1995).

Last, we calculate the seismogram for a complex geometry depicted in Figure 4-7. The scatterers are roughly 180 m long and 35 m thick. The velocity and density in the background are respectively 2000 m/s and 2000 kg/m^3. The velocity and the density in the two scatterers are 3000 m/s and 2000 kg/m^3. Each finite element is 3 m by 3 m in size. For each scatterer, five centers of expansion are used. At each center $\mathbf{x}_m$, an expansion of the form

$$\sum_{n=-8}^{8} p_{mn}^{O} e^{in\theta} H_{|n|}^{(1)} \left(k_O \left|\mathbf{x} - \mathbf{x}_m\right|\right)$$

is set up. The incident field P^{inc} is an explosive line source modulated by a Ricker pulse (Ricker, 1977) of 50 Hz center frequency. Altogether, 64 receivers will measure the pressure of the scattered field. The resulting seismogram is shown in Figure 4-9a.

To demonstrate the effect of heterogeneous scatterers, we replace the constant velocities in the scatterers by random velocities described by their mean velocity (3000 m/s), the standard deviation (500 m/s) and the spatial autocorrelation $\mathrm{R}(\Delta_x, \Delta_z)$ (Frankel and Clayton, 1986). For simplicity, we choose a Gaussian autocorrelation function depending on two

perpendicular correlation lengths a_1, a_2 and the angle ζ between a_1 and the horizontal direction $\hat{\mathbf{x}}$.

$$\mathrm{R}(\Delta_x, \Delta_z) = \exp\left(-\left\{\frac{\Delta_x \cos\zeta + \Delta_z \sin\zeta}{a_1}\right\}^2 - \left\{\frac{\Delta_z \cos\zeta - \Delta_x \sin\zeta}{a_2}\right\}^2\right) \tag{4.57}$$

For the present example, we choose $a_1 = 18\,\mathrm{m}$, $a_2 = 6\,\mathrm{m}$ and $\zeta = -10°$. The geometry is depicted in Figure 4-8. The density as well as the geometry and locations of the scatterers, source and receivers are the same as in the prior experiment. The resulting seismogram is shown in Figure 4-9b. The difference to the seismogram for the homogeneous scatterers (Figures 4-9a) is prominent. The comparison clearly shows the need for numerical modelling techniques which can incorporate small scale variations into the models.

4.5 Numerical Results: Elastics

As in the acoustic case, the first test is to embed a homogeneous region in a homogeneous fullspace and illuminate it with an incident plane wave. The wavefields in the embedded region are modelled by FE, while the scattered wavefields in the fullspace are expanded into a MMP series. Because the material parameters in both regions are the same, all coefficients of the MMP expansion should be zero and the FE solution should perfectly interpolate the incoming field. The P-wave velocity is $2000\,\mathrm{m/s}$, the S-wave velocity $1300\,\mathrm{m/s}$ and the density $2000\,\mathrm{kg/m^3}$. Clearly, due to the discretization of the fields in the interior, the solution will deviate from the incident field and thus, additional scattered fields will be induced. The strength of these induced fields is both a function of the number of elements per wavelength and the angle of incidence of the source field. The embedded region consists of $18 * 18$ square elements, each $4\,\mathrm{m} * 4\,\mathrm{m}$ in size. The MMP expansion is the same as (4.30) with $M = 4$ and $N = 4$. Altogether, $2 * 36$ expansion functions are used. Figure 4-3 shows the exact position of node points and expansion centers. As source fields, we use plane waves of purely P or S polarization. Both experiments are performed at four different frequencies corresponding to 100, 25, 10 and 5 elements per P-wavelength (EPW). Figure 4-10 shows the resulting relative boundary errors $\langle |\mathbf{w} - \mathbf{w}^{inc}|/|\mathbf{w}^{inc}| \rangle$ along the inclusion as a function

of the angle of incidence. As expected, the errors increase with increasing frequency or accordingly with decreasing EPW. Not surprisingly, the errors for incident S-waves are in general larger than for incident P-waves of the same frequency. This observation is readily explained by the shorter wavelengths of the S-phases. As in the acoustic case, less spurious fields are induced for incident P- or S-waves propagating in diagonal direction. For 25 EPW, we obtain a maximal relative error of about 5% for normal incidence.

To test the accuracy of the MMP-FE technique in the elastic case, we compare the scattering from a cylinder with the analytical series solution (Pao and Mow, 1973). Inside the cylinder, the P-velocity is 3000 m/s, the S-velocity is 1700 m/s, and Poisson's ratio 0.26. Outside the cylinder, the P-velocity is 2000 m/s, the S-velocity is 1300 m/s, and Poisson's ratio 0.13. In both regions, the density is 2000 kg/m^3. The radius a of the cylinder is 12 m. To simplify the generation of the FE mesh, a square region larger than the actual cylinder is discretized by 24 elements in either direction. Due to the symmetry of the problem, we use only one multipole (4.30) located at the origin, where $M = 1$ and $N = 20$. The geometry is similar to the one shown in Figure 4-5. The size of the elements is 1 m. The wavelength of the incident P-wave is 50 m ($ka = 1.5$) and the wavelength of the incident S-wave is 32 m ($la = 2.3$). The magnitude and phase of the u and the v components are shown in Figure 4-11. For all incident phases, the match between the analytical solution and the results obtained from the MMP-FE method is excellent.

Last, we calculate the seismogram for a complex geometry depicted in Figure 4-12. A scatterer is illuminated by a line source. The scatterer is roughly 180 m long and 35 m thick. The P- and S-velocities and density in the scatterer are 3000 m/s, 1730 m/s and 2000 kg/m^3, respectively. Poisson's ratio is $\sigma = 0.26$. In the background, the P- and S-velocities and density are 2000 m/s, 1300 m/s and 2000 kg/m^3, respectively. Poisson's ratio is $\sigma = 0.13$. Each finite element is 2 m by 2 m in size. In the scatterer, five expansions of the form (4.30) with $M = 5$ and $N = 7$ are used. Two different incident fields are chosen: a compressional and a rotational line source. Each source is modulated with a Ricker pulse (Ricker, 1977) of 50 Hz center frequency. Altogether, 64 receivers measure the vertical displacement component of the scattered field. The resulting seismograms are

shown in Figures 4-14a to 4-19a. While Figure 4-14a shows the scattered field due to the compressional line source, the seismogram in Figure 4-16a contains only the mode converted S-waves. Similarly for the rotational line source. While Figure 4-17a shows the complete scattered wavefield, the seismogram in Figure 4-18a contains only the mode converted P-waves. For both source fields, energy is mode converted by the scatterer.

To show the effect of a heterogeneous scatterer, we replace the constant velocities in the scatterer by random fields described by the mean velocities, the standard deviations and the spatial autocorrelations $R(\Delta_x, \Delta_z)$. We choose a Gaussian autocorrelation function (4.57) with two perpendicular correlation lengths $a_1 = 18\,\mathrm{m}$, $a_2 = 6\,\mathrm{m}$ and an angle $\zeta = -10°$. The mean P-velocity is 3000 m/s, the mean S-velocity 1730 m/s, and the standard deviation of the P-velocity 500 m/s. Everywhere within the scatterer, the S-velocity is chosen to preserve a Poisson's ratio of 0.26. The density as well as the geometry and locations of the scatterer, source and receivers are the same as in the prior experiment. The heterogeneous scatterer is shown in Figure 4-13. For both a compressional and a rotational source, the respective seismograms are shown in Figures 4-14b to 4-19b. Comparing the seismogram due to the homogeneous scatterers (Figures 4-14a to 4-19a) with the ones for the heterogeneous scatterer (Figures 4-14b to 4-19b) clearly shows the importance of allowing small scale variations in the material properties and thus the need for hybrid techniques.

4.6 Summary

The MMP code has been successfully coupled with the FE method in both acoustic and elastic media. The coupling of the two methods enhances their usefulness for a range of problems. The FE technique allows the simulation of wave propagation in heterogeneous materials. The MMP expansions allow to calculate propagating waves in homogeneous (unbounded) regions in an efficient manner because they commonly need fewer unknowns to be evaluated and solved for than comparable methods.

Steady-state solutions, as well as seismograms obtained by Fourier synthesis, were calcu-

lated for a range of different problems for both acoustic and elastic media. Where available, the solutions obtained by the combined MMP-FEM scheme compared favorably with the analytical solutions. Comparisons between homogeneous and heterogeneous scatterers expose major differences for the resulting wavefields which show the need for hybrid schemes allowing for variations in the material parameters. For the elastic case, we automatically obtain the scattered wavefields decomposed into P- and S-modes. This feature allows us to study the conversion of modes from $P \rightarrow S$ or vice versa due to the heterogeneous scattering region.

The combined scheme compensates the individual weaknesses of MMP and FEM and takes advantage of both their strengths. Thus, the method is well-suited to solve two-dimensional scattering problems for a range of problems which neither method could handle alone.

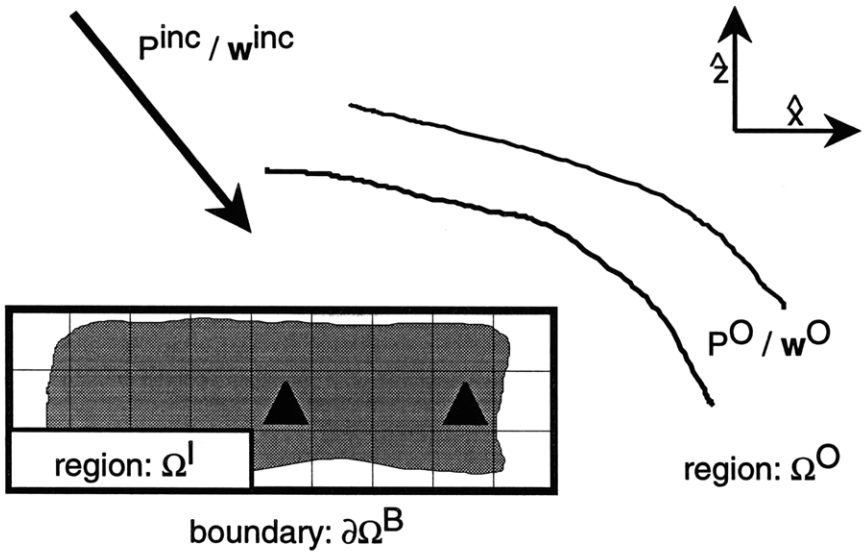

Figure 4-1: The generic scattering problem to be solved by the hybrid MMP-FEM technique. A heterogeneous scatterer Ω^I is embedded in a homogeneous background Ω^O. In the acoustic case, the incident field is P^{inc} and the scattered field is P^O. In the elastic case, the incident field is $\mathbf{w}^{inc}$ and the scattered field $\mathbf{w}^O$. The triangles symbolize expansion centers for the MMP.

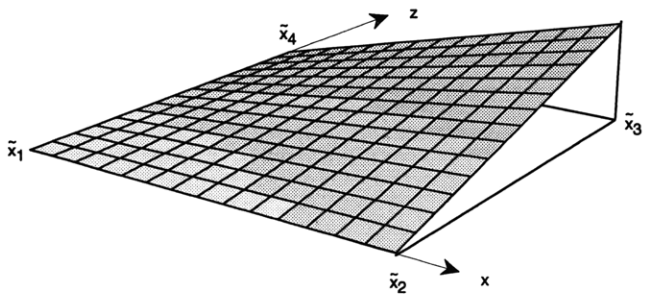

Figure 4-2: The shape function $\tilde{N}_3(\mathbf{x}) = xz$ for a square unit element $\tilde{\Omega}$ and bilinear interpolation. The other shape functions $\tilde{N}_1(\mathbf{x})$, $\tilde{N}_2(\mathbf{x})$, and $\tilde{N}_4(\mathbf{x})$ are obtained by rotations of $-180°$, $-90°$, and $90°$.

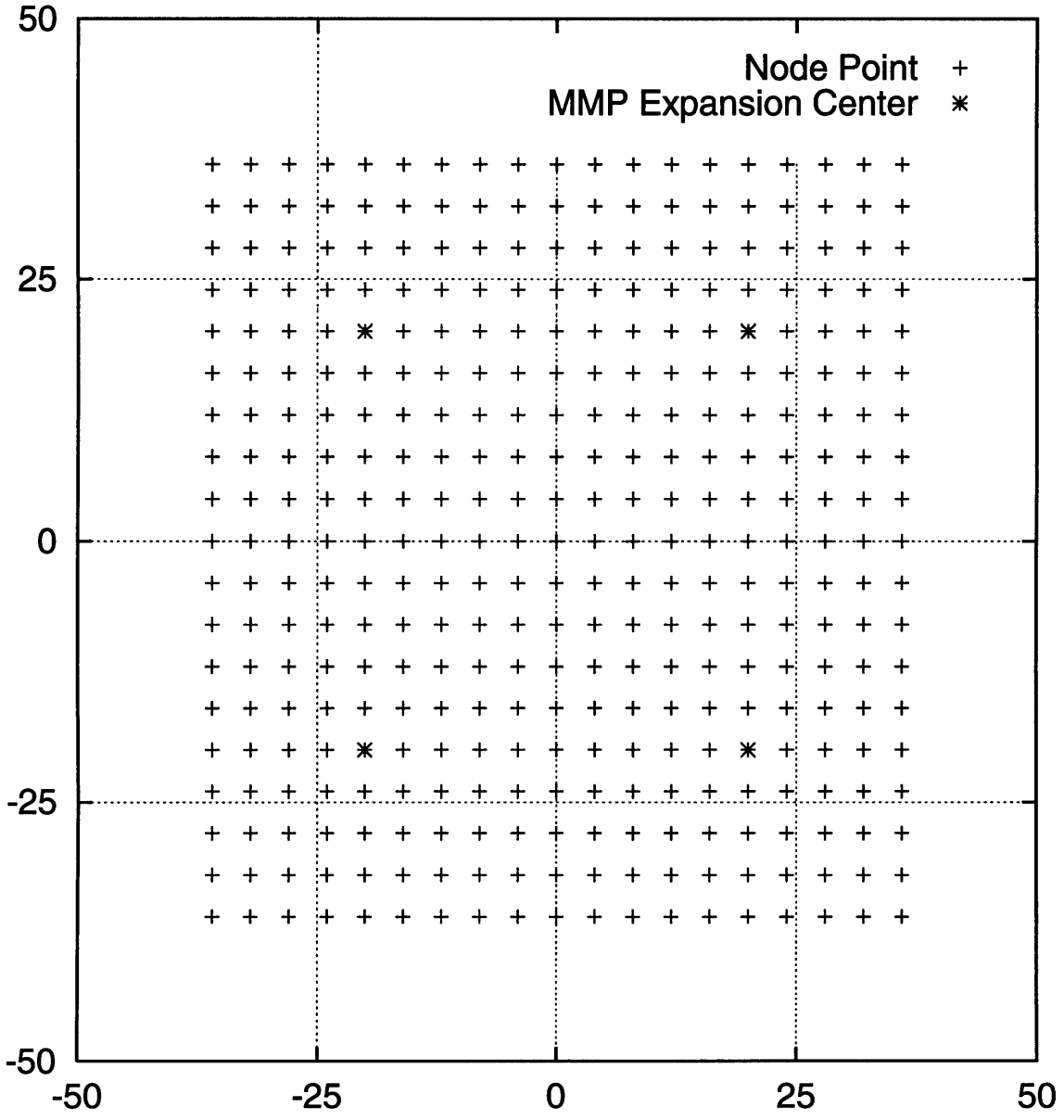

Figure 4-3: An embedded homogeneous region. Each cross represents a node point $\mathbf{x}_i$ and each star a MMP expansion center $\mathbf{x}_m$. From each expansion center, we set up an expansion $\sum_{n=-4}^{4} p_{mn}^{O} e^{in\theta} H_{|n|}^{(1)}(k_O |\mathbf{x} - \mathbf{x}_m|)$.

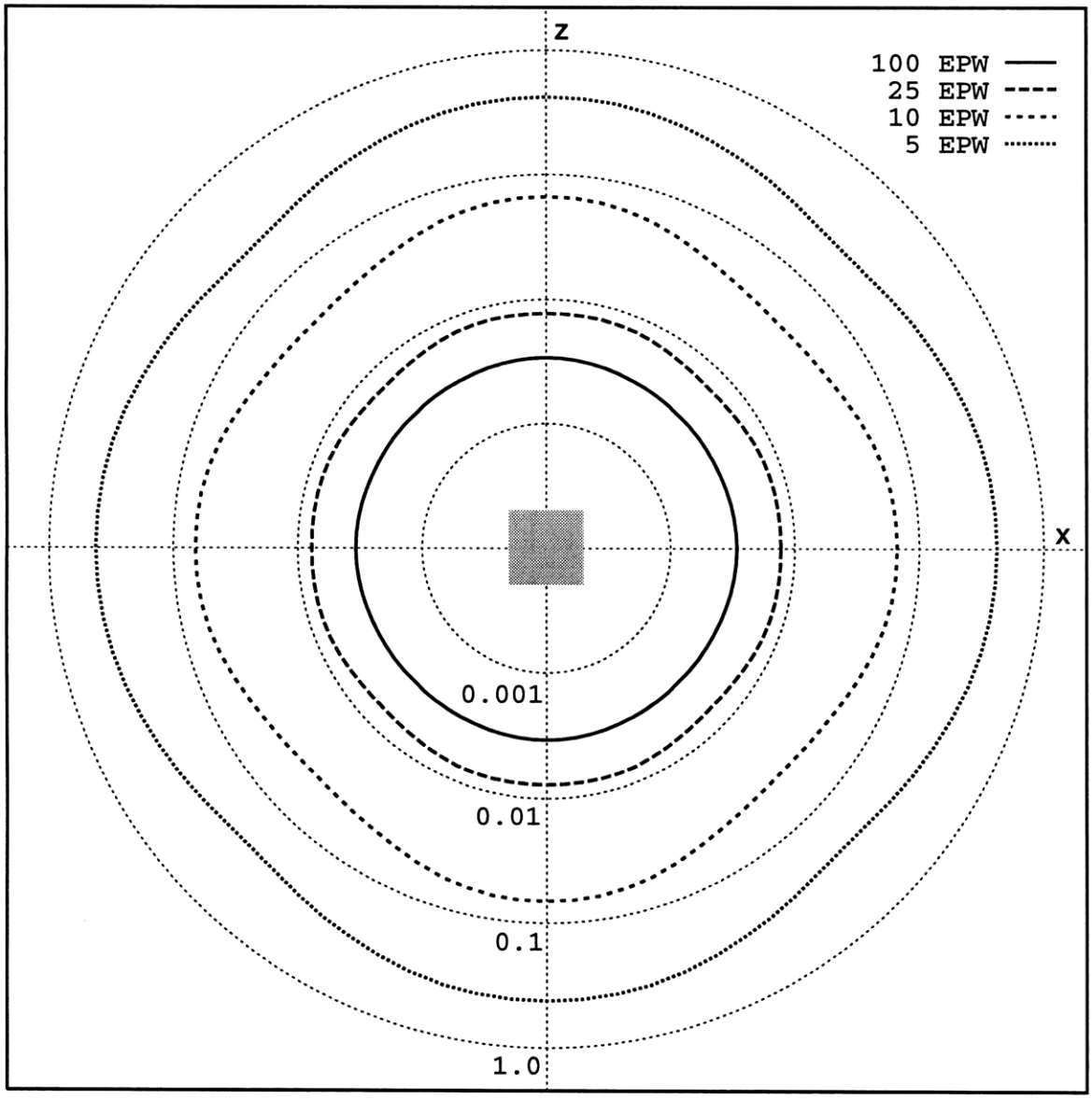

Figure 4-4: Acoustics: relative boundary error $\langle |P - P^{inc}|/P^{inc}| \rangle$ as a function of continuous angle of incidence of a planar sourcefield with respect to the finite elements for different numbers of elements per wavelength (EPW). 10 EPW yield an error of about 5%. The grid anisotropy is clearly visible for small wavelengths or correspondingly small EPWs.

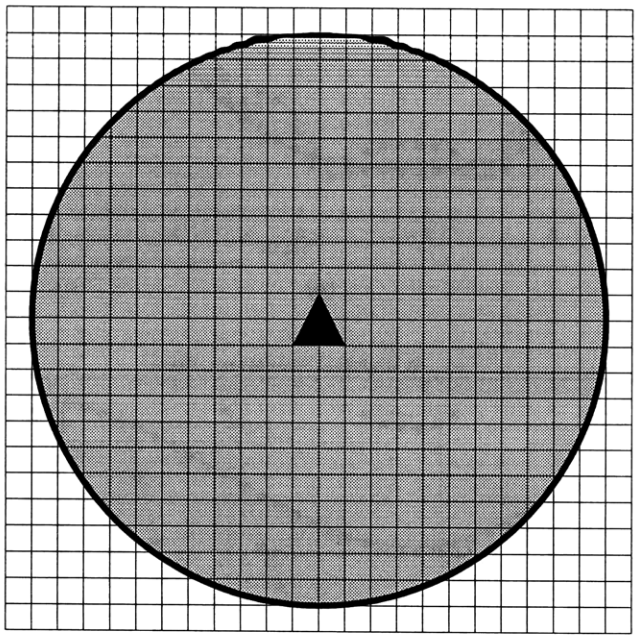

Figure 4-5: A cylindrical scatterer is illuminated by a plane wave. Outside, the velocity is 2000 m/s; inside, the velocity is 3000 m/s. The grid represents the finite elements used. The grid spacing is 4 m and the radius of the cylinder is 44 m. The triangle denotes the expansion center for the multipole.

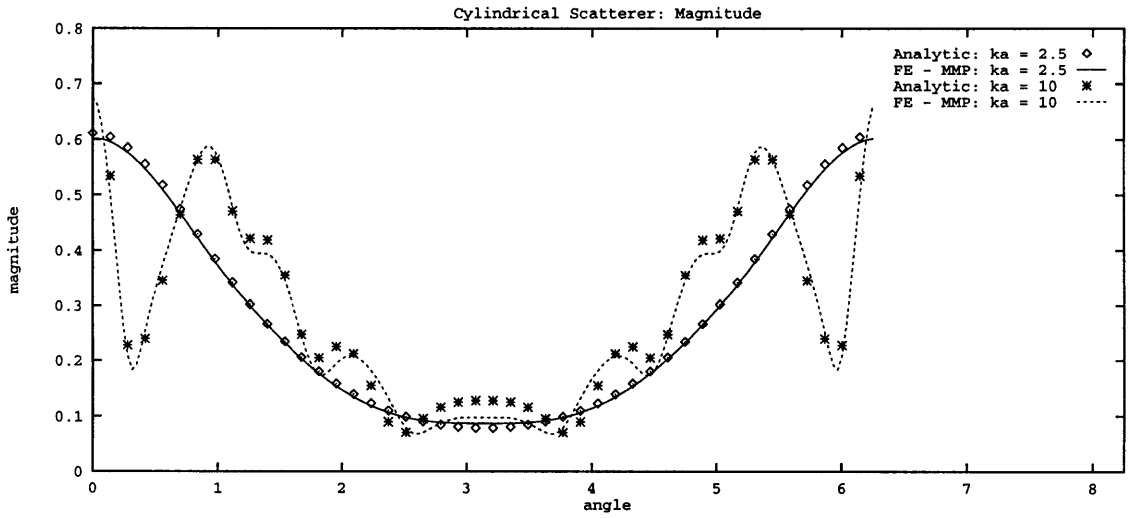

(a)

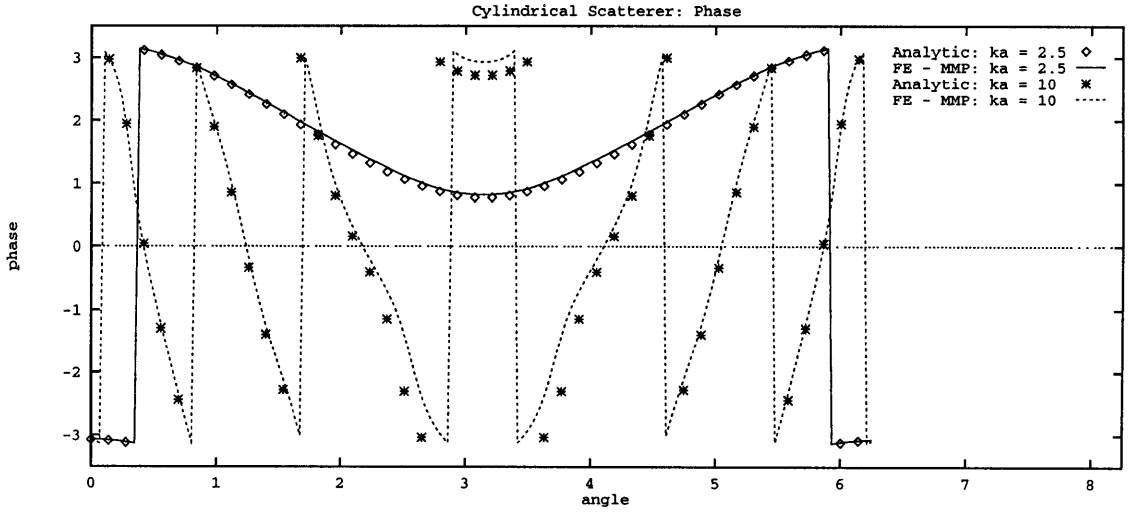

(b)

Figure 4-6: Acoustics: a cylindrical scatterer is illuminated by a plane wave propagating in the positive, horizontal direction. (a) The magnitude $|P|$ for $ka = 2.5$ and $ka = 10$ shown as a function of angle where a is the radius of the cylinder and k the wave number. (b) The phase $\arg(P)$ for $ka = 2.5$ and $ka = 10$ as a function of angle.

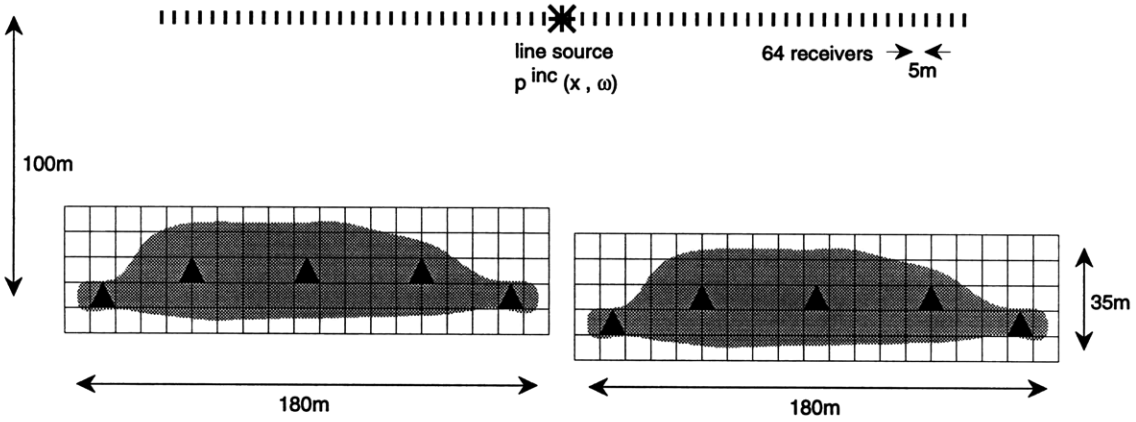

Figure 4-7: Acoustics: generic scatterers used to calculate acoustic seismograms. Two scatterers are embedded in a homogeneous background with a velocity of 2000 m/s and a density of 2000 kg/m^3. The scatterers are homogeneous with a velocity of 3000 m/s and a density of 2000 kg/m^3. The triangles show the location of the centers for the MMP expansion. Also indicated are the regions with the finite element grids.

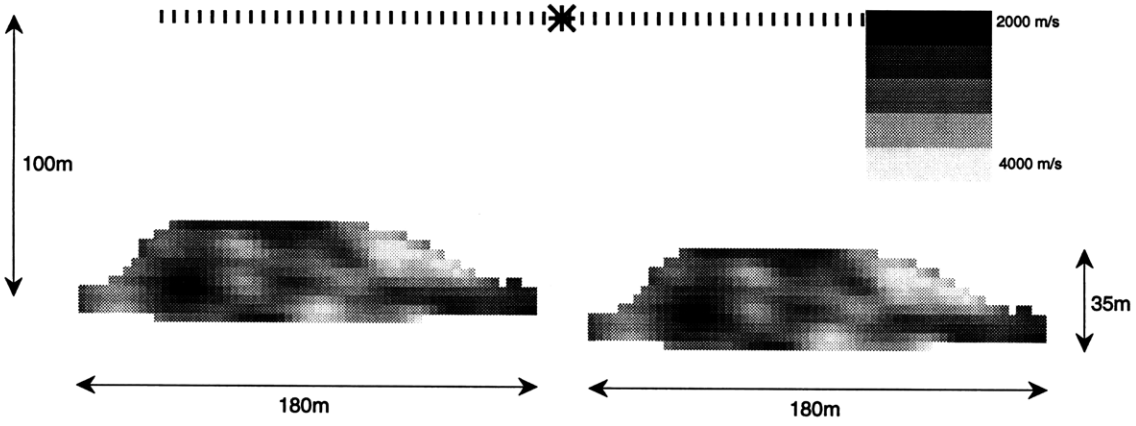

Figure 4-8: Acoustics: two heterogeneous scatterers are embedded in a homogeneous background with a velocity of 2000 m/s and a density of 2000 kg/m^3. The scatterers have a mean velocity of 3000 m/s with 500 m/s standard deviation and a Gaussian spatial autocorrelation with correlation lengths of $a_1 = 18$ m, $a_2 = 6$ m and a tilt of $-10°$.

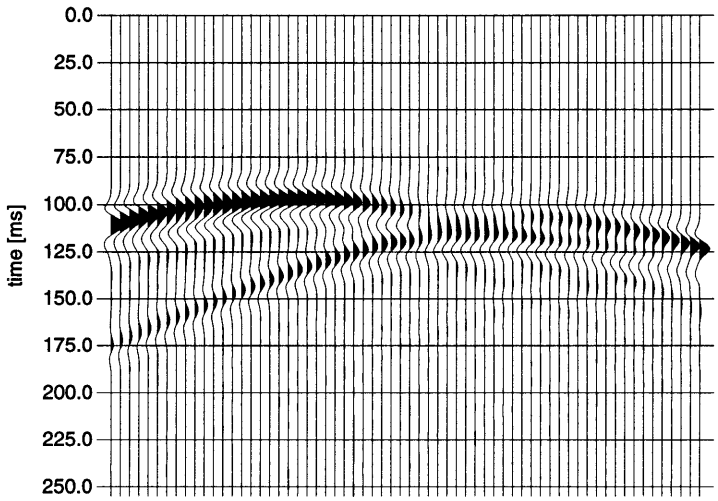

(a)

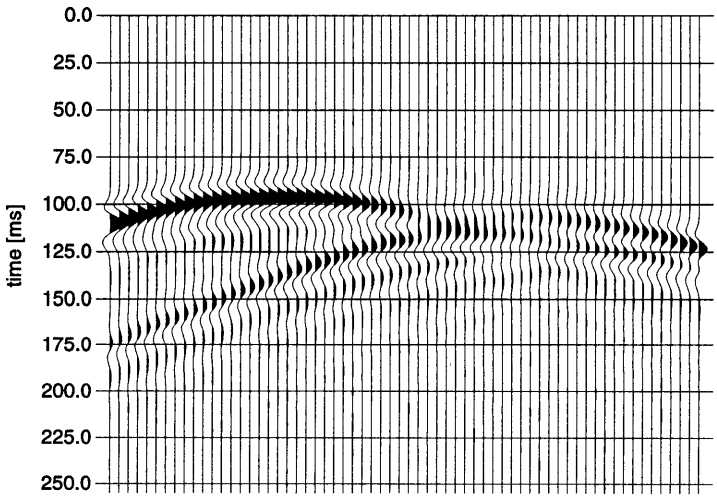

(b)

Figure 4-9: Acoustics: the resulting seismograms for the two acoustic scatterers. In (a), the scatterers are homogeneous as depicted in Figure 4-7, while in (b) the scatterers are heterogeneous (Figure 4-8). The incident field is suppressed.

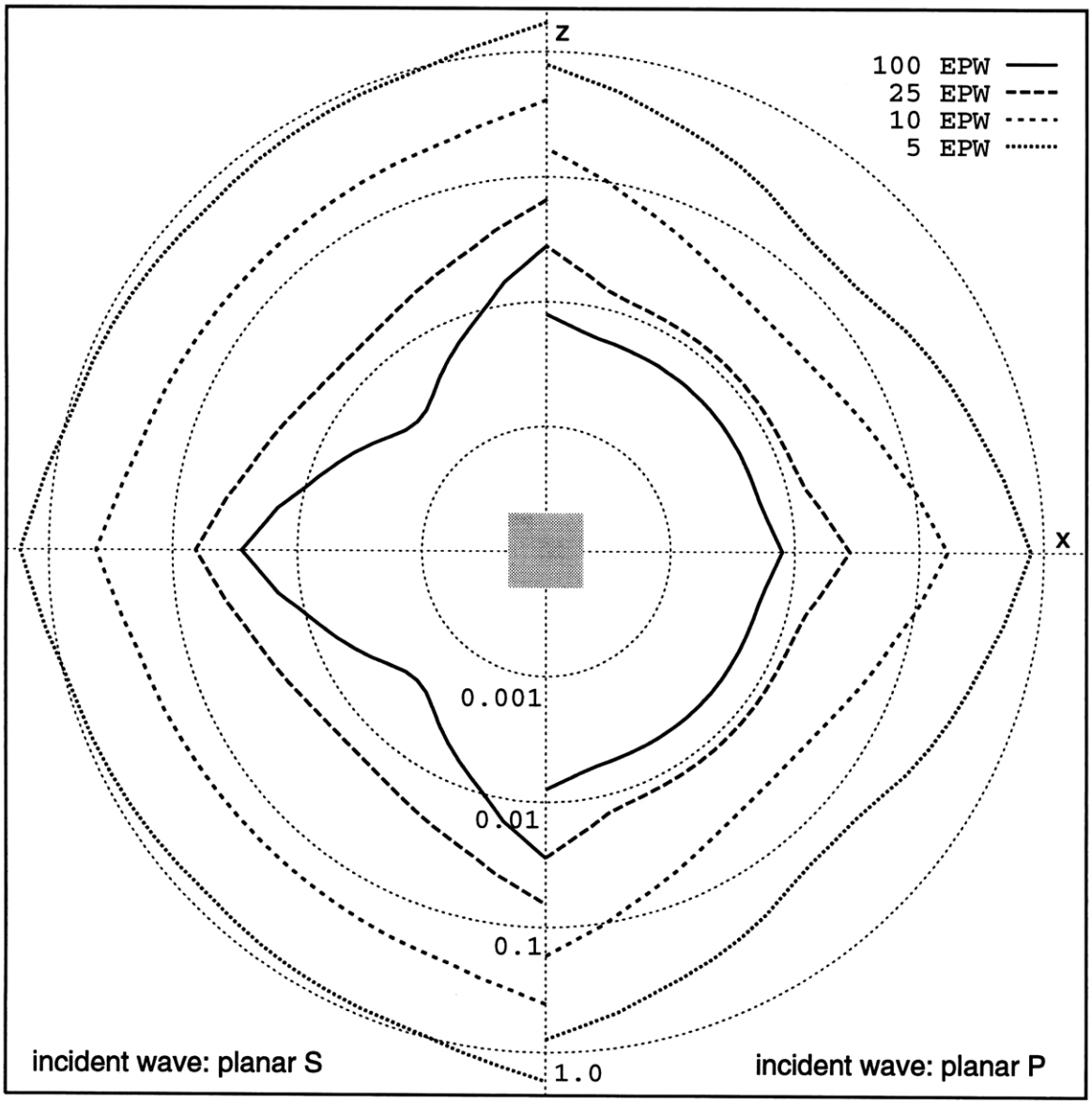

Figure 4-10: Elastics: relative boundary error $\langle |\mathbf{w} - \mathbf{w}^{inc}|/|\mathbf{w}^{inc}| \rangle$ as a function of the continuous angle of incidence of the source field with respect to the finite elements for a series of number of elements per P-wavelength (EPW). On the left-hand-side, the incident field is a planar S-wave. On the right-hand-side, the incident field is a planar P-wave. An incident S-wave is more affected by the EPW because its wavelength is only about half as long as the corresponding P-wave's. 25 EPW yield a maximal relative error of 5% for the incident S-wave.

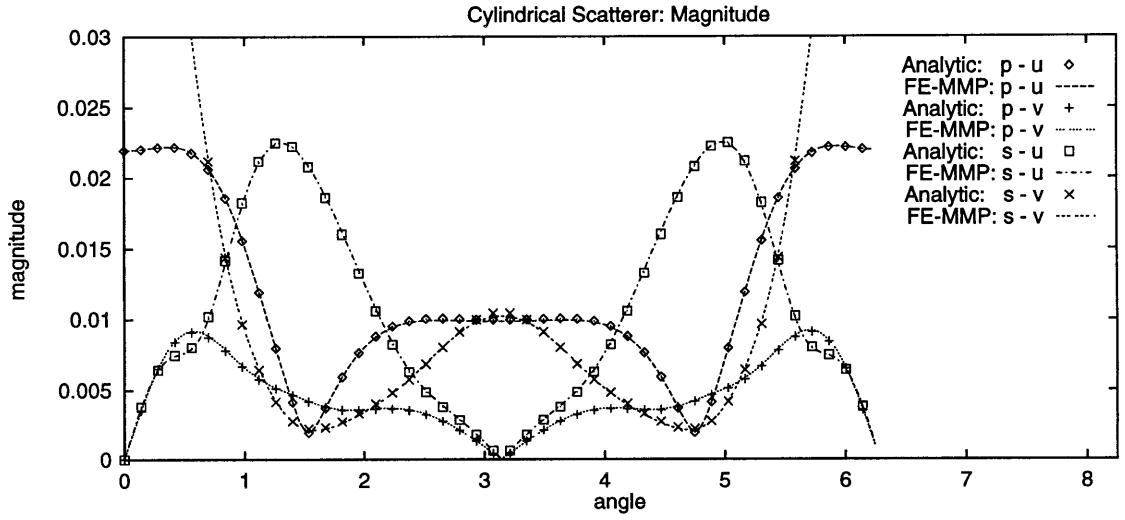

(a)

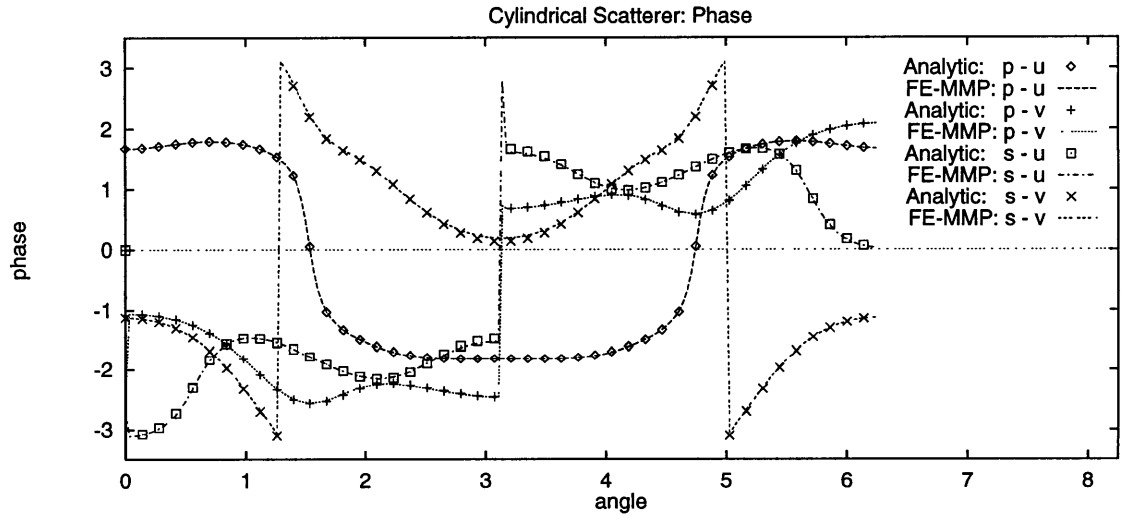

(b)

Figure 4-11: Elastics: a cylindrical scatterer is illuminated by a plane wave propagating in the positive, horizontal direction. Both P and S modes are used as incident fields. (a) The magnitudes $|u|$ and $|v|$ for $ka = 1.5$ and $la = 2.3$ shown as a function of angle where a is the radius of the cylinder, k is the P wave number and l is the S wave number. (b) The phases $\arg(u)$ and $\arg(v)$ for $ka = 1.5$ and $la = 2.3$ as a function of angle.

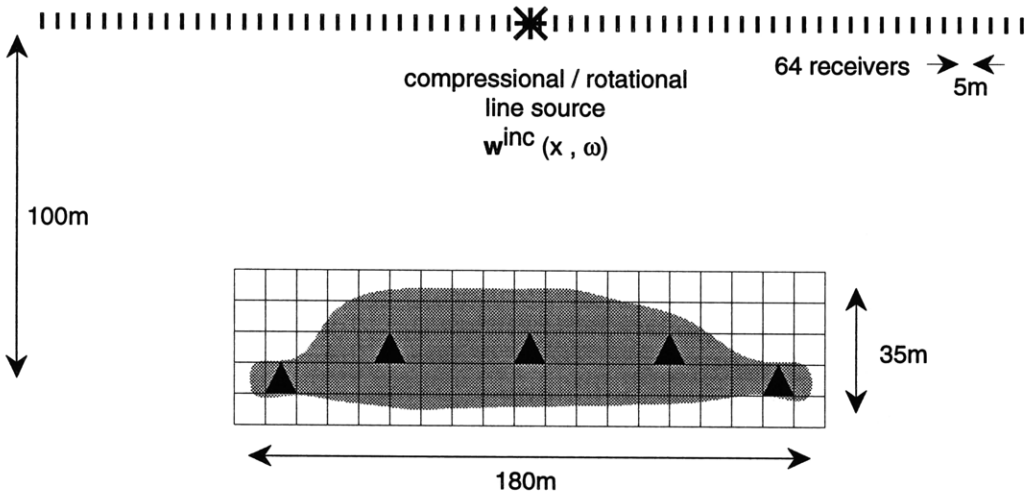

Figure 4-12: Elastics: the generic scatterer used to calculate elastic seismograms. The scatterer is embedded in a homogeneous background. The P- and S-velocities and density in the background are respectively 2000 m/s, 1300 m/s and 2000 kg/m^3. The scatterer is homogeneous. Its P- and S-velocities and density are, respectively, 3000 m/s, 1730 m/s and 2000 kg/m^3. The triangles show the centers for the MMP expansion.

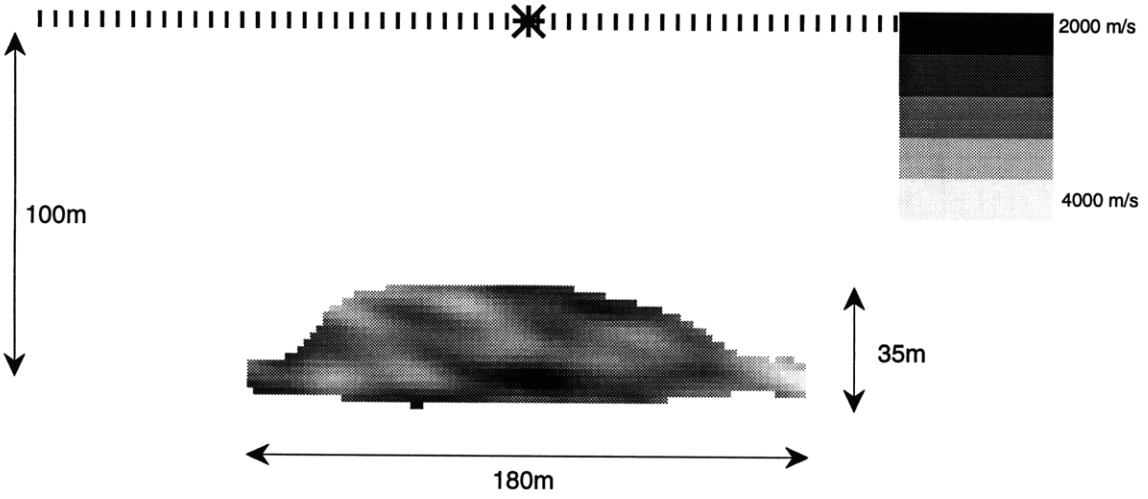

Figure 4-13: Elastics: heterogeneous scatterer where the velocities in the scatterer are replaced by random fields with a mean P-velocity of 3000 m/s, a standard deviation of the P-velocity of 500 m/s and a Gaussian spatial autocorrelation with correlation lengths of $a_1 = 18$ m, $a_2 = 6$ m and a tilt of $-10°$. The S-velocity is chosen to preserve a Poisson's ratio of 0.26 everywhere in the scatterer.

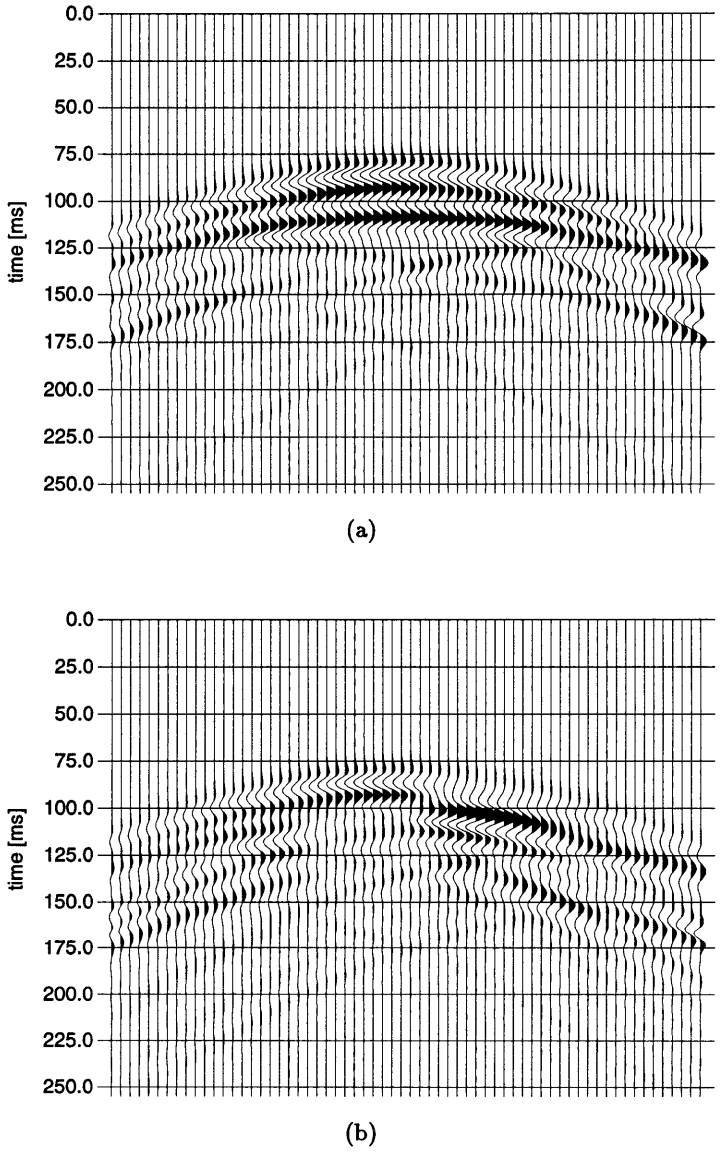

Figure 4-14: Elastics, compressional line source: Shown are the vertical components of the scattered fields (a) for the homogeneous scatterer depicted in Figure 4-12, and (b) for the heterogeneous scatterer (Figure 4-13).

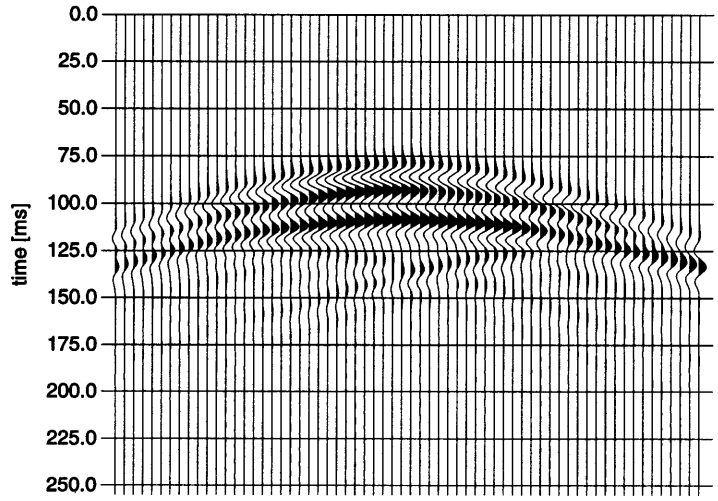

(a)

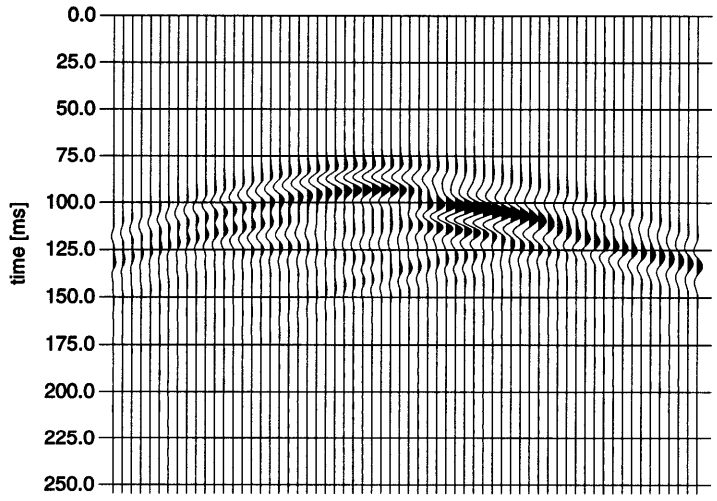

(b)

Figure 4-15: Elastics, compressional line source: The vertical displacement of the $P \rightarrow P$ reflection (a) from the homogeneous scatterer (Figure 4-12), and (b) from the heterogeneous scatterer (Figure 4-13).

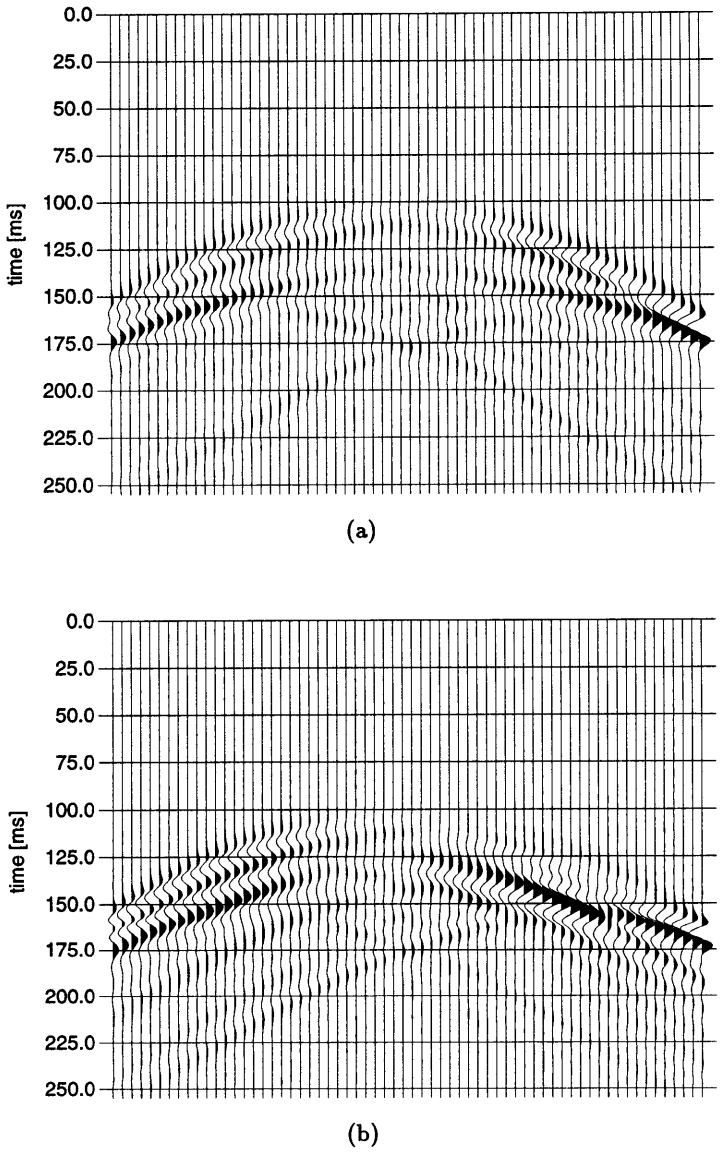

Figure 4-16: Elastics, compressional line source: The vertical displacement of the $P \rightarrow S$ conversion (a) from the homogeneous scatterer depicted in Figure 4-12, and (b) from the heterogeneous scatterer (Figure 4-13).

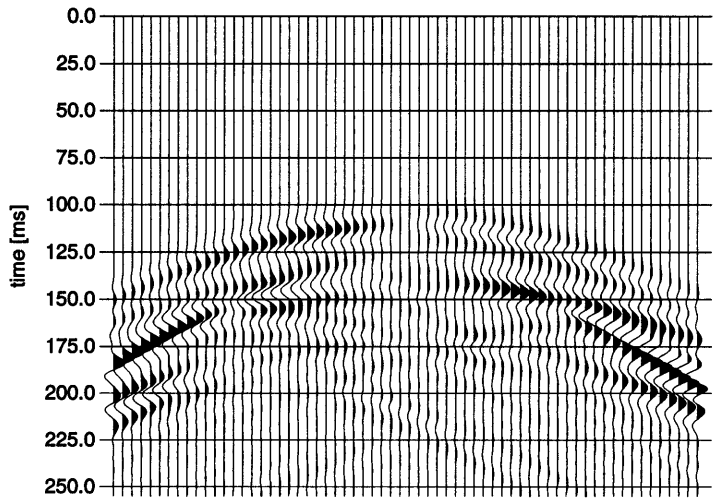

(a)

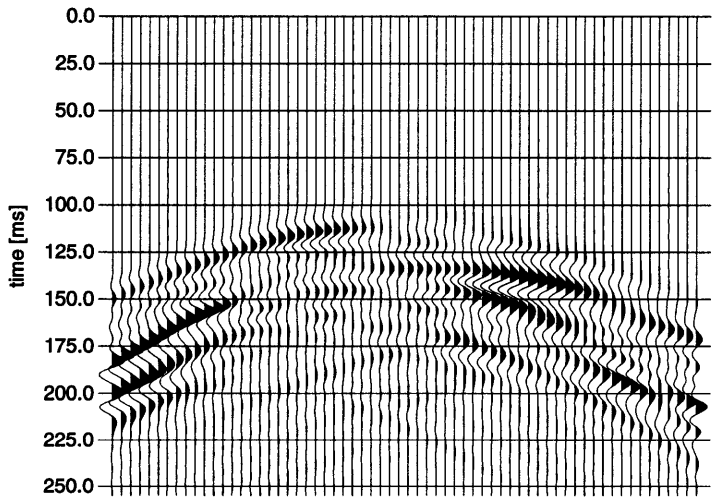

(b)

Figure 4-17: Elastics, rotational line source: The vertical component of the displacement scattered (a) from the homogeneous scatterer depicted in Figure 4-12, or (b) from the heterogeneous scatterer (Figure 4-13).

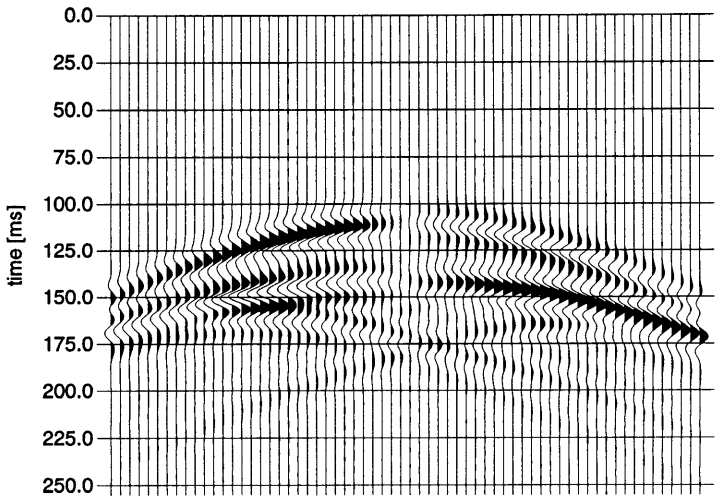

(a)

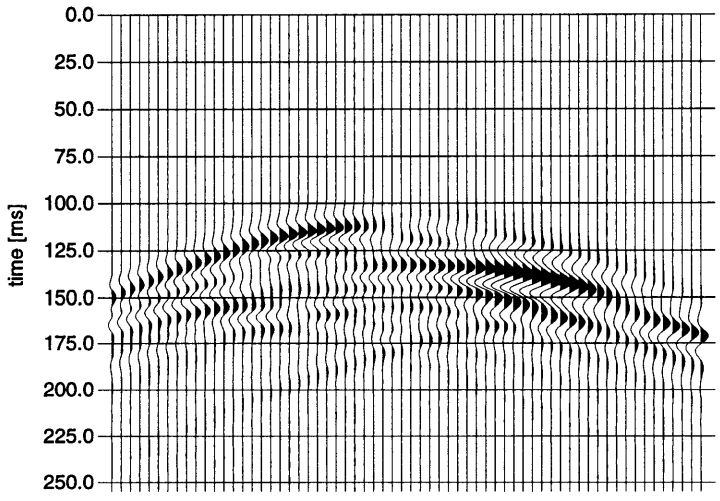

(b)

Figure 4-18: Elastics, rotational line source: The vertical displacement of the $S \rightarrow P$ conversion (a) from the homogeneous scatterer (Figure 4-12), or (b) from the heterogeneous scatterer (Figure 4-13).

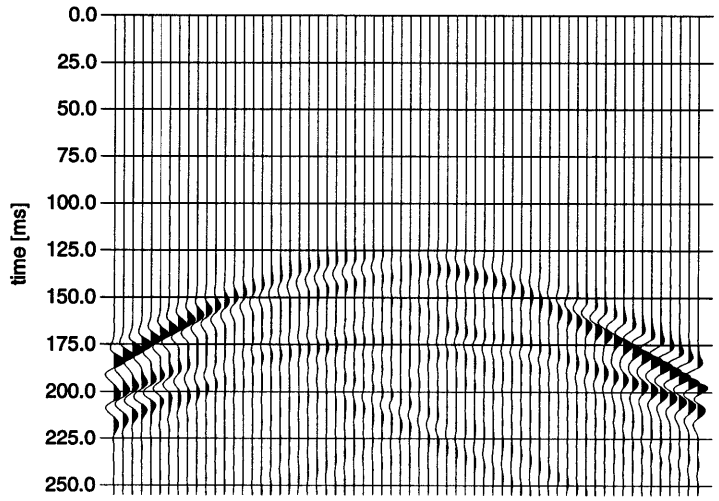

(a)

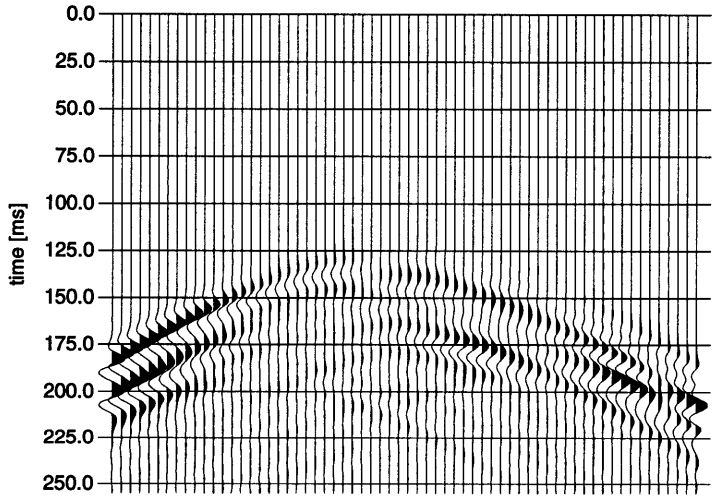

(b)

Figure 4-19: Elastics, rotational line source: The vertical displacement of the $S \rightarrow S$ reflection (a) from the homogeneous scatterer (Figure 4-12), or (b) from the heterogeneous scatterer (Figure 4-13).

Chapter 5

Acousto-Elastic Multiple Scattering: a Comparison of Ultrasonic Experiments with Multiple Multipole Expansions

Abstract

The wavefield scattered from only three solid rods submerged in water is very complex. Although the major events can readily be interpreted as direct reflections, the remaining wavefield consists of complicated interactions of the wavefields with the scatterers and the water surface. Forward modelling of the situation is a viable interpretative aid, especially if the method decomposes the wavefields by their respective origins. Multiple multipole expansions have already been used as a versatile tool to model acoustic or elastic multiple scattering problems where homogeneous scatterers were embedded in a homogeneous full-space. In the present paper, the scheme is expanded to multiple scattering between solids submerged in a fluid. For each scatterer, the waves induced in the fluid are expressed by sets

of multipole solutions with different origins. Thus by construction, the scattered wavefields are decomposed by scatterer. Ultrasonic experiments are performed for two different geometries of three submerged rods. To aid the interpretation of the results, the experiments are numerically modelled by the multiple multipoles method.

5.1 Introduction

The scattering of acoustic waves from solids submerged in a fluid has received well deserved attention for a long time (Everstine and Au-Yang, 1984; Junger and Feit, 1986). Even for very simple cases, the scattered wavefields become very complex. For example, in the case of several submerged solid objects, the major events can readily be interpreted as direct reflections. However, the remaining wavefield consists of complicated interactions of the wavefields with the scatterers and the water surface. Forward modelling of the situation is a valuable aid to understand these interacting events better. Especially useful are methods which decompose the scattered wavefields by their origin. Thus, forward modelling schemes such as the finite differences method are less interesting as interpretative tools because they only yield the total wavefields. Various other methods have been applied. For a few simple geometries, analytic solutions are available, e.g. cylindrical objects (Pao and Mow, 1973). For more complicated geometries, other methods have been used: integral equations (de Hoop, 1990; Luke and Martin, 1995), the T-matrix (Boström, 1980b), perturbation schemes (Norris, 1990), or boundary element methods (Jensen *et al.*, 1994) which might be coupled to finite elements (Mathews, 1986; Everstine and Henderson, 1990; Fyfe *et al.*, 1991).

Multiple multipole expansions (MMP) have already been shown to be a versatile tool to solve scattering problems in fluids (Imhof, 1995) or solids (Chapter 3). In either case, homogeneous scatterers were embedded in a homogeneous fullspace. In the present paper, a combination of the acoustic with the elastic scheme is introduced as an interpretative aid to multiple scattering between solids submerged in a fluid. There are various reasons to use MMP expansions. First, they have been shown to converge faster than more traditional

methods (Chapters 2,3). The resulting scheme is very naturally applied to situations of multiple scattering objects. Most important, the scattered fields are by construction decomposed by scatterer. Although we will not exploit it, the wavefield in each solid scatterer is also decomposed into P and S body waves.

The paper is structured as follows. In an ultrasonic watertank, we measure the scattering between three rods of lucite and the water surface. Even though the situation is rather simple, we find the scattered field to contain complex interactions between the rods and the surface. To aid the interpretation, we derive the acousto-elastic MMP scheme which we use to model the two ultrasonic experiments. A comparison of the experimental and numerical data not only validates the acousto-elastic scheme but also explains various events as internal multiples in the rods or reverberations between the scatterers and the water surface. The numerical data also identifies some events as reflections being diffracted by the other scatterers.

5.2 Ultrasonic Modelling

A simple fluid-solid scattering experiment is performed in an ultrasonic watertank. Three rods of lucite are submerged in the tank. Two different geometries are used. The first shown in Figure 5-1 resembles a syncline structure. The second geometry resembles an anticline shown in Figure 5-2. For both geometries, an acoustic source is placed above the rods. Receivers placed along a line perpendicular to the rods measure the signals reflected from the rods. Although the ultrasonic tank is of finite dimensions ($100 \times 60 \times 50\,\mathrm{cm}$), the experiment is designed that reflections from the sides and the bottom of the tank are outside the time window of interest. The tank is equipped with a PC-based control and data acquisition system. A schematic thereof is presented in Figure 5-3. Computer controlled holders allow movement of a source and a receiver along a prescribed path within the tank. For a fixed source - scatterer - receiver geometry, the computer controlled acquisition system allows to perform the same experiment a number of times to improve the signal-to-noise ratio. Without waveform averaging, the smaller events would vanish in the ambient noise

which reaches the same amplitude level as the reflections.

Piezoelectric transducers act as source and receiver. The source (Panametrix V323) has a strong nonuniform vertical radiation pattern, as most of its energy is pointed vertically downward as expected from a vertical point force (Schultz and Toksöz, 1995). The receiver (Panametrix V1091) has a receiver pattern very similar to the source radiation pattern. This source-receiver combination tends to emphasize waves propagating in the vertical direction and to suppress waves propagating in the horizontal direction. The transducers are placed just beneath the water surface to suppress the source and receiver ghosts.

The rods have a P-wave velocity $\alpha = 2570\,\mathrm{m/s}$, a S-wave velocity $\beta = 1200\,\mathrm{m/s}$, and a density ρ_s of $1180\,\mathrm{kg/m^3}$. The P-wave velocity γ in the water is $1460\,\mathrm{m/s}$, the density ρ_f is $1000\,\mathrm{kg/m^3}$. The width of the first scatterer is 45 mm, the second 60 mm, and the third 30 mm. All scatterers are 20 mm thick. Exiting the source transducer with a sharp pulse, the transducer emits a wavelet of approximately 190 kHz center frequency shown in Figure 5-4. In the water, the resulting dominant wavelength is around 6 mm. Thus, the scatterers are 3 to 10 times larger than the propagating pulse which allows to discriminate between reflections from the top or bottom of the scatterers. The sampling interval is chosen to be 400 ns which yields a corresponding Nyquist frequency of 1.25 MHz. The cutoff-frequencies of the bandpass filter are set to 5 KHz, respectively 300 KHz. For each trace, 512 samples are recorded. The recording is delayed by $120\,\mu s$ to mute the direct arrivals and to maximize the time window of interest. The traces are averaged over 2048 sweeps to reduce the noise amplitudes. The receiver transducer is placed at 75 different positions along a line perpendicular to the rods. The spacing between the receiver points is 5 mm. The source transducer is located in the center of the receiver spread at position 38.

Figure 5-5 shows the measured record for the syncline model defined in Figure 5-1. As expected for a syncline geometry, we obtain the typical butterfly pattern (Haartsen *et al.*, 1994). Figure 5-6 shows the measured record for the anticline model defined in Figure 5-2. For both geometries, the major events can readily be interpreted as direct reflections. But the remaining wavefields consist of complicated interactions of the wavefields with the

scatterers and the water surface. Despite the simple geometries, it is not obvious how to interpret the different events. As a consequence, we resort to forward-modelling as an interpretative aid.

5.3 Theoretical Background

We need to model how the acoustic pulse described by the displacement $\mathbf{u}^{inc}(\mathbf{x},\omega)$ propagating in the water scatters from submerged solids. To distinguish the different regions, we will use the symbol Γ^d. The fluid domain is denoted by Γ^0. Often, the fluid region will also be called 'background'. The three solid scatterers are denoted by Γ^1, Γ^2, and Γ^3. The boundary between the fluid Γ^0 and, e.g., the solid Γ^1 is denoted by $\partial\Gamma_{01}$.

In the frequency domain, the displacement $\mathbf{u}_f$ of a wave travelling in a two dimensional, homogeneous fluid is described by

$$\frac{1}{k_f^2}\nabla\nabla\cdot\mathbf{u}_f+\mathbf{u}_f=0\,, \tag{5.1a}$$

where we defined the wave number $k_f=\omega/\gamma$ for a particular frequency ω and the propagation velocity γ. The fluid velocity can also be written as $\gamma=\sqrt{\lambda_f/\rho_f}$ where λ_f is the Lamé parameter and ρ_f the density of the fluid. Note that we suppress a common time factor $e^{i\omega t}$. Elastic P-SV waves $\mathbf{u}_s$ travelling in a two dimensional, homogeneous solid are described by

$$\frac{1}{k_s^2}\nabla\nabla\cdot\mathbf{u}_s-\frac{1}{l_s^2}\nabla\times\nabla\times\mathbf{u}_s+\mathbf{u}_s=0\,, \tag{5.1b}$$

where we defined the wave numbers $k_s=\omega/\alpha$ and $l_s=\omega/\beta$ for a particular frequency ω and the propagation velocities $\alpha=\sqrt{\lambda_s+2\mu_s/\rho_s}$ and $\beta=\sqrt{\mu_s/\rho_s}$. The parameter ρ_s, λ_s, and μ_s denote the density and the Lamé parameters of the medium.

Instead of working with the vector forms (5.1) of the wave equations, we will use the potentials $\Xi(\mathbf{x},\omega)$, $\Phi(\mathbf{x},\omega)$, and $\mathbf{\Psi}(\mathbf{x},\omega)=\hat{\mathbf{y}}\Psi(\mathbf{x},\omega)$ which relate to the displacements $\mathbf{u}_f$

and $\mathbf{u}_s$ by

$$\mathbf{u}_f(\mathbf{x},\omega) = \mathbf{u}^{\Xi}(\mathbf{x},\omega) = \nabla\Xi(\mathbf{x},\omega)\,, \tag{5.2a}$$

$$\mathbf{u}_s(\mathbf{x},\omega) = \mathbf{u}^{\Phi}(\mathbf{x},\omega) + \mathbf{u}^{\Psi}(\mathbf{x},\omega) = \nabla\Phi(\mathbf{x},\omega) + \nabla\times\Psi(\mathbf{x},\omega)\,. \tag{5.2b}$$

Each scalar potential itself satisfies a scalar wave equation:

$$\nabla^2\Xi(\mathbf{x},\omega) + k_f^2\Xi(\mathbf{x},\omega) = 0\,, \tag{5.3a}$$

$$\nabla^2\Phi(\mathbf{x},\omega) + k_s^2\Phi(\mathbf{x},\omega) = 0\,, \tag{5.3b}$$

$$\nabla^2\Psi(\mathbf{x},\omega) + l_s^2\Psi(\mathbf{x},\omega) = 0\,. \tag{5.3c}$$

Similar to the purely acoustic or elastic cases (Chapters 2,3), we expand the potential fields due to the $D = 3$ scatterers as

$$\Xi(\mathbf{x},\omega) = \sum_{d=1}^{D}\sum_{p=1}^{P_d^{\Xi}}\sum_{n=-N_{pd}^{\Xi}}^{+N_{pd}^{\Xi}} a_{pnd}\cdot\xi_{pnd}(\mathbf{x},\mathbf{x}_{pd}^{\Xi},k_f) + e^{\Xi}\,, \tag{5.4a}$$

$$\Phi_d(\mathbf{x},\omega) = \sum_{p=1}^{P_d^{\Phi}}\sum_{n=-N_{pd}^{\Phi}}^{+N_{pd}^{\Phi}} b_{pnd}\cdot\phi_{pnd}(\mathbf{x},\mathbf{x}_{pd}^{\Phi},k_s) + e_d^{\Phi}\,, \tag{5.4b}$$

$$\Psi_d(\mathbf{x},\omega) = \sum_{p=1}^{P_d^{\Psi}}\sum_{n=-N_{pd}^{\Psi}}^{+N_{pd}^{\Psi}} c_{pnd}\cdot\psi_{pnd}(\mathbf{x},\mathbf{x}_{pd}^{\Psi},l_s) + e_d^{\Psi}\,, \tag{5.4c}$$

where the subscript $d \le D$ denotes the index of the scatterer. The expansions $\xi_{pnd}(\mathbf{x},\mathbf{x}_{pd}^{\Xi},k_f)$, $\phi_{pnd}(\mathbf{x},\mathbf{x}_{pd}^{\Phi},k_s)$, and $\psi_{pnd}(\mathbf{x},\mathbf{x}_{pd}^{\Psi},l_s)$ are all solutions to their respective Helmholtz equations (5.3). For each scatterer d and each expansion, e.g. Φ, we choose a set of P_d^{Φ} expansion centers located at $\mathbf{x}_{pd}^{\Phi}$. At each expansion center $\mathbf{x}_{pd}^{\Phi}$, we place a multipole $\sum_n \phi_{pnd}(\mathbf{x},\mathbf{x}_{pd}^{\Phi},k_s)$ of order $-N_{pd} \le n \le +N_{pd}$. Because the maximal orders of the multipoles are finite and the resulting expansion is non-orthogonal, we also need to include an error term e_d^{Φ}. The other two potential fields Ξ and Ψ are defined in exactly the same way. This form of the expansion allows to choose different numbers and locations of the expansion centers for each scatterer and each field Ξ, Φ, and Ψ. Also, the maximal orders for the different multipoles

can be chosen independently.

An expansion of the form (5.4) is known as multiple multipole (MMP) expansion because we have in fact a summation over, e.g., P_d^{Φ} multipoles located at $\mathbf{x}_{pd}^{\Phi}$. In the fluid, we choose the propagatory solutions $H_{|n|}^{(1)}(k_f r)\, e^{in\theta}$ to the Helmholtz equation (5.3a):

$$\xi_{pnd}(\mathbf{x}, \mathbf{x}_{pd}^{\Xi}, k_f) = H_{|n|}^{(1)}(k_f\, |\mathbf{x} - \mathbf{x}_{pd}^{\Xi}|)\, e^{in\theta_{pd}^{\Xi}} \qquad \text{with } \mathbf{x}_{pd}^{\Xi} \text{ inside scatterer } d\,, \tag{5.5a}$$

where θ_{pd}^{Ξ} is the angle $\measuredangle(\hat{\mathbf{x}}, \mathbf{x} - \mathbf{x}_{pd}^{\Xi})$ with respect to the unit vector $\hat{\mathbf{x}}$ in the x-direction. Foreseeing the need of a free surface in the fluid phase, we directly add the stationary phase contribution of the field reflected at the surface (Chew, 1988; Imhof, 1995) to the expansion function (5.5a):

$$\xi_{pnd}(\mathbf{x}, \mathbf{x}_{pd}^{\Xi}, k_f) = H_{|n|}^{(1)}(k_f\, |\mathbf{x} - \mathbf{x}_{pd}^{\Xi}|)\, e^{in\theta_{pd}^{\Xi}} - H_{|n|}^{(1)}(k_f\, |\mathbf{x} - \boldsymbol{x}_{pd}^{\Xi}|)\, e^{-in\varphi_{pd}^{\Xi}}\,, \tag{5.5b}$$

where $\varphi_{pd}^{\Xi} = \measuredangle(\hat{\mathbf{x}}, \mathbf{x} - \boldsymbol{x}_{pd}^{\Xi})$. The location $\boldsymbol{x}_{pd}^{\Xi}$ of the corresponding mirror source is obtained by reflection of the expansion center $\mathbf{x}_{pd}^{\Xi}$ across the free surface.

In the solid, we can choose between two different sets of expansion functions for ϕ_{pnd} and ψ_{pnd}. Either we use the propagatory solutions $H_{|n|}^{(1)}(k_s r)e^{in\theta}$ and $H_{|n|}^{(1)}(l_s r)e^{in\theta}$, or we choose the standing wave solutions $J_{|n|}(k_s r)\, e^{in\theta}$ and $J_{|n|}(l_s r)\, e^{in\theta}$:

$$\phi_{pnd}(\mathbf{x}, \mathbf{x}_{pd}^{\Phi}, k_s) = \begin{cases} J_{|n|}(k_s\, |\mathbf{x} - \mathbf{x}_{pd}^{\Phi}|)\, e^{in\theta_{pd}^{\Phi}} & \text{if } \mathbf{x}_{pd}^{\Phi} \text{ is inside scatterer } d \quad , \quad (5.6a) \\ H_{|n|}^{(1)}(k_s\, |\mathbf{x} - \mathbf{x}_{pd}^{\Phi}|)\, e^{in\theta_{pd}^{\Phi}} & \text{if } \mathbf{x}_{pd}^{\Phi} \text{ is outside scatterer } d \quad . (5.6b) \end{cases}$$

Similarly, we have:

$$\psi_{pnd}(\mathbf{x}, \mathbf{x}_{pd}^{\Psi}, l_s) = \begin{cases} J_{|n|}(l_s\, |\mathbf{x} - \mathbf{x}_{pd}^{\Psi}|)\, e^{in\theta_{pd}^{\Psi}} & \text{if } \mathbf{x}_{pd}^{\Psi} \text{ is inside scatterer } d \quad , \quad (5.7a) \\ H_{|n|}^{(1)}(l_s\, |\mathbf{x} - \mathbf{x}_{pd}^{\Psi}|)\, e^{in\theta_{pd}^{\Psi}} & \text{if } \mathbf{x}_{pd}^{\Psi} \text{ is outside scatterer } d \quad . (5.7b) \end{cases}$$

The three different wavefields are coupled by the boundary conditions along the interface of the fluid and the solid. The boundary conditions require continuity of the normal displace-

ment $\hat{\mathbf{n}} \cdot \mathbf{u}$, continuity of normal traction $\hat{\mathbf{n}} \cdot \boldsymbol{\sigma} \cdot \hat{\mathbf{n}}$ and vanishing tangential traction $\hat{\mathbf{t}} \cdot \boldsymbol{\sigma} \cdot \hat{\mathbf{n}}$. For a point $\mathbf{x}$ on the interface with the unit normal $\hat{\mathbf{n}}$ and the unit tangential direction $\hat{\mathbf{t}}$, we have

$$\begin{aligned}
\hat{\mathbf{n}} \cdot \left(\mathbf{u}^{inc}(\mathbf{x},\omega) + \mathbf{u}^{\Xi}(\mathbf{x},\omega)\right) &= \hat{\mathbf{n}} \cdot \left(\mathbf{u}^{\Phi}(\mathbf{x},\omega) + \mathbf{u}^{\Psi}(\mathbf{x},\omega)\right) && \text{(5.8a)} \\
\hat{\mathbf{n}} \cdot \left(\boldsymbol{\sigma}^{inc}(\mathbf{x},\omega) + \boldsymbol{\sigma}^{\Xi}(\mathbf{x},\omega)\right) \cdot \hat{\mathbf{n}} &= \hat{\mathbf{n}} \cdot \left(\boldsymbol{\sigma}^{\Phi}(\mathbf{x},\omega) + \boldsymbol{\sigma}^{\Psi}(\mathbf{x},\omega)\right) \cdot \hat{\mathbf{n}} && \text{(5.8b)} \\
0 &= \hat{\mathbf{t}} \cdot \left(\boldsymbol{\sigma}^{\Phi}(\mathbf{x},\omega) + \boldsymbol{\sigma}^{\Psi}(\mathbf{x},\omega)\right) \cdot \hat{\mathbf{n}} && \text{(5.8c)}
\end{aligned}$$

where the displacements are defined in (5.2). The stress tensor in the fluid is given by $\boldsymbol{\sigma}^{\Xi}(\mathbf{x},\omega) = \mathbf{I}p(\mathbf{x},\omega) = -\mathbf{I}k_f^2\lambda_f\Xi(\mathbf{x},\omega)$ which also defines the pressure $p(\mathbf{x},\omega)$. The stress tensors $\boldsymbol{\sigma}^{\Phi}(\mathbf{x},\omega)$ and $\boldsymbol{\sigma}^{\Psi}(\mathbf{x},\omega)$ are defined in a local coordinate system (r,y,θ) centered at the expansion center of the multipole.

$$\begin{aligned}
\sigma_{rr}^{\Phi} &= -\lambda_s k_s^2 \Phi + 2\mu \frac{\partial^2 \Phi}{\partial r^2} & \sigma_{rr}^{\Psi} &= 2\mu \frac{\partial}{\partial r}\left(\frac{1}{r}\frac{\partial \Psi}{\partial \theta}\right) \\
\sigma_{\theta\theta}^{\Phi} &= -\lambda_s k_s^2 \Phi + 2\mu \frac{1}{r}\left(\frac{\partial \Phi}{\partial r} + \frac{1}{r}\frac{\partial^2 \Phi}{\partial \theta^2}\right) & \sigma_{\theta\theta}^{\Psi} &= 2\mu \left[\frac{1}{r}\left(\frac{1}{r}\frac{\partial \Psi}{\partial \theta} - \frac{\partial^2 \Psi}{\partial r \partial \theta}\right)\right] \\
\sigma_{r\theta}^{\Phi} &= 2\mu \left[\frac{1}{r}\frac{\partial^2 \Phi}{\partial r \partial \theta} - \frac{1}{r^2}\frac{\partial \Phi}{\partial \theta}\right] & \sigma_{r\theta}^{\Psi} &= 2\mu \left[\frac{1}{2r^2}\frac{\partial^2 \Psi}{\partial \theta^2} - \frac{r}{2}\frac{\partial}{\partial r}\left(\frac{1}{r}\frac{\partial \Psi}{\partial r}\right)\right]
\end{aligned} \qquad (5.9)$$

Note that the components of displacements and of the stress tensors have to be transformed or rotated into the global coordinate frame (x,y,z) in which the unit normal $\hat{\mathbf{n}}$ and the unit tangential direction $\hat{\mathbf{t}}$ are defined.

We solve for the unknown coefficients a_{pnd}, b_{pnd}, and c_{pnd} by enforcing the boundary conditions (5.8) on discrete matching points $\mathbf{x}_m$ along the boundaries of the scatterers. We

obtain a linear system of equations

$$\begin{pmatrix} -\Xi_{11}^{n} & -\Xi_{12}^{n} & -\Xi_{13}^{n} & \Phi_{11}^{n} & \Psi_{11}^{n} & 0 & 0 & 0 & 0 \\ -\Xi_{11}^{nn} & -\Xi_{12}^{nn} & -\Xi_{13}^{nn} & \Phi_{11}^{nn} & \Psi_{11}^{nn} & 0 & 0 & 0 & 0 \\ 0 & 0 & 0 & \Phi_{11}^{nt} & \Psi_{11}^{nt} & 0 & 0 & 0 & 0 \\ -\Xi_{21}^{n} & -\Xi_{22}^{n} & -\Xi_{23}^{n} & 0 & 0 & \Phi_{22}^{n} & \Psi_{22}^{n} & 0 & 0 \\ -\Xi_{21}^{nn} & -\Xi_{22}^{nn} & -\Xi_{23}^{nn} & 0 & 0 & \Phi_{22}^{nn} & \Psi_{22}^{nn} & 0 & 0 \\ 0 & 0 & 0 & 0 & 0 & \Phi_{2}^{nt} & \Psi_{2}^{nt} & 0 & 0 \\ -\Xi_{31}^{n} & -\Xi_{32}^{n} & -\Xi_{33}^{n} & 0 & 0 & 0 & 0 & \Phi_{33}^{n} & \Psi_{33}^{n} \\ -\Xi_{31}^{nn} & -\Xi_{32}^{nn} & -\Xi_{33}^{nn} & 0 & 0 & 0 & 0 & \Phi_{33}^{nn} & \Psi_{33}^{nn} \\ 0 & 0 & 0 & 0 & 0 & 0 & 0 & \Phi_{33}^{nt} & \Psi_{33}^{nt} \end{pmatrix} \cdot \begin{pmatrix} \mathbf{a}_1 \\ \mathbf{a}_2 \\ \mathbf{a}_3 \\ \mathbf{b}_1 \\ \mathbf{c}_1 \\ \mathbf{b}_2 \\ \mathbf{c}_2 \\ \mathbf{b}_3 \\ \mathbf{c}_3 \end{pmatrix} \approx \begin{pmatrix} \mathbf{u}_1^n \\ \sigma_1^{nn} \\ 0 \\ \mathbf{u}_2^n \\ \sigma_2^{nn} \\ 0 \\ \mathbf{u}_3^n \\ \sigma_3^{nn} \\ 0 \end{pmatrix} \tag{5.10}$$

where we used the submatrices Ξ_{sd}^{n}, Φ_{sd}^{n}, and Ψ_{sd}^{n} to denote the normal displacements $\hat{\mathbf{n}} \cdot \mathbf{u}$ at the matching points along the scatterer $s \in \{1,2,3\}$ due to ξ_{pnd}, ϕ_{pnd}, and ψ_{pnd}. The submatrices Ξ_{sd}^{nn}, Φ_{sd}^{nn}, and Ψ_{sd}^{nn} are the same but for the normal stress $\hat{\mathbf{n}} \cdot \boldsymbol{\sigma} \cdot \hat{\mathbf{n}}$. The submatrices Φ_{sd}^{nt} and Ψ_{sd}^{nt} contain the tangential stresses $\hat{\mathbf{t}} \cdot \boldsymbol{\sigma} \cdot \hat{\mathbf{n}}$. For the sake of clarity, the index d is used to indicate which scatterer induces the field. The index s indicates along which scatterer the boundary conditions are evaluated and thus on which boundary the matching points $\mathbf{x}_m$ lie. All three scatterers contribute to the scattered field $\Xi(\mathbf{x},\omega)$ in the fluid. Therefore, we have submatrices Ξ_{sd} for each scatterer d and each boundary s. But because, e.g., scatterer 1 has no common boundary with scatterer 2, the fields $\Phi_1(\mathbf{x},\omega)$, $\Psi_1(\mathbf{x},\omega)$ and $\Phi_2(\mathbf{x},\omega)$, $\Psi_2(\mathbf{x},\omega)$ do not interact with each other. Thus for $s \neq d$, the submatrices Φ_{sd} and Ψ_{sd} vanish. The individual scatterers are only coupled by the scattered fields $\Xi_1(\mathbf{x},\omega)$, $\Xi_2(\mathbf{x},\omega)$, and $\Xi_3(\mathbf{x},\omega)$ propagating in the fluid. All multiple scattering is automatically accounted for by the boundary conditions. The only contribution for the fields within, e.g., scatterer 1 are due to the (self) interactions of $\Phi_1(\mathbf{x}_m,\omega)$ and $\Psi_1(\mathbf{x}_m,\omega)$.

Defining the matching points by their location $\mathbf{x}_{ms}$ along the boundary of scatterer s, we

can write the submatrices as

$$\begin{aligned}
\Xi^{n}_{sd} &= \left[u_n\Big(\xi_{pnd}(\mathbf{x}_{ms},\omega)\Big)\right], \quad \Phi^{n}_{sd} = \left[u_n\Big(\phi_{pnd}(\mathbf{x}_{ms},\omega)\Big)\right], \quad \Psi^{n}_{sd} = \left[u_n\Big(\psi_{pnd}(\mathbf{x}_{ms},\omega)\Big)\right], \\
\Xi^{nn}_{sd} &= \left[\sigma_{nn}\Big(\xi_{pnd}(\mathbf{x}_{ms},\omega)\Big)\right], \quad \Phi^{nn}_{sd} = \left[\sigma_{nn}\Big(\phi_{pnd}(\mathbf{x}_{ms},\omega)\Big)\right], \quad \Psi^{nn}_{sd} = \left[\sigma_{nn}\Big(\psi_{pnd}(\mathbf{x}_{ms},\omega)\Big)\right], \\
&\qquad\qquad \Phi^{nt}_{sd} = \left[\sigma_{nt}\Big(\phi_{pnd}(\mathbf{x}_{ms},\omega)\Big)\right], \quad \Psi^{nt}_{sd} = \left[\sigma_{nt}\Big(\psi_{pnd}(\mathbf{x}_{ms},\omega)\Big)\right].
\end{aligned} \tag{5.11}$$

Similarly, the vectors $\mathbf{u}^{n}_{s}$ and $\boldsymbol{\sigma}^{nn}_{s}$ on the right hand side represent the incident wavefield in the fluid evaluated at the matching points $\mathbf{x}_{ms}$:

$$\mathbf{u}^{n}_{s} = \left[u^{inc}_{n}(\mathbf{x}_{ms},\omega)\right], \qquad \boldsymbol{\sigma}^{nn}_{s} = \left[\sigma^{inc}_{nn}(\mathbf{x}_{ms},\omega)\right]. \tag{5.12}$$

Finally, the vectors $\mathbf{a}_d$, $\mathbf{b}_d$, and $\mathbf{c}_d$ contain the unknown coefficients a_{pnd}, b_{pnd}, and c_{pnd}. Because the MMP expansions (5.4) are commonly non-orthogonal, the system (5.10) is made overdetermined by choosing more matching points than needed. It is then solved in the least-squares sense by QR decomposition (Strang, 1988) using Givens updating (Schwarz, 1989).

5.4 Numerical Modelling

To interpret the ultrasonic results, we model the scattering problems depicted in Figures 5-1 and 5-2. Three rods of lucite are submerged in water. The rods have a P-wave velocity $\alpha = 2570\,\mathrm{m/s}$, a S-wave velocity $\beta = 1200\,\mathrm{m/s}$, and a density ρ_s of $1180\,\mathrm{kg/m^3}$. In the water, the P-wave velocity γ and the density ρ_f are $1460\,\mathrm{m/s}$ and $1000\,\mathrm{kg/m^3}$. A vertical dipole source excites an acoustic wave which propagates downwards and interacts with the elastic scatterers. The source pulse is modulated by a Ricker wavelet (Ricker, 1977) of 200 kHz. The resulting scattered fields are measured at 75 locations along the surface. Source, scatterers and receivers are separated by at least 30 dominant wavelengths of 6 mm. Due to the resulting long propagation times, many frequencies are needed to calculate the traces. For a sampling interval of 400 ns, we will use 512 frequencies.

To damp resonances, we account for the intrinsic attenuation in the scatterers by making the wave number k complex

$$k = k_r + ia \tag{5.13}$$

where a is the attenuation coefficient. Alternatively, we use the quality factor Q_c which relates to the attenuation coefficient a by

$$Q_c = \frac{\omega}{2ac} \tag{5.14}$$

where the velocity c is either α or β. Both quality factors Q_α and Q_β are assumed to be 100.

The scattered wavefield in the fluid is expanded as (5.4a) where we choose $D = 3$, $P_1^\Xi = 4$, $P_2^\Xi = 5$, and $P_3^\Xi = 3$. For each of these multipoles, we choose $N_{pd}^\Xi = 6$. As expansion function, we use (5.5b) which includes the reflections from the free surface. Figure 5-7 defines the exact locations of the expansion centers for the syncline model (Figure 5-1). For the anticline model, the same locations relative to the solids are used for the expansion centers.

The wavefields in the solid scatterers are expanded as (5.4b) and (5.4c) for the P- and the S-wave. For scatterer Γ^1, we choose $P_1^\Phi = P_1^\Psi = 12$. For scatterer Γ^2, we use $P_2^\Phi = P_2^\Psi = 14$. Finally, for the third scatterer Γ^3 we employ $P_3^\Phi = P_3^\Psi = 10$ expansion centers. At each expansion center, we use only the orders between -3 and 3. Thus, $N_{pd}^\Phi = N_{pd}^\Psi = 3$. Because we placed the expansion centers for the wavefields in the solids *outside* the scatterers (Figure 5-7), we have to use (5.6b) and (5.7b) to describe the P- and the S-waves. For resonating geometries such as the posed problem, the propagatory solutions (5.6b) and (5.7b) are superior to the standing wave solutions (5.6a) and (5.7a). First, their amplitudes decay faster (Hafner, 1990). But they also force us to illuminate the scatterers from all sides which decouples the multipoles and the interfaces because each multipole illuminates mainly the region of the interface closest to its expansion center. This effect lowers the condition number and thus enhances the stability of the numerical matrix inversion. For

both models, 660 expansion functions and 444 matching points (= 1332 equations) are used.

Figures 5-9 and 5-14 show the synthetic seismograms as calculated by the MMP expansions for the syncline- and the anticline model. The first 120 μs are suppressed since they only contain the direct arrival.

5.5 Comparison of the Tank Data with the MMP Solutions

The advantage of the MMP solution over the ultrasonic watertank data is that, by construction, the wavefields are decomposed by scatterer. Once the equation system (5.10) is solved for a particular model, we fix the summation index d to 1, 2, or 3 in expression (5.4a) when evaluating the seismograms. Remember that the index d denotes the scatterer which emits a particular field. Thus, we can plot the scattered wavefields for each of the three scatterers independently which simplifies the seismograms and allows correlation of events with scatterers.

In the ultrasonic experiment, we use a point source and a point receiver. The models contain no variation perpendicular to the source-receiver plane. Hence, the experiments are in fact $2\frac{1}{2}$-D experiments. However, the numerical MMP scheme is derived and applied to 2-D only. Comparing the experimental results to the numerical ones might be problematic. But Esmersoy (1986) and Lo (1987) showed that the differences between 2-D and $2\frac{1}{2}$-D are negligible as long as the scatterers are in the far field with respect to both the source and the receivers. At the center frequency of 190 kHz, the scatterers are at least 15 wavelengths away from either source or receivers for both geometries. Clearly, the far field condition is satisfied.

5.5.1 Syncline Model

A comparison between the ultrasonic record (Figure 5-5) and the MMP solution (Figure 5-9) shows that the arrival times and amplitudes for different events match very well. The main

difference between the Figures 5-5 and 5-9, the real and the synthetic data, are the strong, repetitive events in the central part of the real seismogram. The cause is the signature of the source tranducer (Figure 5-4) which rings more than a Ricker wavelet.

The butterfly pattern typical for synclines can easily be seen (Haartsen *et al.*, 1994). As expected, each scatterer reflects twice with opposing polarity corresponding to reflections from the top and from the bottom. The two events are typically $14\,\mu$s separated. Toward the end of the traces at $300\,\mu$s, reverberations of the reflection from scatterer Γ^2 can be found which bounced between the surface and the scatterers Γ^1 and Γ^3. These effects can be seen more clearly in the MMP solution decomposed by scatterer shown in Figures 5-10 to 5-12. All synthetic seismograms are scaled similarly which allows to compare the amplitudes between the different figures.

The decomposed MMP solution in Figures 5-10 to 5-12 shows that the event around $180\,\mu$s in the tank data (Figure 5-5) is in reality composed of different events. First, there is the direct reflection from scatterer Γ^2. But this reflection was also diffracted through the scatterers Γ^1 and Γ^3 as the seismograms 5-10 and 5-12 show. Also, the first multiple reflections from inside Γ^1 and Γ^3 appear nearly at that time. Another interesting set of events appears at $256\,\mu$s and $270\,\mu$s. Figure 5-10 correlates these two events with scatterer Γ^1. The traveltimes prove them to be reflections from Γ^1 bouncing between the water surface and Γ^1. The prior one reflected twice from the top of Γ^1. The latter one reflected once from the top, once from the bottom. Thus, one would expect another event about $14\,\mu$s later corresponding to a wave bouncing between the bottom of Γ^1 and the water surface. Indeed, a very weak event appears at the expected time in the tank data (Figure 5-5) and the MMP solutions (Figures 5-9 and 5-10). A final subtlety are the multiples arriving around $300\,\mu$s which justify the stationary phase reflections into the MMP expansion functions (5.5b). The scattered fields in Figures 5-10 to 5-12 show very nicely that these events are a combination of different waves. First, there are waves reflected from Γ^2, then bounced off the water surface and finally rebounded from either Γ^1 or Γ^3. But we also encounter the opposite: waves reflecting from Γ^1 or Γ^3, bouncing off the water surface and finally rebounding from Γ^2. To demonstrate the effect of the multiple scattering, we calculate the acousto-elastic

response for each scatterer separately and subtract them from the complete MMP solution (Figure 5-9). The residual wavefield is shown in Figure 5-13. The amplitudes in both figures are scaled by the same amount to ease a direct comparison of single scattering versus multiple scattering. Clearly, the two scatterers Γ^1 and Γ^3 speed up the reflection from Γ^2. The remaining events are waves bouncing between the three scatterers and the water surface as well as internal multiples sped up passing through Γ^1 and Γ^3.

5.5.2 Anticline Model

Both the ultrasonic record (Figure 5-6) and the MMP solution (Figure 5-14) clearly show the reflections from the top and the bottom of each scatterer. Not surprisingly, scatterer Γ^2 shadows Γ^1 as the rather abrupt change in the reflection-amplitude around $170\,\mu$s demonstrates. To identify a few other events, we decompose the MMP solution by scatterer. The decomposed seismograms are shown in Figures 5-15 to 5-17.

For example, Figure 5-16 shows that part of the ringing main reflection around $130\,\mu$s is caused by multiple scattering inside Γ^2. The bottom reflection even splits into 2 events forming a butterfly pattern which repeats every $14\,\mu$s. At $170\,\mu$s, the main reflection from scatterer Γ^1 appears in the scattered field of Γ^2. This event can be interpreted as reflection from Γ^1 but propagating through Γ^2. Similarly at $190\,\mu$s, Figure 5-16 shows the reflection of Γ^3 being diffracted through Γ^2. After both events, internal multiples from Γ^1 and Γ^3 show up in the fields scattered from Γ^1 and Γ^3, respectively. Diffractions of these multiples passing through Γ^2 are again present in Figure 5-16.

To demonstrate the effect of the multiple scattering, we calculate the response of each scatterer alone and subtract it from the complete MMP solution (Figure 5-14). The residual wavefield is shown in Figure 5-18. The amplitudes in both figures are scaled by the same amount to allow a direct comparison of single scattering versus multiple scattering. For the first $170\,\mu$s, the events emanated by scatterer Γ^2 are the same for single or multiple scattering. Clearly, the reflection from scatterer Γ^1 separates into two events in the residual

seismogram shown in Figure 5-18. Scatterer Γ^2 not only shadows Γ^1 but also speeds up the arrival time of the reflection passing through the fast solid. The same holds for some of the later events in Figure 5-18 corresponding to internal multiples. The remaining events are generated by waves bouncing between the three scatterers and the water surface. For example, the reflections around $300\,\mu$s are caused by multiple scattering between Γ^2, the water surface, and either of Γ^1 or Γ^3.

5.6 Summary

Already for simple geometries, the wavefield scattered from solids submerged in water can be rather complex. Furthermore, the scattered wavefield becomes even more complicated if the water surface interacts with the scatterers. Especially the syncline experiment, where three lucite rods were submerged in an ultrasonic watertank, demonstrates this point. Although the main reflections are simple to identify, the remaining events are very hard to interpret.

To aid the interpretation, we forward-modelled the situations numerically using the multiple multipole method (MMP). For each submerged solid, the scattered wavefield induced in the fluid is expanded into a MMP expansion (Imhof, 1995). Similarly, in each solid two MMP expansions are used to describe the P- and S-components of the elastic wavefields. The advantage of the MMP scheme is that the scattered wavefields are, by construction, decomposed by scatterer as well as by mode of propagation. Hence, the wavefields scattered from each solid can be plotted independently which facilitates the correlation of particular events with individual scatterers. Curiously, this allows to distinguish direct reflections from reflections diffracted by another scatterer along their path of propagation.

In conclusion, we found that acousto-elastic multiple multipole expansions are a versatile tool either to directly solve scattering problems or to aid in their interpretation. This work should find uses in a variety of fields, notable in geophysics and oil exploration, as well as in naval underwater applications.

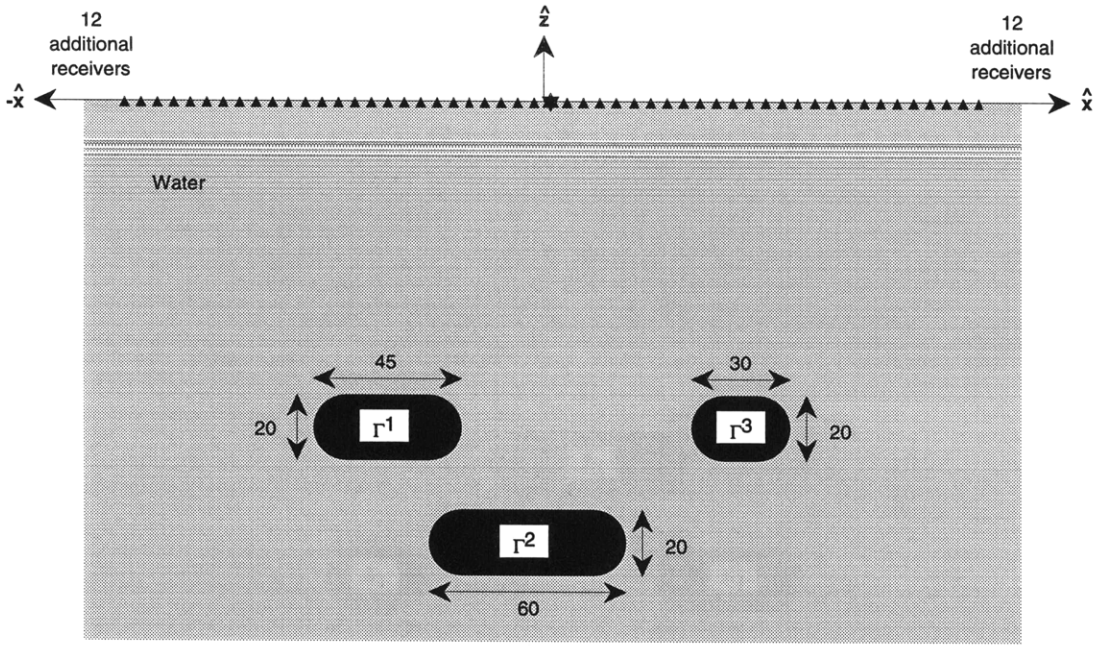

Figure 5-1: 'Syncline' model: Three oval rods of lucite are submerged in water. The source-transducer (star) generates a pressure wave which scatters between the rods and the water surface until it is picked up by the 75 receivers (triangles). All dimensions are in millimeters. The respective centers of the scatterers Γ^1, Γ^2, and Γ^3 are located at $(-42.5, -99)$, $(0, -136)$ and $(65, -98)$. Both the source and receiver 38 are positioned at $(8, 0)$. The spacing between the receivers is 5 mm.

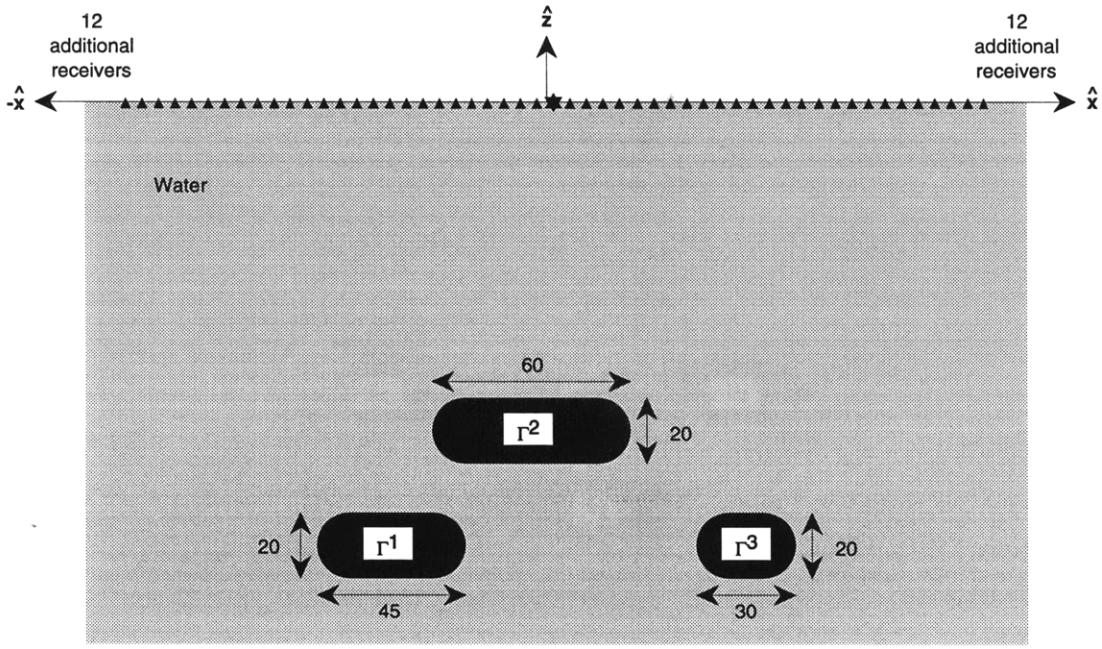

Figure 5-2: 'Anticline' model where the star denotes the source and the triangles symbolize the receivers. All dimensions are in millimeters. The respective centers of the oval scatterers Γ^1, Γ^2, and Γ^3 are located at $(-42.5, -135)$, $(0, -99)$ and $(65, -138)$. Both the source and receiver 38 are positioned at $(8, 0)$. The spacing between the receivers is 5 mm.

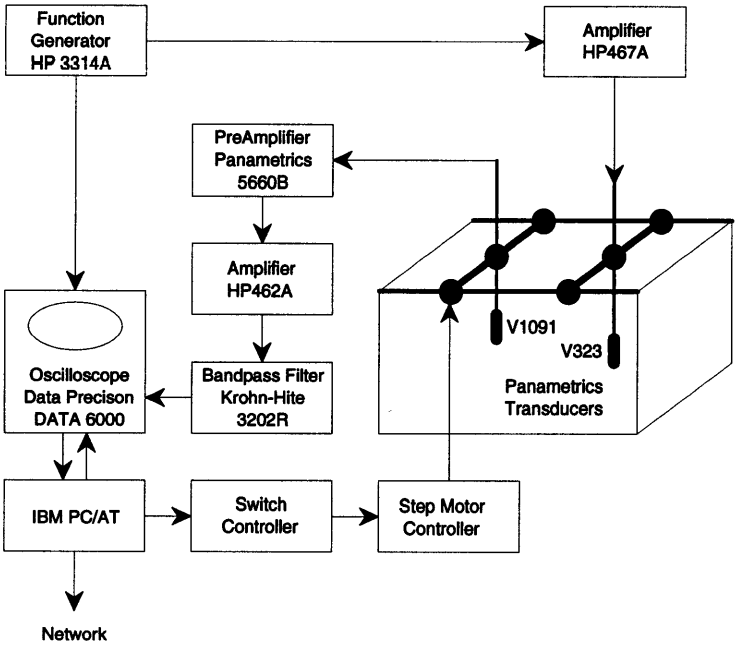

Figure 5-3: Block diagram of the computer-based ultrasonic data-acquisition system.

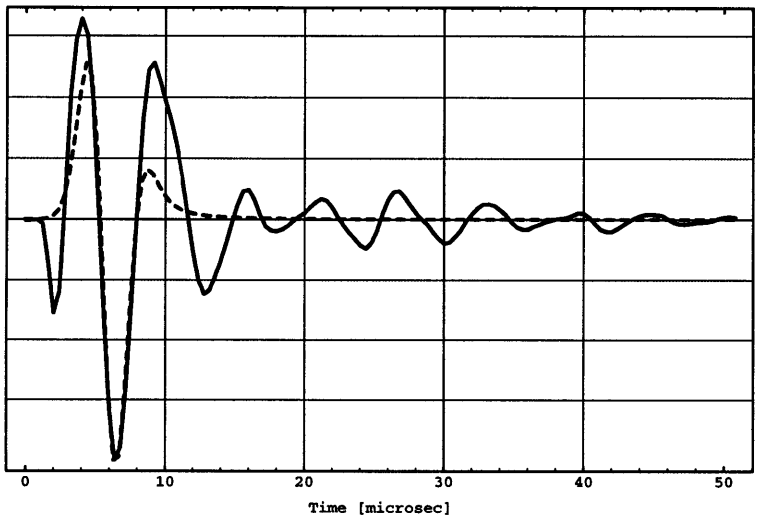

Figure 5-4: Wavelets after propagating 30 wavelengths: measured in ultrasonic watertank (solid), Ricker wavelet used for numerical models (dashed).

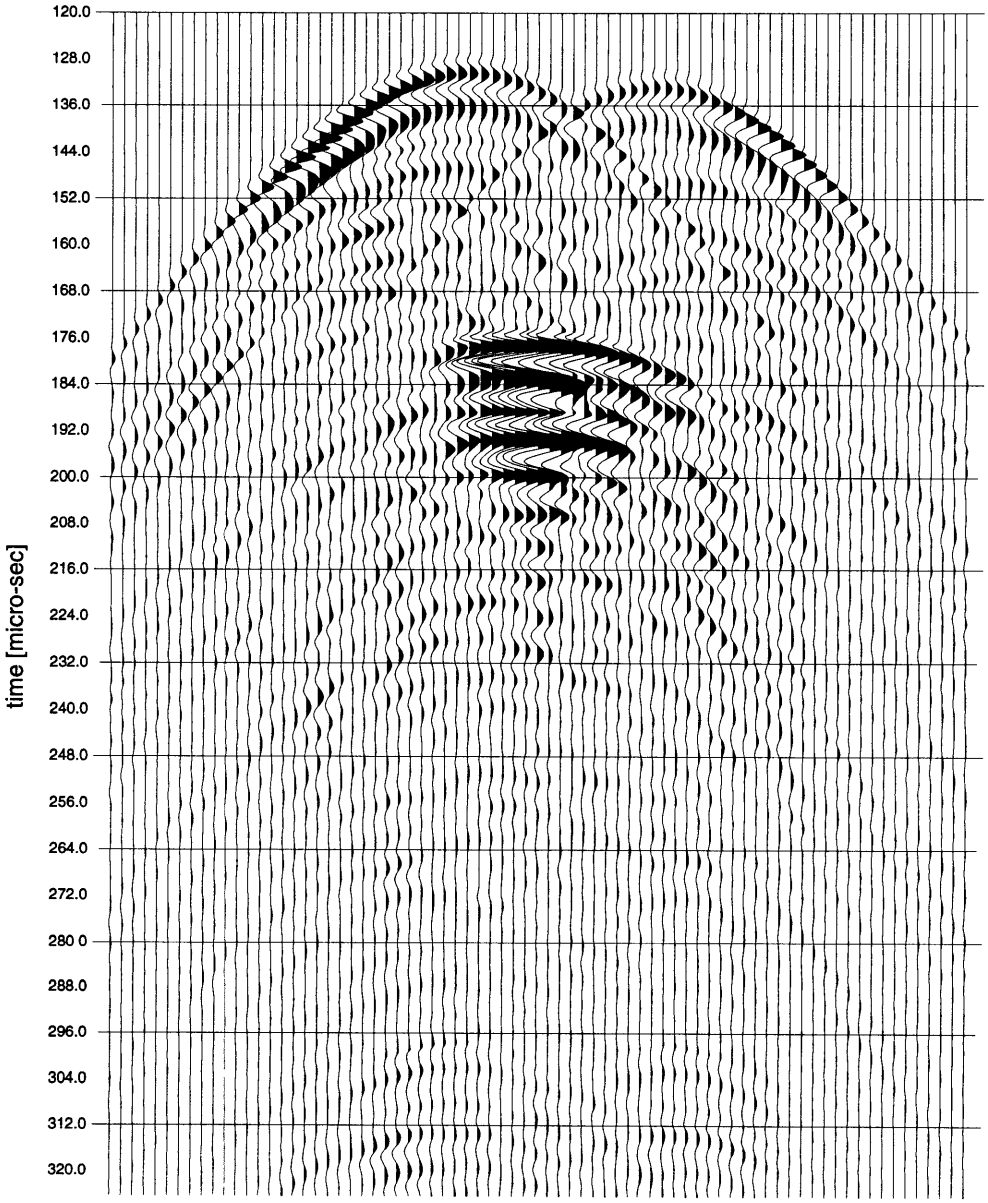

Figure 5-5: The seismogram for the syncline model defined in Figure 5-1 as measured in the ultrasonic watertank.

Figure 5-6: The seismogram for the anticline model defined in Figure 5-2 as measured in the ultrasonic watertank.

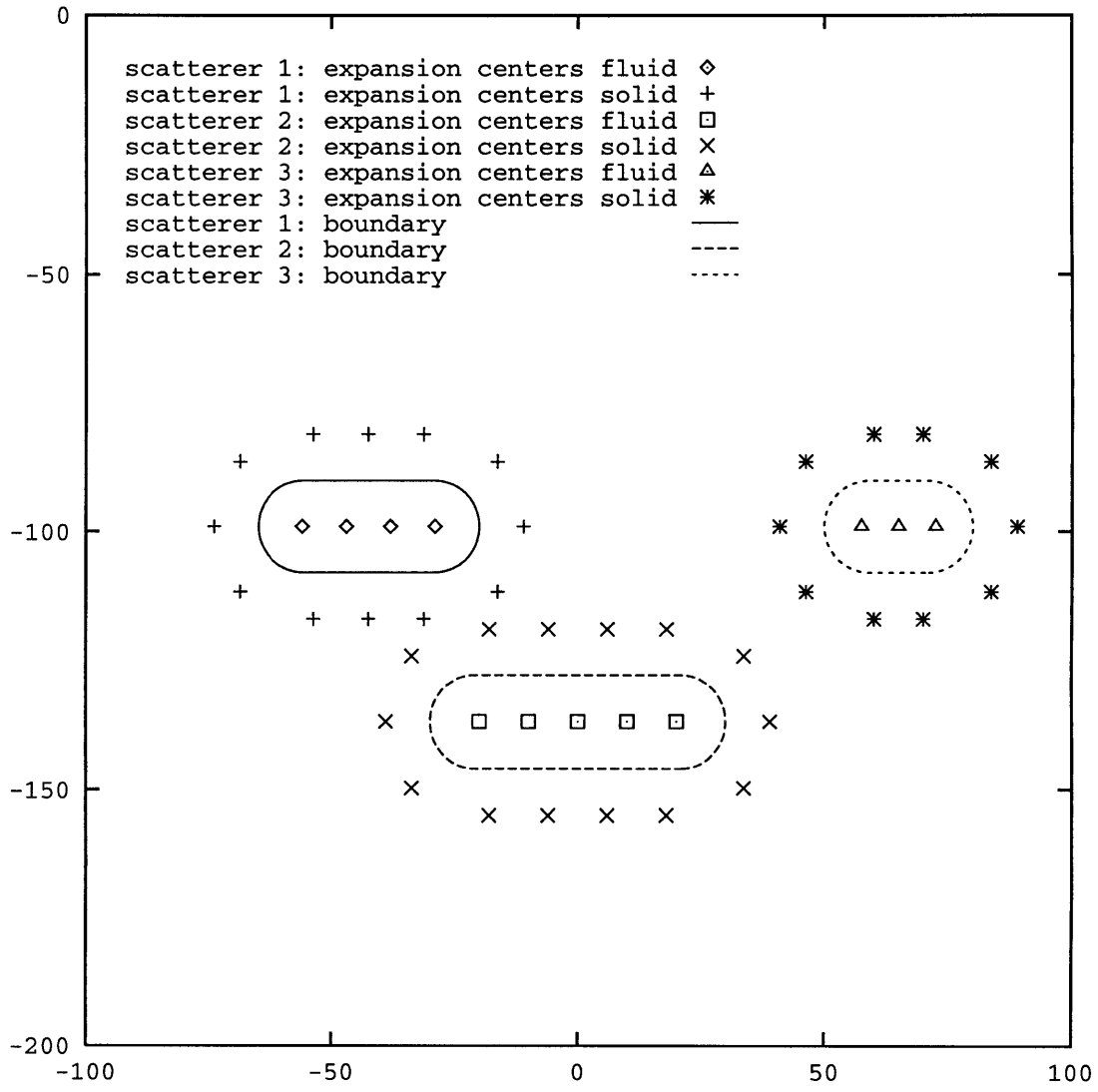

Figure 5-7: MMP discretization for the syncline model. Shown are the locations of the expansion centers for the multipoles. The multipoles inside the scatterers govern the wavefield in the fluid background. Multipoles are placed all around the scatterers to model the P- and S-waves on the inside. The discretization for the anticline model is the same but upside-down.

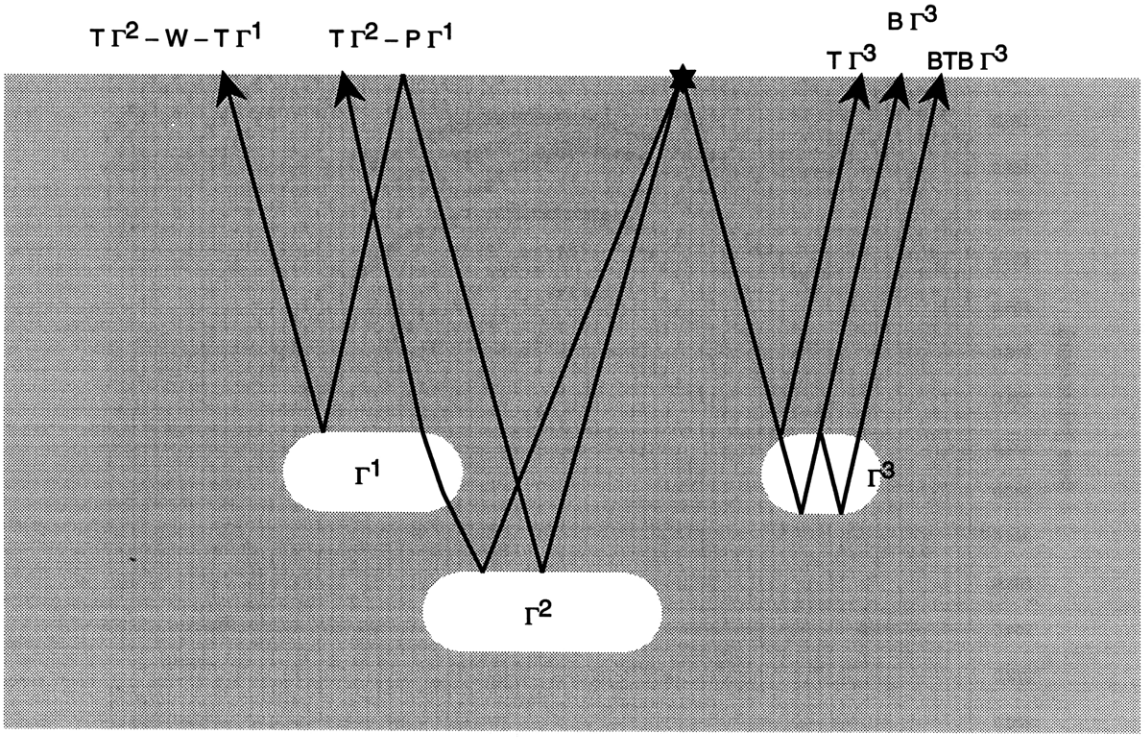

Figure 5-8: Notation used to label different events. The symbol 'T' denotes a reflection from the top of a scatterer, 'B' a reflection from the bottom, 'W' a reflection from the water surface, and 'P' a diffraction caused by the scatterer.

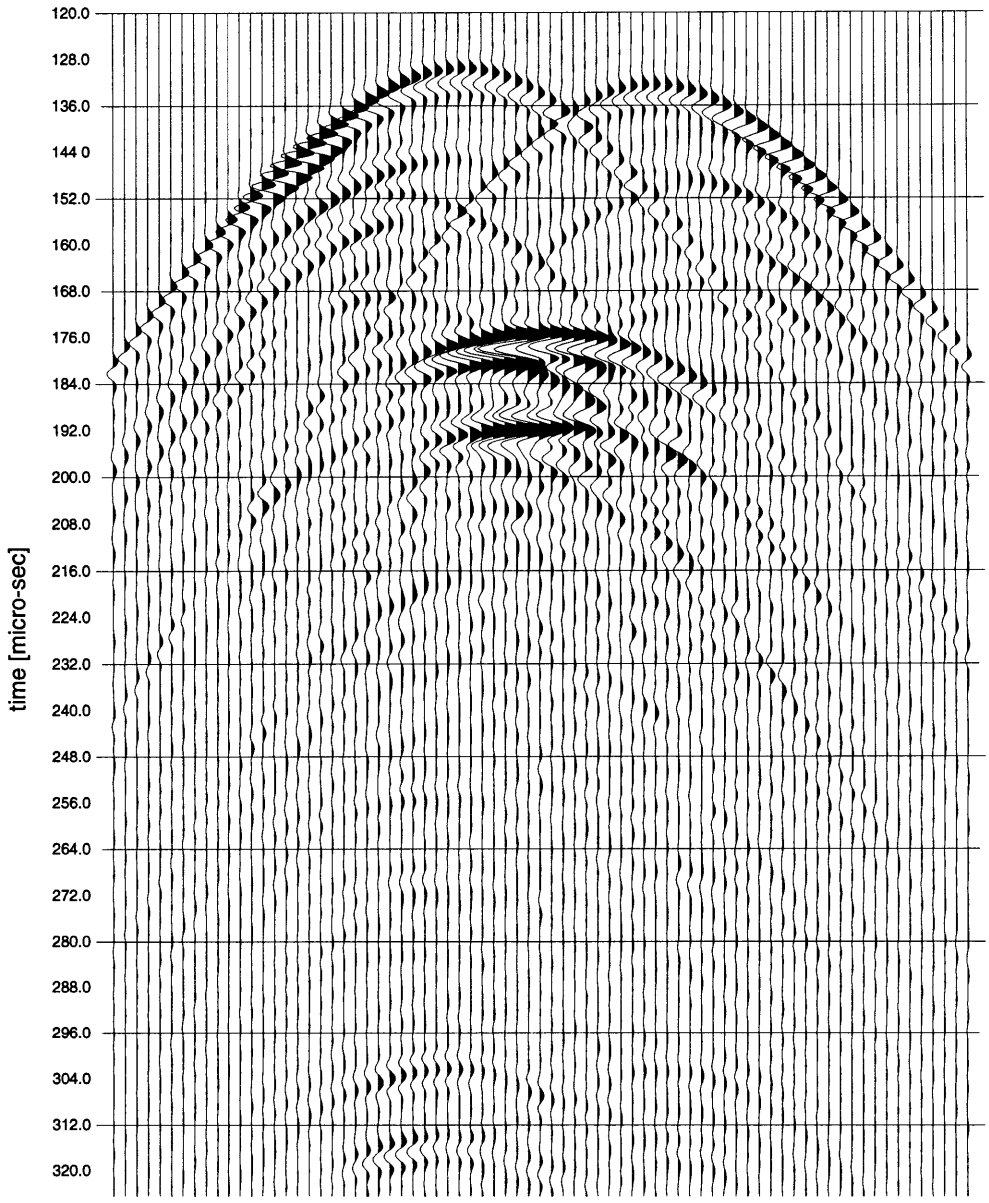

Figure 5-9: The seismogram for the syncline model (Figure 5-1) calculated by the MMP method.

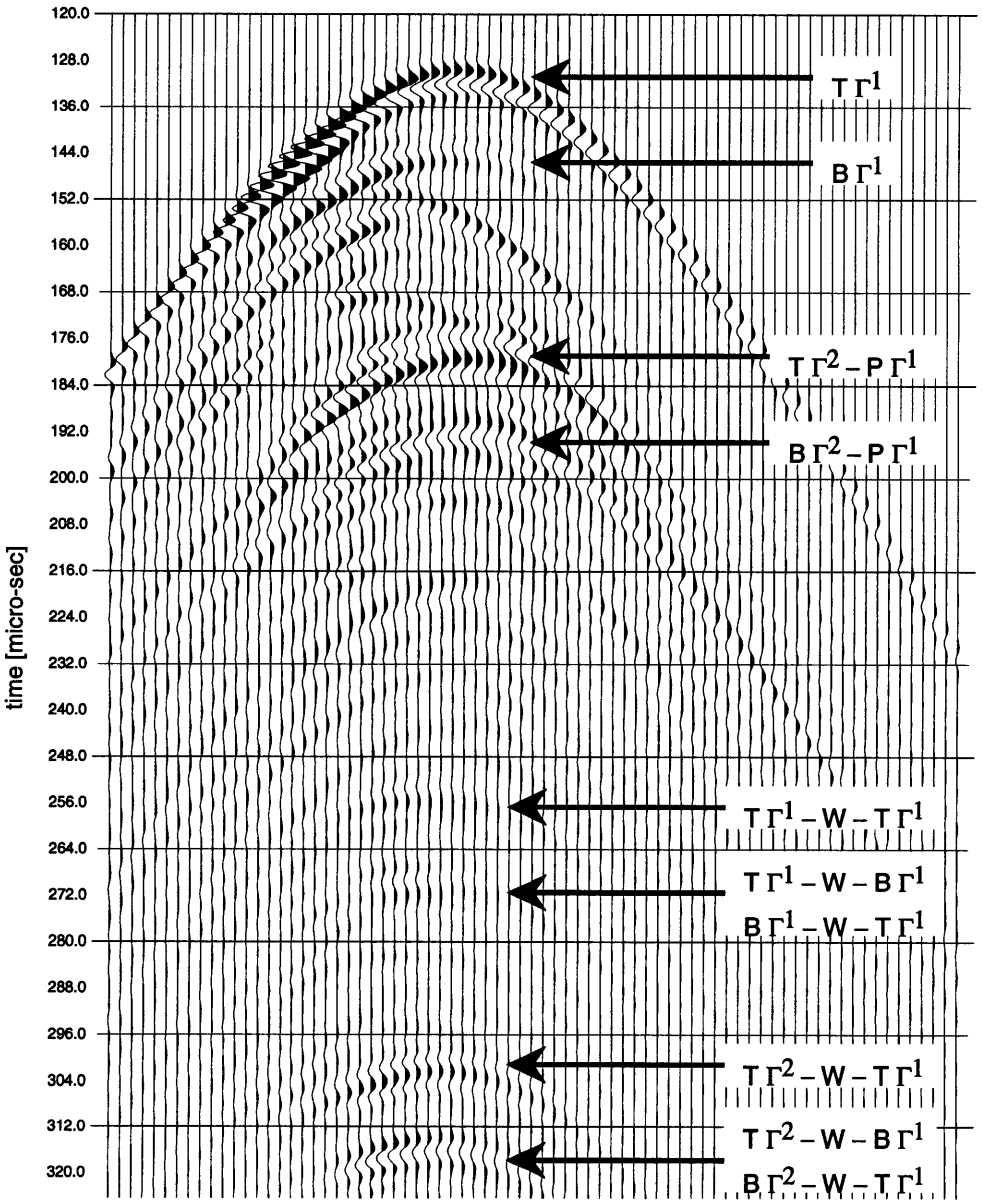

Figure 5-10: Syncline model: The scattered field emanated by Γ^1. The events around 180 μs are reflections originating at scatterer Γ^2 but passing through scatterer Γ^1. The events at 300 μs are reflections from Γ^2 bouncing between the surface and Γ^1. The notation used to label different events is defined in Figure 5-8.

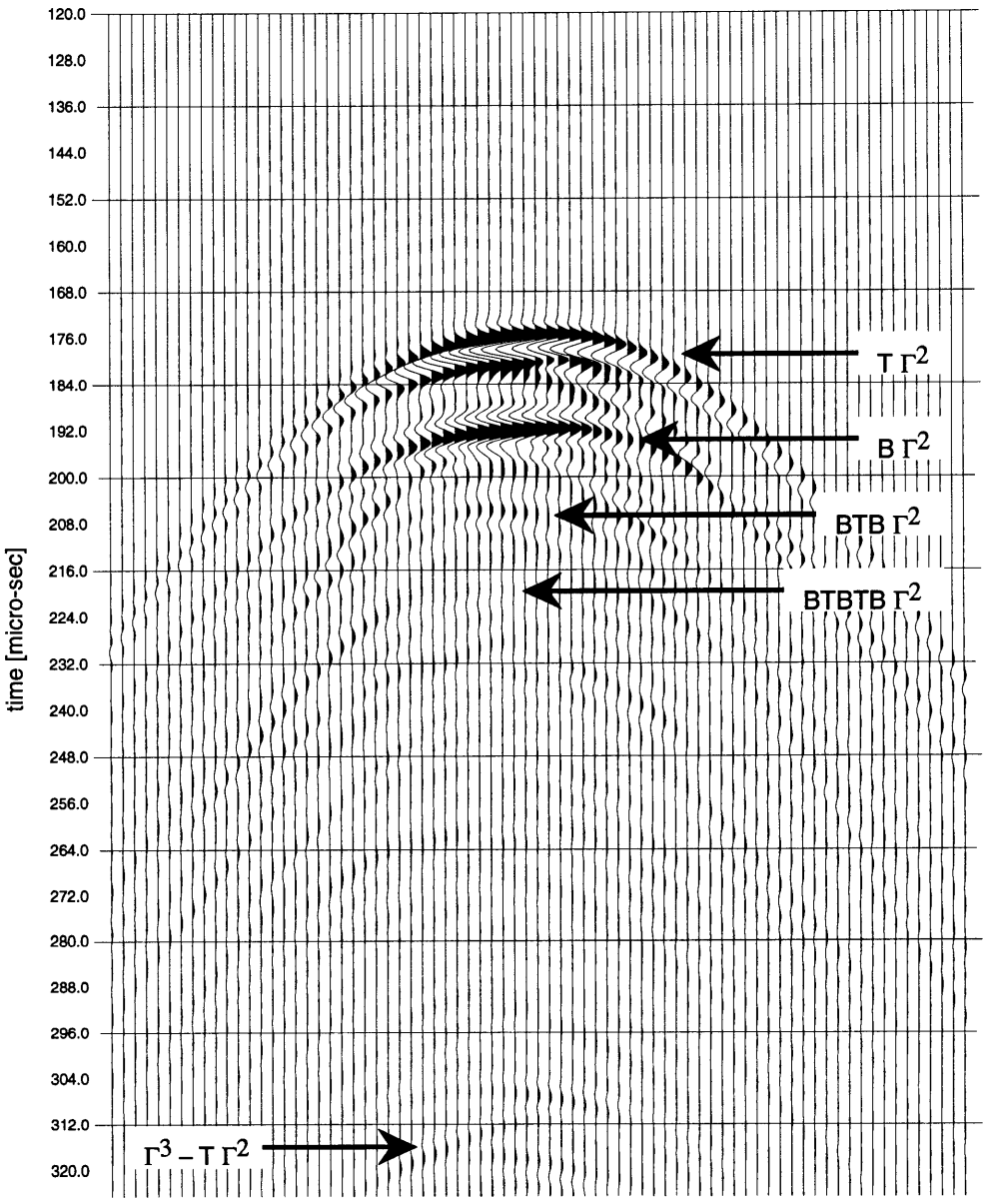

Figure 5-11: Syncline model: The scattered field emanated by Γ^2 into the fluid.

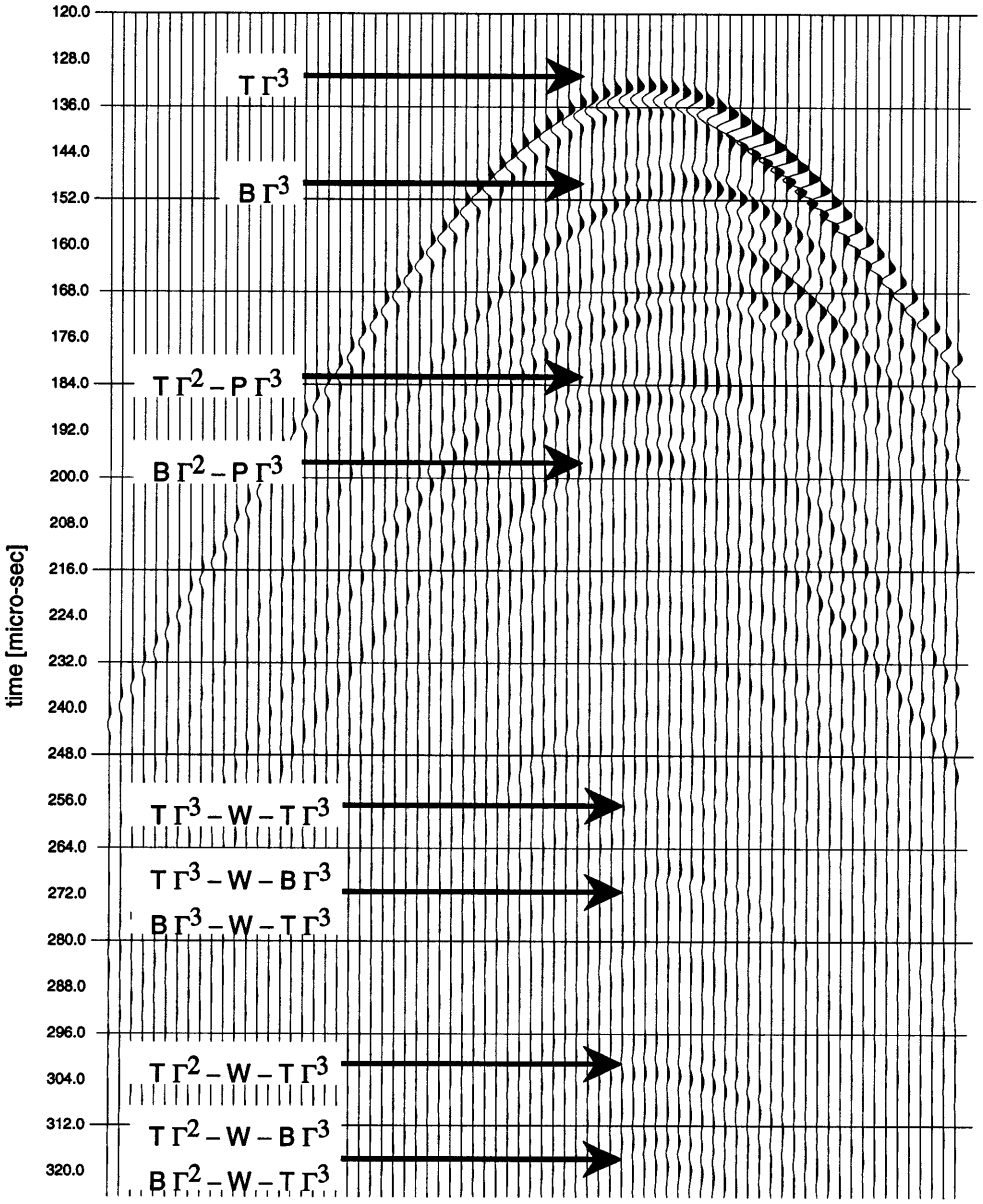

Figure 5-12: Syncline model: The scattered field emanated by Γ^3. The events around 180 μs are reflections from scatterer Γ^2 passing through scatterer Γ^3. The events at 260 μs are reflections from Γ^3 bouncing between the water surface and scatterer Γ^3. The events at 300 μs are reflections from scatterer Γ^2 bouncing between the surface and scatterer Γ^3.

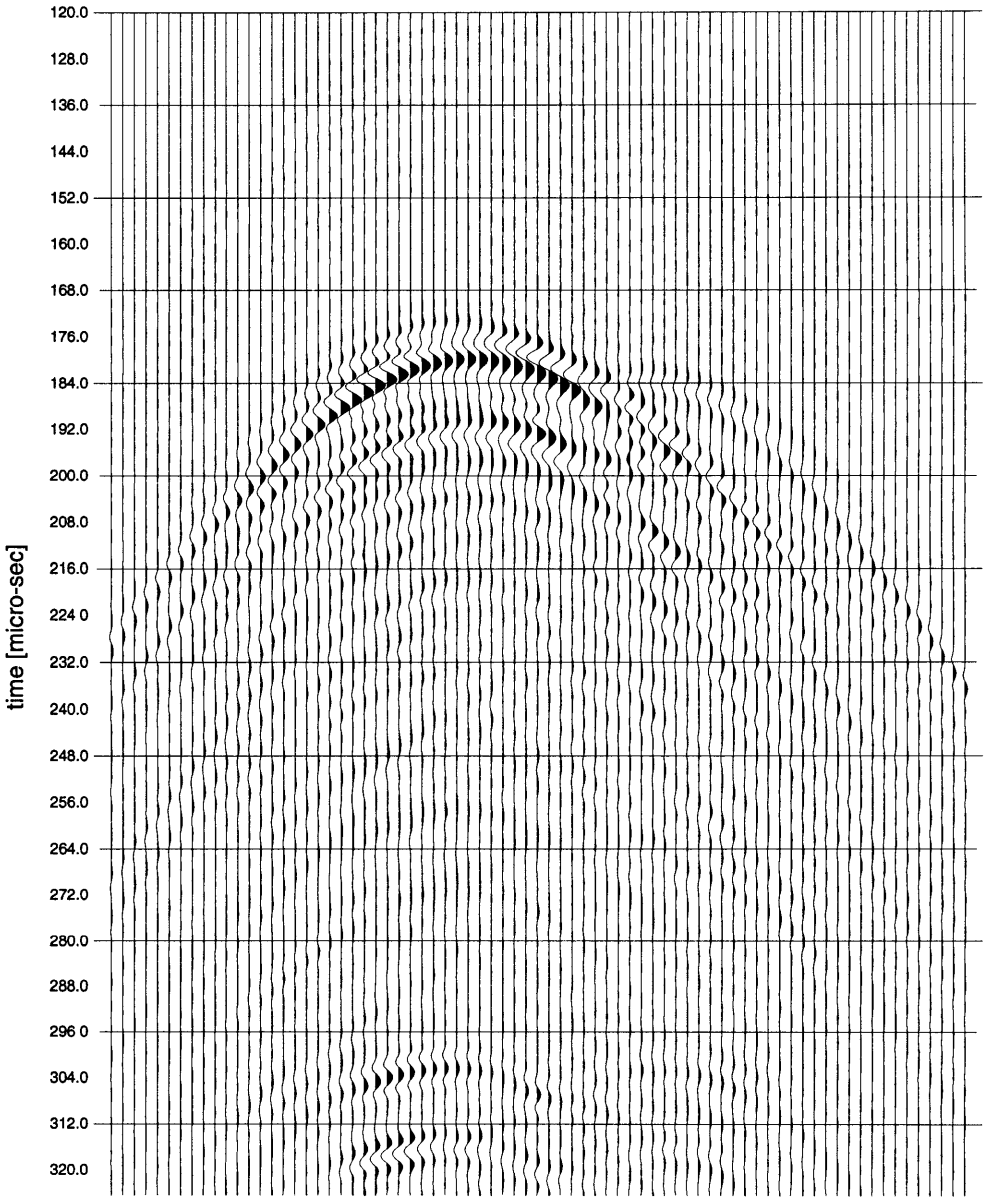

Figure 5-13: Syncline model: The residual field between the complete MMP solution (Figure 5-9) and the three scattered wavefields calculated for each rod separately.

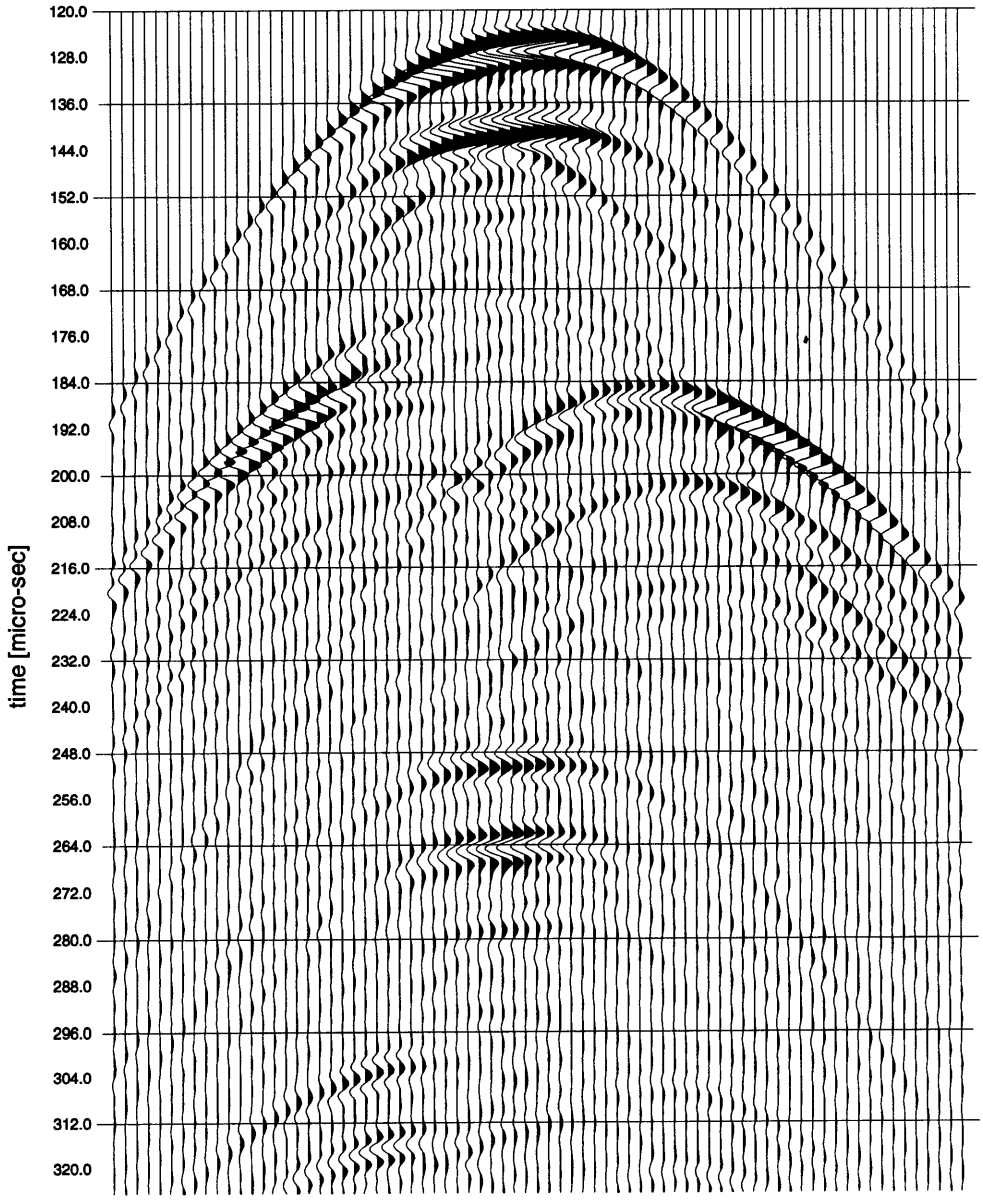

Figure 5-14: The seismogram for the anticline model defined in Figure 5-2 as calculated by the MMP method.

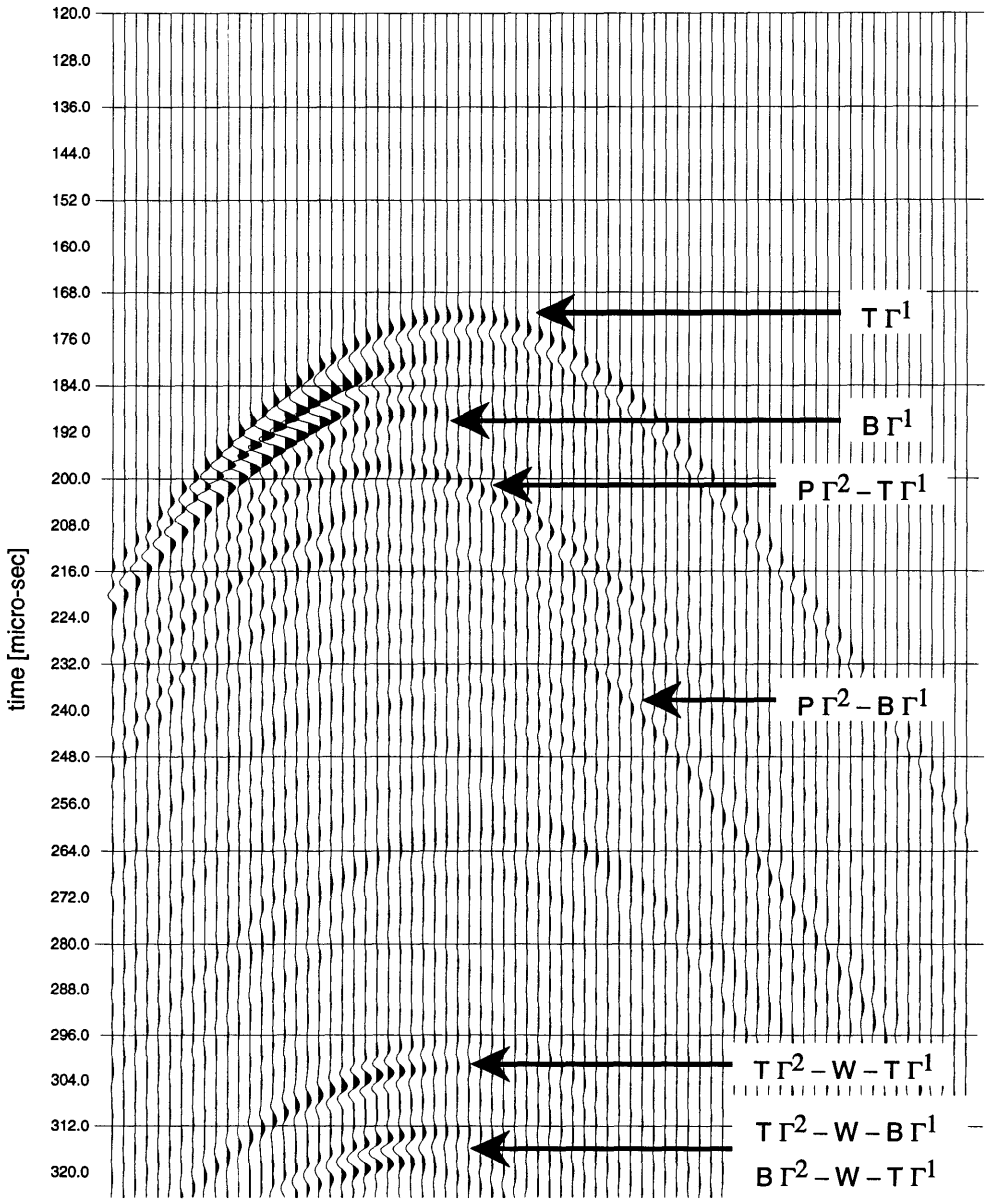

Figure 5-15: Anticline model: The scattered field emanated by Γ^1. The events at 300 μs are reflections from Γ^2 bouncing between the surface and scatterer Γ^1. The notation used to label different events is defined in Figure 5-8.

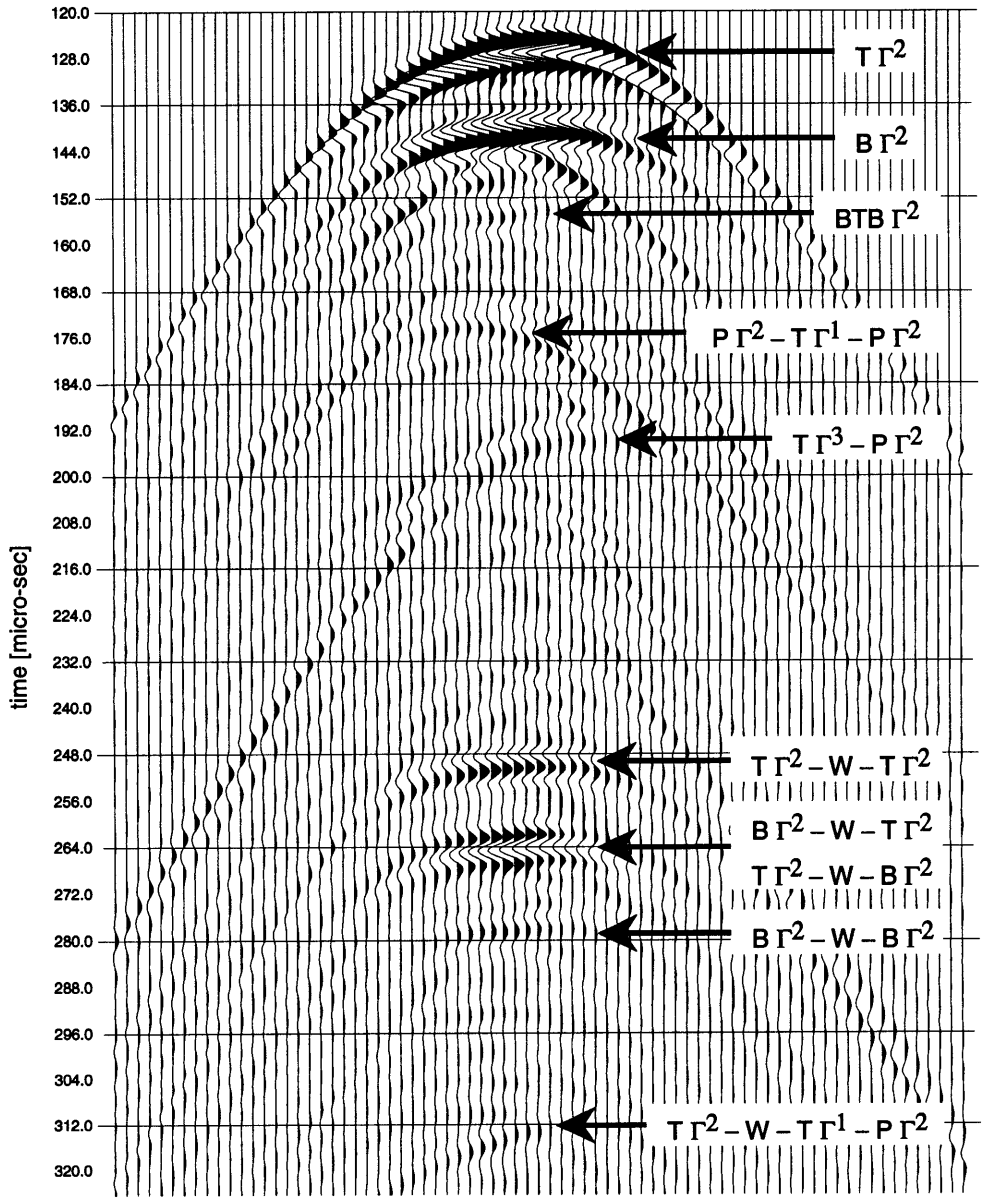

Figure 5-16: Anticline model: The scattered field emanated by Γ^2 into the fluid. The events at 170 μs and 190 μs are the reflections from Γ^1, respectively Γ^3, being transmitted through Γ^2.

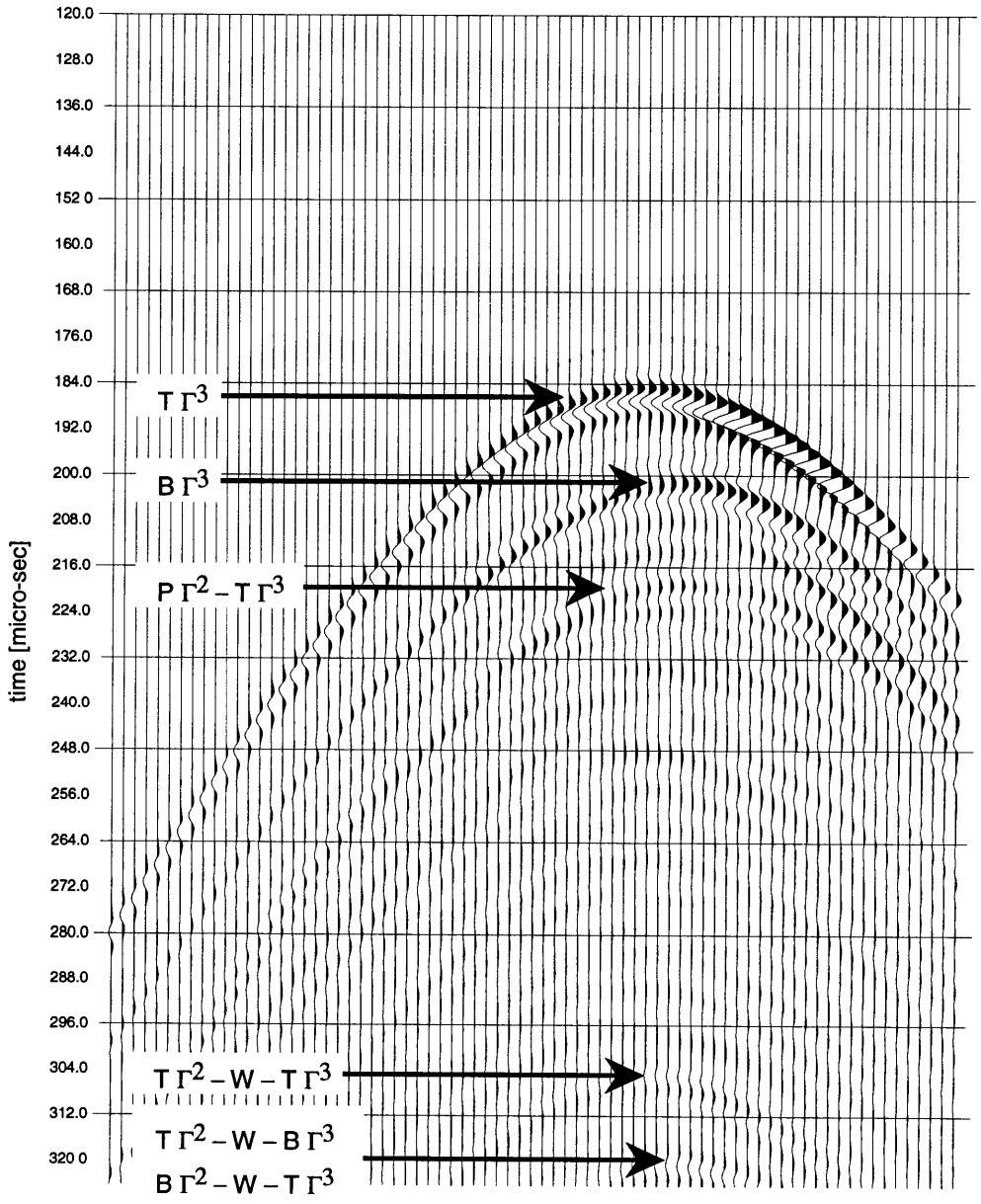

Figure 5-17: Anticline model: The scattered field emanated by Γ^3. The events at 300 μs are reflections from scatterer Γ^2 bouncing between the surface and scatterer Γ^3.

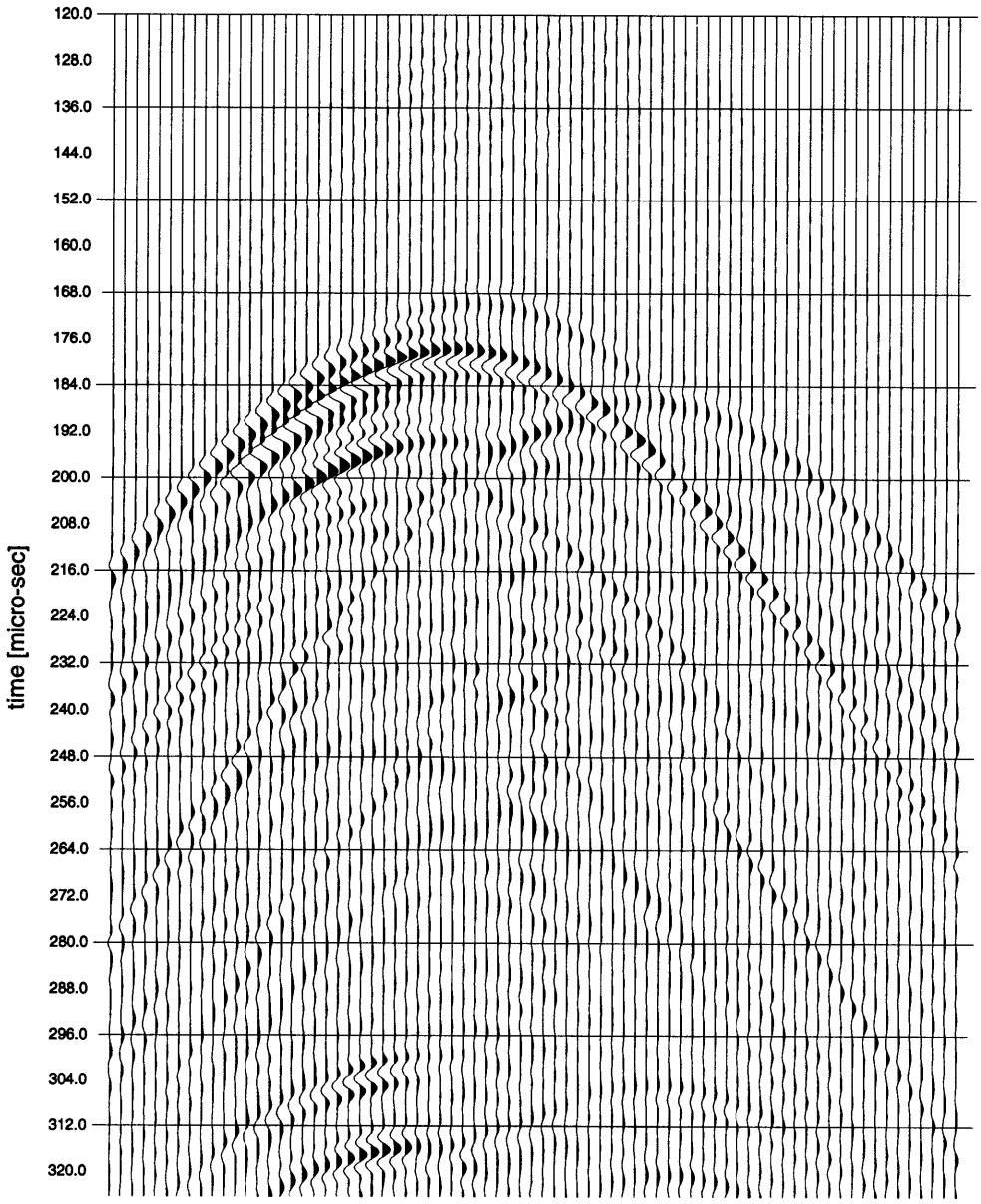

Figure 5-18: Anticline model: The residual field between the complete MMP solution (Figure 5-14) and the three scattered wavefields calculated for each rod separately.

Chapter 6

A Study of Near-Surface Scattering

Abstract

Seismic data acquired directly over near-surface limestone formations are commonly observed to be of inferior quality. One possible cause is scattering in the near-surface layer effecting this degradation. Postulating solution cavities in this layer, a numerical scattering scheme is constructed to study the effects of these very strong scatterers. Energy density and energy flux density are used to interpret the results of the forward modelling. Three different regimes of behaviors were seen. It is found that different frequency bands are affected differently by the presence of cavities in the near-surface. 'Low' frequencies are hardly affected. For 'medium' frequencies, complex interference patterns appear. Also, the cavities create waveguides. Finally for 'high' frequencies, the energy flux loses most of its spatial coherence.

6.1 Introduction

In many areas of the world, the nature of the local geology hinders reflection seismic exploration. Commonly, it is the presence of high-velocity layers in the near-subsurface which

makes it difficult to image deeper reflectors. Examples of such geologies are layers of basalt, carbonates or permafrost. The P-wave penetration problem often seems to occur when these high velocity layers are juxtaposed against much lower velocity materials. Reflections from depth are almost impossible to interpret on surface seismic data acquired in this region. One reason are strong reverberations due to energy trapped in zones of lower velocity (Pujol *et al.*, 1989). These reverberations may mask any deeper reflections present in the data. Also, the waves transmitted through the high velocity layer are subject to attenuation by wave absorption or by scattering at heterogeneities (Wu and Aki, 1985). But not only the P-wave, but also source-generated noises such as surface waves are strongly scattered, delayed by variable amounts and rendered incoherent. All this noise clouds the sought reflections even more (Pritchett, 1990). Mode conversion of both reflected and transmitted waves also becomes very efficient in all these situations. Pujol *et al.* (1989) and Papworth (1985) associated strong S-wave arrivals with $P \rightarrow S$ conversion at basalt surfaces encountered in land surveys. Finally in the near-subsurface or within waveguides such as a low velocity layer, body waves convert to surface waves and vice versa. All these different mechanisms render the wavefields less coherent, generate additional 'noise' and amplify source generated noise effects.

Conoco provided a data set acquired in West Texas over high-velocity carbonate formations. As examples, two shot gathers are shown in Figures 6-1 and 6-2. Both records are badly contaminated by 'noise'. The data processors found many problems to be associated with backscattered Rayleigh waves. In the present paper, we examine numerically how topography and near-surface heterogeneities such as cavities might cause the reported degradations.

6.2 West Texas Dataset

Conoco acquired the data set in West Texas over cretaceous formations (Mazzullo, 1978; Kettenbrink, 1983; Laroche, 1994). Unfortunately, not much more information has been released, yet. For example, neither the location nor the source- and receiver-patterns have

been disclosed. Figure 6-3 presents the elevation of the geophone and source stations relative to an unknown datum. Two distinct elevations can be seen: Elevations over 1750 ft are on mesas. Geomorphological experience indicates that mesas are built of hard formations. Structurally, mesas commonly correspond to uplifts or anticlines (Rice, 1977; Bloom, 1978). Typically, they are only covered by a very thin weathering layer because rocks broken from the outcrop tend to be carried toward lower elevations by rock falls, soil creep, and slope wash (Press and Siever, 1986). Contrarily, elevations below 1750 ft constitute valleys. Very likely, the valleys are filled with debris from the mesas. Geomorphological experience suggests that valleys form preferably in in softer formations and in regions of reduced elevation such as grabens or synclines (Bloom, 1978). Furthermore, weathering is much stronger in these mechanically weakened facies. All these elements contribute to a very heterogeneous near-surface layer.

Not surprisingly, seismic records shot over the valley region differ drastically from records acquired on a mesa. For example, the seismogram shown in Figure 6-1 was shot across the valley with the source located at station 1045. The other seismogram (Figure 6-2) is shot on top of the mesa with the source located at station 1153. One of the main differences is the appearance of the Rayleigh wave. The valley record (1045) contains some Rayleigh waves, especially for later arrival times and larger offsets. But it is neither a coherent nor a linear event. Contrarily in the mesa record (1153), the Rayleigh wave is the dominant feature. A minor difference is the appearance of the first break. In the valley record (1045), the first break is a fading event strongly affected by static shifts. In the mesa record (1153), the first break is a rather strong and very linear feature.

From the records shot on top of the mesa, we estimated the seismic wave velocities of the surface layer: the P-wave velocity $\alpha = 4630\,\mathrm{m/s}$, the S-wave velocity $\beta = 2122\,\mathrm{m/s}$, and the Rayleigh velocity $c = 1990\,\mathrm{m/s}$. The P- and the Rayleigh velocity are directly extracted from the records, while the S-velocity is inferred from the Rayleigh function for a uniform,

elastic halfspace (Aki and Richards, 1980).

$$\frac{c^2}{\beta^2}\left[\frac{c^6}{\beta^6} - 8\frac{c^4}{\beta^4} + \left(24 - 16\frac{\beta^2}{\alpha^2}\right)\frac{c^2}{\beta^2} - 16\left(1 - \frac{\beta^2}{\alpha^2}\right)\right] = 0 \tag{6.1}$$

This set of velocities yields a Poison's ratio σ of 0.36. For the density ρ, we use an average limestone density of $2600\,\mathrm{kg/m^3}$ (Clark, 1966). Also used is some attenuation with the quality factors $Q_\alpha = 15$ and $Q_\beta = 12$ (Toksöz *et al.*, 1979). The center frequency of the propagating pulse is around 30 Hz for early arrivals.

Conoco's data processors reported serious problems with surface statics, the valley fill and the topography. Near-surface limestone layers are commonly highly heterogeneous, despite their massive appearance. Although the matrix velocity is rather high, these layers often contain a substantial amount of pore space which may contain low velocity materials such as gases, liquids, or soil which contains fluids in itself. For compressional waves, the velocity of the composite material decreases markedly in going from dense rock to porous rock, and from liquid pore fluid to porous rock with free gas or air (White, 1975; Mavko and Nur, 1979). A compressional wave propagating through these layers will experience variable delay depending upon the amount of pore space along its path and the percentage of free gas or air contained in it (Domenico, 1976). Moreover, the compressional waves will be scattered due to variation in the velocity and density of these layers ranging from dense rock to quite porous rock containing gas or air. A coherent wave emanating from the source will be disrupted when it reaches the massive but inhomogeneous limestone layers (Wu and Aki, 1985; Roth and Korn, 1993; Muijres and Herman, 1994). A reflected wave propagating from the target region to the receivers will be even less coherent after passing through the surface layer a second time. Also, source-generated noise will be scattered, will be delayed by variable amounts, and will be rendered less coherent. All this noise clouds the desired reflections even more. Both effects are strongly scale dependent (Mukerji *et al.*, 1995).

Interestingly, Conoco's processors considered the main problem to be scattered Rayleigh waves clouding the reflections. But suppressing specific waves is very problematic. First, the surface layers have relatively high velocities which make it difficult to suppress source

generated noises without suppressing the desired reflections as well (Pritchett, 1990). On high velocity surfaces, the angle of arrival of reflections at the surface at moderate to long offsets is larger, which shortens the apparent horizontal wavelengths of the reflections relative to the wavelengths of some source generated noise. Therefore, wavelength filters such as source patterns or geophone arrays during the acquisition or FK-filtering during the processing are less capable of separating reflected signals from noise. The contamination appears to be worst in the mesa region. Thus, we will focus on records shot on the mesa such as record 1153. Details of three seismograms (1123, 1153, 1183) shot on top of the mesa are presented in Figures 6-4 to 6-6. All three records exhibit backscattered events. Some events can be identified as Rayleigh waves by their velocity. Different scattering mechanisms could be responsible for the scattered wavefields as the ones shown in Figures 6-4 to 6-6: (1) strongly heterogeneous layers of debris, (2) topography, or (3) heterogeneities such as cavities. Robertsson *et al.* (1996) assumed strongly heterogeneous surface-layers forming waveguides. Using a finite difference method to examine the effect, he obtained results which look very much like the present data. The mechanism nicely explains the seismograms shot in the valleys filled with debris. But for the mesas, the mechanism has to be discarded for geomorphological reasons (Bloom, 1978). A buildup of such a surface layer on the mesa is just too unlikely.

Irregular topography is well known to cause significant effects of amplification and deamplification of propagating waves at the irregularity itself and in a substantial neighborhood around it (Sanchez-Sesma and Campillo, 1991). Rough surface topography often converts wavemodes, generating strong backscattered waves (Jih *et al.*, 1988; Tessmer *et al.*, 1992). But in the present case, topography can be discarded as the major scattering mechanism for records shot on top of the mesas. While the station spacing is 110 ft, the maximal surface undulation is less than 100 ft as can be seen in Figure 6-3. Unless the spatial sampling of the topography is grossly aliased, the topography is just too smooth to yield strong contaminations of the wavefields. To demonstrate the effect of the topography, we use the finite difference method (Jih *et al.*, 1988) to calculate the seismograms 1123, 1153 and 1183. The main feature in the presented seismograms is the Rayleigh wave. Hence, a compact Rayleigh

wave-packet of 30 Hz center frequency is used as incident wavefield. Initially, the packet propagates in the direction of increasing station numbers. Interactions of the propagating wave packet with the rough surface will generate scattered Rayleigh- and body waves. The seismograms are presented in Figures 6-7 to 6-9.

The amount of scattered energy correlates with the surface roughness. Record 1123 is shot across the rough part of the mesa. Compared to the other finite difference solutions, it contains the largest amount of 'noise' (Figure 6-7). Contrarily, there is very little topography variation for the first 56 geophone stations of record 1183. There are only very few scattered events visible in Figure 6-9. It is very instructive to look at a few snapshoots obtained from the finite difference simulations. They are presented in Figures 6-10 to 6-12. The initial Rayleigh packet is the most prominent feature in all snapshots. Although there are body waves generated at slopes, most of the remaining events correspond to scattered Rayleigh waves.

Clearly, the topography contributes to the scattered energy. But the flavor of the simulations (Figures 6-7 – 6-9) is very different from the corresponding shot records (Figures 6-4 – 6-6). Although the rough topography induces backscattered Rayleigh waves as well as forward scattered P-waves, it does not generate all the events propagating with P- and Rayleigh wave velocity both in forward and backward direction. These simulations suggest that topography is not the predominant scattering mechanism in the present dataset.

The last mechanism to be considered is strong heterogeneities such as vugs, joints, or cavities which are encountered frequently in limestone (Bögli, 1980; Jennings, 1985). Commonly, there are clusters of these features aligned along fault planes or structural boundaries (Bögli, 1980). Unless the diameter of these cavities is a sizeable proportion of the seismic wavelength, the surface layers can conveniently be described by bulk parameters for velocity, density and Poisson's ratio (Vandenberghe *et al.*, 1986). Then, effective media theories, e.g. the Kuster and Toksöz model (1974), can be used to relate interacting heterogeneities to bulk material properties. But for larger heterogeneities such as solution cavities, other approaches have to be chosen which allow to model individual heterogeneities.

6.3 Theoretical Modelling

Not directly addressing near-surface cavities, Robertsson *et al.* (1996) used a finite difference method to examine the effect of heterogeneities in the near-surface. Blonk *et al.* (1994,1995) used Born scattering theory to construct a model of the surface layer and the resulting scattered surface waves. Interestingly, they never claimed to find the correct model. Instead, they construct an equivalent model which causes the same effects. Integral equation based methods are alternative approaches in the frequency domain. Muijres and Herman (1994) described a fully deterministic method to compute the wavefield for a medium containing a large number of small cracks. Unfortunately, the scheme was only worked out for cracks embedded in an acoustic fullspace.

Instead, we will use the scheme derived in Appendix C. The advantage of this scheme is that we have a scattered wavefield for each individual scatterer. Furthermore, the wavefield is automatically decomposed into direct waves, waves reflected and mode converted by the free surface, and surface waves for both P- and S-phases. Assuming we have D cavities, the displacement $\mathbf{u}^s$ of the scatterered wavefield can be expressed as

$$\mathbf{u}^s(\mathbf{x}) = \sum_{d=1}^{D} \sum_{n=-N}^{+N} a_{dn}\mathbf{u}_n^{\Phi}(\mathbf{x},\mathbf{x}_d) + b_{dn}\mathbf{u}_n^{\Psi}(\mathbf{x},\mathbf{x}_d)\,, \tag{6.2}$$

where the functions $\mathbf{u}_n^{\Phi}(\mathbf{x},\mathbf{x}_d)$ and $\mathbf{u}_n^{\Psi}(\mathbf{x},\mathbf{x}_d)$ are given in (B.23) and (B.24). These functions contain the asymptotic wavefield for compressional and rotational multipole sources of order n located at $\mathbf{x}_d$ in the presence of a free surface. Direct wave, the reflection, the conversion, and the first Rayleigh surface mode are all included in these expressions. The highest order N of the virtual multipole sources is 5. Instead of using (6.2), it is easier to rename the expansions functions for P-sources $\mathbf{u}_n^{\Phi}(\mathbf{x},\mathbf{x}_d)$ and S-sources $\mathbf{u}_n^{\Psi}(\mathbf{x},\mathbf{x}_d)$ to yield a single expansion function $\mathbf{u}_m(\mathbf{x},\mathbf{x}_d)$ hiding the type of wave and order of the source. Thus, we obtain

$$\mathbf{u}^s(\mathbf{x}) = \sum_{d=1}^{D} \sum_{m=1}^{M} a_{dm}\mathbf{u}_m(\mathbf{x},\mathbf{x}_d)\,. \tag{6.3}$$

In analogy to (6.3), we also expand the scattered stress tensor as

$$\boldsymbol{\sigma}^s(\mathbf{x}) = \sum_{d=1}^{D} \sum_{m=1}^{M} a_{dm} \boldsymbol{\sigma}_m(\mathbf{x}, \mathbf{x}_d)\,, \tag{6.4}$$

where $\boldsymbol{\sigma}_m(\mathbf{x}, \mathbf{x}_d)$ is the stress tensor associated with the displacement function $\mathbf{u}_m(\mathbf{x}, \mathbf{x}_d)$. This allows us to use the projection method described in Chapter A.4.2 to obtain equations for the yet unknown weighting coefficients a_{dm}. The exact scheme is given in Appendix C.

As additional quantities, we also define the time averaged Poynting vector (Ben-Menahem and Singh, 1981; Frisk, 1994) and the energy density (Aki and Richards, 1980; Ben-Menahem and Singh, 1981) of the wavefields. The instantaneous Poynting vector $\mathbf{S}(\mathbf{x}, t)$ is defined as

$$\mathbf{S}(\mathbf{x}, t) = \Re e\, \boldsymbol{\sigma}(\mathbf{x}, t) \cdot \Re e\, \dot{\mathbf{u}}(\mathbf{x}, t) \tag{6.5}$$

where the dot denotes the derivative with respect to time. Keeping in mind that we neglected the common factor $e^{i\omega t}$ in all the previous expressions, we easily obtain the time averaged Poynting vector $\mathbf{S}(\mathbf{x})$:

$$\begin{aligned} \mathbf{S}(\mathbf{x}) &= \big\langle \mathbf{S}(\mathbf{x}, t) \big\rangle \\ &= \frac{1}{T} \int_0^T \mathbf{S}(\mathbf{x}, t)\, dt \\ &= \frac{i\omega}{4} \big(\boldsymbol{\sigma}^*(\mathbf{x}) \cdot \mathbf{u}(\mathbf{x}) - \boldsymbol{\sigma}(\mathbf{x}) \cdot \mathbf{u}^*(\mathbf{x}) \big) \end{aligned} \tag{6.6}$$

where the superscript * denotes the complex conjugate. The Poynting vector $\mathbf{S}(\mathbf{x})$ is associated with the direction of energy flux. Its magnitude is the energy flux density. Thus, we can use it as a measure of how much energy flows in a given direction. Plotted as a vector field, it yields an idea of how coherent the scattered wavefield is. We also define the energy

density $E(\mathbf{x})$ as

$$\begin{aligned} E(\mathbf{x}) &= \frac{\rho(\mathbf{x})}{2}\, \dot{\mathbf{u}}(\mathbf{x}) \cdot \dot{\mathbf{u}}^*(\mathbf{x}) + \frac{1}{2}\, \boldsymbol{\sigma}(\mathbf{x}) : \boldsymbol{\epsilon}^*(\mathbf{x}) \\ &= \rho(\mathbf{x})\, \dot{\mathbf{u}}(\mathbf{x}) \cdot \dot{\mathbf{u}}^*(\mathbf{x}) \\ &= \omega^2 \rho(\mathbf{x})\, \mathbf{u}(\mathbf{x}) \cdot \mathbf{u}^*(\mathbf{x}) \end{aligned} \tag{6.7}$$

where $\boldsymbol{\epsilon}(\mathbf{x})$ is the strain tensor due to the displacement field $\mathbf{u}(\mathbf{x})$. Assuming that the total energy density is evenly split into kinetic- and strain-energy density (Aki and Richards, 1980), we need only one term. Hence, we choose the kinetic one which is easier to evaluate. The energy density $E(\mathbf{x})$ is a useful measure because it shows where the energy is concentrated.

6.4 A Numerical Study of Scattering

Four models of the mesa scenario are calculated, with the models defined in Table 6.1. All models consist of one or two rows of cavities embedded in limestone. All cavities have the same elliptical geometry. They are 4 m wide and 3 m high. They are located on a perturbed grid to ensure that no two cavities overlap. Finally, the source is assumed to be an explosive line source 5 m below the free surface.

Source and receivers will be the same for all four models. The vertical displacements are measured 1 m and 150 m below the free surface. Figure 6-13 shows the seismic records for these two source – receiver geometries without scatterers. In fact, these are records of the incident field used in all four models. The dominant event in both cases is the Rayleigh wave. As expected, amplitude and center frequency of the Rayleigh wave are greatly reduced for the seismogram measured at a depth of 150 m. Also, the P-wave splits into two events due to the free surface. The later event arrives about 100 ms after the first break. Additional insight into the scattering phenomena will be gained by looking at the Poynting vector $\mathbf{S}(\mathbf{x})$ derived in (6.6) and the energy density $E(\mathbf{x})$ as defined by (6.7). The quantities $\frac{\mathbf{S}(\mathbf{x})}{|\mathbf{S}(\mathbf{x})|} \log |\mathbf{S}(\mathbf{x})|$ and $\log E(\mathbf{x})$ are shown for 3 different frequencies (10 Hz, 50 Hz,

and 120 Hz) in Figures 6-14, 6-15, and 6-16. While the vectors show the scaled Poynting vector $\mathbf{S}(\mathbf{x})$, the grayscale denotes the scaled energy density $E(\mathbf{x})$ where bright levels correspond to high energy densities. The wiggling of the Poynting vectors is an interference effect of the direct P-wave, the reflected P-wave, the converted S-wave, and the Rayleigh wave along the surface. A comparison with the discrete wave-number integration (Bouchon and Aki, 1977) showed that the wiggling is not an artifact of the asymptotics defined in (B.23) and (B.24). Clearly, the free surface changes the energy density dramatically. Instead of rotational symmetry around the source, the energy is concentrated in two lobes.

In Model 1, only one row of cavities about 30.0 ± 15.0 m below the surface is present. Figure 6-17 shows the vertical displacement component of the seismograms 1 m and 150 m, below the surface. For the shallow seismogram, the scatterers emit mainly Rayleigh waves as can be seen from the velocities of the scattered events. These events emerge from the direct P-wave. Thus, it is the direct P-wave which acts as the source and not the Rayleigh wave. A comparison with the seismogram 6-13a, containing only the incident field, shows that the presence of the scatterers strongly affects the amplitude decay of the first break. For the seismogram measured at 150 m depth, the scattered field consists of the direct P-wave scattered mainly into P-waves. The diffraction hyperbolas of the forward scattered waves even merge with the direct P. As a comparison with the incident field in Figure 6-13b shows, the scattering dramatically enhances the second P-wave arriving 100 ms after the first break. Altogether, the coherence and crispness of the incident field shown in Figure 6-13b is greatly reduced due to these cavities close to the surface. Figure 6-18 shows $\mathbf{S}(\mathbf{x})$ and $E(\mathbf{x})$ for the scattered and the total field in Model 1 at a frequency of 10 Hz. Although the scattered field (Figure 6-18a) has a very distinct appearance, the difference between incident field in Figure 6-14 and the total field in Figure 6-18b is minimal. The waves are hardly affected by the cavities for a frequency this low. Increasing the frequency to 50 Hz and 120 Hz yields a different picture. Figures 6-19 and 6-20 show $\mathbf{S}(\mathbf{x})$ and $E(\mathbf{x})$ for these higher frequencies. Especially for 50 Hz, relevant amounts of energy begin to be entrapped between scatterers and the free surface (Figure 6-19). Also, minor amounts of energy cling to and around the scatterers. For 120 Hz finally, the energy flux $\mathbf{S}(\mathbf{x})$ is strongly affected

by the presence of the scatterers, as a comparison of the incident field (Figure 6-16) with the total field in Figure 6-20b shows.

Especially for higher frequencies, large amounts of scattered energy appear behind the scatterers. The reason lies in the radiation patterns of the scatterers. To show these patterns, we perform a numerical experiment. An elliptical cavity with an aspect ratio of 4 : 3 is illuminated by a planar P-wave propagating along the major principal axis. A schematic is shown in Figure 6-21. Using the MMP method (Chapter 3), we calculate the scattered energy at a distance of 30 m from the center of the ellipse. Then, the experiment is repeated for P-waves propagating along the minor principal axis as well as for S-waves propagating along the major or the minor principal axis. All four cases are performed with three different frequencies: 10 Hz, 50 Hz, and 120 Hz. For 10 Hz (Figure 6-22), we basically obtain a dipole pattern for the P-waves and a quadrupole pattern for the S-waves. Increasing the frequency to 50 Hz changes the patterns dramatically (Figure 6-23). For incident P-waves, energy begins to scatter in directions diagonal to the incident wave. For incident S-waves, energy scatters in directions perpendicular to the incident wave. For 120 Hz, incident P-waves scatter perpendicular to the direction of incidence (Figure 6-24). Incident S-waves scatter mainly into two directions: perpendicular to the incident field and along the incident field. These scattering patterns show that P-waves are more likely to generate high energy densities in front of the cavities. Contrarily, S-waves scatter mainly in directions perpendicular and along the incident field. Thus, incident S-waves are more likely to generate the higher energy densities behind the cavities.

In Model 2, only one row of cavities about 85.0 ± 15.0 m below the surface is present. Figure 6-25 presents the vertical displacement component of the seismograms 1 m and 150 m below the surface. In contrast to Model 1, the scatterers are located too deep to induce Rayleigh waves. All the scattered fields are propagating with the P-wave velocity. Also, the amplitudes of the scattered fields are reduced dramatically compared to Model 1 (Figure 6-17). Although Model 2 induces a strong scattered field (Figure 6-26a) at 10 Hz, the total field (Figure 6-26b) is hardly affected as a comparison with the incident field (Figure 6-14) shows. This contrasts strongly with the effect of the scatterers at 50 Hz (Figure 6-27).

Especially at larger offsets, the scatterers trap enough energy in between them to change the energy balance as compared to the unperturbed incidence field (Figure 6-15). An interesting effect is the appearance of an interference pattern. Spots of higher energy begin to show up between the scatterers and the free surface as well as below the scatterers. These spots also affect the Poynting vector $\mathbf{S}(\mathbf{x})$. Especially for larger offsets, the energy is not flowing straight away from the source. Instead, a rather complex flow pattern emerges. These effects become even more pronounced for 120 Hz. As shown in Figure 6-28b, the two lobes of the original source pattern (Figure 6-16) dissolve into streaks of higher energy and a cell-like arrangement of energy fluxes.

Model 3 contains 2 rows of cavities. As evident from the seismogram (Figure 6-29a) measured 1 m below surface, the scatterers induce both P- and Rayleigh-waves. Compared to Model 1 (Figure 6-17a), the regularity of the amplitudes of the first break is strongly reduced. As in the prior models, the presence of the scatterers hardly affects the Poynting vector $\mathbf{S}(\mathbf{x})$ or the energy density $E(\mathbf{x})$ at 10 Hz as evident from Figure 6-30b. However at 50 Hz, a complex interference pattern emerges for the scattered energy density presented in Figure 6-31a. As $E(\mathbf{x})$ for the total wavefield in Figure 6-31b shows, the interactions of scatterers and the free surface manifest themselves by a waveguide just below the free surface. Finally for the high frequency (120 Hz), the scatterers destroy the regular energy flux pattern of the incident field (Figure 6-16) completely as shown in Figure 6-32b.

For Model 4, all the observations made for Model 3 still hold. The main difference between Models 3 and 4 is that the effects are much more pronounced for the later case. The seismograms are shown in Figure 6-33. The presence of twice as many scatterers manifests itself with larger amplitudes and consistency of the individual events. As expected, the seismograms of Model 4 are also much 'noisier' than for Model 3. The total field at 50 Hz is shown in Figure 6-35b where the waveguide found in Model 3 turns up even stronger.

6.5 Discussion and Conclusions

Although the size of the cavities are on the large side, the observable effects of the scatterers are still rather interesting. Clearly, the seismograms are affected by the large dimensions of the scatterers. But the energy density $E(\mathbf{x})$ and the energy flux $\mathbf{S}(\mathbf{x})$ were presented as functions of frequency or wavelength. The results depend only on the ratio between the size of the scatterers and the incident wavelength. Even for 120 Hz, the P-wavelength is around 40 m and an order of magnitude larger than the size of the cavity. As demonstrated in Appendix C, the scheme performs correctly in this high frequency case.

The model assumed cavities with a small aspect ratio, namely 4 : 3. For larger aspect ratios, the performance of the scheme degrades rapidly because the cylindrical expansion functions are poor approximations for elliptic geometries. Mathieu functions should be used as expansion functions (Morse and Feshbach, 1953). Unfortunately, they are computationally rather costly. Each evaluation of a Mathieu function first demands solution of an eigenvalue problem and then evaluation of a number of Bessel functions. Furthermore, a Mathieu function for the P-wave of one particular order couples to all orders of the corresponding Mathieu functions for the S-wave. The scattering from cavities with larger aspect ratios such as joints or fractures of finite dimensions needs to be addressed in future works.

The models also indicate another problem. Different frequencies are affected differently by these cavities in the near-surface. For three different bands of frequency, we found three different responses. As expected, low frequencies (10 Hz) hardly interact with the scatterers. Medium frequencies (50 Hz) interact in a complex fashion with the scatterers. Waveguides begin to emerge (Figure 6-35b). Involved interference patterns arise as visible in Figure 6-31a. Finally for high frequencies (120 Hz) and away from the main lobe of energy flux, the fluxes appear to become chaotic. Different scattering mechanisms are involved even for nearby frequency-bands. Hence, seismic pulses propagating through this medium are affected by frequency dependent scattering. The result will be dispersion and attenuation effects depending strongly on frequency.

A problem not addressed in this work is the difference between 2-D and 3-D. There appears to be a fundamental change in the scattering behavior going from 2-D to 3-D, e.g. localization of scattered waves (Kirkpatrick, 1985; Bayer and Niederdränk, 1993). In 2-D, scattered fields always seem to be localized. Contrarily in 3-D, localization is expected to appear for certain scatterers and certain frequencies only. Therefore, future work needs to address the near-surface problem in 3-D.

Nevertheless, especially the final Model 4 shows that even cavities with small aspect ratios destroy the crispness of the incident field completely. The wavefield emanating from this surface layer is very noisy as exemplified in the seismogram 6-33b. Moreover, reflections from deeper layers will have to propagate back through this layer, degrading the sought reflections further.

In an example seismic dataset, we found the data acquired on top of a limestone mesa to be of very poor quality. 'Noise' and a very strong Rayleigh wave dominate the records. We assumed that the degradation is caused by scattering of the source field, the ground roll, and the reflections from deeper layers. Due to their commonness in outcropping limestone, we proposed small cavities or vugs to generate this scattering (Pritchett, 1990). In cases where other mechanisms are predominant, the scheme is still applicable by replacing the real scattering mechanism by an *equivalent* distribution of cavities. The scattered wavefields caused by the cavities are expanded into asymptotic modal solutions satisfying the wave equation in a homogeneous halfspace. Using a projection technique, we find a system of linear equations for the weighting coefficients of the modal solutions. Forward modelling turned out to be very dependent on frequency. Waves incident at low frequencies were hardly affected by the cavities. For medium frequencies, waveguides and complex interference patterns began to emerge which rendered the total wavefield at high frequencies incoherent.

Model	Rows	Number of Cavities	Δx [m]	δx [m]	Depth z [m]	δz [m]
1	1	100	32.0	± 10.0	-30.0	± 15.0
2	1	100	32.0	± 10.0	-85.0	± 15.0
3	2	110	32.0	± 10.0	$-30.0, -85.0$	± 15.0
4	2	200	32.0	± 10.0	$-30.0, -85.0$	± 15.0

Table 6.1: Definition of the models used. Cavities are arranged on a grid with one or two rows. The grid spacing is Δx. The locations of the cavities are perturbed by a random amount of uniform distribution between $\pm\delta x$ and $\pm\delta z$. Actually, Model 1 is just the top row of Model 4. Model 2 contains only the bottom row of Model 4. In Model 3, each cavity of Model 4 has a probability of 0.5 to be present in the model.

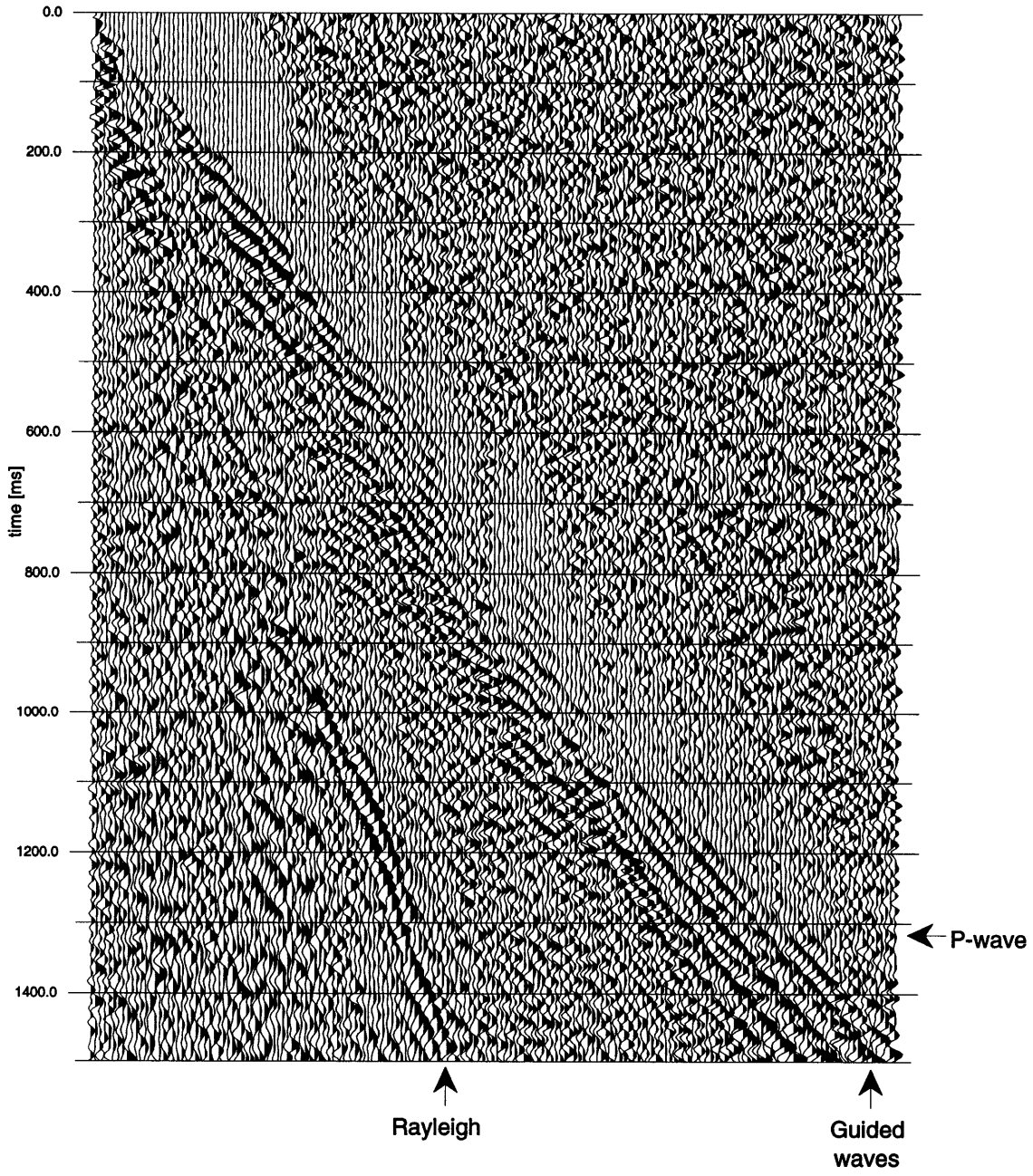

Figure 6-1: The first 1.5 s of the seismogram shot with the source located in the valley at station 1045. Shown are the traces located between station 1045 and 1221.

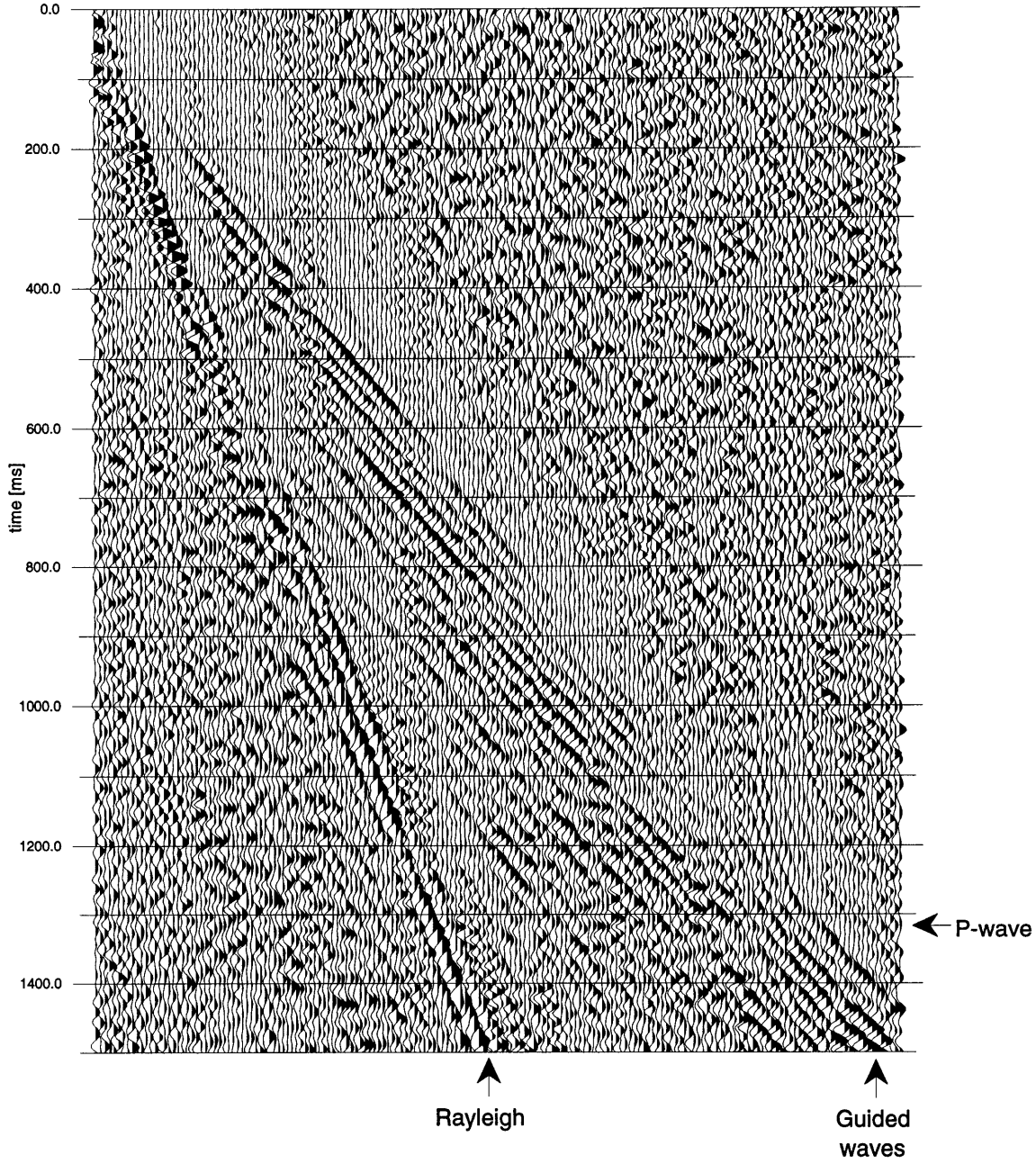

Figure 6-2: The first 1.5 s of the seismogram shot with the source on top of the mesa at station 1153. Shown are the traces located between station 1153 and 1329.

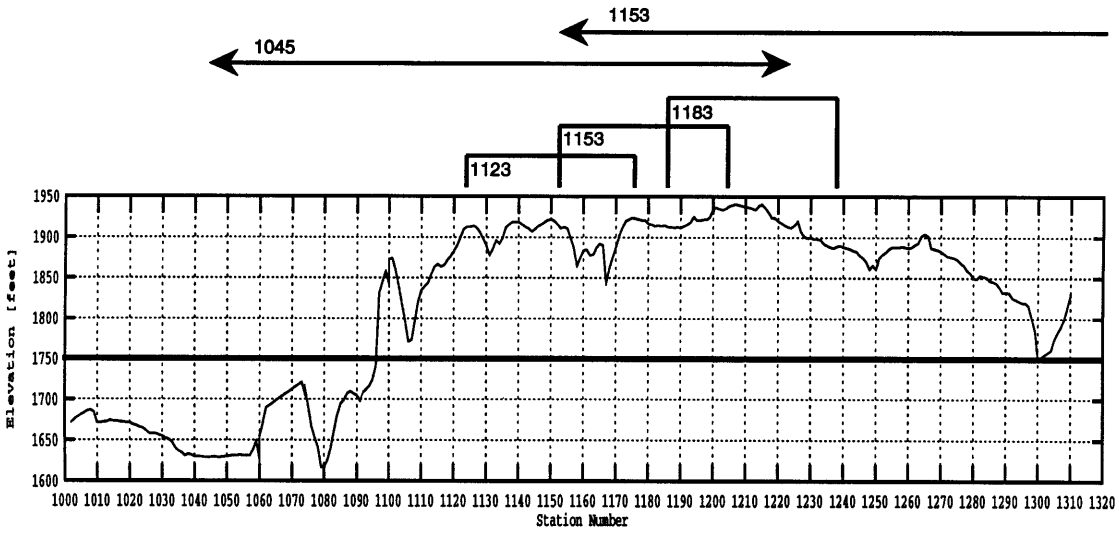

Figure 6-3: Elevation as a function of station number for the seismic data set. A slow and heterogeneous surface layer exists for elevations lower than 1750 ft. For higher elevations, a fast and more homogeneous limestone is exposed at the surface. The distance between stations is 110 ft. Arrows indicate the receiver locations for the example records 1045 and 1153. Braces indicate the location of the excerpts from records 1123, 1153, and 1183.

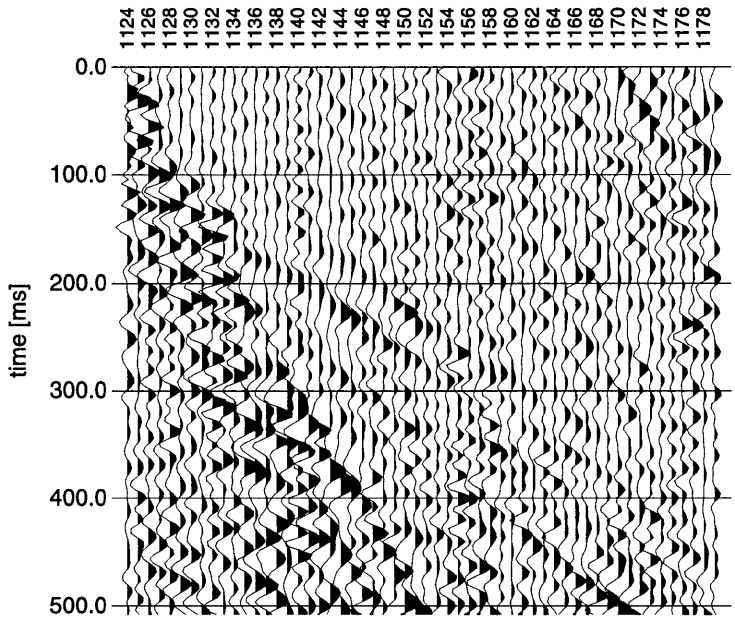

(a)

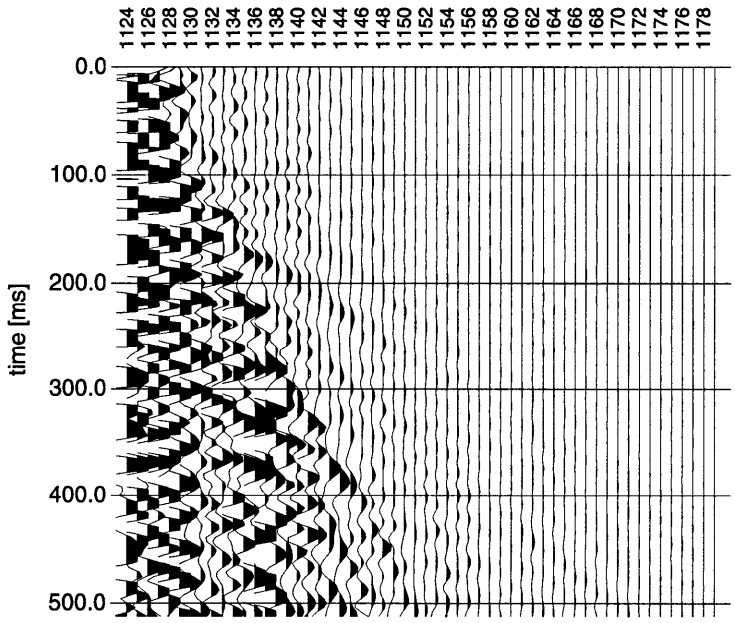

(b)

Figure 6-4: Details of shot 1123. Only the first 56 receivers and the first 512 ms are shown: (a) Automatic Gain Controlled (AGC) 500 ms, (b) raw record.

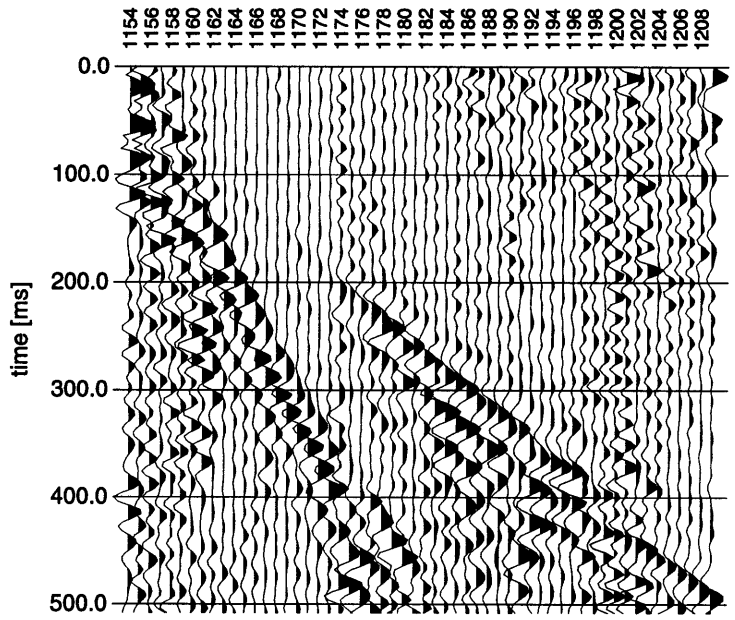

(a)

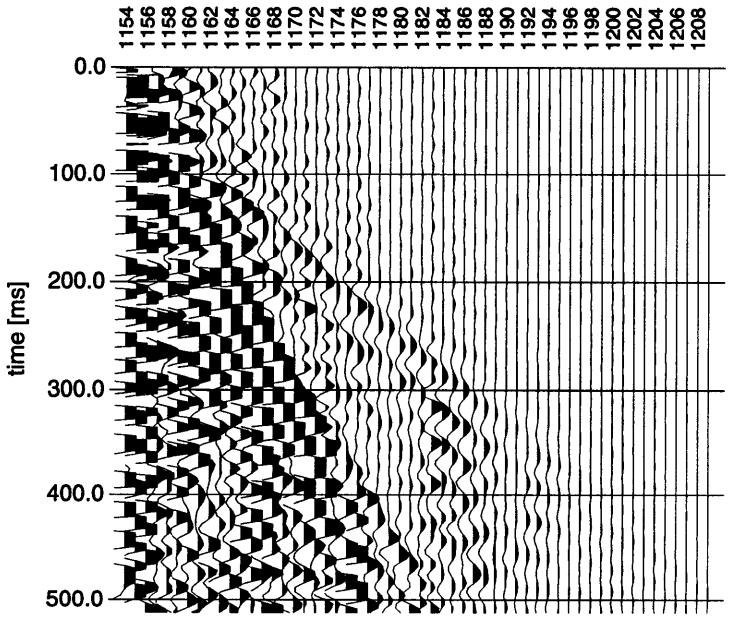

(b)

Figure 6-5: Details of shot 1153. Only the first 56 receivers and the first 512 ms are shown: (a) AGC 500 ms, (b) raw record.

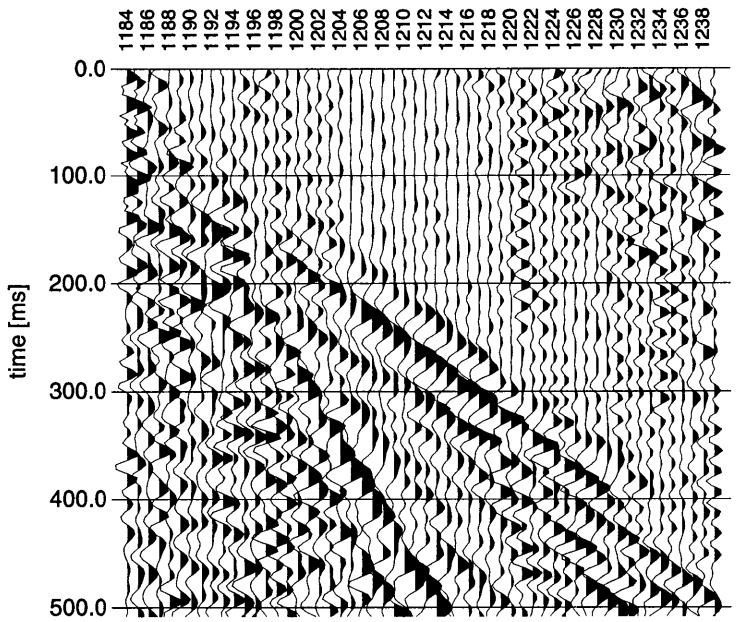

(a)

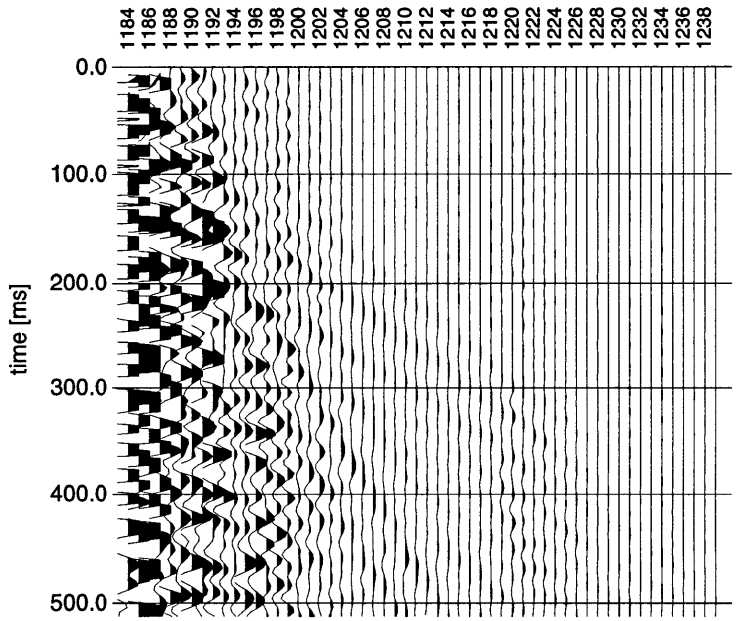

(b)

Figure 6-6: Details of shot 1183. Only the first 56 receivers and the first 512 ms are shown: (a) AGC 500 ms, (b) raw record.

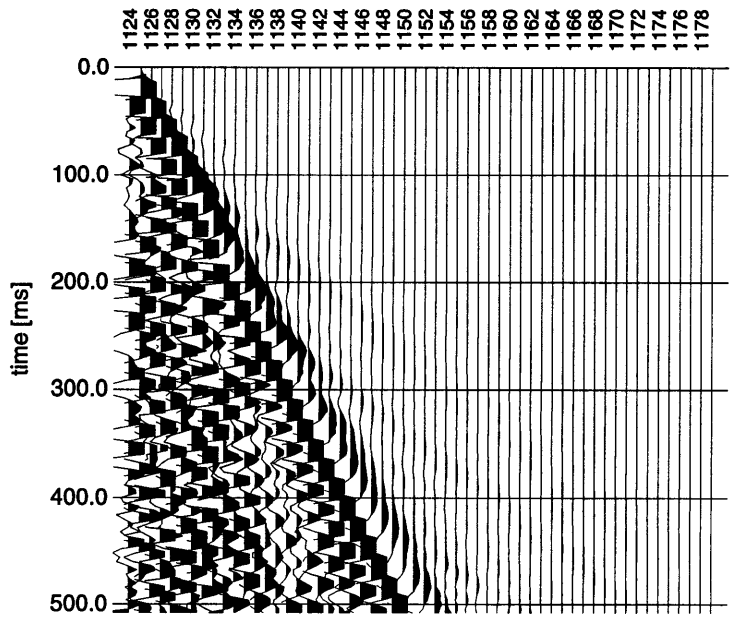

(a)Synthetic Record

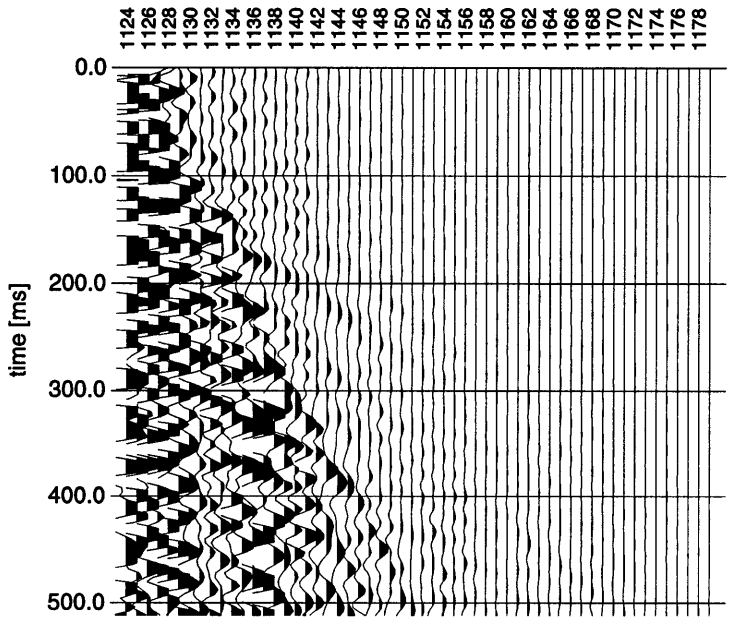

(b)Field Record

Figure 6-7: Record 1123: (a) Finite difference simulation. The incident wavefield is a Rayleigh wave emanating from station 1123. To facilitate comparisons, the raw field record 6-4b is reprinted as (b).

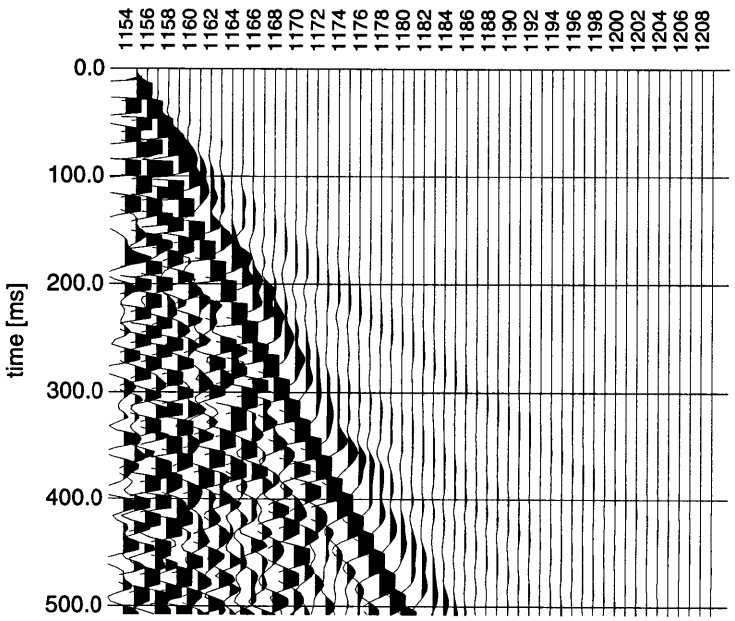

(a)Synthetic Record

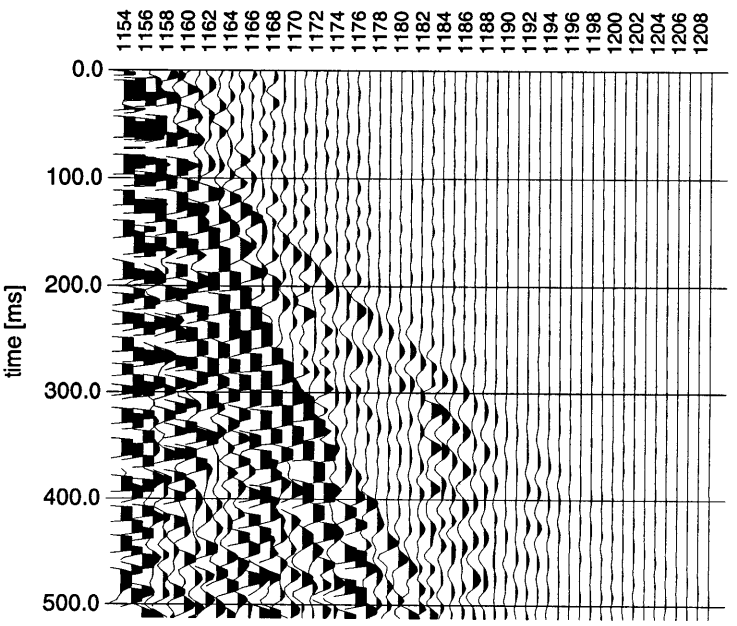

(b)Field Record

Figure 6-8: Record 1153: (a) Finite difference simulation. The incident wavefield is a Rayleigh wave emanating from station 1153. To facilitate comparisons, the raw field record 6-5b is reprinted as (b).

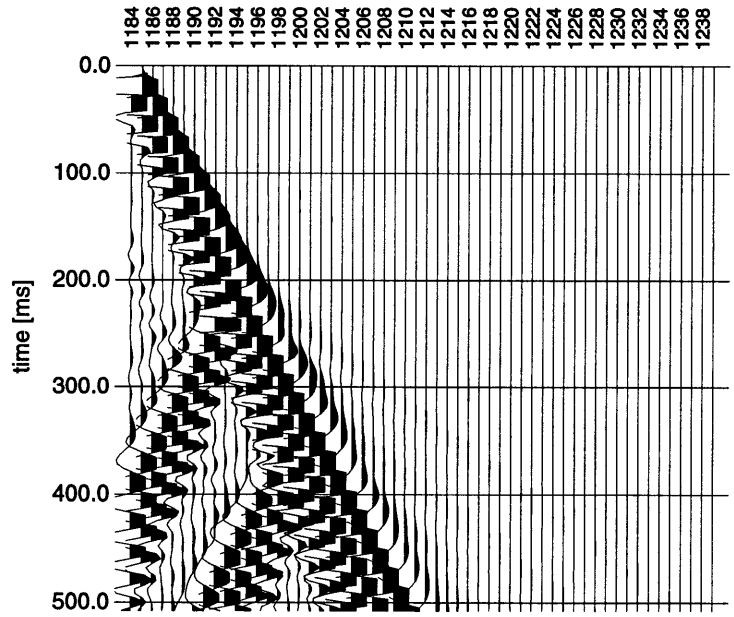

(a)Synthetic Record

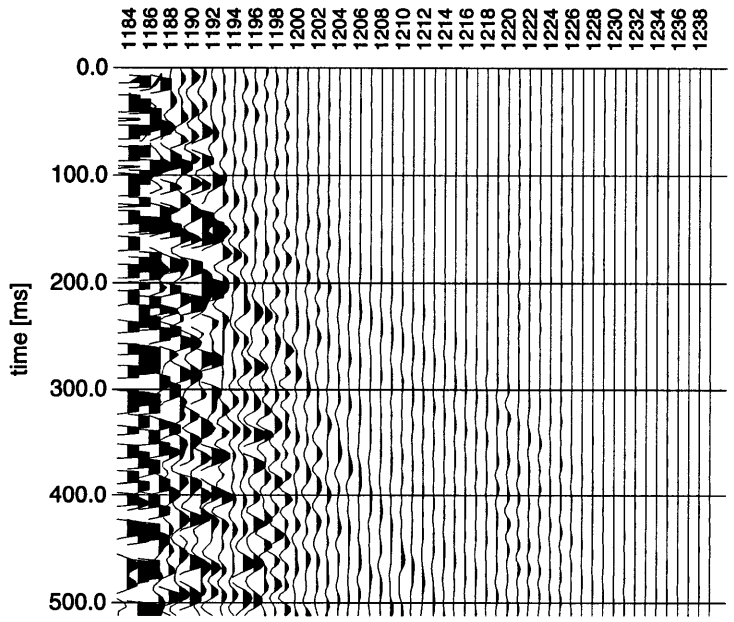

(b)Field Record

Figure 6-9: Record 1183: (a) Finite difference simulation. The incident wavefield is a Rayleigh wave emanating from station 1183. To facilitate comparisons, the raw field record 6-6b is reprinted as (b).

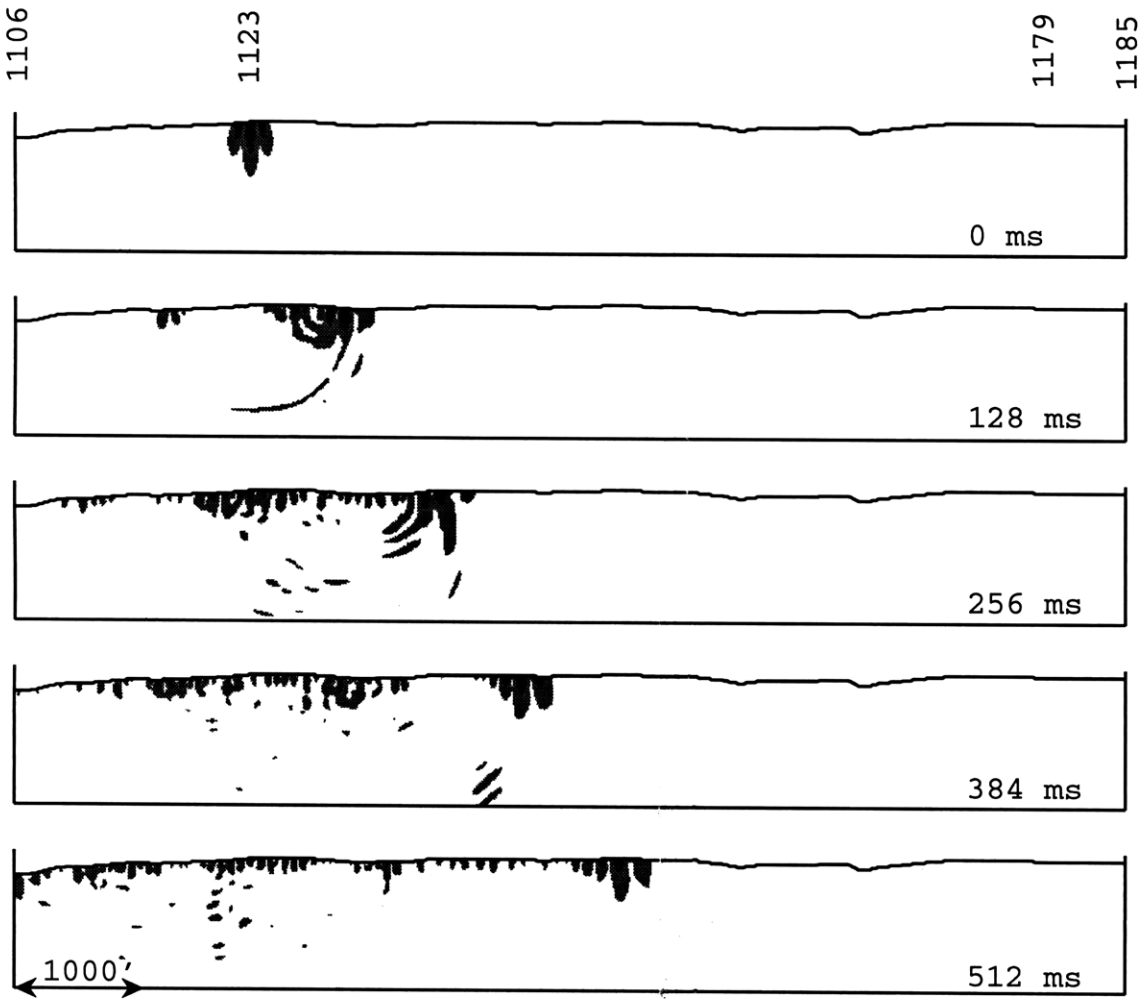

Figure 6-10: Finite difference snapshots of record 1123. The incident wavefield is a Rayleigh wave emanating from station 1123. The snapshot is not exaggerated in vertical direction indicating how little topography there is.

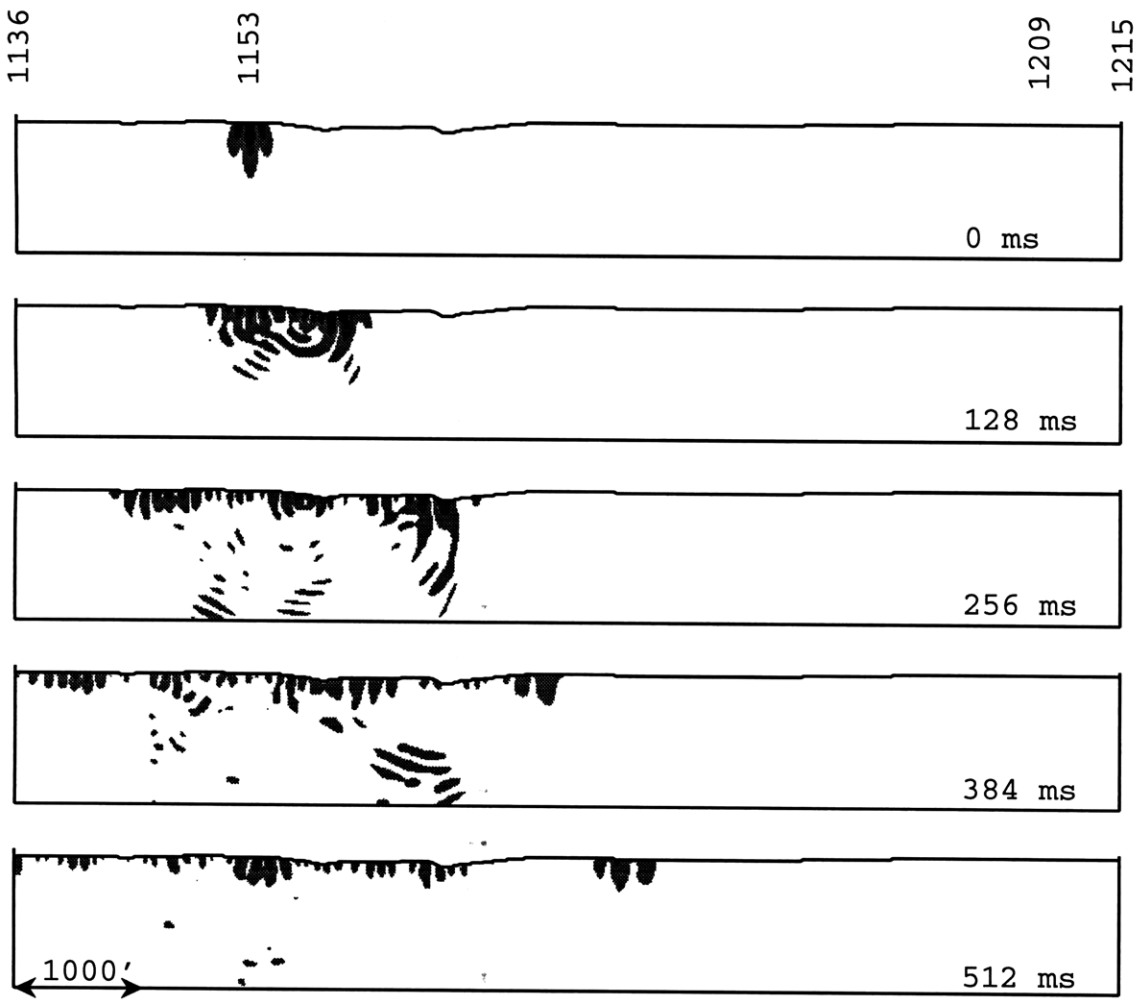

Figure 6-11: Finite difference snapshots of record 1153. The incident wavefield is a Rayleigh wave emanating from station 1153.

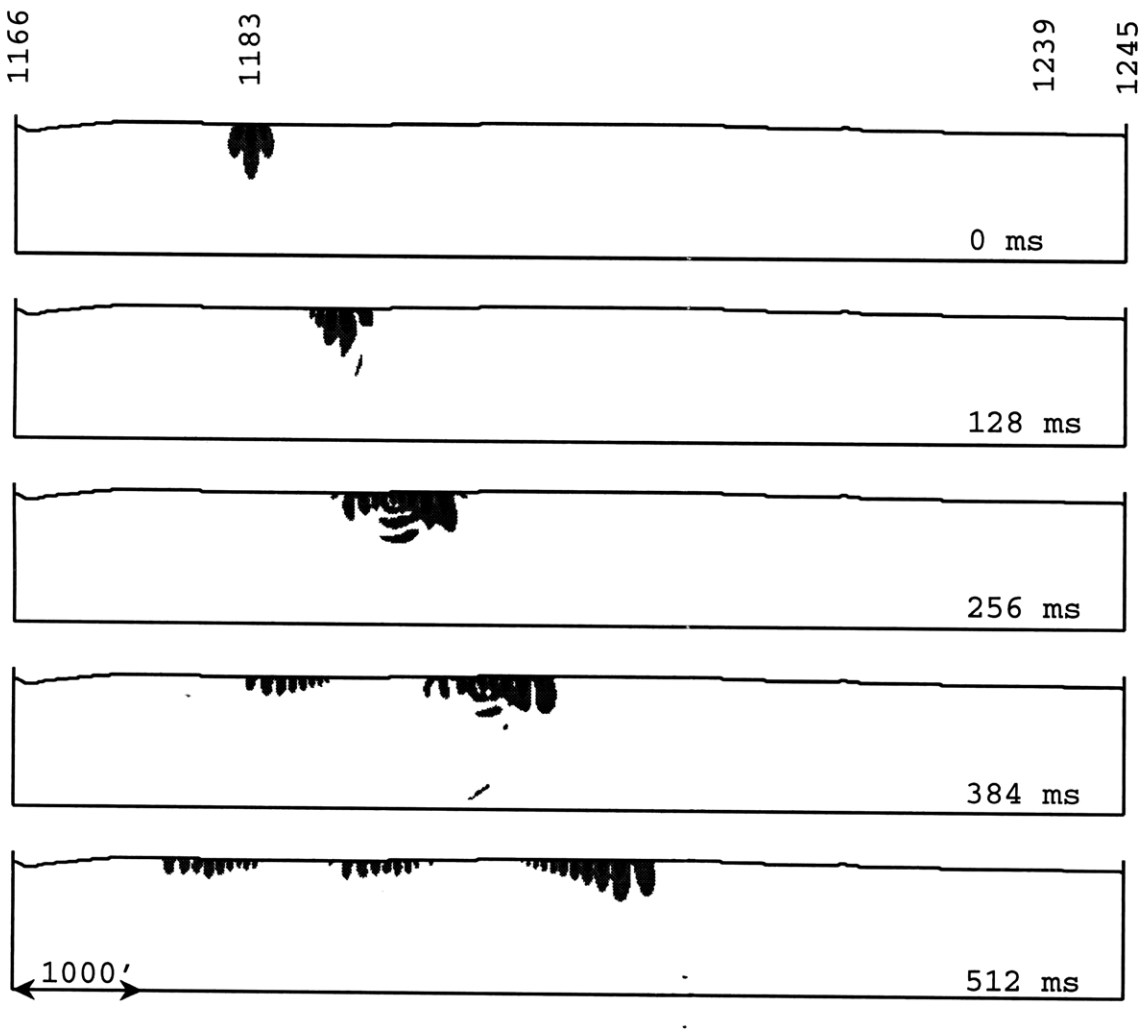

Figure 6-12: Finite difference snapshots of record 1183. The incident wavefield is a Rayleigh wave emanating from station 1183.

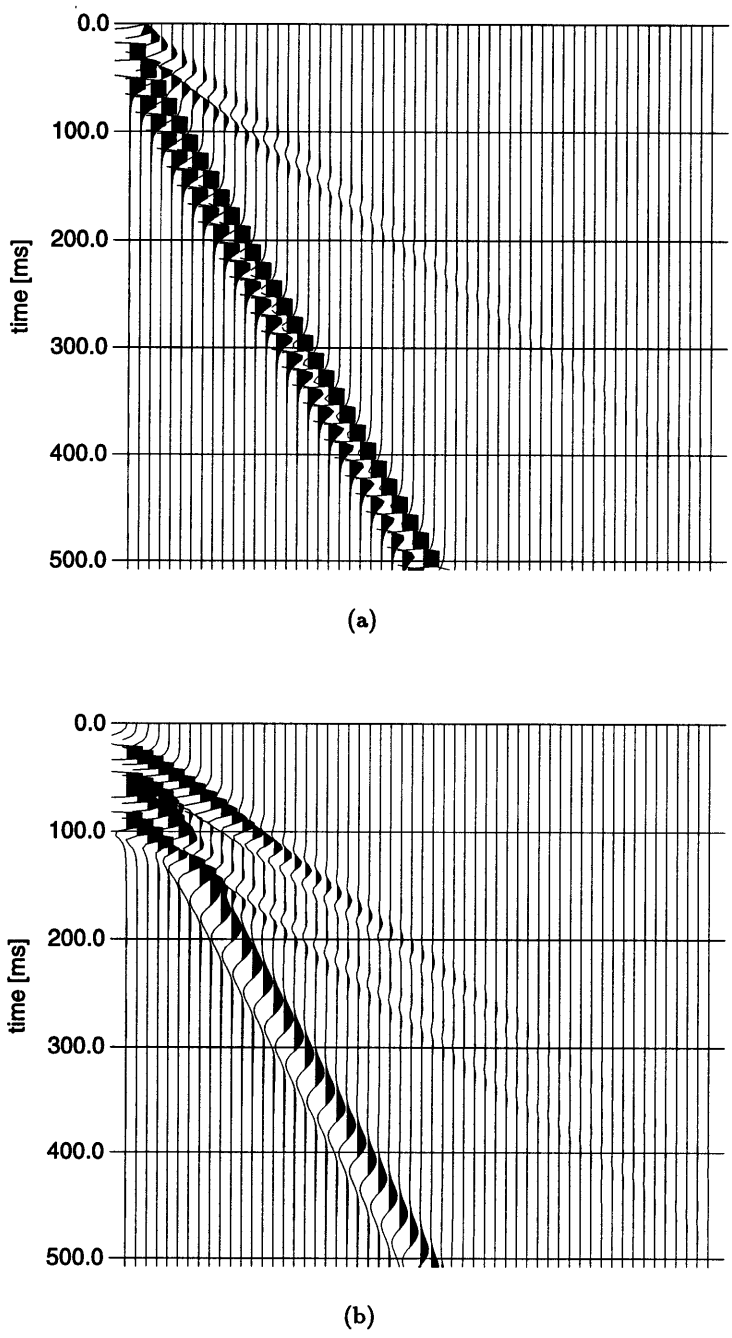

Figure 6-13: The vertical displacement due to the incident field only: (a) receivers located 1 m below the surface, (b) receivers located 150 m below the surface.

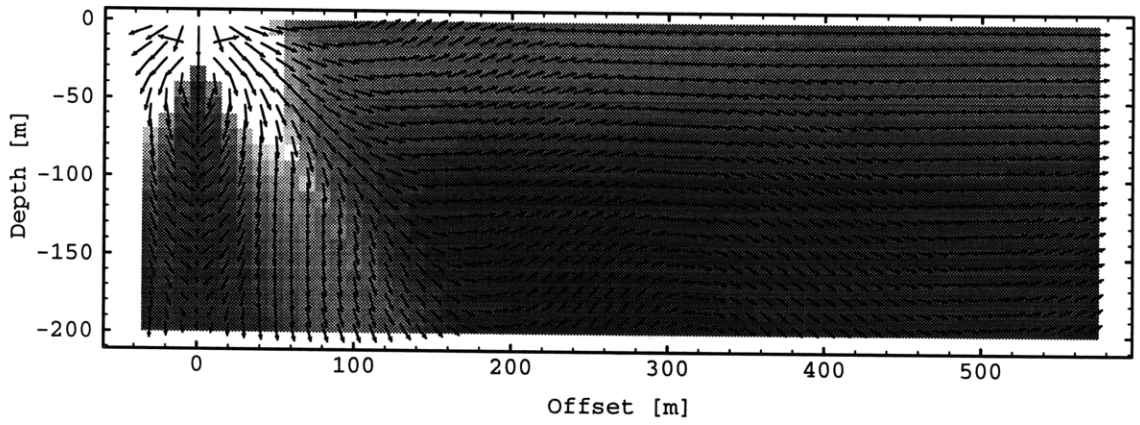

Figure 6-14: The logarithmic Poynting vector $\frac{\mathbf{S}(\mathbf{x})}{|\mathbf{S}(\mathbf{x})|}\log|\mathbf{S}(\mathbf{x})|$ and the logarithmic energy density $\log E(\mathbf{x})$ of the incident field (10 Hz) used in all models. Bright colors correspond to high energy densities. The values are normalized to their respective maximum.

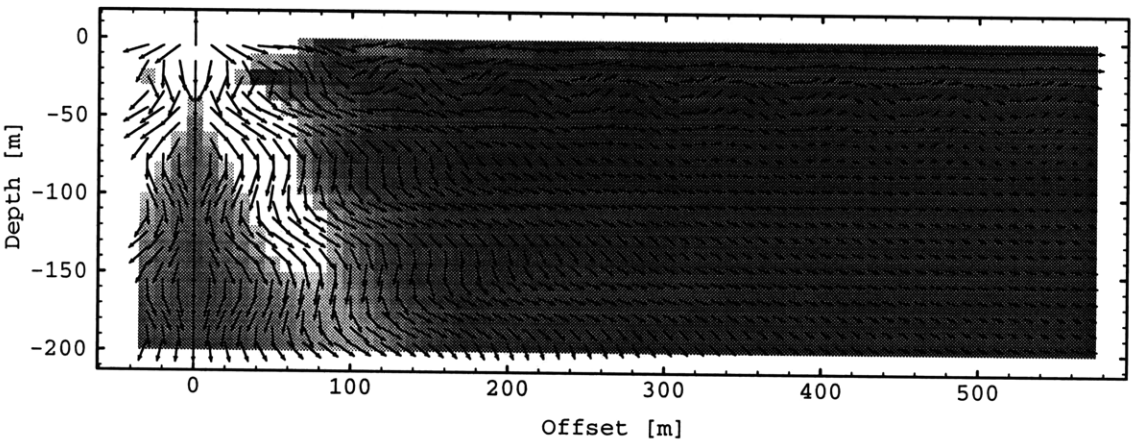

Figure 6-15: The logarithmic Poynting vector $\frac{\mathbf{S}(\mathbf{x})}{|\mathbf{S}(\mathbf{x})|}\log|\mathbf{S}(\mathbf{x})|$ and the logarithmic energy density $\log E(\mathbf{x})$ of the incident field used in all models. The frequency is 50 Hz.

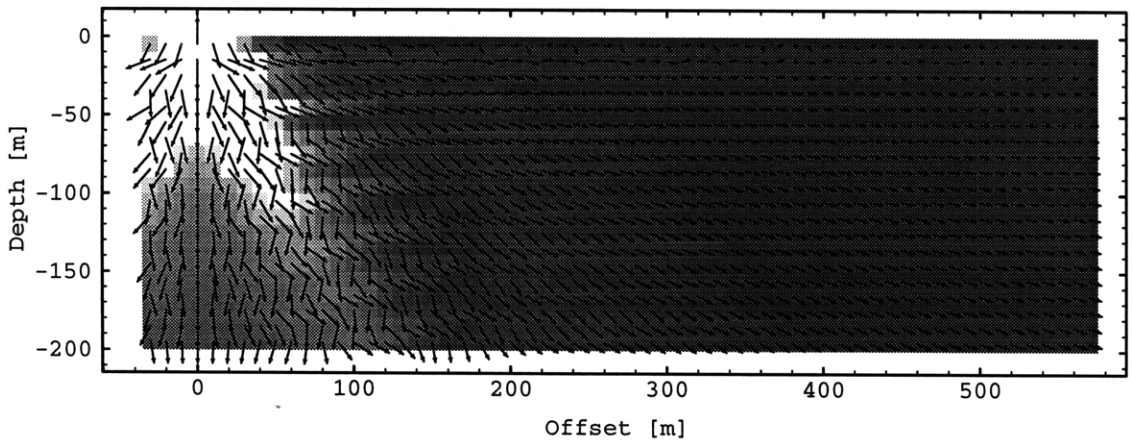

Figure 6-16: The logarithmic Poynting vector $\frac{\mathbf{S}(\mathbf{x})}{|\mathbf{S}(\mathbf{x})|} \log |\mathbf{S}(\mathbf{x})|$ and the logarithmic energy density $\log E(\mathbf{x})$ of the incident field used in all models. The frequency is 120 Hz.

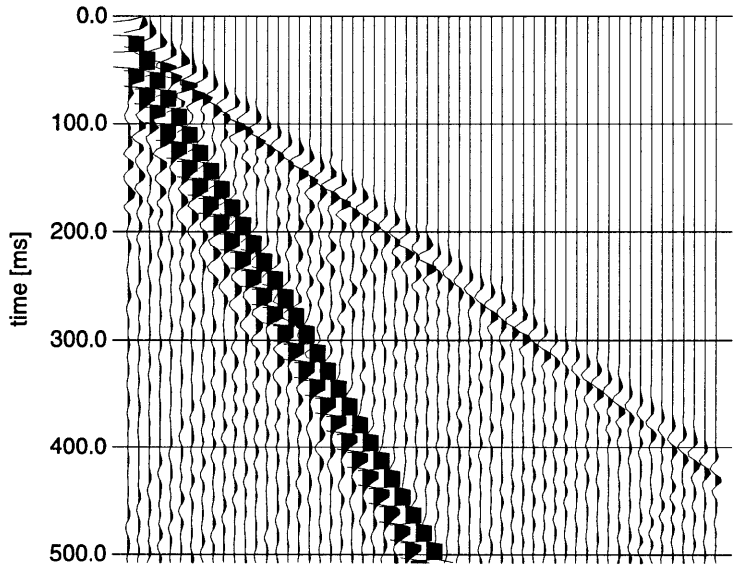

(a)

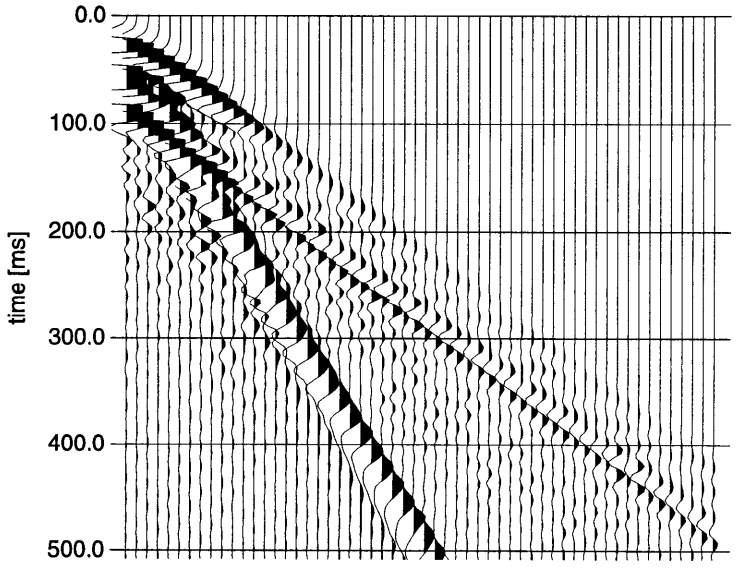

(b)

Figure 6-17: The vertical displacement for Model 1: (a) receivers located 1 m below the surface, (b) receivers located 150 m below the surface.

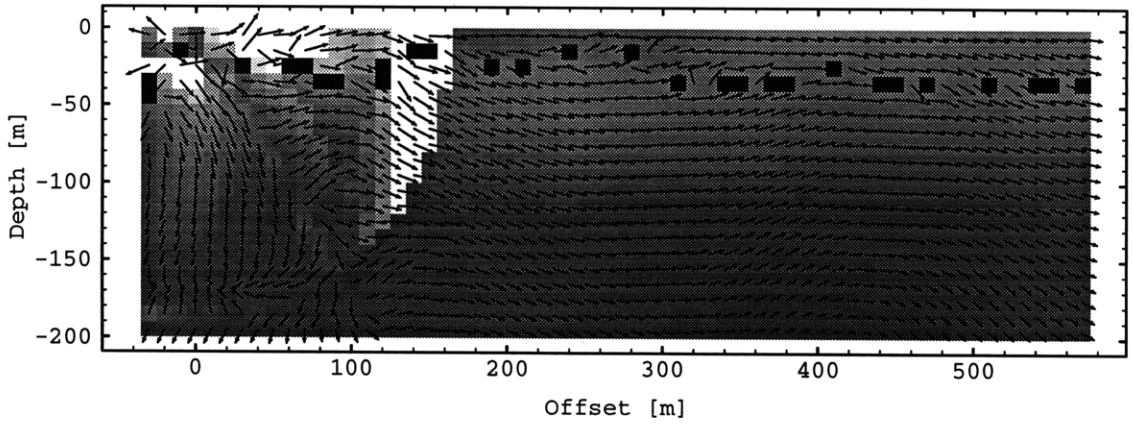

(a)

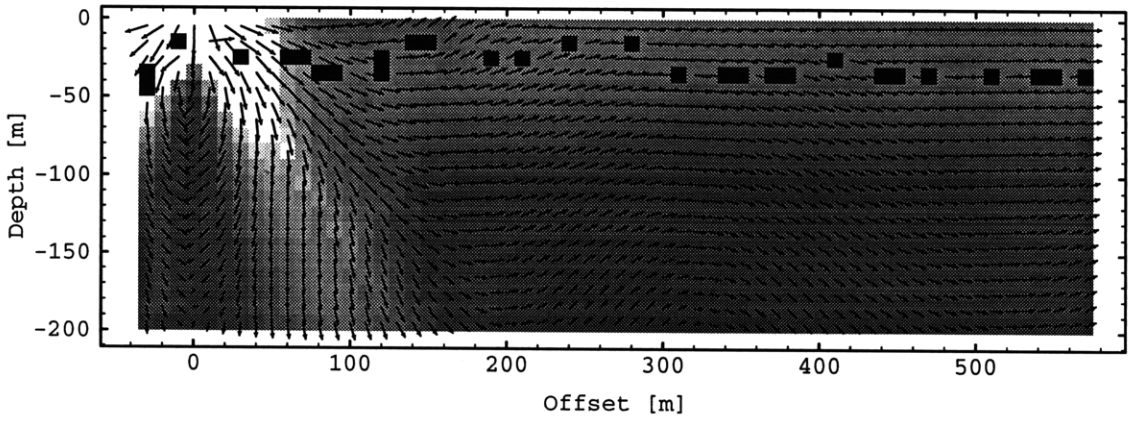

(b)

Figure 6-18: The logarithmic Poynting vector $\frac{\mathbf{S}(\mathbf{x})}{|\mathbf{S}(\mathbf{x})|}\log|\mathbf{S}(\mathbf{x})|$ and the logarithmic energy density $\log E(\mathbf{x})$ for Model 1 at 10 Hz: (a) scattered field, (b) total field. The black speckles denote the cavities.

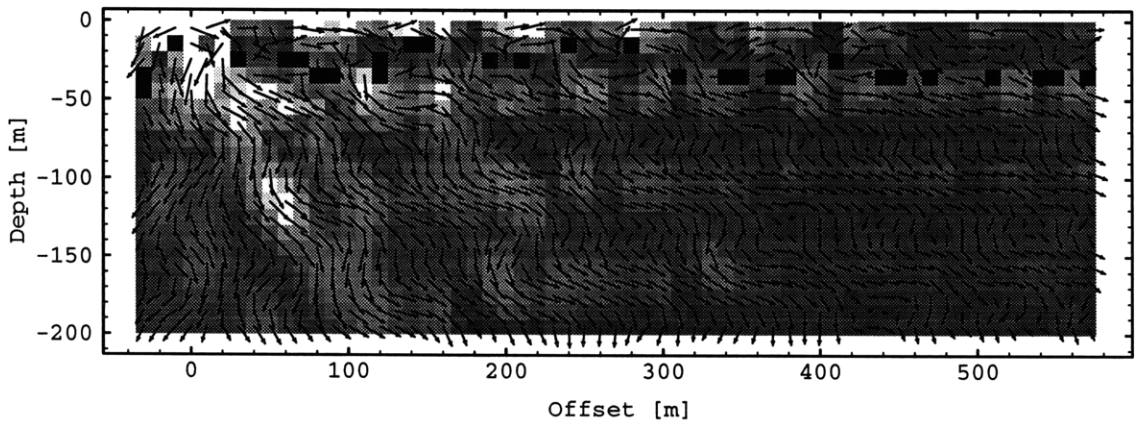

(a)

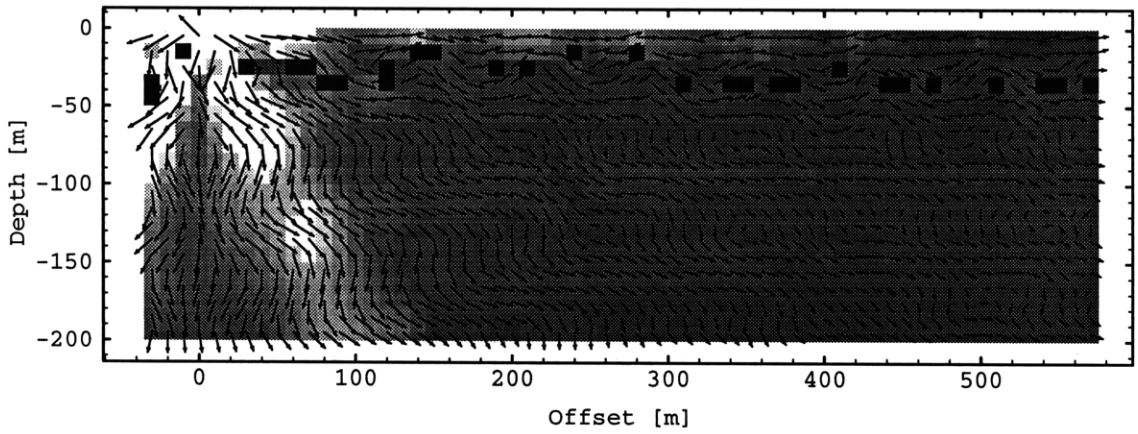

(b)

Figure 6-19: The logarithmic Poynting vector $\frac{\mathbf{S}(\mathbf{x})}{|\mathbf{S}(\mathbf{x})|}\log|\mathbf{S}(\mathbf{x})|$ and the logarithmic energy density $\log E(\mathbf{x})$ for Model 1: (a) scattered field, (b) total field. The frequency is 50 Hz.

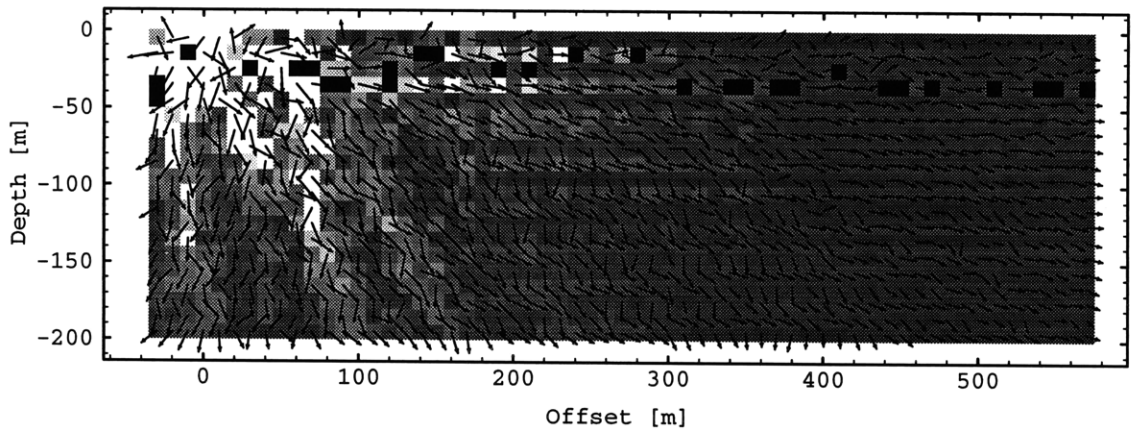

(a)

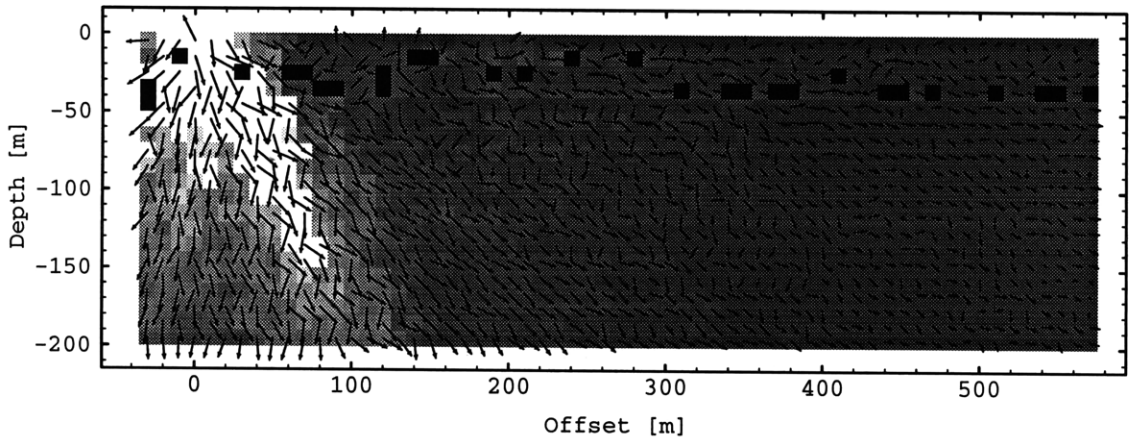

(b)

Figure 6-20: The logarithmic Poynting vector $\frac{\mathbf{S}(\mathbf{x})}{|\mathbf{S}(\mathbf{x})|}\log|\mathbf{S}(\mathbf{x})|$ and the logarithmic energy density $\log E(\mathbf{x})$ for Model 1: (a) scattered field, (b) total field. The frequency is 120 Hz.

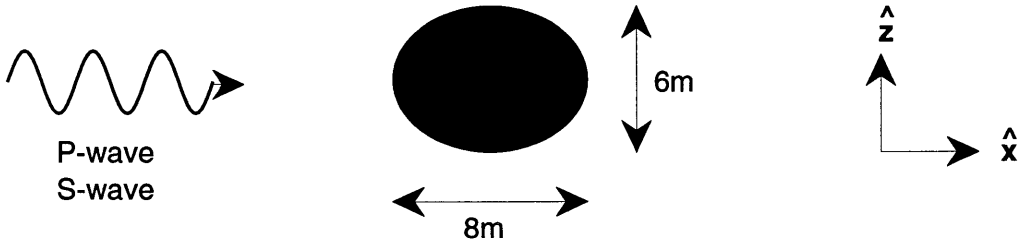

Figure 6-21: Energy scattering patterns: An elliptical cavity is illuminated by planar P- or S-waves propagating along the principal axes. The principal axes are aligned with the coordinate frame.

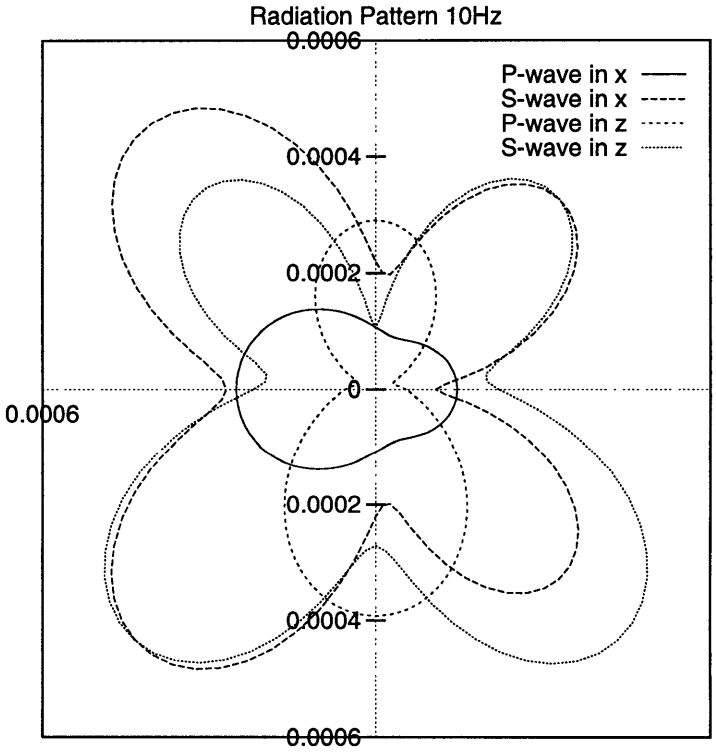

Figure 6-22: Energy scattering patterns for the cavity presented in Figure 6-21. The frequency of the incident P- and S-waves is 10 Hz. The incident waves propagate along the principal axes of the cavity in $\hat{\mathbf{x}}$ and $\hat{\mathbf{z}}$-direction.

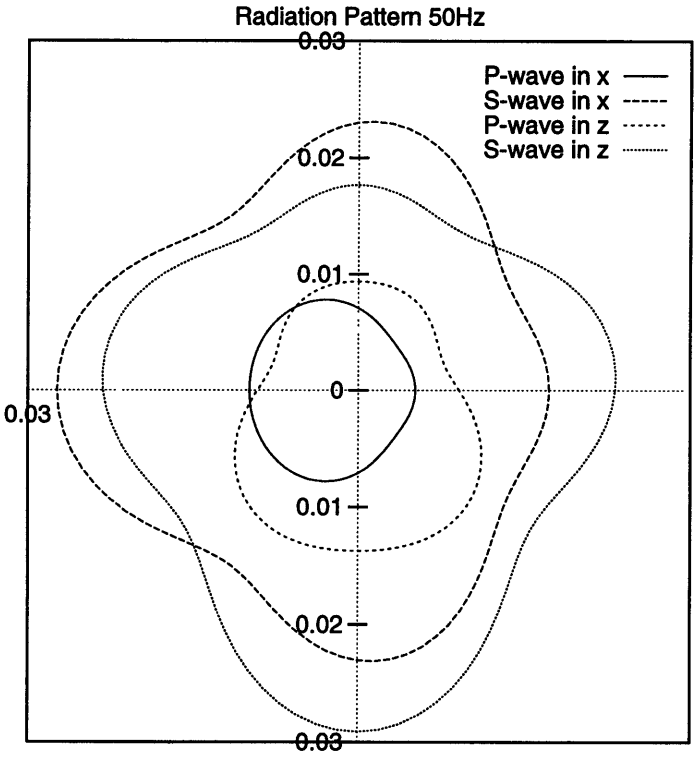

Figure 6-23: Energy scattering patterns: The frequency of the incident P- and S-waves is 50 Hz.

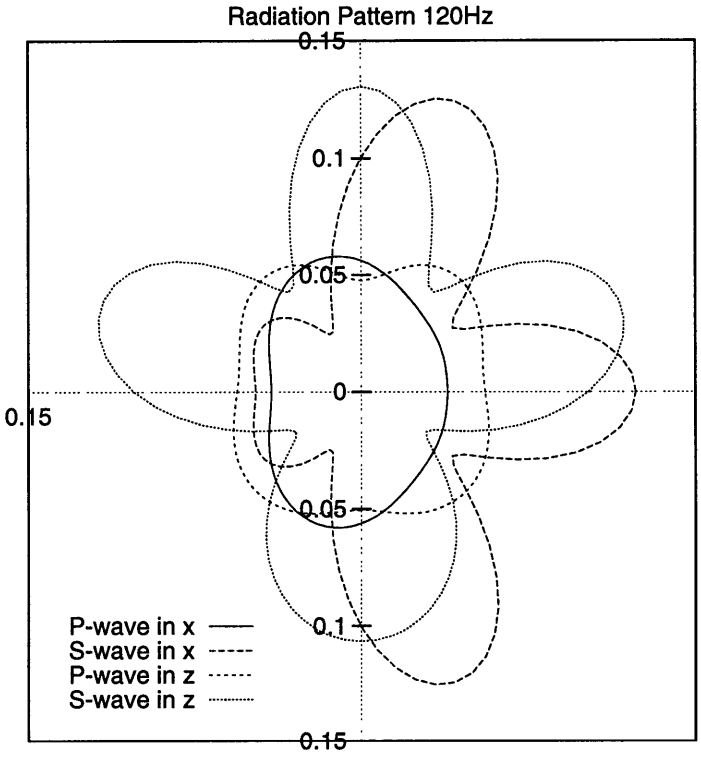

Figure 6-24: Energy scattering patterns: The frequency of the incident P- and S-waves is 120 Hz.

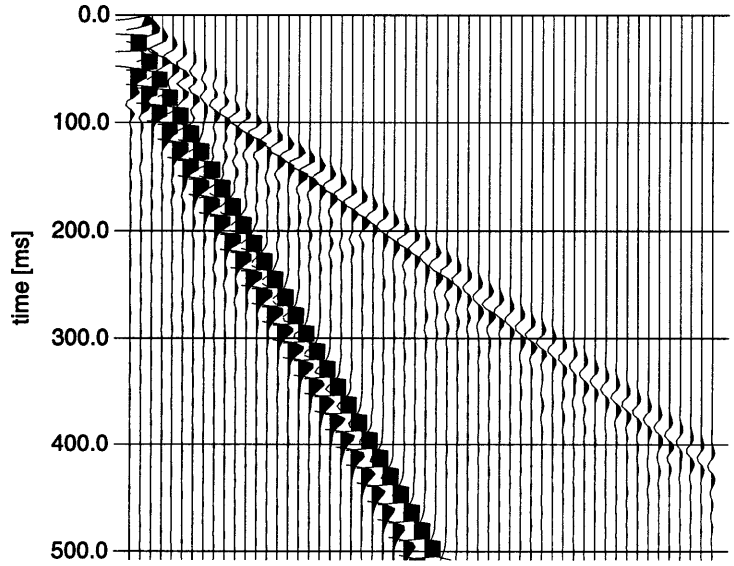

(a)

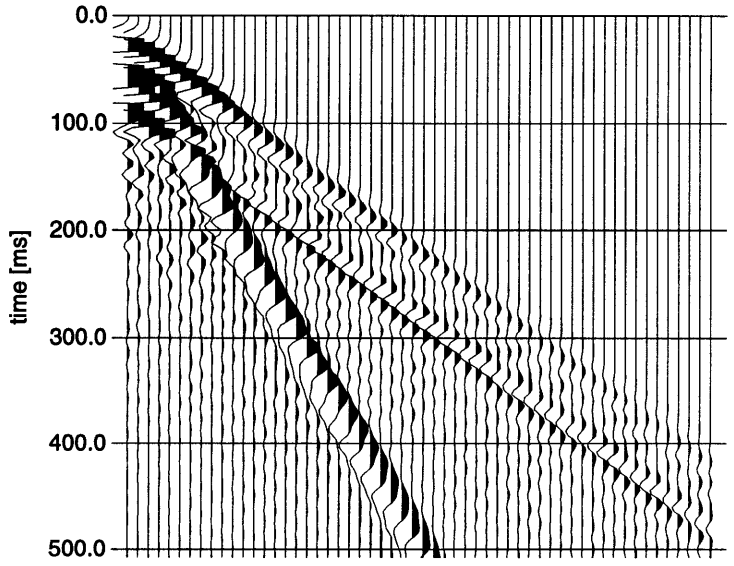

(b)

Figure 6-25: The vertical displacement for Model 2: (a) receivers located 1 m below the surface, (b) receivers located 150 m below the surface.

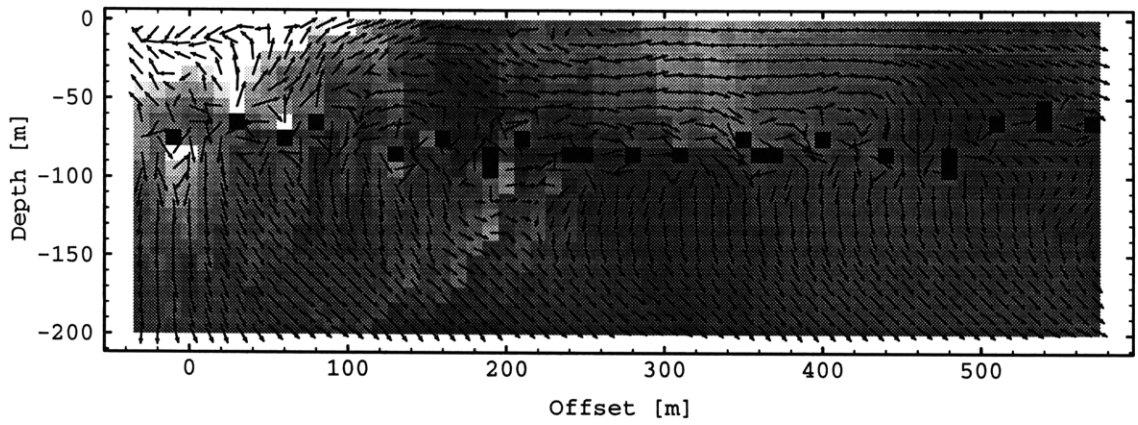

(a)

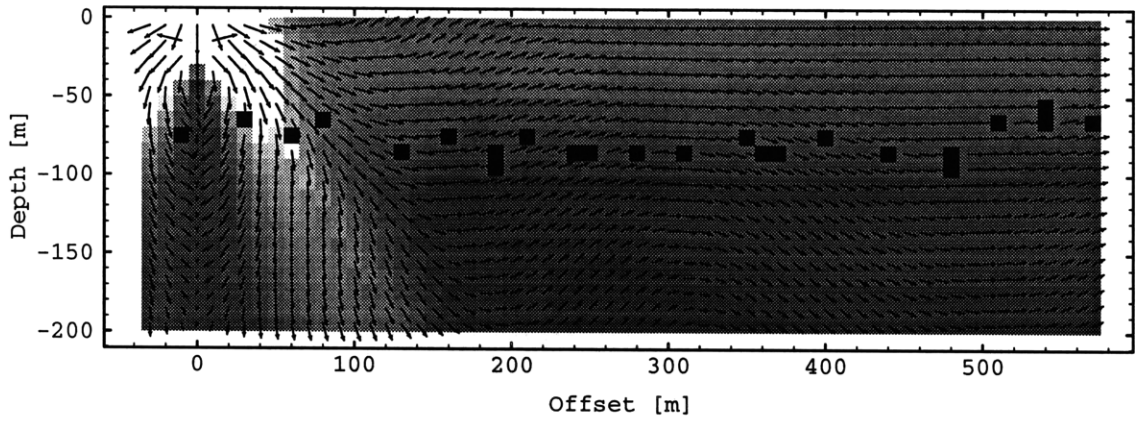

(b)

Figure 6-26: The logarithmic Poynting vector $\frac{\mathbf{S}(\mathbf{x})}{|\mathbf{S}(\mathbf{x})|}\log|\mathbf{S}(\mathbf{x})|$ and the logarithmic energy density $\log E(\mathbf{x})$ of the wavefields for Model 2. The frequency is 10 Hz: (a) scattered field, (b) total field.

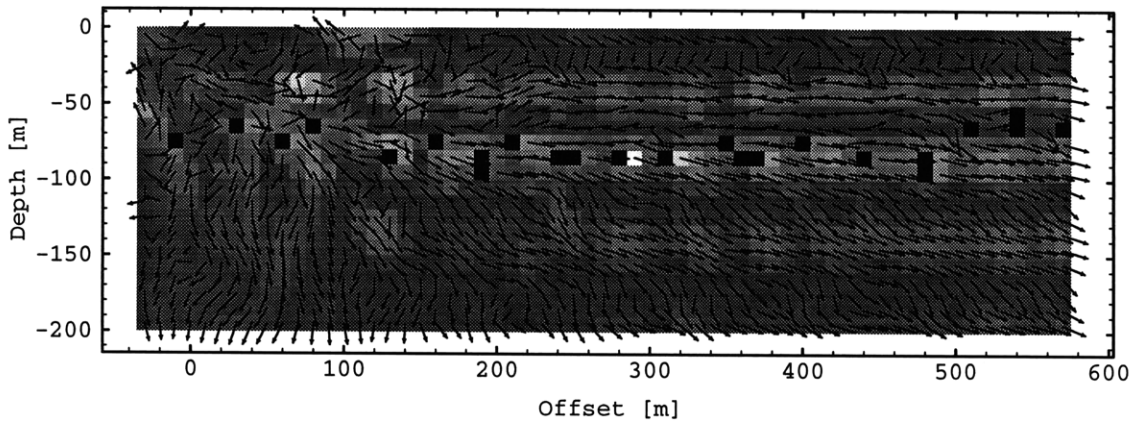

(a)

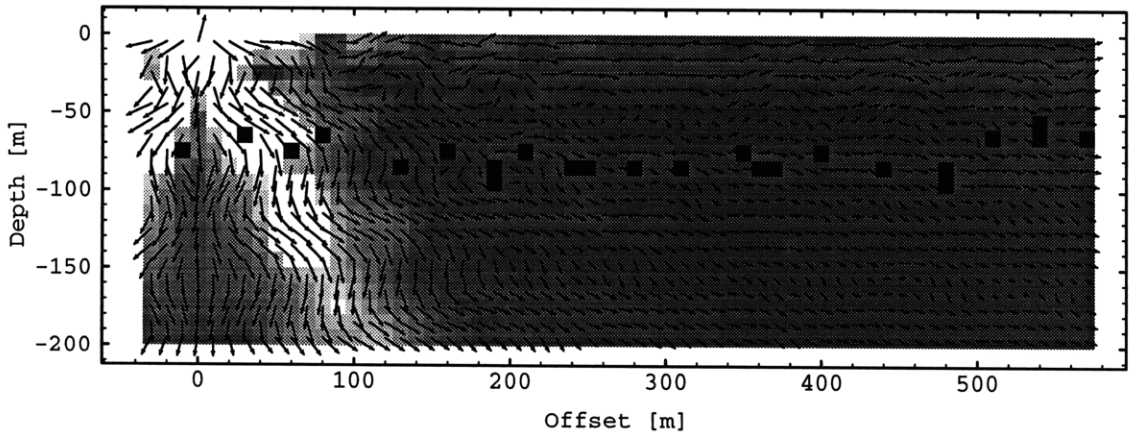

(b)

Figure 6-27: The logarithmic Poynting vector $\frac{\mathbf{S}(\mathbf{x})}{|\mathbf{S}(\mathbf{x})|}\log|\mathbf{S}(\mathbf{x})|$ and the logarithmic energy density $\log E(\mathbf{x})$ of the wavefields for Model 2. The frequency is 50 Hz: (a) scattered field, (b) total field.

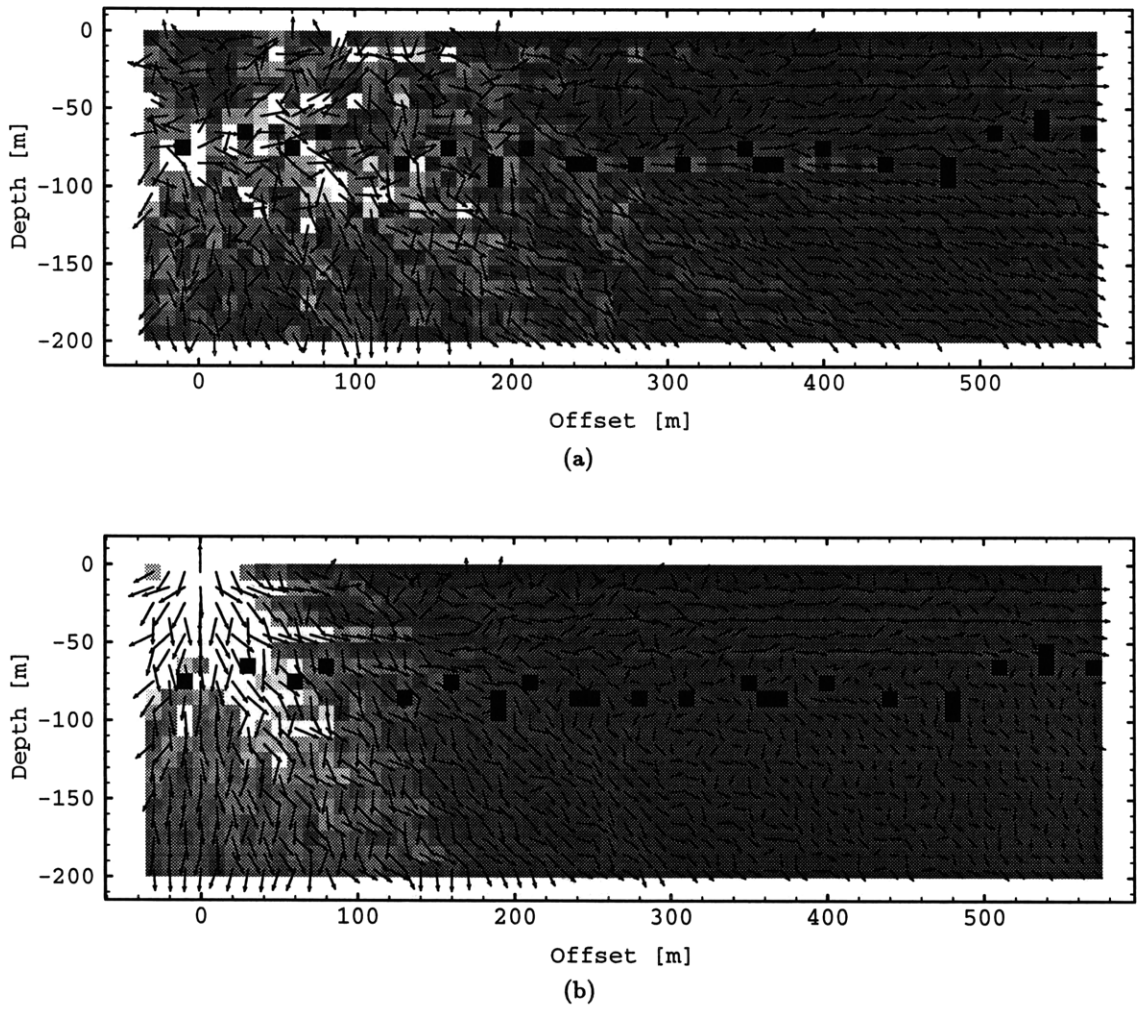

Figure 6-28: The logarithmic Poynting vector $\frac{\mathbf{S}(\mathbf{x})}{|\mathbf{S}(\mathbf{x})|}\log|\mathbf{S}(\mathbf{x})|$ and the logarithmic energy density $\log E(\mathbf{x})$ of the wavefields for Model 2. The frequency is 120 Hz: (a) scattered field, (b) total field.

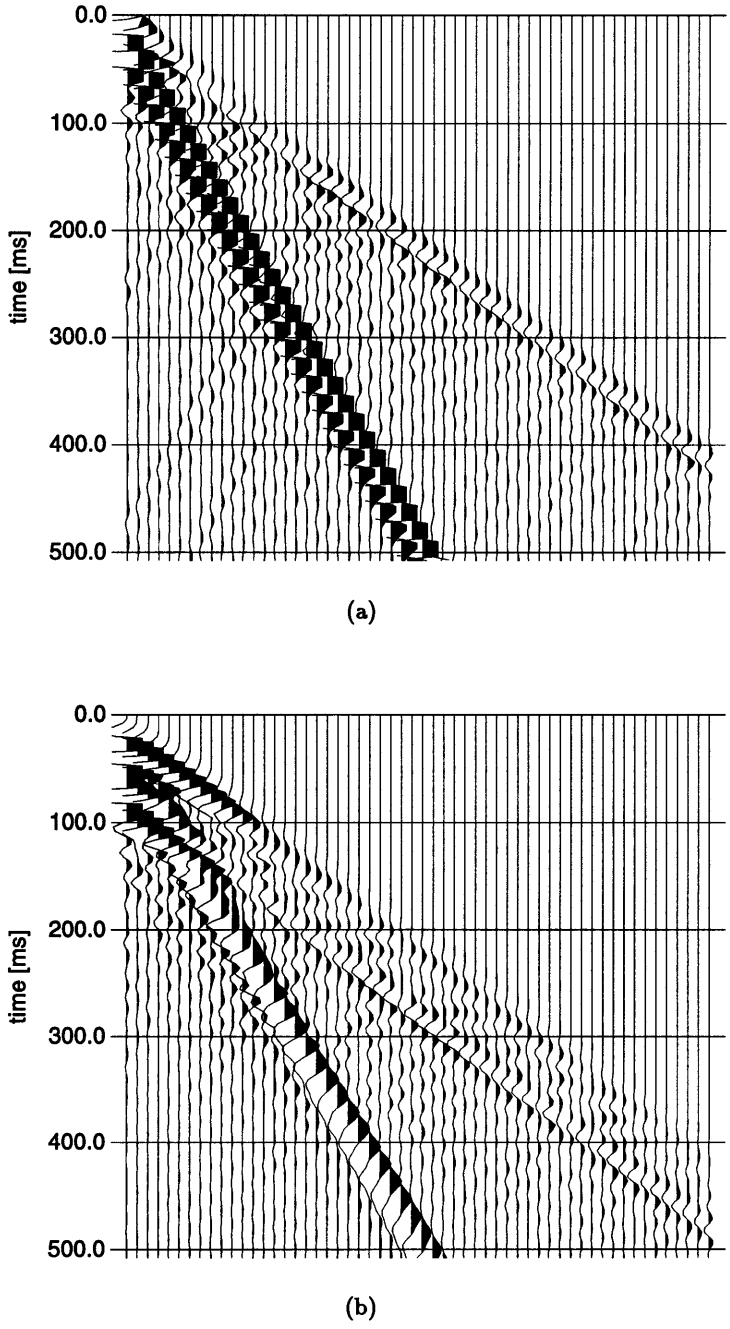

Figure 6-29: The vertical displacement for Model 3: (a) receivers located 1 m below the surface, (b) receivers located 150 m below the surface.

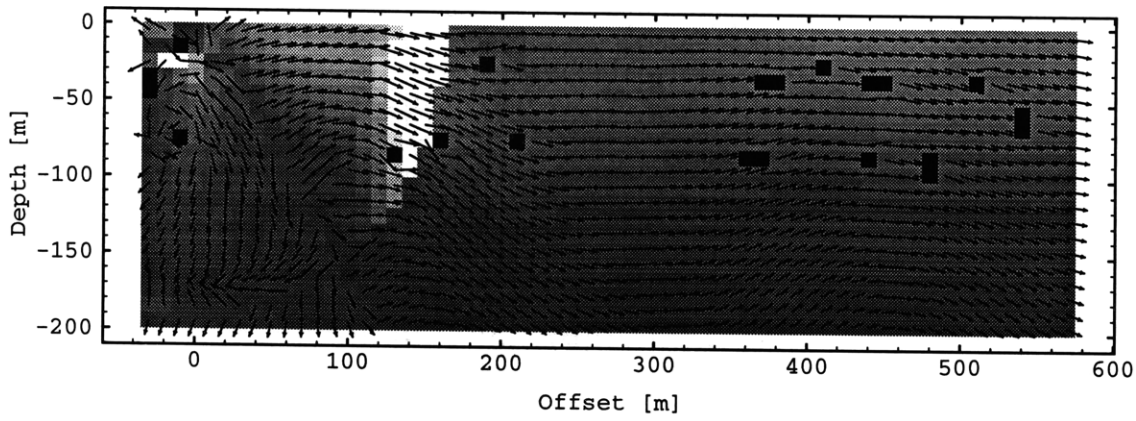

(a)

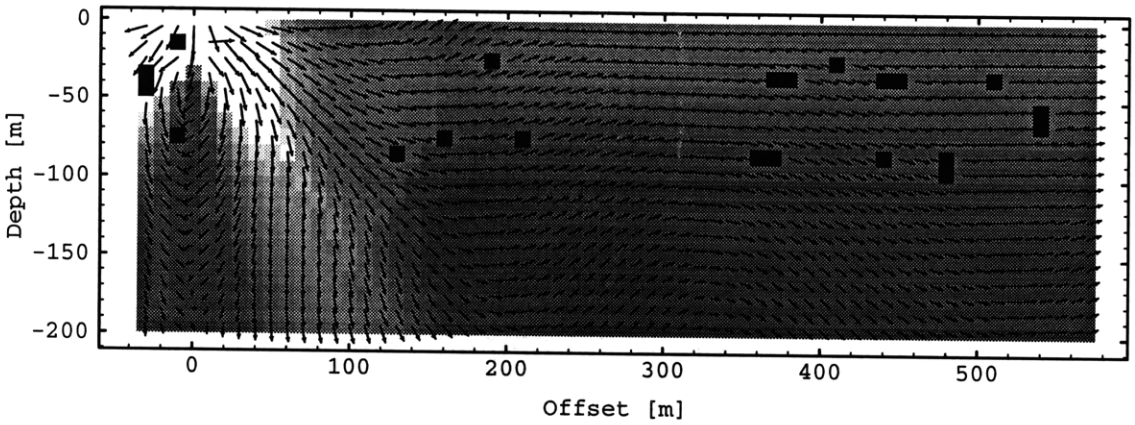

(b)

Figure 6-30: The logarithmic Poynting vector $\frac{\mathbf{S}(\mathbf{x})}{|\mathbf{S}(\mathbf{x})|}\log|\mathbf{S}(\mathbf{x})|$ and the logarithmic energy density $\log E(\mathbf{x})$ of the wavefields for Model 3. The frequency is 10 Hz: (a) scattered field, (b) total field.

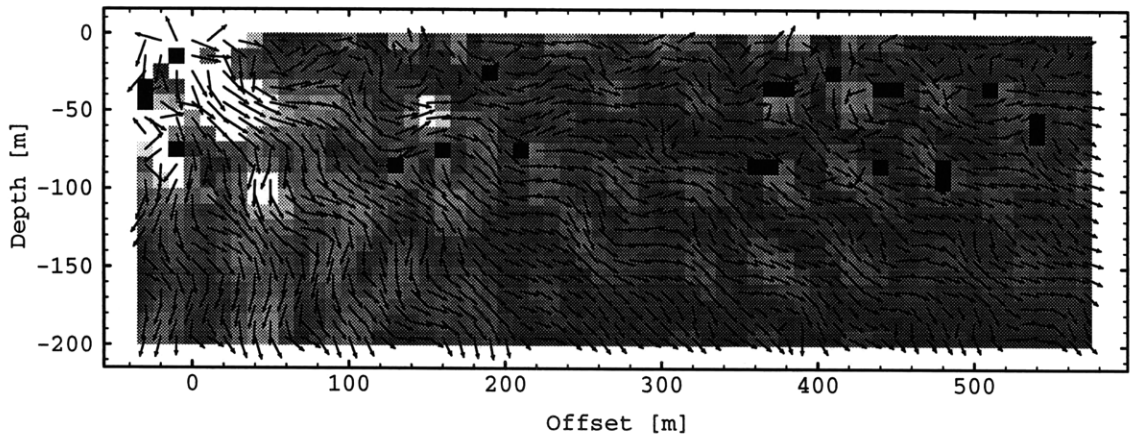

(a)

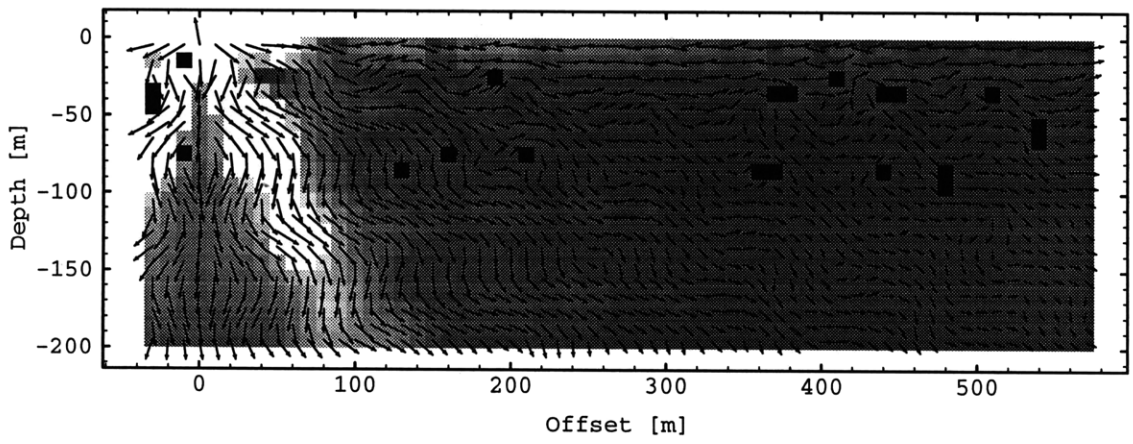

(b)

Figure 6-31: The logarithmic Poynting vector $\frac{\mathbf{S}(\mathbf{x})}{|\mathbf{S}(\mathbf{x})|}\log|\mathbf{S}(\mathbf{x})|$ and the logarithmic energy density $\log E(\mathbf{x})$ of the wavefields for Model 3. The frequency is 50 Hz: (a) scattered field, (b) total field.

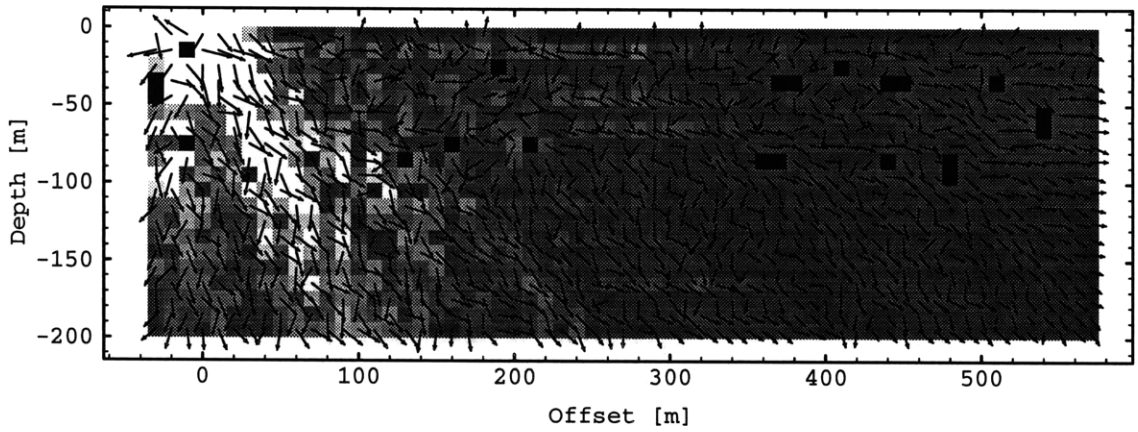

(a)

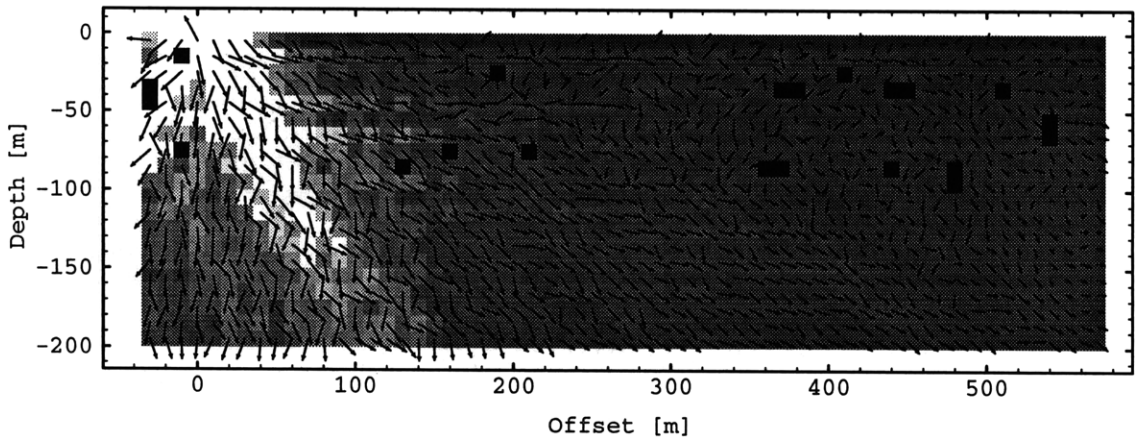

(b)

Figure 6-32: The logarithmic Poynting vector $\frac{\mathbf{S}(\mathbf{x})}{|\mathbf{S}(\mathbf{x})|}\log|\mathbf{S}(\mathbf{x})|$ and the logarithmic energy density $\log E(\mathbf{x})$ of the wavefields for Model 3. The frequency is 120 Hz: (a) scattered field, (b) total field.

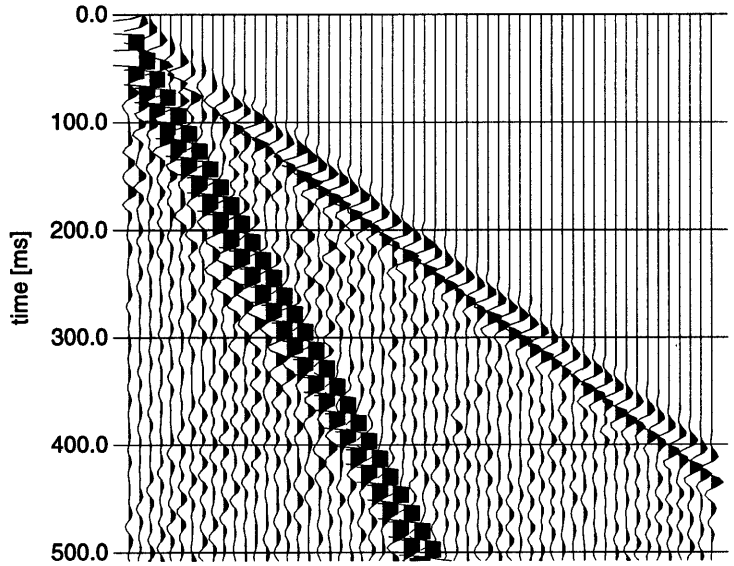

(a)

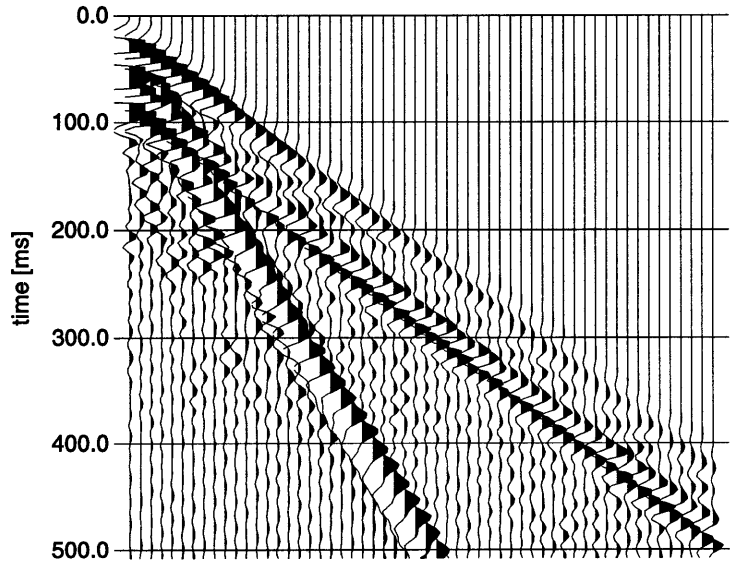

(b)

Figure 6-33: The vertical displacement for Model 4: (a) receivers located 1 m below the surface, (b) receivers located 150 m below the surface.

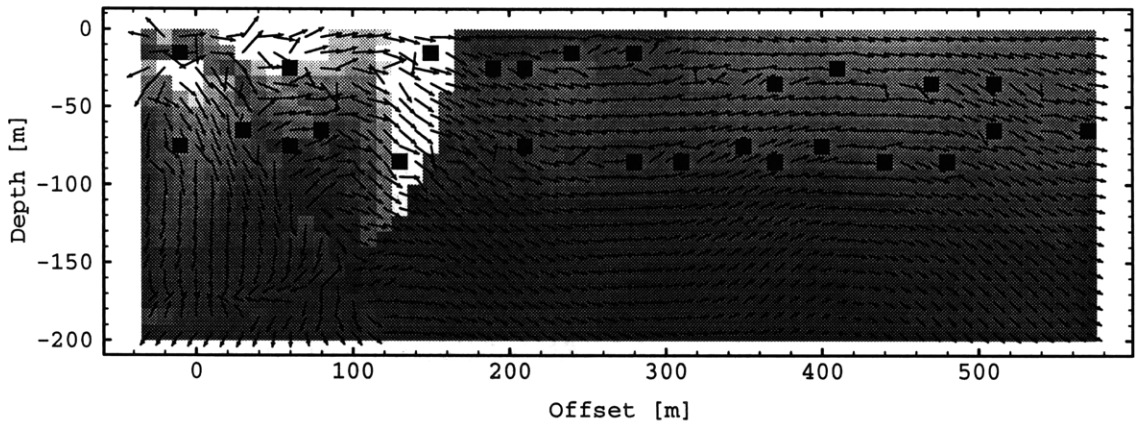

(a)

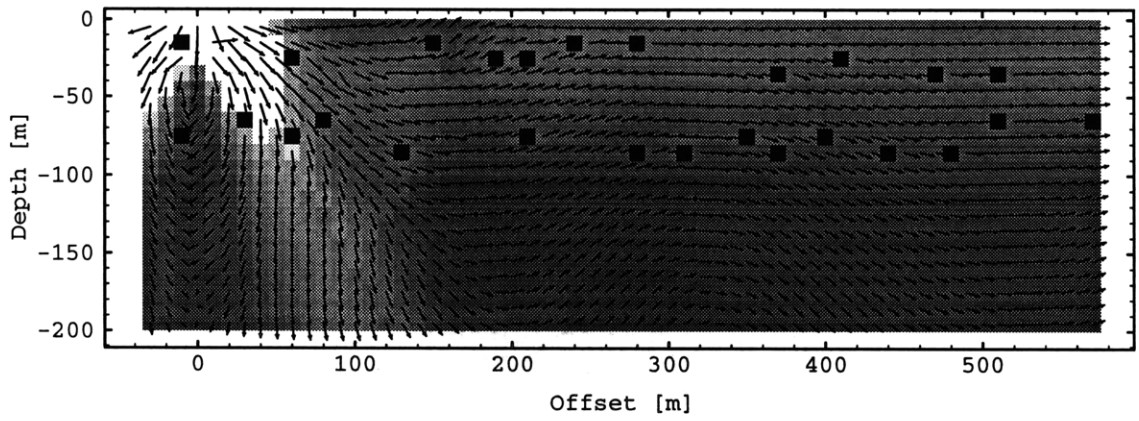

(b)

Figure 6-34: The logarithmic Poynting vector $\frac{\mathbf{S}(\mathbf{x})}{|\mathbf{S}(\mathbf{x})|}\log|\mathbf{S}(\mathbf{x})|$ and the logarithmic energy density $\log E(\mathbf{x})$ of the wavefields for Model 4. The frequency is 10 Hz: (a) scattered field, (b) total field.

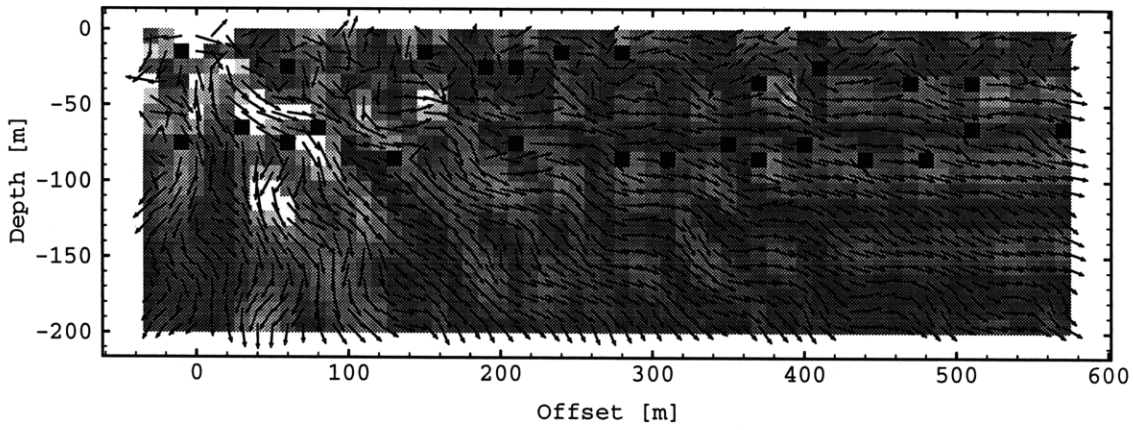

(a)

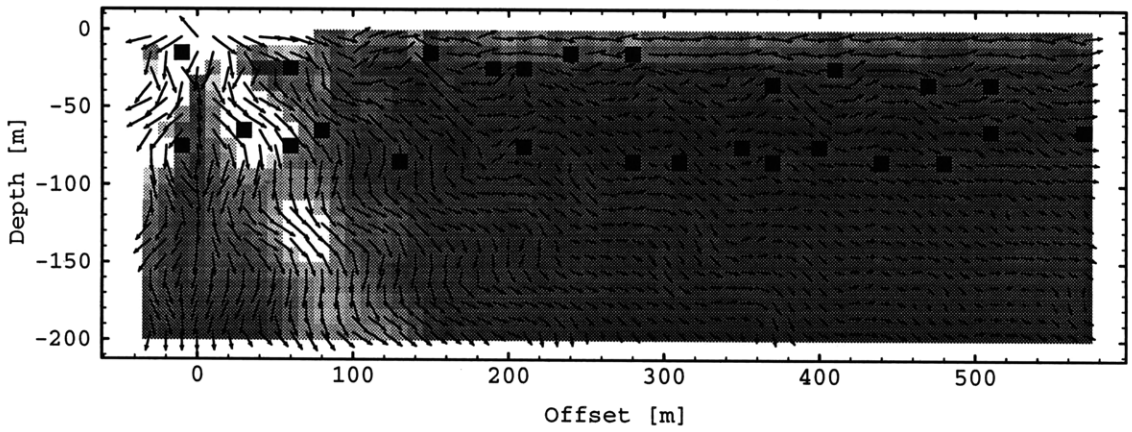

(b)

Figure 6-35: The logarithmic Poynting vector $\frac{\mathbf{S}(\mathbf{x})}{|\mathbf{S}(\mathbf{x})|}\log|\mathbf{S}(\mathbf{x})|$ and the logarithmic energy density $\log E(\mathbf{x})$ of the wavefields for Model 4. The frequency is 50 Hz: (a) scattered field, (b) total field.

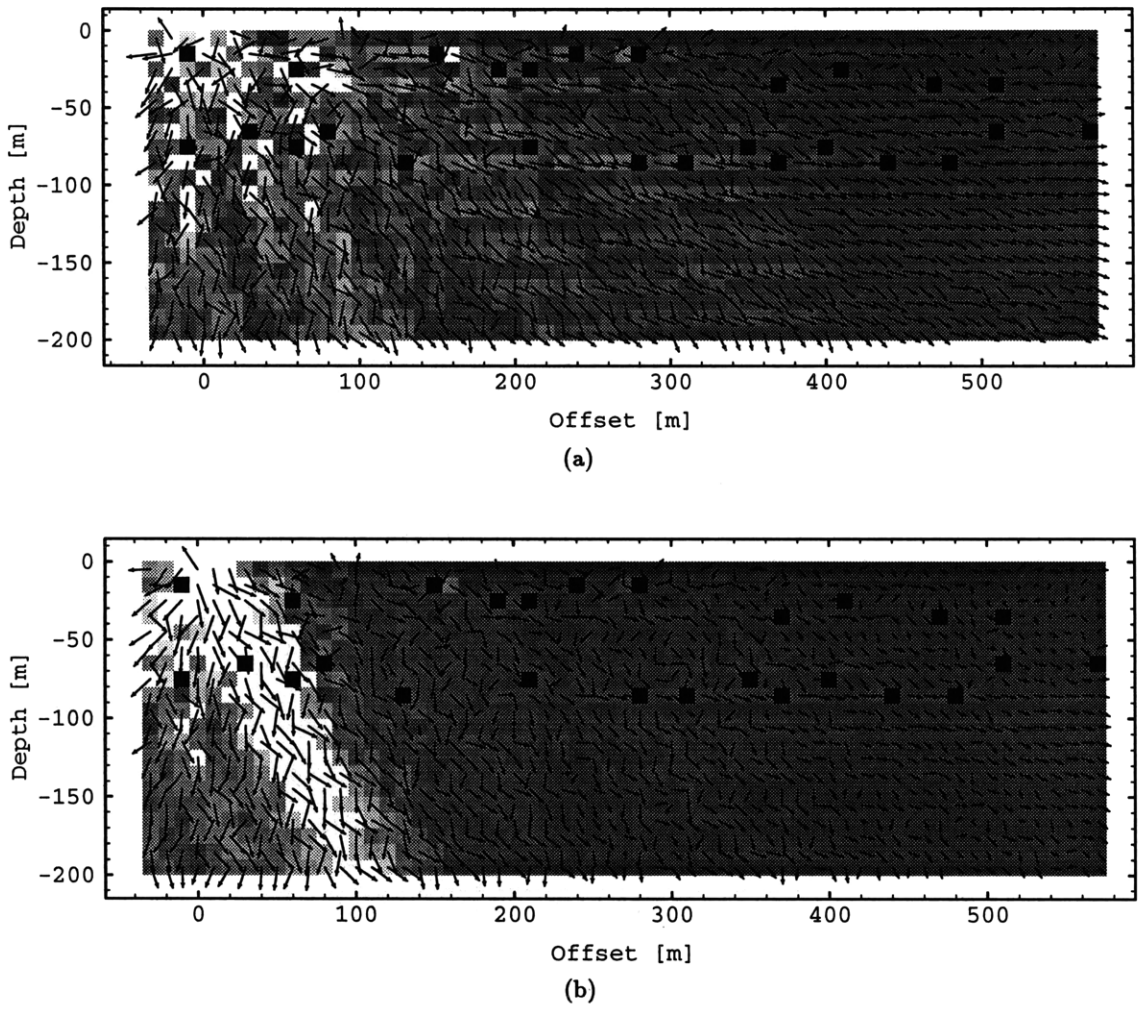

Figure 6-36: The logarithmic Poynting vector $\frac{\mathbf{S}(\mathbf{x})}{|\mathbf{S}(\mathbf{x})|}\log|\mathbf{S}(\mathbf{x})|$ and the logarithmic energy density $\log E(\mathbf{x})$ of the wavefields for Model 4. The frequency is 120 Hz: (a) scattered field, (b) total field.

Chapter 7

Discussion and Outlook

In the course of this thesis, I constructed a framework to solve scattering problems in the frequency domain. In order to obtain full waveform solutions, only deterministic media have been used. The scattering problems were restricted to 2-D which can be calculated in a relatively short time. But the framework is not necessarily restricted to 2-D. The common denominator of the framework is that the scattered wavefields are expanded into some set of basis functions. As a novelty, the set of basis functions does not have to be orthogonal. Numerical experiments showed that non-orthogonal expansion functions are often superior because they need less terms. Also, the approach enhances convergence dramatically. We encountered problems which did not even converge for an orthogonal set of basis functions. The framework is flexible enough to make use of generalized modal expansions (multiple multipole expansions, MMP) which are non-orthogonal, or interpolation functions (finite elements) which are normally orthogonal. In either case, the boundary conditions are used to obtain linear sets of equations which determine the weighting coefficients for the expansion or interpolation functions.

We started with the discrete acoustic scattering problem. One or multiple, fluid scatterers are embedded in a fluid fullspace. Both fluid and scatterers are homogeneous. This problem was used to derive and test the multiple multipole (MMP) method where the scattered

wavefields are expanded into a *non-orthogonal* set of expansion functions which satisfy the homogeneous and unbounded wave equation. The method is named multiple multipole expansions because the wavefield induced by each scatterer is commonly described by a sum over a few multipole solutions with different origins. Each multipole consists of only the first few lower orders. But because the expansion is already non-orthogonal, other solutions to the wave equation can be incorporated as well. In fact, any solution can be used as expansion function which would allow to use the complete solution to another problem as one expansion function. The weighting coefficients are found by evaluating the boundary conditions at discrete points along the boundaries. Because the expansions might be non-orthogonal, more boundary points than needed are used. The resulting overdetermined system of equations is then solved in the least square sense.

The scheme was then expanded to elastic wave propagation. Again, one or multiple homogeneous, elastic scatterers are embedded in a homogeneous background medium. The scattered wavefields are expanded into two MMP solutions, one for P-waves, one for S-waves. Extensive testing yielded a set of rules where to place expansion centers, how many orders of multipole solutions to use and so on.

The MMP expansions were then coupled to the finite element method to overcome the limitation of homogeneous scatterers embedded in a homogeneous background. The waves in the heterogeneous scatterers are modelled by finite elements. MMP expansions are used to propagate the waves from the source to the scatterers, in between scatterers, and then toward the receivers. This hybrid algorithm combines the strengths of both methods and eliminates their main deficiencies. The hybrid problem is solved for both the acoustic as well as the elastic case. As a bonus, the scattered wavefield in the homogeneous regions is by construction decomposed into P- and S-modes for each scatterer.

As an additional test of the MMP method, we combined the acoustic and the elastic cases to calculate the scattering from lucite bars submerged in water. The same model is numerically calculated with MMP expansions and physically measured in an ultrasonic watertank. While the ultrasonic experiments yielded only the total field, the MMP method also pro-

vided the scattered wavefields decomposed by scatterer which aided the interpretation of the ultrasonic experiment. Therefore, particular events in the seismograms could be associated with the emitting lucite bar. The numerical modelling also allowed to extract the effects of the waves interacting with the solids and the water surface.

The expansion functions do not necessarily need to be of multipole form. This feature is exploited to incorporate the effects of a free surface into expansion functions for the elastic background. Thus, it allows to embed scatterers into homogeneous, elastic halfspaces without actually modelling the halfspace. To each multipole solution, we add the asymptotic contribution from reflections, conversions and surface waves. These asymptotic expansion functions were then used to study the effect of small, elliptical cavities embedded in limestone. Interestingly, we found three different regimes of behavior depending on the frequency band of the incident wavefield. 'Low' frequencies are hardly affected by the near-surface cavities. For 'medium' frequencies, complex interference patterns appeared. Also, the cavities began to can act as waveguides. For 'high' frequencies, the energy flux turned increasingly chaotic.

Altogether, multiple multipole expansions proved to be a very effective means to model wave scattering. The overall framework turns out to be flexible enough to encompass MMP expansions, finite elements and the method of moments. Unfortunately, in the scope of the present work only the 2-D case could be covered. An obvious but straight forward expansion is to apply MMP expansions to 3-D problems. An extension of the MMP method to 3-D is both conceptually and algorithmically very simple: the 2-D expansion functions as well as the boundary conditions have to be replaced by their respective 3-D counterparts.

Using the MMP method in 3-D, it is nearly inevitable to replace the direct solver scheme with an iterative schemes, e.g. a conjugate gradient method. Iterative schemes fit perfectly into the present framework because they allow (or even demand) the use of prior solutions, e.g. from a different frequency, as initial solution to enhance the convergence and to speed up the algorithm. An iterative solver scheme would have been useful in the 2-D case as well. Unfortunately, there exist two different kinds of convergence which need to be

distinguished. First, there is the convergence of a particular discretization. How accurate is a solution obtained from a particular discretization, e.g. number, order, and location of multipoles and matching points? Which discretizations are 'good'? The second kind of convergence is due to the solver scheme. Direct methods, e.g. QR decomposition, are very robust and yield good results. The performance of iterative schemes often depends on the initial solution and the applied preconditioning. Although direct schemes are slower, we favored them while trying to infer the rules of MMP discretizations. We abstained from iterative schemes to avoid the additional complications. Now that rules are found and MMP discretizations are fairly stable, iterative solver schemes should be used. The direct solvers will still be useful to obtain benchmark solutions for the iterative schemes.

The study of near surface scattering hints toward another extension of this work: to use this and similar schemes to study the effect of many discrete, deterministic scatterers. Due to the dramatic change in the behavior of scattering when going from 2-D to 3-D, the schemes should be adapted to 3-D in order to be useful for real, geophysical problems. With increasing complexity of the models, some combination of deterministic and stochastic scattering will be necessarily. Actually, this final step would close the circle as wave propagation in random medium was the initial starting point to the present thesis.

Appendix A

Matrix Methods for Numerical Wave Scattering

Many methods to solve wave propagational problems expand the solution in some kind of series:

$$p(\mathbf{x}) = \sum_{i=-\infty}^{+\infty} a_i \phi_i(\mathbf{x}) \,. \tag{A.1}$$

Even solutions which appear to be exact and analytic are in fact series: e.g. $\sin(kx)$ or $H_0^{(1)}(kr)$. They are actually *defined by their series expansions* which is called the Frobenius series (Hildebrand, 1976). The unknown coefficients a_i are defined by a recurrence relation and the initial conditions. But in the general case, the coefficients a_i are not related by recurrence and are determined by the initial and boundary conditions.

Expressing the solution as series commonly means to discretize the solution by truncating the range of the series or by choosing a finite sampling interval. Examples are:

- Mode Matching (MM) (Chew *et al.*, 1984; Peng and Toksöz, 1994)
- Modal Expansions (ME) (Morse and Feshbach, 1953; Pao and Mow, 1973)

- Method of Moments (MoM) (Harrington, 1968; Thompson *et al.*, 1994)
- Finite Differences (FD) (Kelly *et al.*, 1976; Virieux, 1985, 1986; Cheng *et al.*, 1994)
- Finite Elements (FE) (Zienkiewicz, 1977; Murphy and Chin-Bing, 1989, 1991)
- Boundary Element Methods (BEM) (Brebbia and Dominguez, 1989; Bouchon, 1993; Dong *et al.*, 1995) or Boundary Integral Methods (BIEM) (Schuster and Smith, 1985)
- Discrete Wavenumber Integration methods (DWI) (Bouchon and Aki, 1977; Haartsen *et al.*, 1994) or Aki-Larner Method (AL) (Aki and Larner, 1970)
- Spectral Domain Analysis (SDA) (Gottlieb and Orszag, 1977; Voigt *et al.*, 1984; Chu *et al.*, 1992; Kuo, 1995)
- Multiple Multipole Expansions (MMP) and Generalized Matching Techniques (GMT) (Hafner and Ballisti, 1983; Hafner, 1990; Imhof, 1995)

All these methods reduce the task of determining $p(\mathbf{x})$ at *all* points in space to finding a finite number of coefficients a_i. Moreover, using a series solution also means to transform the original integro-differential equation into a set of linear equations and thus into a matrix problem.

Altogether, (1) the fields, (2) the geometry, (3) time or frequency and, (4) the field equations in the domains or the boundary conditions have to be made discrete to facilitate numerical computations (Hafner, 1990; Hafner and Bomholt, 1993).

A.1 Discretization of Fields

The fields can be made discrete in various manners (Hafner, 1990; Hafner and Bomholt, 1993). For example, one can just give their values in distinct points of space, or break the fields into suitable components, and so on. In general, every field or field component either can be approximated directly by a series expansion or can be derived from other

quantities or field components. The former will be called *primary* and the later *secondary.* For example, if pressure is chosen to be the primary quantity, the displacement becomes a secondary one. Thus, the primary pressure field p is expanded into the following series expansion:

$$p = p_0 + \sum_{n=1}^{N} a_n p_n + \epsilon\,, \tag{A.2}$$

where p_n are the basis functions and a_n are the corresponding weighting coefficients which have to be determined. Finally, ϵ denotes the error function due to truncation and discretization. The function p_0 does not seem to make much sense here. But we will use it later to take care of the particular solution of inhomogeneous field equations, boundary conditions, and to implement sources. If a secondary field $\mathbf{u}$ can be derived from p by a linear operator $\mathcal{F}$, one has

$$\mathbf{u} = \mathcal{F}p = \mathcal{F}p_0 + \sum_{n=1}^{N} a_n \mathcal{F}p_n + \mathcal{F}\epsilon \tag{A.3}$$

or

$$\mathbf{u} = \mathbf{u}_0 + \sum_{n=1}^{N} a_n \mathbf{u}_n + \epsilon\,. \tag{A.4}$$

The wave equation in operator notation can be written as

$$\mathcal{D}p = d \tag{A.5}$$

where $\mathcal{D}$ is the wave operator, p the unknown function, e.g., the pressure and d is an inhomogeneity such as a source. We assume that the relation (A.5) has a unique solution and that $\mathcal{D}$ is linear. It is also assumed that the space can be explicitly divided into domains Γ^i and boundaries $\partial\Gamma_{ij}$ between the domains Γ^i and Γ^j. For the sake of simplicity, we assume that there is only one domain Γ with boundary $\partial\Gamma$. However, it can easily generalized for

multiple domains and boundaries. Then, the operator equation (A.5) splits up into

$$Lp = g \qquad \text{in} \quad \Gamma \tag{A.6a}$$

$$\mathcal{L}p = h \qquad \text{on} \quad \partial\Gamma\,. \tag{A.6b}$$

The analytical solution of (A.5) or (A.6) is usually only possible for very simple geometries. Otherwise, expansion methods have to be used which means to discretize (A.5) into a series such as (A.1).

For fast codes for numerical field computations, one may believe that basis functions which are easily computed are preferable. Such functions are to their first order similar to Dirac delta functions (Morse and Feshbach, 1953) which have the value 1 in a single point $\mathbf{x}$ and the value 0 everywhere else or boxcar functions which have the value 1 over a small extended region and vanish everywhere else. These functions have the important drawbacks that their derivatives are not defined around $\mathbf{x}$. Hence, integral formulations are required which move the derivatives to other terms by partial integration. Sometimes, methods based on integral equations are claimed to be superior to those based on a differential formulation for exactly this reason. However, it seems that a choice of basis functions requiring an integral formulation is inferior to a choice which allows the direct application of differential formulations as well.

Furthermore with the exception of very small problems, the average computation time for the basis functions is quite small compared to the time spent solving for the unknown parameters a_i. But the total number of unknowns, N, can often be reduced dramatically if more appropriate basis functions are used. It is worthwhile to look for more complicated functions like piecewise linear functions, polynomials, spline functions, harmonic functions and others which allow the application of differential operators such as the Laplacian one and solve either the field equations or the boundary conditions. On the other hand, functions or analytical solutions which solve both the boundary conditions and the field equations can usually only be found for very simple problems. To distinguish the different approaches, we introduce four different sets of basis functions: (1) analytical, (2) semianalytical, (3)

seminumerical, and (4) numerical (Hafner, 1990; Hafner and Bomholt, 1993).

A.1.1 Analytical Discretization

The basis function p_0 of a purely analytical approach satisfies both the field equations and the boundary conditions. Thus, p_0 is the unique solution of problems with an inhomogeneity either in the field equations or in the boundary conditions. The additional expansion functions p_n obey the corresponding homogeneous field equations and boundary conditions. In fact, the functions p_n are the eigenfunctions or modes of the eigenvalue problem. Although they are analytical solutions, the functions p_0 and p_n have to be approximated numerically for any problem of interest which limits the accuracy and use of the approach.

A.1.2 Semianalytical Discretization

The basis functions are chosen to satisfy (A.6a) exactly while (A.6b) is only approximated. The general solution of (A.6a) has the form

$$p = p_0 + \sum_{n=1}^{N} a_n p_n + \epsilon\,, \tag{A.7}$$

where p_0 is the particular solution of the inhomogeneous problem $\mathcal{L}p_0 = g$ and the functions p_n are the homogeneous solutions to $\mathcal{L}p_n = 0$. Thus, we have

$$\sum_{n=1}^{N} a_n \mathcal{L}p_n = h - \mathcal{L}p_0 + \epsilon = h' + \epsilon\,, \tag{A.8}$$

where the inhomogeneity h and the particular solution can be merged into a new inhomogeneity $h' = h - \mathcal{L}p_0$. Without any loss in generality, we will therefore incorporate $\mathcal{L}p_0$ in the inhomogeneity h

$$\sum_{n=1}^{N} a_n \mathcal{L}p_n = h + \epsilon\,. \tag{A.9}$$

Examples for semianalytical methods are MMP or BEM.

A.1.3 Seminumerical Discretization

Seminumerical discretization is similar to semianalytical discretization, but the roles of the boundary and the domain are exchanged. The basis functions satisfy (A.6b) exactly while (A.6a) is only approximated. Thus, in analogy to (A.9), the following equation is obtained:

$$\sum_{n=1}^{N} a_n L p_n = g + \epsilon \,. \tag{A.10}$$

Examples for seminumerical methods are MoM or FEM.

A.1.4 Numerical Discretization

In many cases, it is impossible to choose expansion functions p_n which solve either of (A.6) exactly. Expansion functions have to be chosen which only approximate (A.5) or both of (A.6). Thus, we obtain the following equation to solve.

$$\sum_{n=1}^{N} a_n \mathcal{D} p_n = d + \epsilon \tag{A.11}$$

This situation is commonly encountered when the materials are heterogeneous. For simple interpolation functions, the FEM uses a numerical discretization.

A.2 Discretization of Geometry

Each of the different methods described previously has different requirements of how the geometry and thus the material properties should be given (Hafner, 1990; Hafner and Bomholt, 1993).

1. Purely analytical approaches usually require no discretization of the geometry at all. The complete configuration is contained in the expansions. As stated previously, such solutions are normally only available for problems with a very simple geometry.

2. Semianalytical approaches require at least a discretization of the boundaries.

3. Seminumerical approaches require at least a discretization of the domains.

4. Purely numerical approaches require a discretization of both boundaries and domains.

A.3 Discretization of Time and Frequency

Not only do we have to discretize space, but also time requires discretization. To introduce the dependence on time, we write (A.5) as

$$\mathcal{D}p(t) = d(t)\,. \tag{A.12}$$

Unless we can find analytical expressions, it is not possible to solve this for an infinite duration. But even if the duration is limited to some time interval $[0,T]$, the problem is often still far too complex. Thus, the time evolution is only solved at discrete times, $k\Delta t$, where $k \in \{0,1,2,\ldots,N\}$, Δt is the sampling interval and $N = T/\Delta t$. If needed, the time evolution between $(n-1)\Delta t$ and $n\Delta t$ can be obtained by interpolation.

Alternatively, linear problems can be transformed into the frequency domain. Instead of solving (A.13) for all frequencies, it is only solved for some discrete frequencies, $n\Delta\omega$, where $n \in \{0,1,2,\ldots,N\}$ where $\Delta\omega = 2\pi/N\Delta t$.

$$\tilde{\mathcal{D}}\tilde{p}(\omega) = \tilde{d}(\omega)\,. \tag{A.13}$$

Because both frequency and time are discrete parameters, a discrete Fourier transformation (DFT) can be used to go from the frequency to time (Bracewell, 1986; Brigham, 1988).

Thus, we have

$$p(k\Delta t) = \frac{1}{N} \sum_{n=0}^{N-1} \tilde{p}(n\Delta\omega) e^{2\pi i k n/N} . \tag{A.14}$$

In practice, the use of the DFT will result in aliasing in the time-domain due to the periodicity in time and frequency implied by the DFT (Aki and Larner, 1970). This effect can be removed by giving a small imaginary part, $\omega_I = \pi/N\Delta t$, to the frequency, chosen such that disturbances which do not belong to the time window of interest are attenuated enough for their contribution to be negligible. The effect of the imaginary part of the frequency can be removed from the time window of interest by scaling with $e^{\omega_I k \Delta t}$. Equivalently, the DFT can be written as

$$p(k\Delta t) = \frac{e^{\omega_I k \Delta t}}{N} \sum_{n=0}^{N-1} \tilde{p}(n\Delta\omega) e^{2\pi i k n/N} . \tag{A.15}$$

A.4 Discretization of Equations

In order to solve a particular scattering problem, we have to solve for the unknown weighting coefficients a_n (Hafner, 1990; Hafner and Bomholt, 1993). We aim at setting up a linear system of equations

$$[A_{ij}][a_j] \approx [b_i] \qquad \text{where} \quad 1 \leq i \leq M \quad \text{and} \quad 1 \leq j \leq N \leq M \tag{A.16}$$

which minimizes the error ϵ defined in the discretizations (A.9) to (A.11) in some way. This system (A.16) can then be solved by known methods of linear algebra.

Both the primary and secondary fields are involved either directly or indirectly in the field equations and the boundary conditions. The unknown coefficients a_n have to be chosen in such a way that the error function ϵ is sufficiently small. Of course, we would like to minimize the error function ϵ in some sense. We need a mathematical measure which allows us to define the minimum. For a scattering problem which contains primary and secondary fields,

there are different choices possible. One could try to minimize ϵ. Choosing a functional $\mathcal{F}\epsilon$ to obtain a secondary field, we could also minimize $\mathcal{F}\epsilon$ or even the combination $\alpha\epsilon + \beta\mathcal{F}\epsilon$ where α and β are arbitrary constants.

A.4.1 Error Minimization Method

In the error minimization method, a functional $\mathcal{E}$ of the error e shall be minimized:

$$\mathcal{E}\epsilon = \min . \tag{A.17}$$

Commonly, the chosen functional $\mathcal{E}$ is square norm of the error function ϵ within the function space spanned by the p_n:

$$\mathcal{E}\epsilon = \oint_{\partial\Gamma} w_\epsilon \epsilon^* \epsilon \, ds = \min , \tag{A.18}$$

where the superscript * implies the complex conjugate. The factor w_ϵ is a positive real weighting function. For the semianalytical approach (A.9) we obtain:

$$\mathcal{E}\epsilon = \oint_{\partial\Gamma} w_\epsilon \left(\sum^{n} a_n \mathcal{L}p_n - h \right)^* \left(\sum^{n} a_n \mathcal{L}p_n - h \right) ds = \min \tag{A.19}$$

which expands into

$$\sum^{i}\sum^{j} a_i^* \cdot \oint_{\partial\Gamma} w_\epsilon \left(\mathcal{L}p_i\right)^* \left(\mathcal{L}p_j\right) \, ds \cdot a_j - \sum^{i} a_i^* \cdot \oint_{\partial\Gamma} w_\epsilon \left(\mathcal{L}p_i\right)^* h \, ds - \sum^{j} \oint_{\partial\Gamma} w_\epsilon h^* \left(\mathcal{L}p_j\right) \, ds \cdot a_j = \min \tag{A.20}$$

where constant terms have been neglected because they do not affect the minimization. Differentiating (A.20) with respect to the unknown weighting coefficients a_j^* yields a set of

linear equations

$$\sum^{i}\sum^{j}\oint_{\partial\Gamma} w_\epsilon\,(\mathcal{L}p_i)^*\,(\mathcal{L}p_j)\;ds\cdot a_j = \sum^{i}\oint_{\partial\Gamma} w_\epsilon\,(\mathcal{L}p_i)^*\,h\,. \tag{A.21}$$

In matrix notation, this reduces to

$$[A_{ij}][a_j] = [b_i] \qquad \text{where} \quad 1\le i\le N \quad \text{and} \quad 1\le j\le N\,. \tag{A.22}$$

In fact, the error minimization method corresponds to the traditional least-squares method.

A.4.2 Projection Method

In the projection method, the error function ϵ is orthogonalized relative to a function space spanned by testing functions t_i defined on the boundary. We define the inner product (f,g) to be

$$\oint_{\partial\Gamma} w_t f^* g\,ds\,, \tag{A.23}$$

where w_t is a positive real weighting function. By orthogonality, we obtain the condition

$$(\epsilon, t_i) = 0 \qquad \text{for} \quad 1\le i\le N\,. \tag{A.24}$$

Applying (A.24) onto (A.9) yields a set of linear equations:

$$\sum^{i}\sum^{j}\oint_{\partial\Gamma} w_t t_i^*\,(\mathcal{L}p_j)\;ds\cdot a_j = \sum^{i}\oint_{\partial\Gamma} w_t t_i^* h\,ds\,. \tag{A.25}$$

In matrix notation, this reduces to

$$[A_{ij}][a_j] = [b_i] \qquad \text{where} \quad 1\le i\le M \quad \text{and} \quad 1\le j\le N\,. \tag{A.26}$$

Usually as many testing functions t_i as unknowns a_j are used ($M=N$). For $M>N$, the system is underdetermined. For $M>N$, the resulting overdetermined system of equations

cannot be solved without admitting a residual error in (A.24) which should be minimized by the solution.

Commonly, one chooses some functional $\mathcal{H}p_i$ of expansion functions p_i as testing functions t_i. In particular, *Galerkin's method* (Galerkin, 1915; Fletcher, 1984) chooses $t_i = \mathcal{I}p_i = p_i$. The choice of $t_i = \mathcal{L}p_i$ yields formally the same result as the error minimization method. Another possibility is to use the secondary fields as testing functions $t_i = \mathcal{F}p_i$. Especially for large M, N numerical evaluation of all these inner products is very costly. To reduce computational effort, one also chooses piecewise constant functions (boxcars) or even the Dirac delta functions δ_i as testing functions t_i.

A.4.3 Point Matching Methods

In the point matching method, the error function ϵ is set to zero in single points s_i along the boundary $\partial\Gamma$.

$$\epsilon(s_i) = 0 \qquad \text{for} \quad 1 \leq i \leq N \quad \text{and} \quad s_i \in \partial\Gamma \tag{A.27}$$

Formally, this can be achieved by using the Dirac delta functions $\delta_i = \delta(s_i)$ as test functions t_i in (A.25):

$$\sum^{i}\sum^{j} \oint_{\partial\Gamma} w_p \delta_i^* \left(\mathcal{L}p_j\right) \, ds \cdot a_j = \sum^{i} \oint_{\partial\Gamma} w_p \delta_i^* h \,, \tag{A.28}$$

where w_p is a positive real weighting function. Evaluating the integrals, the expression reduces to

$$\sum^{i}\sum^{j} w_p \mathcal{L}p_j\Big|_{s_i} \cdot a_j = \sum^{i} w_p h\Big|_{s_i} \tag{A.29}$$

or in matrix notation

$$[A_{ij}][a_j] = [b_i] \qquad \text{where} \quad 1 \leq i \leq M \quad \text{and} \quad 1 \leq j \leq N \,. \tag{A.30}$$

The simple case where $M = N$ is also called *collocation*. The general case $M > N$ leads to an overdetermined system of equations. A solution can only be found when a residual error $\epsilon_i = \epsilon(s_i)$ at the matching point s_j is allowed. The desired solution minimizes the residual errors ϵ_i in the least-squares sense

$$\sum^{i} \epsilon_i^* \epsilon_i = \min \tag{A.31}$$

which means to solve the normal equations

$$\sum^{i}\sum^{j}\sum^{k} w_p^2 (\mathcal{L}p_k)^* \mathcal{L}p_j \Big|_{s_i} \cdot a_j = \sum^{i}\sum^{k} w_p^2 (\mathcal{L}p_k)^* h \Big|_{s_i} \tag{A.32}$$

or in matrix notation

$$[A_{ki}]^* [A_{kj}][a_j] = [A_{ki}]^* [b_i] \tag{A.33}$$

instead of the system (A.30). Experience shows that the solution of the collocation method depends much more on the actual position of the matching points than in the generalized case. Although the error is exactly zero in the matching points, it can oscillate wildly between them. Allowing a residual error in the matching point leads to a much flatter and smoother error function ϵ.

A.4.4 Comparison of the Methods

Some equivalences between the methods have already been described:

1. The error minimization method (A.21) is equivalent to a projection method with the testing functions $t_i = \mathcal{L}p_i$.

2. The point matching method is equivalent to a projection method with Dirac delta functions as testing functions.

3. The error method and Galerkin's method become equivalent if the p_i are eigenfunctions of $\mathcal{L}$ and thus $p_i \propto \mathcal{L}p_i$.

Both integrals (A.21) and (A.25) are normally evaluated numerically which allows us to reformulate them as Riemann sums (Schwarz, 1989):

$$\oint_{\partial\Gamma} wf^*g\,ds \approx \sum_{k=1}^{K} wf^*g\Big|_{s_k} \Delta s_k\,. \tag{A.34}$$

Thus, the integration in the error method (A.21) becomes

$$\sum^{i}\sum^{j}\sum^{k} w_\epsilon\,(\mathcal{L}p_i)^*\,(\mathcal{L}p_j)\Big|_{s_k} \Delta s_k \cdot a_j = \sum^{i}\sum^{k} w_\epsilon\,(\mathcal{L}p_i)^*\,h\Big|_{s_k} \Delta s_k\,. \tag{A.35}$$

Similarly, the integration in the projection method reduces to

$$\sum^{i}\sum^{j}\sum^{k} w_t t_i^*\,(\mathcal{L}p_j)\Big|_{s_k} \Delta s_k \cdot a_j = \sum^{i}\sum^{k} w_t t_i^* h\Big|_{s_k} \Delta s_k\,. \tag{A.36}$$

For comparison, we also repeat the resulting expressions (A.29) and (A.32) for the point matching method. Note that the indices i and k are switched to facilitate comparisons.

$$\sum^{j}\sum^{k} w_p \mathcal{L}p_j\Big|_{s_k} \cdot a_j = \sum^{k} w_p h\Big|_{s_k} \tag{A.29$'$}$$

$$\sum^{i}\sum^{j}\sum^{k} w_p^2 (\mathcal{L}p_i)^* \mathcal{L}p_j\Big|_{s_k} \cdot a_j = \sum^{i}\sum^{k} w_p^2 (\mathcal{L}p_i)^* h\Big|_{s_k} \tag{A.32$'$}$$

Additional equivalences can be identified if the matching points s_k in (A.35) are the same in (A.36), (A.29$'$), and (A.32$'$).

4. The generalized point matching method with least-squares solutions (A.32$'$) becomes equivalent to the error minimization method (A.35) if the weighting function w_p is chosen appropriately

$$w_p^2 = w_\epsilon \Delta s_k\,. \tag{A.37}$$

5. The projection method (A.36) can be viewed as a preconditioning of the generalized point matching method (A.29′) with a another matrix $[T_{ik}]$ of size N by M whose elements t_{ik} are the testing functions t_i evaluated at position at position s_k. Of course, this is just another way to obtain a square system of linear equations.

$$[T_{ik}]^*[A_{ij}][a_j] = [T_{ik}]^*[b_k]\,. \tag{A.38}$$

But (A.33) is more common and yields often 'better' results.

An additional advantage of the generalized point matching technique is that the normal equations (A.33) or the more general (A.38) never have to be build explicitly. Instead, (A.30) can be solved directly in the least-squares sense which is numerically superior because the condition number of $[A_{ij}]$ is much smaller than for $[A_{ij}]^*[A_{ij}]$.

A.5 Solving the System of Equations

In the most general case we consider, all three methods are used to obtain equations which yields an equation system, $\mathbf{A} \cdot \mathbf{a} = \mathbf{h}$. After rearranging rows and columns, we end up with an equation system of the following form: The equations arising from the error minimization method compose a hermitian, positive definite submatrix $\mathbf{H}$ of size $N_H \times N_H$. Often, $\mathbf{H}$ even has a banded structure. Equations derived by the projection method build a square submatrix $\mathbf{S}$ of size $N_S \times N_S$ which is normally just dense without additional symmetry. Lastly, equations obtained by generalized point matching form a rectangular, dense submatrix $\mathbf{R}$ of size $M_R \times N_R$. Additional submatrices $\mathbf{A}_{12}$, $\mathbf{A}_{21}$ (square) and $\mathbf{A}_{13}$, $\mathbf{A}_{23}$, $\mathbf{A}_{31}$, $\mathbf{A}_{32}$ (rectangular) couple $\mathbf{H}$, $\mathbf{S}$ and $\mathbf{R}$ together.

$$\begin{pmatrix} \mathbf{H} & \mathbf{A}_{12} & \mathbf{A}_{13} \\ \mathbf{A}_{21} & \mathbf{S} & \mathbf{A}_{23} \\ \mathbf{A}_{31} & \mathbf{A}_{32} & \mathbf{R} \end{pmatrix} \cdot \begin{pmatrix} \mathbf{a}_H \\ \mathbf{a}_S \\ \mathbf{a}_R \end{pmatrix} = \begin{pmatrix} \mathbf{h} \\ \mathbf{s} \\ \mathbf{r} \end{pmatrix} \tag{A.39}$$

The problem at hand is to reduce this combined system to solve for the solution vector **a**. Unfortunately, the three different submatrices **H**, **S** and **R** have totally different structures, mathematical properties, and physical meanings. Figure A-1 depicts the submatrices and the completely reduced matrix we seek.

The hermitian submatrix **H** would be solved best by a Cholesky decomposition (Strang, 1988) which yields $\mathbf{H} = \mathbf{L}\mathbf{L}^\dagger$ or $\mathbf{H} = \mathbf{U}^\dagger\mathbf{U}$ where the superscript † denotes conjugate transpose and **L**, **U** are lower, respectively upper, triangular matrices. The reason to use Cholesky decomposition is to take advantage of the symmetry of the matrix **H**. As mentioned priorly, the evaluation of the matrix elements (A.21) might be costly due to the integrations. Thus, making use of the symmetry cuts the time to evaluate the integrals roughly in half. Also, the amount of memory needed to store the matrix is approximately halfed.

The square submatrix **S** can be solved exactly by LU decomposition (Strang, 1988) which yields $\mathbf{S} = \mathbf{L}\mathbf{U}$ where **L**, **U** are lower, respectively upper, triangular matrices.

Finally, the rectangular matrix **R** is reduced directly by Givens rotations (Strang, 1988) which decompose **R** into **QU** where **Q** is a square, unitary matrix and **U** is again an upper triangular matrix. There is no need to build the normal equations implicitly or explicitly.

Chaining all three decomposition one after the other yields:

$$\begin{pmatrix} \mathbf{H} & \mathbf{A}_{12} & \mathbf{A}_{13} \\ \mathbf{A}_{21} & \mathbf{S} & \mathbf{A}_{23} \\ \mathbf{A}_{31} & \mathbf{A}_{32} & \mathbf{R} \end{pmatrix} \xrightarrow{\mathbf{U}^\dagger\mathbf{U}} \begin{pmatrix} \tilde{\mathbf{H}} & \tilde{\mathbf{A}}_{12} & \tilde{\mathbf{A}}_{13} \\ \mathbf{0} & \mathbf{S}' & \mathbf{A}'_{23} \\ \mathbf{0} & \mathbf{A}'_{32} & \mathbf{R}' \end{pmatrix}$$
$$\xrightarrow{\mathbf{LU}} \begin{pmatrix} \tilde{\mathbf{H}} & \tilde{\mathbf{A}}_{12} & \tilde{\mathbf{A}}_{13} \\ \mathbf{0} & \tilde{\mathbf{S}} & \tilde{\mathbf{A}}_{23} \\ \mathbf{0} & \mathbf{0} & \mathbf{R}'' \end{pmatrix} \xrightarrow{\mathbf{QU}} \begin{pmatrix} \tilde{\mathbf{H}} & \tilde{\mathbf{A}}_{12} & \tilde{\mathbf{A}}_{13} \\ \mathbf{0} & \tilde{\mathbf{S}} & \tilde{\mathbf{A}}_{23} \\ \mathbf{0} & \mathbf{0} & \tilde{\mathbf{R}} \end{pmatrix} \quad \text{(A.40)}$$

where $\tilde{\mathbf{H}}$, $\tilde{\mathbf{S}}$ and $\tilde{\mathbf{R}}$ are all of upper triangular form. Explicitly, the decomposition scheme works as follows:

1. (a) In a first step, the subsystem $\begin{pmatrix} \mathbf{H} & \mathbf{A}_{12} & \mathbf{A}_{13} \end{pmatrix}$ is reduced by Cholesky decomposition which transforms $\mathbf{H}$ into upper triangular form $\tilde{\mathbf{H}}$.

   (b) Because $\tilde{\mathbf{H}}$ is of triangular form, it is very easy to eliminate the first N_H unknowns from the remaining subsystem $\begin{pmatrix} \mathbf{A}_{21} & \mathbf{S} & \mathbf{A}_{23} \\ \mathbf{A}_{31} & \mathbf{A}_{32} & \mathbf{R} \end{pmatrix}$ which eliminates both $\mathbf{A}_{21}$ and $\mathbf{A}_{31}$ and leaves $\begin{pmatrix} \mathbf{S}' & \mathbf{A}'_{23} \\ \mathbf{A}'_{32} & \mathbf{R}' \end{pmatrix}$

2. (a) In the second step, the subsystem $\begin{pmatrix} \mathbf{S}' & \mathbf{A}'_{23} \end{pmatrix}$ is reduced by Gaussian elimination or LU decomposition transforming $\mathbf{S}'$ into upper triangular form $\tilde{\mathbf{S}}$.

   (b) Again, because $\tilde{\mathbf{S}}$ is of triangular form, it is very easy to eliminate the next N_S unknowns from the remaining subsystem $\begin{pmatrix} \mathbf{A}'_{32} & \mathbf{R}' \end{pmatrix}$ which eliminates $\mathbf{A}'_{32}$ and leaves $\begin{pmatrix} \mathbf{R}'' \end{pmatrix}$.

3. In the last and final step, the remaining subsystem $\mathbf{R}''$ is reduced. The subsystem $\mathbf{R}''$ is still a dense and rectangular matrix which is reduced by Givens rotations to yield a square, upper triangular matrix $\tilde{\mathbf{R}}$.

Interestingly, all these decompositions can be performed in a row by row manner by rearranging the loops. Thus, the complete system is never needed. We start with an empty upper triangular matrix $\tilde{\mathbf{A}}$ of size $(N_H + N_S + N_R) \times (N_H + N_S + N_R)$. Whenever a new equation or row is available, it is decomposed or equivalently, unknowns are eliminated until it can be stored in the first available empty row of the triangular matrix. The decomposition and updating scheme is completely analogous to the updating QU and Cholesky decompositions (Dongarra *et al.*, 1979, Chapter 10) with the addition that all three decomposition schemes are used consecutively.

Because the combined decomposition scheme is completely row oriented, it is very easy to parallelize by assigning each node a trapezoidal part of the triangular matrix $\tilde{\mathbf{A}}$. The first node receives the new equations, updates and decomposes its share, and passes the remaining equation to the next processor. A schematic of this pipeline is shown in Figure A-2.

Finally, the solution vector $\mathbf{a}$ is retrieved by backsubstitution.

$$\begin{pmatrix} \tilde{\mathbf{H}} & \tilde{\mathbf{A}}_{12} & \tilde{\mathbf{A}}_{13} \\ \mathbf{0} & \tilde{\mathbf{S}} & \tilde{\mathbf{A}}_{23} \\ \mathbf{0} & \mathbf{0} & \tilde{\mathbf{R}} \end{pmatrix} \cdot \begin{pmatrix} \mathbf{a}_H \\ \mathbf{a}_S \\ \mathbf{a}_R \end{pmatrix} = \begin{pmatrix} \tilde{\mathbf{h}} \\ \tilde{\mathbf{s}} \\ \tilde{\mathbf{r}} \end{pmatrix} \tag{A.41}$$

A.6 Discussion

In Chapter 2, we tackled large acoustic scatterers embedded in a homogeneous, acoustic media. By large we meant that the scatterers were of the same size as the characteristic wavelength of the incident wavefield. Assuming that the scatterers were homogeneous, we used the semianalytical scheme because we knew the Greens functions and its higher order modes analytically. It was advantageous to choose a *non-orthogonal* set of basis functions which basically forced us to choose the generalized point matching scheme to enforce the boundary conditions along the scatterers. Thus, we ended up with a dense rectangular subsystem $\mathbf{R}$. The overall method is called the multiple multipole method MMP (Hafner and Ballisti, 1983; Hafner, 1990; Ludwig, 1989).

In Chapter 4, we replaced the homogeneous scatterers by heterogeneous ones. Thus, neither the Greens function nor any other solution to the wave equation were known a priori. We had to construct the wavefields in the scatterers by the finite element method which we classified earlier as seminumerical or purely numerical depending on the kind of expansion or interpolation functions chosen. To obtain equations, we used the projection method, which yielded a hermitian subsystem $\mathbf{H}$. Because the scatterers were embedded in a homogeneous fullspace, we used again MMP expansions to describe the scattered wavefields in the fullspace. Therefore, we had to solve a hybrid system built by $\mathbf{H}$ (FEM), $\mathbf{R}$ (MMP) and the necessary coupling matrices.

In Appendix C, we sought the wavefields scattered from cavities or rigid bodies smaller than the characteristic wavelength but too large for the Rayleigh approximation (Rayleigh, 1871). We derived a semianalytical scheme which we combined with the projection method. For

one scatterer only, we would have ended up with a hermitian subsystem $\mathbf{H}$. Unfortunately, multiple scatterers the system degenerated to a generic square matrix $\mathbf{S}$.

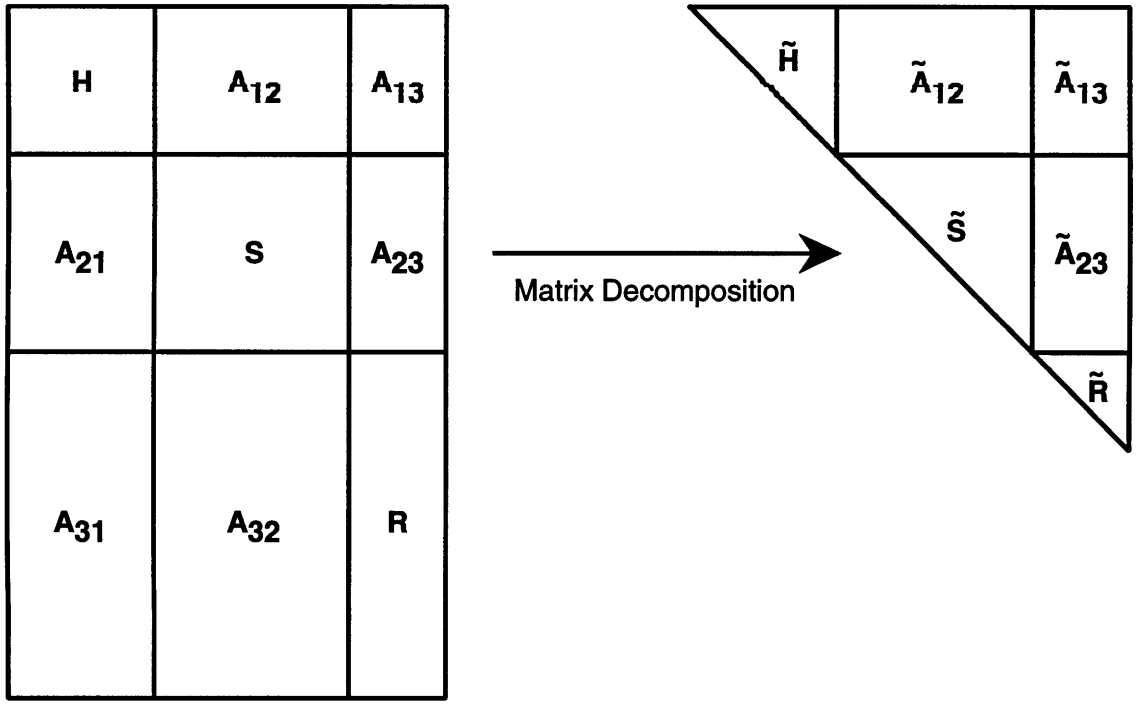

Figure A-1: Reduction of the generic matrix system. The reduced matrix system consists of $\tilde{\mathbf{H}}$ obtained from a hermitian matrix $\mathbf{H}$ by Cholesky decomposition, $\tilde{\mathbf{S}}$ obtained from generic square matrix $\mathbf{S}$ by Gaussian elimination, and $\tilde{\mathbf{R}}$ obtained from a rectangular matrix $\mathbf{R}$ by Givens rotations.

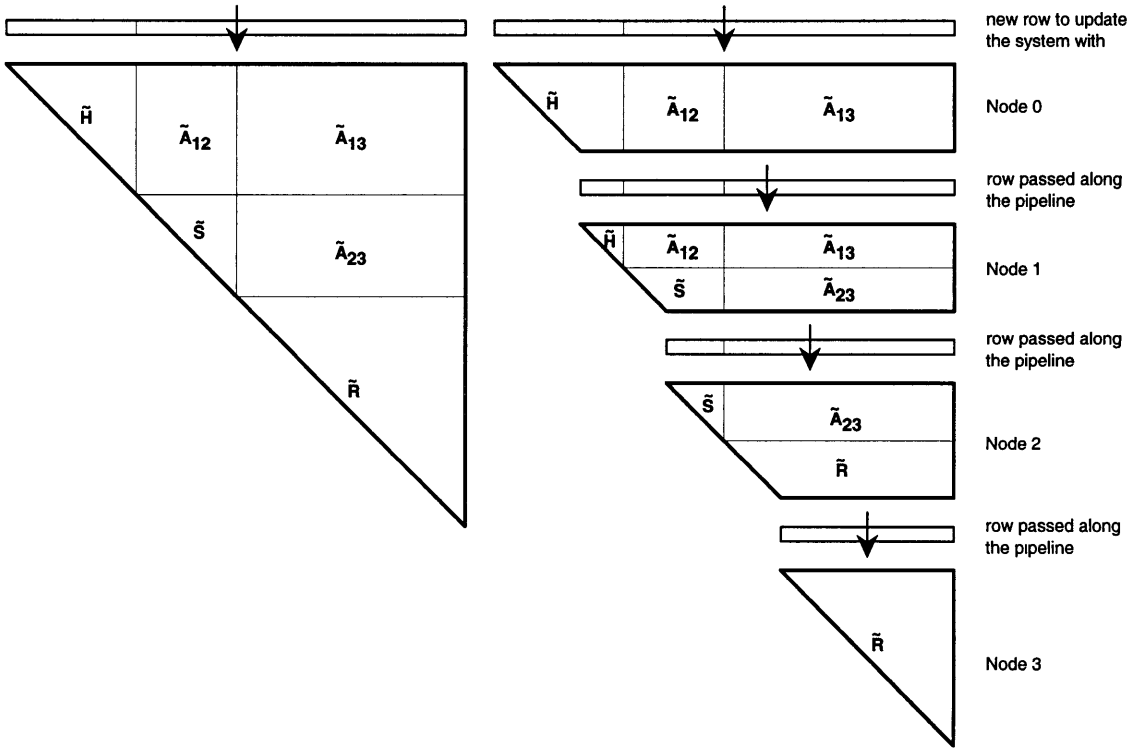

Figure A-2: Schematic of the matrix decomposition pipeline. To the left, the initially empty triangular system is updated by a new row on a single processor. To the right, the triangular system is distributed over 4 nodes. The updating process resembles a pipeline where each processor receives a row, updates its trapezoidal share and passes the remaining row to the next processor. Note that 3 different updating schemes are used together: Cholesky, LU and Givens rotations.

Appendix B

Asymptotic Elastic Free Surface

B.1 Introduction

More realistic models of the earth should include the effect of the free surface which induces additional wave-phases interacting with scatterers. An analytical analysis of the free surface yields the following phases (Lapwood, 1949; Ewing *et al.*, 1957). For a source emanating P-waves, we have:

1. P, a P-wave propagating directly from the source to the receiver.
2. PP, a P-wave reflected as a P at the surface.
3. PS, a P-wave converted into a S-wave at the surface.
4. pSp, the surface S-wave which started and ended as a P but propagated along the surface as a S-wave. It does not satisfy a stationary-time criterion. It is a surface wave being confined to the near neighborhood of the free surface. It is not able to propagate itself and depends on energy supplied by the incident P wave. It is insignificant unless both source and receiver depths are small.

5. pS, the secondary S-wave which started as a P but converted into a S-wave at the interface. Contrarily to the PS-phase, it does not follow a stationary-time path. It is like the pSp except that the attenuation depends only on the source depth.

6. Rayleigh wave: R, a true surface wave which loses no energy to the interior of the elastic but proceeds with undiminished amplitude along the free surface.

Similarly, for a source generating S waves, we obtain:

7. S, the S-wave travelling directly from the source to the receiver.

8. SS, a S-wave reflected at the surface as a S-wave

9. SP, a S wave converted into a P-wave at the surface

10. sPs which started and ended as a S-wave, but travelled most of it's way as a P-wave along the surface. It is not a true surface wave but resembles a body wave being reflected twice at the surface. The path is a minimum time path where the wave propagated to and from the surface as a S wave, but as a P wave along the surface.

11. sP, the secondary P-wave which started as a S-wave but converted into a P-wave at the interface. Contrarily to the SP-phase, it does not follow a stationary-time path.

12. Rayleigh wave: Q. Similar to R, but generated by the incident S wave.

A schematic definition of these waves is presented in Figure B-1. Of these waves, P, PP, PS, S, SS, and SP arise in the case of planar waves. The others are diffraction effects due to the curvature of the wave-fronts impinging on the free surface. In the special case of a receiver close to the surface, P, PP and PS combine, pS and pSp combine, S, sPs and SP combine, and S, SS, sP combine.

Different techniques and methods exist to obtain the exact solution to the free surface problem. Some popular methods are discrete wave number integration DWI (Bouchon and Aki, 1977), the Cagniard-De Hoop method (de Hoop, 1960) or direct evaluation of the complex

contour integral, e.g., by the Sommerfeld path (Chew, 1990; Kong, 1990). Unfortunately, with the exception of DWI these methods are not easily performed numerically. Foreseeing that we will have to evaluate the wavefields for many sources (e.g. scatterers) and many receivers (e.g. boundary conditions along the interfaces of the scatterers), even the DWI is computationally too costly. Thus, we need a different method to account for the free surface. Instead of using the exact but costly solution, we sacrifice accuracy and derive approximative solutions which are numerically more efficient to evaluate. The main difference between the approximation and the exact solution will be the absence of some of the forementioned wave phases 1 – 12.

B.2 Theory

The most prominent features induced by the free surface are the Rayleigh waves R and Q and the primary reflections PP, PS, SP, and SS. Thus, we will concentrate on these phases and neglect the other ones. Describing P-waves as a function of a scalar potential ϕ where the displacement $\mathbf{u} = \nabla\phi$, we synthesize an arbitrary P-wave propagating toward the free surface by superposing all possible plane waves:

$$\phi = \frac{1}{\pi}\int_{-\infty}^{+\infty} \mathrm{w}(k,p)\frac{e^{ipx+i|h-z|\gamma}}{\gamma}\,dp\,, \tag{B.1}$$

where h and z denote the depths of source and receiver, respectively. Also, x is the horizontal distance between source and receiver. For a given wave number $k = \omega/\alpha$, p and $\gamma = \sqrt{k^2 - p^2}$ are the tangential and perpendicular component of the wave number with respect to the free surface. To satisfy the radiation condition, we choose the root such that $\Im m\,\gamma < 0$ for $z < 0$. Finally, $\mathrm{w}(k,p)$ is a weighting function which varies continuously and slowly with the argument p.

To satisfy the boundary conditions at the free surface, we need a P- as well as a S-wave propagating downwards. Describing the S-wave by a vector potential $\boldsymbol{\psi} = \psi\hat{\mathbf{y}}$, we can again

synthesize the fields by superposition:

$$\phi_{pp} = \frac{1}{\pi}\int_{-\infty}^{+\infty} \mathrm{w}(k,p)\,\mathrm{PP}(p)\frac{e^{ipx+i(h+z)\gamma}}{\gamma}\,dp\,, \tag{B.2}$$

$$\psi_{ps} = \frac{1}{\pi}\int_{-\infty}^{+\infty} \mathrm{w}(k,p)\,\mathrm{PS}(p)\frac{e^{ipx+ih\gamma+iz\delta}}{\gamma}\,dp\,, \tag{B.3}$$

where $\delta = \sqrt{l^2-p^2}$ and $l = \omega/\beta$. Again we require that $\Im m\,\delta < 0$ for $z < 0$. The coefficients $\mathrm{PP}(p)$ and $\mathrm{PS}(p)$ are the reflection coefficients necessary to satisfy the boundary conditions along the free surface:

$$\mathrm{PP}(p) = \frac{4p^2\gamma\delta - \left[l^2-2p^2\right]^2}{4p^2\gamma\delta + \left[l^2-2p^2\right]^2} = -1 + \frac{8p^2\gamma\delta}{\mathrm{R}(p)} \tag{B.4}$$

$$\mathrm{PS}(p) = -\frac{4p\gamma\left[l^2-2p^2\right]}{4p^2\gamma\delta + \left[l^2-2p^2\right]^2} = -\frac{4p\gamma\left[l^2-2p^2\right]}{\mathrm{R}(p)} \tag{B.5}$$

where $\mathrm{R}(p) = 4p^2\gamma\delta + \left[l^2-2p^2\right]^2$ defines the Rayleigh function. At $p = p_r$ the Rayleigh function $\mathrm{R}(p)$ vanishes. The resulting singularity gives rise to an additional propagatory mode, the Rayleigh wave.

Similarly, we also synthesize the scalar potential of an arbitrary S-wave propagating toward the free surface by superposing all possible plane waves.

$$\psi = \frac{1}{\pi}\int_{-\infty}^{+\infty} \mathrm{w}(l,p)\frac{e^{ipx+i|h-z|\delta}}{\delta}\,dp \tag{B.6}$$

Again, to satisfy the boundary conditions at the free surface, we need a P- as well as a S-wave propagating downwards. Both fields are synthesized by superposition.

$$\phi_{sp} = \frac{1}{\pi}\int_{-\infty}^{+\infty} \mathrm{w}(l,p)\,\mathrm{SP}(p)\frac{e^{ipx+ih\delta+iz\gamma}}{\delta}\,dp \tag{B.7}$$

$$\psi_{ss} = \frac{1}{\pi}\int_{-\infty}^{+\infty} \mathrm{w}(l,p)\,\mathrm{SS}(p)\frac{e^{ipx+i(h+z)\delta}}{\delta}\,dp \tag{B.8}$$

The coefficients $\mathrm{SP}(p)$ and $\mathrm{SS}(p)$ are the reflection coefficients necessary to satisfy the bound-

ary conditions along the free surface.

$$\mathrm{SP}(p) = \frac{4p\delta\left[l^2-2p^2\right]}{4p^2\gamma\delta+\left[l^2-2p^2\right]^2} = \frac{4p\delta\left[l^2-2p^2\right]}{\mathrm{R}(p)} \tag{B.9}$$

$$\mathrm{SS}(p) = \frac{4p^2\gamma\delta-\left[l^2-2p^2\right]^2}{4p^2\gamma\delta+\left[l^2-2p^2\right]^2} = -1+\frac{8p^2\gamma\delta}{\mathrm{R}(p)} \tag{B.10}$$

Instead of solving (B.2), (B.3) (B.7) and (B.8) exactly, we evaluate all integrals by the steepest decent approximation and add the contribution of the Rayleigh pole (Lapwood, 1949; Aki and Richards, 1980; DeSanto, 1992). Thus, for (B.2) we obtain:

$$\begin{aligned}\phi_{pp} &\approx \int_{p_{pp}-\epsilon}^{p_{pp}+\epsilon} \mathrm{w}(k,p)\,\mathrm{PP}(p)\frac{e^{ipx+i(h+z)\gamma}}{\pi\gamma}\,dp \\ &\quad + \oint_{\Gamma} \mathrm{w}(k,p)\,\mathrm{PP}(p)\frac{e^{ipx+i(h+z)\gamma}}{\pi\gamma}\,dp \\ &= \sqrt{\frac{2}{\pi}\frac{1}{kr}}\,\mathrm{w}(k,p)\,\mathrm{PP}(p_{pp})e^{ip_{pp}x+i(h+z)\gamma_{pp}-i\frac{\pi}{4}} \\ &\quad + 2\pi i\,\mathrm{Res}\left(\mathrm{w}(k,p)\,\mathrm{PP}(p)\frac{e^{ipx+i(h+z)\gamma}}{\pi\gamma}\right)\Bigg|_{p=p_r}\end{aligned} \tag{B.11}$$

$$\begin{aligned}&= \sqrt{\frac{2}{\pi}\frac{1}{kr}}\,\mathrm{w}(k,p)\,\mathrm{PP}(p_{pp})e^{ip_{pp}x+i(h+z)\gamma_{pp}-i\frac{\pi}{4}} \\ &\quad + \mathrm{w}(k,p)\frac{2ip_r\delta_r}{\gamma_r\delta_r-(l^2-2p_r^2)}e^{ip_rx+i(h+z)\gamma_r}\end{aligned}$$

where $r=\sqrt{x^2+(h+z)^2}$ and p_{pp} denotes the saddle point of (B.2) located at $p_{pp}=kx/r$.

Similarly, the P to S conversion (B.3) yields

$$\begin{aligned}\psi_{ps} &\approx \sqrt{\frac{2}{\pi}\frac{1}{kr_p+lr_s\xi_s}}\,\mathrm{w}(k,p)\,\mathrm{PS}(p_{ps})e^{ip_{ps}x+ih\gamma_{ps}+iz\delta_{ps}-i\frac{\pi}{4}} \\ &\quad - \mathrm{w}(k,p)\,\mathrm{sgn}\,(x)\,i\frac{l^2-2p_r^2}{\gamma_r\delta_r-(l^2-2p_r^2)}e^{ip_rx+ih\gamma_r+iz\delta_r}\end{aligned} \tag{B.12}$$

where $p_{ps}=kx_p/r_p$, $r_p=\sqrt{x_p^2+h^2}$, $r_s=\sqrt{x_s^2+z^2}$, $x_s=x-x_p$, $\xi_s=\frac{\gamma^2}{\delta^2}$ and $0<x_p<x$

is given by

$$(\alpha^2-\beta^2)x_p^4-2x(\alpha^2-\beta^2)x_p^3+\left[\alpha^2(x^2+h^2)-\beta^2(x^2+z^2)\right]x_p^2- \\ 2x\alpha^2h^2x_p+x^2\alpha^2h^2=0 \quad \text{(B.13)}$$

which is numerically solved using a Newton-Raphson algorithm (Press *et al.*, 1988).

For the S to P conversion (B.7), we obtain

$$\begin{aligned}\phi_{sp} \approx \sqrt{\frac{2}{\pi}\frac{1}{lR_r+kR_p\xi_p}}\,\mathrm{w}(l,p)\,\mathrm{SP}(p_{sp})e^{ip_{sp}x+ih\delta_{sp}+iz\gamma_{sp}-i\frac{\pi}{4}} \\ +\,\mathrm{w}(l,p)\,\mathrm{sgn}\,(x)\,i\frac{l^2-2p_r^2}{\gamma_r\delta_r-(l^2-2p_r^2)}e^{ip_rx+ih\delta_r+iz\gamma_r}\end{aligned} \quad \text{(B.14)}$$

where $p_{sp}=lX_s/R_s$, $R_s=\sqrt{X_s^2+h^2}$, $R_p=\sqrt{X_p^2+z^2}$, $X_p=x-X_s$, $\xi_p=\frac{\delta^2}{\gamma^2}$ and $0<X_s<x$ is given by

$$(\alpha^2-\beta^2)X_s^4-2x(\alpha^2-\beta^2)X_s^3+\left[\alpha^2(x^2+z^2)-\beta^2(x^2+h^2)\right]X_s^2+ \\ 2x\beta^2h^2X_s-x^2\beta^2h^2=0 \quad \text{(B.15)}$$

which is again solved numerically using a Newton-Raphson algorithm.

Finally, the S to S reflection (B.8) yields

$$\begin{aligned}\psi_{ss} \approx \sqrt{\frac{2}{\pi}\frac{1}{lr}}\,\mathrm{w}(l,p)\,\mathrm{SS}(p_{ss})e^{ip_{ss}x+i(h+z)\delta_{ss}-i\frac{\pi}{4}} \\ +\,\mathrm{w}(l,p)\frac{2ip_r\gamma_r}{\gamma_r\delta_r-(l^2-2p_r^2)}e^{ip_rx+i(h+z)\delta_r}\end{aligned} \quad \text{(B.16)}$$

where $r=\sqrt{x^2+(h+z)^2}$ and p_{ss} denotes the saddle point of (B.8) located at $p_{ss}=lx/r$.

Setting the weighting function $\mathrm{w}(k,p)=1$, we recognize in equation (B.1) the well known

identity (Watson, 1944; Chew, 1990)

$$H_0(kr) = \frac{1}{\pi}\int_{-\infty}^{+\infty} \frac{e^{ipx+i|z-h|\gamma}}{\gamma}\, dp \tag{B.17}$$

where $r^2 = x^2 + (z-h)^2$. By using the raising or lowering operators $\mathcal{R}(k)$ and $\mathcal{L}(k)$ (Chew, 1990) as weighting functions $\mathrm{w}(k,p)$, we obtain the solution to sources of different angular order $H_{|n|}(kr)e^{in\theta}$. More specifically, the operators $\mathcal{R}(k)$ and $\mathcal{L}(k)$ raise, respectively lower, the angular order of a solution by one:

$$H_n(kr)e^{in\theta} = \mathcal{R}^n(k)H_0(kr) \qquad n \geq 0\,, \tag{B.18}$$

$$H_{|n|}(kr)e^{in\theta} = \mathcal{L}^{|n|}(k)H_0(kr) \qquad n \leq 0\,. \tag{B.19}$$

A little calculation involving the recurrence relations of Bessel functions (Abramowitz and Stegun, 1964) and equation (B.17) shows that the following expressions define the operators.

$$\mathcal{R}(k) = -\frac{1}{k}\left[\frac{\partial}{\partial x} + i\frac{\partial}{\partial z}\right] = -\frac{ip-\gamma}{k} \tag{B.20}$$

$$\mathcal{L}(k) = -\frac{1}{k}\left[\frac{\partial}{\partial x} - i\frac{\partial}{\partial z}\right] = -\frac{ip+\gamma}{k} \tag{B.21}$$

To simplify the notation, we introduce an alternative raising and lowering operator.

$$\mathfrak{R}^n(k) = \begin{cases} \mathcal{R}^n(k) & \text{for } n > 0 \\ 1 & \text{for } n = 0 \\ \mathcal{L}^{|n|}(k) & \text{for } n < 0 \end{cases} \tag{B.22}$$

Thus, replacing $\mathrm{w}(k,p)$ by $\mathfrak{R}^n(k)$ in equations (B.11) and (B.12) allows us to estimate the effect of the free surface on a compressional cylindrical solution of arbitrary angular order n. Similarly, replacing $\mathrm{w}(l,p)$ by $\mathfrak{R}^n(l)$ in equations (B.14) and (B.16) yields the contributions of the free surface to the rotational solution of order n.

For a compressional source of order n located at $\mathbf{x}_d = (0,h)$, we obtain the following

expression for the displacement by combining (B.1), (B.11), and (B.12).

$$\begin{aligned}
\mathbf{u}_n^{\Phi}(\mathbf{x},\mathbf{x}_d) =& \nabla\Big(H_{|n|}(kr)e^{in\theta}\Big) + \\
& \nabla\Big(\sqrt{\frac{2}{\pi}\frac{1}{kr}}\,\Re^n(k)\,\mathrm{PP}(p_{pp})e^{ip_{pp}x+i(h+z)\gamma_{pp}-i\frac{\pi}{4}}\Big) + \\
& \nabla\Big(\Re^n(k)\frac{2ip_r\delta_r}{\gamma_r\delta_r-(l^2-2p_r^2)}e^{ip_rx+i(h+z)\gamma_r}\Big) + \\
& \nabla\times\Big(\sqrt{\frac{2}{\pi}\frac{1}{kr_p+lr_s\xi_s}}\,\Re^n(k)\,\mathrm{PS}(p_{ps})e^{ip_{ps}x+ih\gamma_{ps}+iz\delta_{ps}-i\frac{\pi}{4}}\Big)\hat{\mathbf{y}} - \\
& \nabla\times\Big(\Re^n(k)\,\mathrm{sgn}\,(x)\,i\frac{l^2-2p_r^2}{\gamma_r\delta_r-(l^2-2p_r^2)}e^{ip_rx+ih\gamma_r+iz\delta_r}\Big)\hat{\mathbf{y}}
\end{aligned} \tag{B.23}$$

For a rotational source of order n located at $\mathbf{x}_d = (0, h)$, we obtain the following expression for the displacement by combining (B.1), (B.16), and (B.14).

$$\begin{aligned}
\mathbf{u}_n^{\Phi}(\mathbf{x},\mathbf{x}_d) =& \nabla\times\Big(H_{|n|}(lr)e^{in\theta}\Big)\hat{\mathbf{y}} + \\
& \nabla\times\Big(\sqrt{\frac{2}{\pi}\frac{1}{lr}}\,\Re^n(l)\,\mathrm{SS}(p_{ss})e^{ip_{ss}x+i(h+z)\delta_{ss}-i\frac{\pi}{4}}\Big)\hat{\mathbf{y}} + \\
& \nabla\times\Big(\Re^n(l)\frac{2ip_r\gamma_r}{\gamma_r\delta_r-(l^2-2p_r^2)}e^{ip_rx+i(h+z)\delta_r}\Big)\hat{\mathbf{y}} + \\
& \nabla\Big(\sqrt{\frac{2}{\pi}\frac{1}{lR_s+kR_p\xi_p}}\,\Re^n(l)\,\mathrm{SP}(p_{sp})e^{ip_{sp}x+ih\delta_{sp}+iz\gamma_{sp}-i\frac{\pi}{4}}\Big) + \\
& \nabla\Big(\Re^n(l)\,\mathrm{sgn}\,(x)\,i\frac{l^2-2p_r^2}{\gamma_r\delta_r-(l^2-2p_r^2)}e^{ip_rx+ih\delta_r+iz\gamma_r}\Big)
\end{aligned} \tag{B.24}$$

B.3 Numerical Tests

As an application of the new found expressions (B.23) and (B.24), we compare our approximate results to the exact ones as calculated by the discrete wave number integration method (DWI) (Bouchon and Aki, 1977). Contrary to our approximations, the DWI solves the integrations (B.2),(B.3),(B.7), and (B.8) numerically by summation over many discrete wave numbers p.

The model geometry is depicted in Figure B-2. A line source of either compressional or

rotational type is located 10 m below the free surface. The source is modulated by a Ricker wavelet of 50 Hz. At a horizontal distance of 200 m, we place a vertical array of geophones measuring the x- and z-components of the displacement. The first geophone is 1 m below the surface. Altogether, we will use 64 geophones with a vertical spacing of 5 m. The P-wave velocity is 2000 m/s, the S-wave velocity 1154.7 m/s, and the Rayleigh velocity 1061.6 m/s.

The respective results for compressional or rotational sources, and x- or z-components of the displacement are presented in Figures B-3 to B-6. Clearly, the phases match fairly well. Also, the amplitudes far from the free surface agree very well. Close to the free surface, the amplitudes differ at most by 30%. The approximate expressions predict a smaller amplitude than the DWI. This is to be expected since in the near-field wave numbers other than the saddle point contribute to the wavefields in a constructive manner. Furthermore, the approximations (B.24) and (B.24) do not even contain all wave modes defined in Figure B-1: the pSp, pS, sPs, and sP modes are neglected. This can be seen very clearly in Figure B-5 where we miss a part of the first break corresponding to a sPs phase. Other examples of missing waves can be seen on the seismograms shown in Figures B-9, B-10 and B-11, B-12. In the former ones, the exact solution calculated by DWI contains an additional phase emerging from the Rayleigh wave and blending with the PS wave. A numerical experiment identifies this phase as a S-phase, thus it has to be the pS phase. In Figures B-11, B-12 the DWI solution contains an additional event with a linear traveltime. Another numerical experiment identifies this phase as sPs.

B.4 Discussion

Even without solving the exact free surface problem by a complex contour integration, the discrete wave number technique or the Cagniard-De Hoop method, we obtain fairly reasonable results for wavefields in the presence of a free surface at a much lower numerical cost. Although expressions (B.23) and (B.24) appear to be rather complicated, they can be evaluated very easily and fast. The drawback is that we miss some wave phases, namely pSp, pS, sP, and sPs.

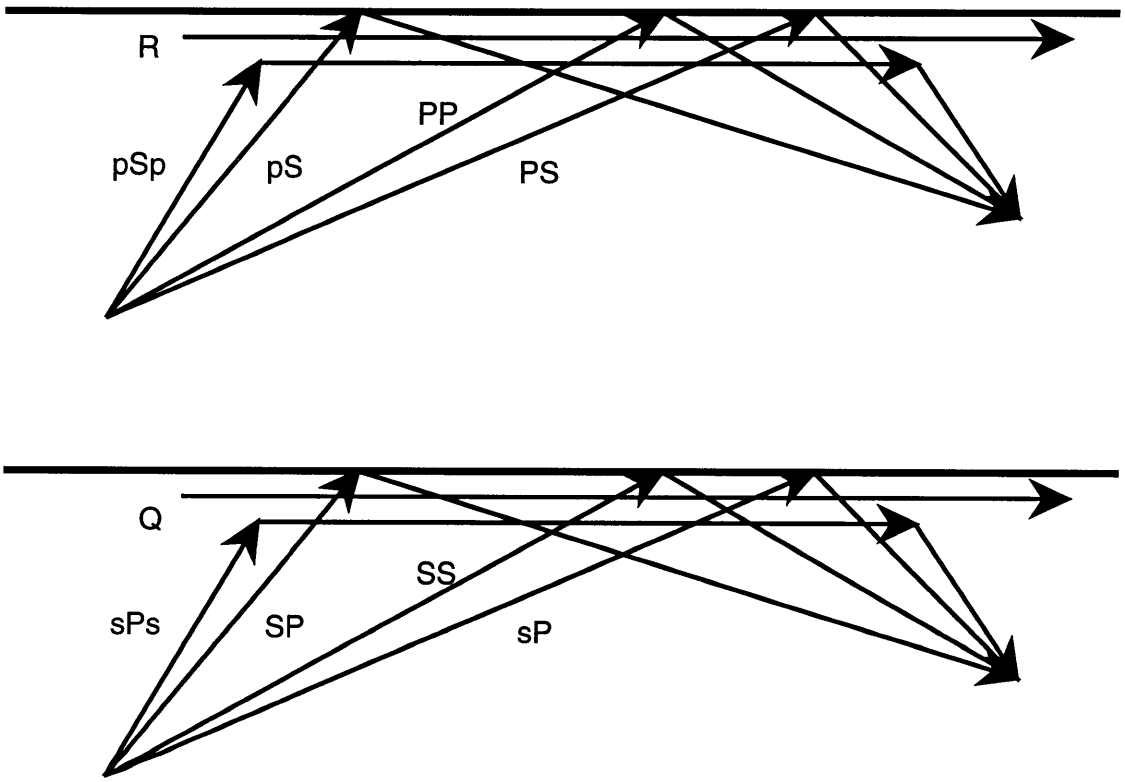

Figure B-1: A summary of elastic waves which propagate due to the interaction of an incident wave and the free surface. PP, PS, SP and SS arise in the case of reflection of plane waves. All others are diffraction effects due to the curvature of the wavefronts impinging on the free surface (Lapwood, 1949).

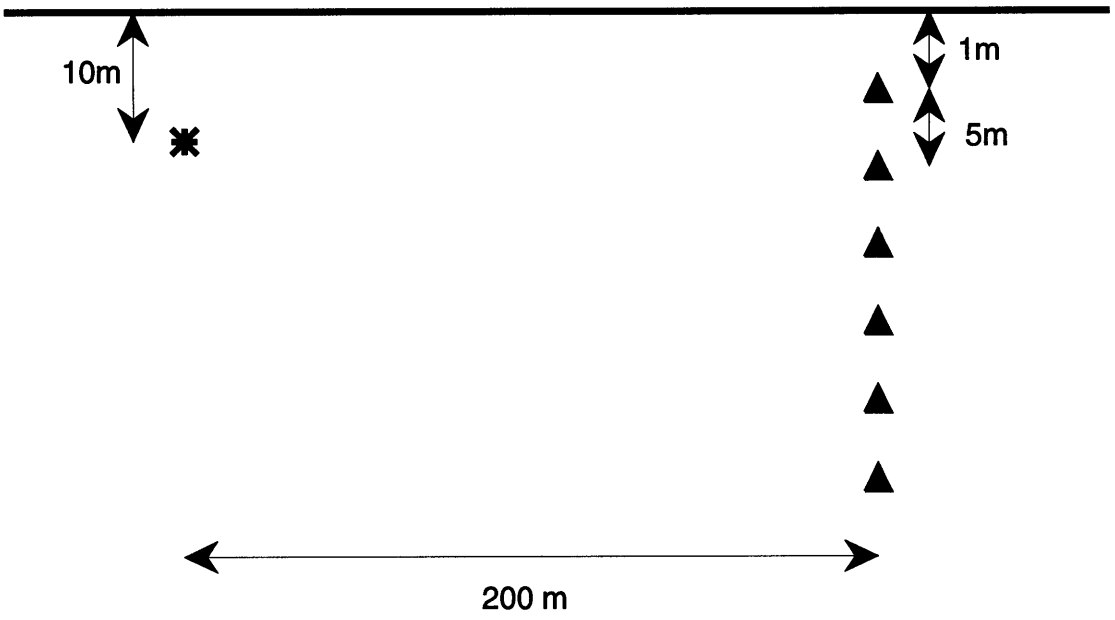

Figure B-2: A line source of either compressional or rotational type is located 10 m below the free surface. At a horizontal distance of 200 m, we place a vertical array of geophones measuring the x- and z-components of the displacement. The first geophone is 1 m below the surface. Altogether, 64 geophones with a vertical spacing of 5 m are used.

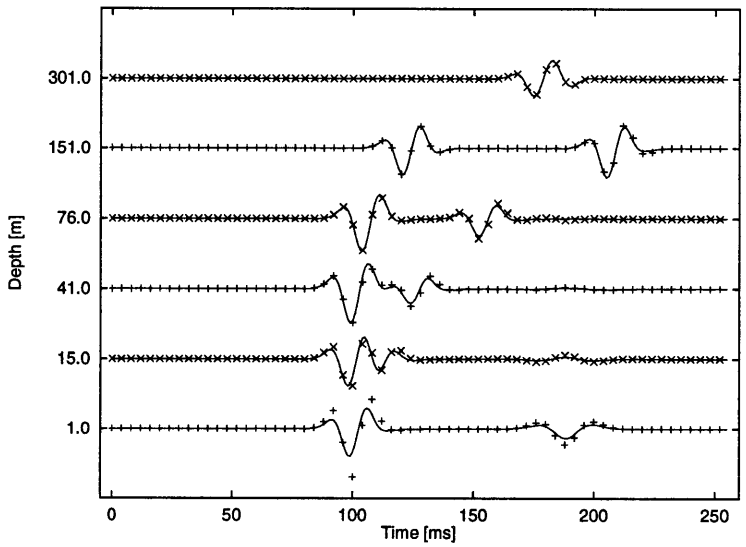

Figure B-3: A comparison of the discrete wave number integration method (dotted) and approximation (B.23) plotted as a solid line. Shown is the x-component of the displacement due to a compressional source. The source is modulated by a Ricker wavelet of 50 Hz. The P-wave velocity is 2000 m/s, the S-wave velocity 1154.7 m/s, and the Rayleigh velocity 1061.6 m/s.

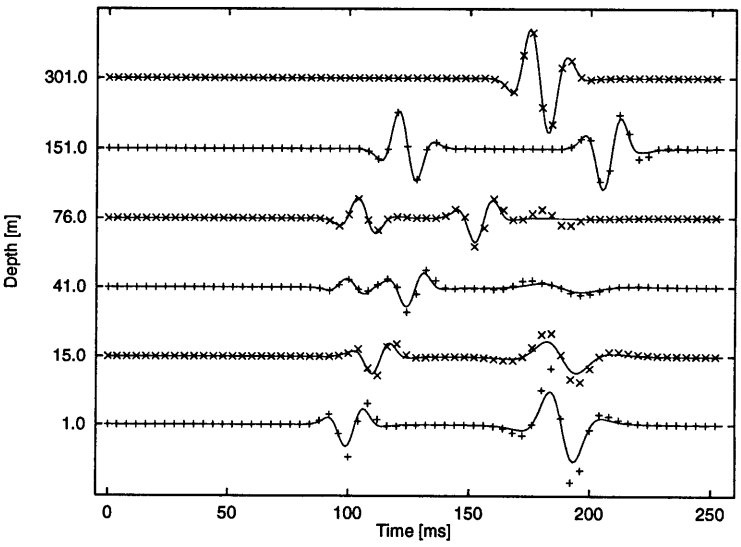

Figure B-4: A comparison of the discrete wave number integration method (dotted) and approximation (B.23) plotted as a solid line. Shown is the z-component of the displacement due to a compressional source.

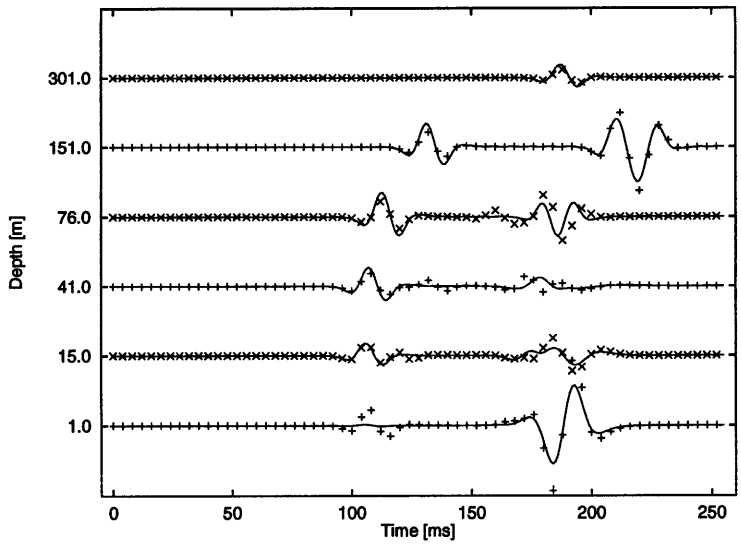

Figure B-5: A comparison of the discrete wave number integration method (dotted) and approximation (B.24) plotted as a solid line. Shown is the x-component of the displacement due to a rotational source.

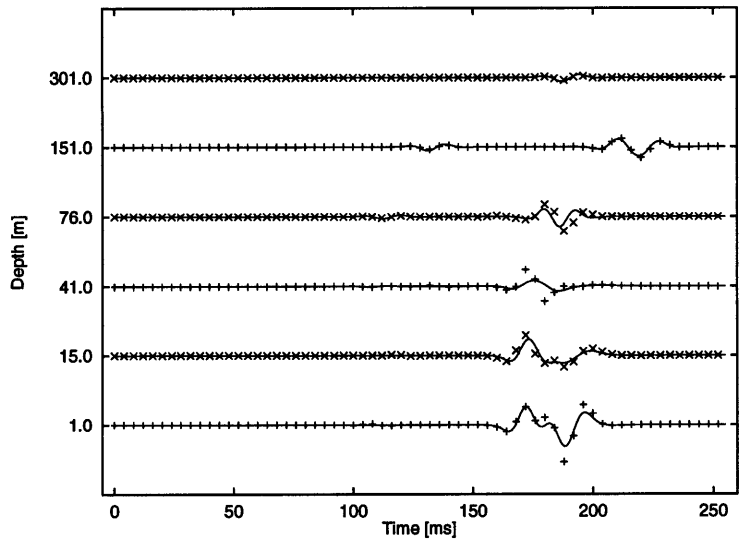

Figure B-6: A comparison of the discrete wave number integration method (dotted) and approximation (B.24) plotted as a solid line. Shown is the z-component of the displacement due to a rotational source.

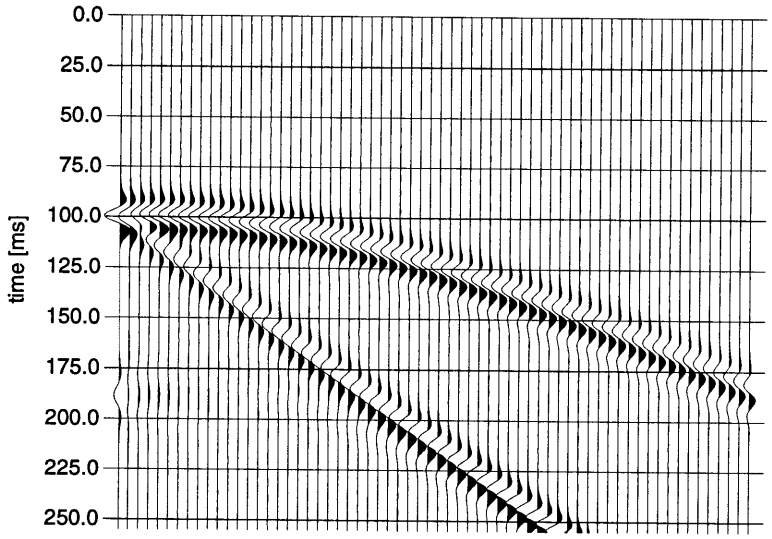

Figure B-7: DWI: compressional source, x-component of the displacement

Figure B-8: Approximation (B.23): compressional source, x-component of the displacement

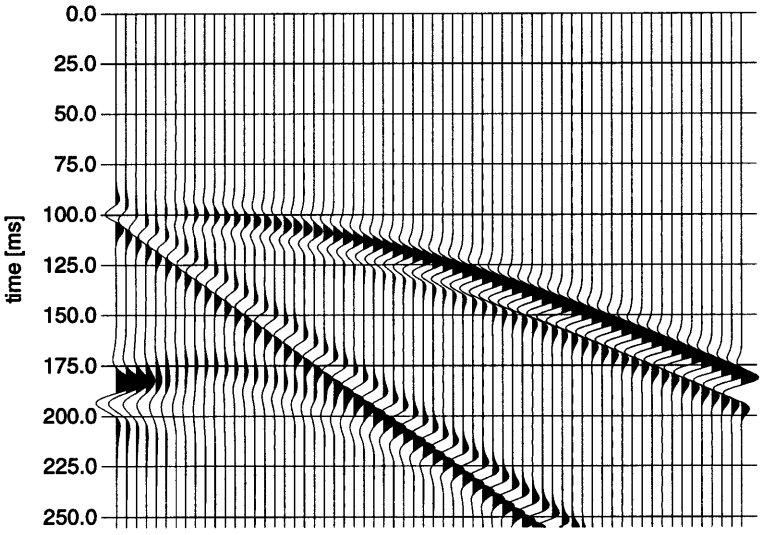

Figure B-9: DWI: compressional source, z-component of the displacement

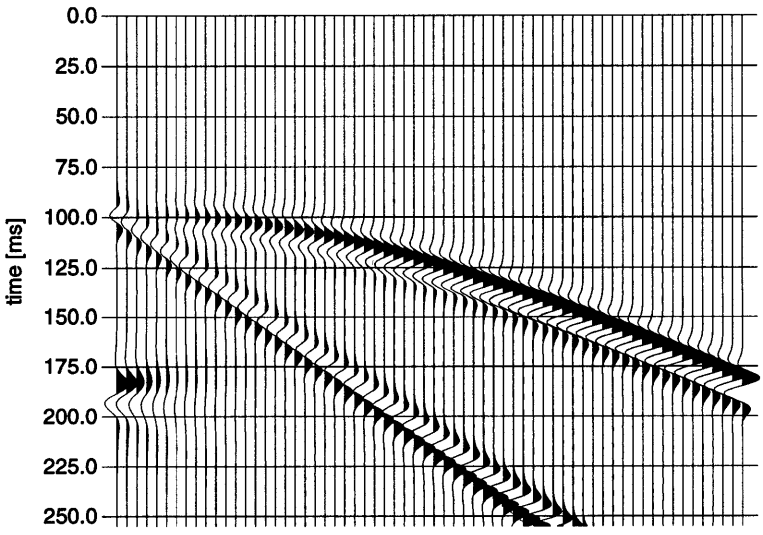

Figure B-10: Approximation (B.23): compressional source, z-component of the displacement

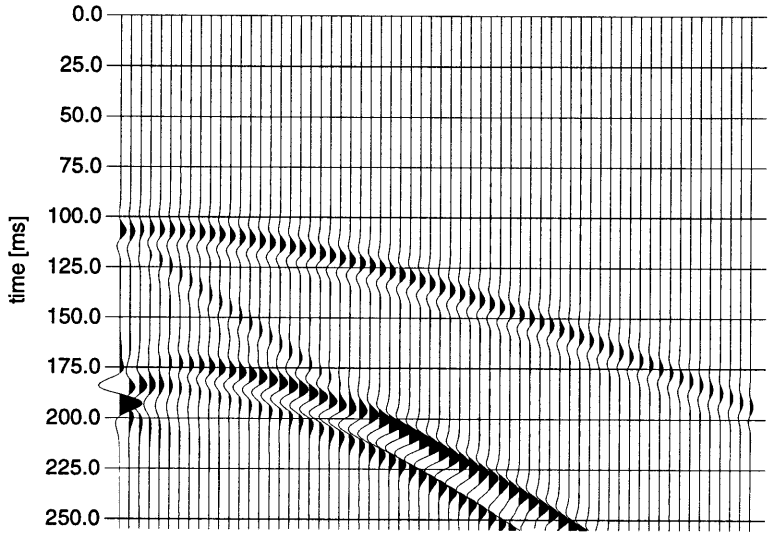

Figure B-11: DWI: rotational source, x-component of the displacement

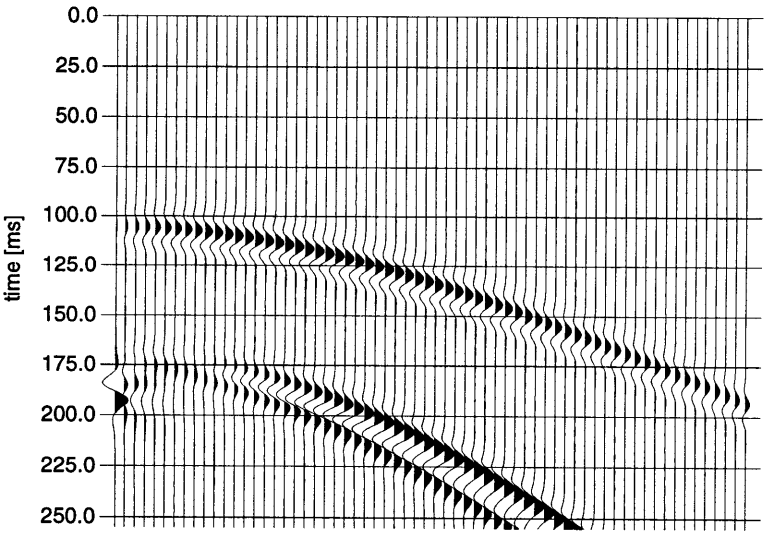

Figure B-12: Approximation (B.24): rotational source, x-component of the displacement

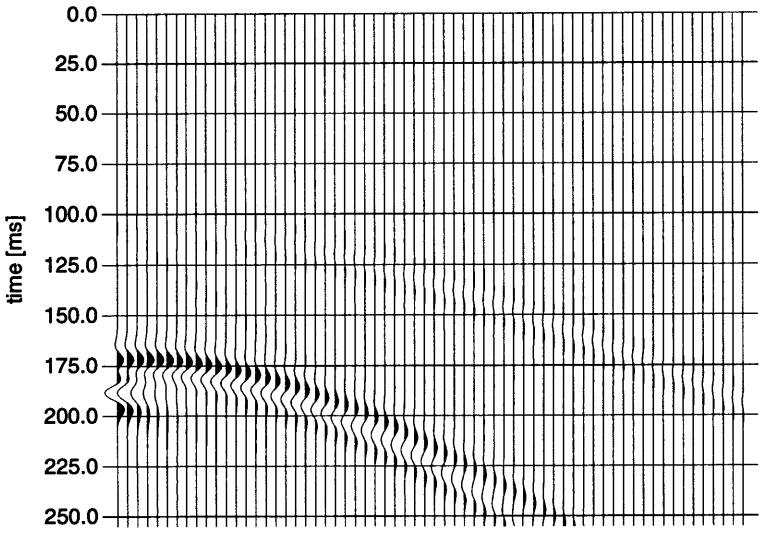

Figure B-13: DWI: rotational source, z-component of the displacement. The linear event is the sPs phase.

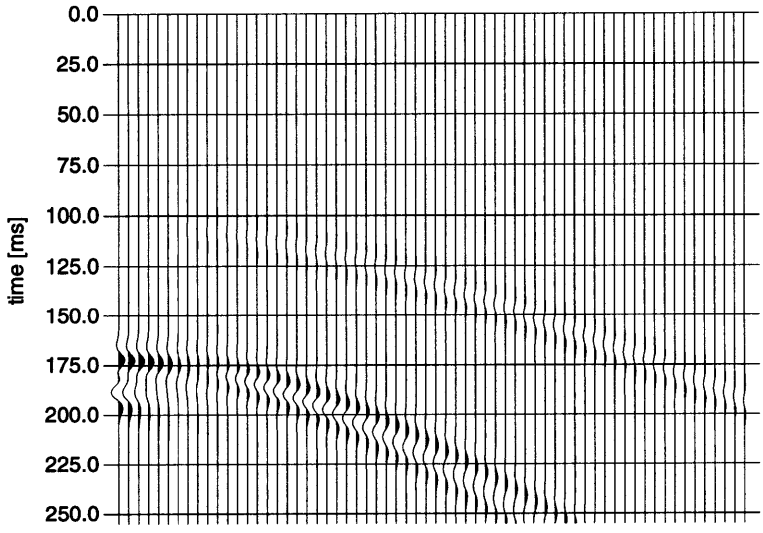

Figure B-14: Approximation (B.24): rotational source, z-component of the displacement. The sPs phase is missing in the approximation.

Appendix C

Intermediate Scattering Approximation

C.1 Theory

In this section, we want to derive a numerical scattering formulation for strong scatterers which are smaller than a characteristic wavelength λ. We assume that $ka < 1$ but not by much. These scatterers are too small to justify an exact treatment, e.g. by the multiple multipole method (Chapter 3). On the other hand, the assumption that the incident wavefield is constant in and around the scatterer is not valid which excludes the use of the Rayleigh approach (Rayleigh, 1871).

We will describe the scatterered wavefield $\mathbf{u}^s$ induced by a scatterer located at the origin as follows:

$$\mathbf{u}^s(\mathbf{x}) = \sum_{n=-N}^{+N} a_n \nabla \left(H_{|n|}(kr) e^{in\theta} \right) + b_n \nabla \times \left(H_{|n|}(lr) e^{in\theta} \right) \hat{\mathbf{y}} \tag{C.1}$$

$$= \sum_{n=-N}^{+N} a_n \mathbf{u}_n^{\Phi}(\mathbf{x}) + b_n \mathbf{u}_n^{\Psi}(\mathbf{x}) \tag{C.2}$$

where $k = \omega/\alpha$ and $l = \omega/\beta$ are the wave numbers of the P-, respectively the S-wave at frequency ω. The parameters α and β are the velocities of the P- and S-waves. N is a small number, typically in the range $1 < N < 5$. Finally, r and θ are distance and direction between the scatterer and the receiver. The first term in (C.1) is derived from a scalar potential Φ and yields the P-waves. The second term is due to a vector potential $\Psi\hat{\mathbf{y}}$ and yields the S-waves. To simplify the notation, we renumber (C.1) in a manner which does not distinguish between the two potentials Φ and Ψ.

$$\mathbf{u}^s(\mathbf{x}) = \sum_{n=1}^{N} a_n \mathbf{u}_n(\mathbf{x}) \tag{C.3a}$$

Similarly, we also expand the stress tensor $\boldsymbol{\sigma}^s$ due to the scattered wavefield as

$$\boldsymbol{\sigma}^s(\mathbf{x}) = \sum_{n=1}^{N} a_n \boldsymbol{\sigma}_n(\mathbf{x}) \tag{C.3b}$$

where $\boldsymbol{\sigma}_n(\mathbf{x})$ is the stress due to $\mathbf{u}_n(\mathbf{x})$ evaluated at location $\mathbf{x}$.

For simplicity, we take the scatterer to be either a rigid body or a cavity. In both cases, this yields very simple boundary conditions which have to be satisfied at every point along the boundary of the scatterer. For an incident wave $\mathbf{u}^{inc}$ and the corresponding stress tensor $\boldsymbol{\sigma}^{inc}$, we have:

$$\mathbf{u}^{inc} + \mathbf{u}^s = \mathbf{u}^{inc} + \sum a_n \mathbf{u}_n = \mathbf{0} \qquad \text{for a rigid scatterer,} \tag{C.4a}$$

$$\boldsymbol{\sigma}^{inc} \cdot \hat{\mathbf{n}} + \boldsymbol{\sigma}^s \cdot \hat{\mathbf{n}} = \boldsymbol{\sigma}^{inc} \cdot \hat{\mathbf{n}} + \sum a_n \boldsymbol{\sigma}_n \cdot \hat{\mathbf{n}} = \mathbf{0} \qquad \text{for a cavity.} \tag{C.4b}$$

The unit vector $\hat{\mathbf{n}}$ denotes the normal pointing into the scatterer.

To obtain equations which determine the unknowns a_n, we apply the projection method as presented in section A.4.2. The fields are projected onto testing functions by integrating along the boundary $\partial\Gamma$. For the case of a rigid body scatterer, we use the displacement

functions $\mathbf{u}_i$ as testing functions. Using † to denote the conjugate transpose, we obtain:

$$\sum^{j} a_j \oint_{\partial\Gamma} \mathbf{u}_i^\dagger(\mathbf{x}_s) \cdot \mathbf{u}_j(\mathbf{x}_s)\, ds + \oint_{\partial\Gamma} \mathbf{u}_i^\dagger(\mathbf{x}_s) \cdot \mathbf{u}^{inc}(\mathbf{x}_s)\, ds = 0\,. \tag{C.5a}$$

For the case of a cavity, we use the traction $\boldsymbol{\sigma}_i \cdot \hat{\mathbf{n}}$ as testing functions. Projecting the tractions $\boldsymbol{\sigma}_j \cdot \hat{\mathbf{n}}$ onto the testing functions yields:

$$\sum^{j} a_j \oint_{\partial\Gamma} \hat{\mathbf{n}}^\dagger(\mathbf{x}_s) \cdot \boldsymbol{\sigma}_i^\dagger(\mathbf{x}_s) \cdot \boldsymbol{\sigma}_j(\mathbf{x}_s) \cdot \hat{\mathbf{n}}(\mathbf{x}_s)\, ds + \oint_{\partial\Gamma} \hat{\mathbf{n}}^\dagger(\mathbf{x}_s) \cdot \boldsymbol{\sigma}_i^\dagger(\mathbf{x}_s) \cdot \boldsymbol{\sigma}^{inc}(\mathbf{x}_s) \cdot \hat{\mathbf{n}}(\mathbf{x}_s)\, ds = 0\,. \tag{C.5b}$$

In either case, choosing each function $\mathbf{u}_i$ or $\boldsymbol{\sigma}_i\hat{\mathbf{n}}$ as testing function yields a set of N equations for the N unknowns a_j.

If there is more than one scatterer, we have an expansion (C.3a) or (C.3b) for each scatterer. For D scatterer located at $\mathbf{x}_d$ we have

$$\mathbf{u}^s(\mathbf{x}) = \sum_{d=1}^{D} \sum_{n=1}^{N} a_{dn} \mathbf{u}_{dn}(\mathbf{x}, \mathbf{x}_d) \tag{C.6a}$$

for the rigid body case. For cavities, we obtain by analogy

$$\boldsymbol{\sigma}^s(\mathbf{x}) = \sum_{d=1}^{D} \sum_{n=1}^{N} a_{dn} \boldsymbol{\sigma}_{dn}(\mathbf{x}, \mathbf{x}_d)\,. \tag{C.6b}$$

For each rigid scatterer $k \in \{1, \ldots, D\}$, we obtain a set of N equations by projecting onto the expansions functions $\mathbf{u}_{ki}$ or $\boldsymbol{\sigma}_{ki}$.

$$\sum^{j} a_{kj} \oint_{\partial\Gamma_k} \mathbf{u}_{ki}^\dagger(\mathbf{x}_{s_k}, \mathbf{x}_k) \cdot \mathbf{u}_{kj}(\mathbf{x}_{s_k}, \mathbf{x}_k)\, ds_k + \sum^{d\neq k} \sum^{j} a_{dj} \oint_{\partial\Gamma_k} \mathbf{u}_{ki}^\dagger(\mathbf{x}_{s_k}, \mathbf{x}_k) \cdot \mathbf{u}_{dj}(\mathbf{x}_{s_k}, \mathbf{x}_d)\, ds_k + \oint_{\partial\Gamma_k} \mathbf{u}_{ki}^\dagger(\mathbf{x}_{s_k}, \mathbf{x}_k) \cdot \mathbf{u}^{inc}(\mathbf{x}_{s_k})\, ds_k = 0 \tag{C.7a}$$

Analogous, we obtain the following expression for the case of multiple cavities.

$$\sum^{j} a_{kj} \oint_{\partial\Gamma_k} \hat{\mathbf{n}}^{\dagger}(\mathbf{x}_{s_k}) \cdot \boldsymbol{\sigma}^{\dagger}_{ki}(\mathbf{x}_{s_k}, \mathbf{x}_k) \cdot \boldsymbol{\sigma}_{kj}(\mathbf{x}_{s_k}, \mathbf{x}_k) \cdot \hat{\mathbf{n}}(\mathbf{x}_{s_k})\, ds_k + \sum^{d\neq k}\sum^{j} a_{dj} \oint_{\partial\Gamma_k} \hat{\mathbf{n}}^{\dagger}(\mathbf{x}_{s_k}) \cdot \boldsymbol{\sigma}^{\dagger}_{ki}(\mathbf{x}_{s_k}, \mathbf{x}_k) \cdot \boldsymbol{\sigma}_{dj}(\mathbf{x}_{s_k}, \mathbf{x}_d) \cdot \hat{\mathbf{n}}(\mathbf{x}_{s_k})\, ds_k + \oint_{\partial\Gamma_k} \hat{\mathbf{n}}^{\dagger}(\mathbf{x}_{s_k}) \cdot \boldsymbol{\sigma}^{\dagger}_{ki}(\mathbf{x}_{s_k}, \mathbf{x}_k) \cdot \boldsymbol{\sigma}^{inc}(\mathbf{x}_{s_k}) \cdot \hat{\mathbf{n}}(\mathbf{x}_{s_k})\, ds_k = 0 \quad \text{(C.7b)}$$

One could argue, that the projection is not valid because D different inner product are used. Instead, one should use the same inner product for all projections. The only way to do that is to integrate along each scatterer for each testing functions. For example, one would then obtain

$$\sum^{p}\sum^{d}\sum^{j} a_{dj} \oint_{\partial\Gamma_p} \mathbf{u}^{\dagger}_{ki}(\mathbf{x}_{s_p}, \mathbf{x}_k) \cdot \mathbf{u}_{dj}(\mathbf{x}_{s_p}, \mathbf{x}_d)\, ds_p + \sum^{p} \oint_{\partial\Gamma_p} \mathbf{u}^{\dagger}_{ki}(\mathbf{x}_{s_p}, \mathbf{x}_k) \cdot \mathbf{u}^{inc}(\mathbf{x}_{s_p})\, ds_p = 0 \quad \text{(C.7a')}$$

where $p \in \{1, \ldots, D\}$. The meaning is: choose the i^{th} testing function $\mathbf{u}_{ki}$ of scatterer k and integrate along the boundaries Γ_p of all scatterers p. In fact, this corresponds to the error minimization methods described in section A.4.1. It even has the advantage that the resulting linear system will be hermitian and positive definite.

However, this also means that every expansion function contributes to the scattered field of every scatterer. But we started out with the assumption that the scattered field due to each scatterer d can be described by (C.6a). To paraphrase Vekua's theorem (1967), the scattered field due to scatterer d should be expanded into the scalar potentials $H_{|n|}(kr_d)e^{in\theta_d}$ and $H_{|n|}(lr_d)e^{in\theta_d}$ centered *in scatterer d*. It is not necessary to use every expansion function to contribute to the scattered field from every scatterer.

The formulation of the scheme (C.7) suggests that the projection method views the scattered fields $\mathbf{u}_{dj}$ and $\boldsymbol{\sigma}_{dj}$ as part of the field incident on scatterer $k \neq d$. But having D scatterers altogether, we can build D systems of this kind and thus obtain just enough equations to

solve the combined system.

For either type of scatterers, we end up with a linear system of equations of the following form:

$$\begin{pmatrix} \mathbf{A}_{11} & \cdots & \mathbf{A}_{1D} \\ \vdots & \ddots & \vdots \\ \mathbf{A}_{D1} & \cdots & \mathbf{A}_{DD} \end{pmatrix} \cdot \begin{pmatrix} \mathbf{a}_1 \\ \vdots \\ \mathbf{a}_D \end{pmatrix} + \begin{pmatrix} \mathbf{h}_1 \\ \vdots \\ \mathbf{h}_D \end{pmatrix} = \mathbf{0}. \tag{C.8}$$

Although the submatrices $\mathbf{A}_{ii}$ are hermitian, the off-diagonal submatrices $\mathbf{A}_{ij}$ where $i \neq j$ are generally not related. Therefore, we have a dense, square system which has to be solved using LU decomposition (Strang, 1988).

A final point to be addressed is how to tackle the integrals in (C.7). For a given shape and type of the scatters and a given set of expansion functions, these integrals could be approximated by some expansion such as a power series in wave number k, distance r and geometrical factors such as the ellipticity e (Bender and Orszag, 1978; Bleinstein and Handelsman, 1986). Instead, the integrals are evaluated numerically by an automatic adaptive integrator (Piessens, 1983). The integrator used is the improved DQXG routine adapted to handle complex integrands (Favati *et al.*, 1991a,b). Because numerical integration is a relatively costly process, we want to evaluate the fewest possible number of integrals. Thus, we prefer the projection method to the least squares scheme which increases the number of integrations by a factor of $D/2$. The factor $1/2$ stems from the fact that the least squares scheme yields a hermitian matrix, thus only half the matrix elements have to be computed. The other ones are then given by the conjugate transpose.

C.2 Numerical Tests

To test the validity of assumption (C.1), we use an elliptical scatterer illuminated by a P-wave. The geometry used in all numerical experiments is shown in Figure C-1. First, we establish the convergence of (C.1) for N large using $N = 41$ and an incident P-wavelength

of 340 m. Since (C.1) satisfies the wave-equation by construction, we only have to test how well the boundary conditions are satisfied. Figure C-2 shows the magnitudes the normal and tangential tractions $\sigma \cdot \hat{\mathbf{n}}$ as a function of angle. As can be seen, the tractions of incident and scattered fields match perfectly. The boundary conditions are satisfied very well. Therefore, the approximation (C.1) is valid for N large. The projection scheme yields the exact answer for N large. But we are not actually interested in the limit as N approaches infinity. In fact, we want to test what happens if N is really small. Without numerical experiment, we know that the boundary conditions are not satisfied anymore: the lower the order N, the worse the misfit on the boundary. Thus, we need a different measure to quantify how good or bad the ansatz (C.1) performs. On a circle with radius $r = 25\,\mathrm{m}$ around the center of the ellipse, we measure the x- and z-components of the displacement for $N \in \{1, 3, 5, \dots\}$. The results are plotted in Figures C-3 and C-4. Also shown are the exact displacements as obtained from the fully converged solution with $N = 41$. For $N = 5$, the error is less than 50%.

The experiments are also performed with incident wavefields of shorter wavelengths, $\lambda = 45\,\mathrm{m}$ and $\lambda = 17\,\mathrm{m}$. The exact solutions and their boundary conditions are shown in Figures C-5 and C-8. The displacements at a distance $r = 25\,\mathrm{m}$ are shown in Figures C-6, C-7 for $\lambda = 45\,\mathrm{m}$, and Figures C-9,C-10 for $\lambda = 17\,\mathrm{m}$. With increasing frequency, the error in the displacements begins to decrease. For example, for $N = 5$, we obtain an error of 30% for $\lambda = 45\,\mathrm{m}$, but only 25% for $\lambda = 17\,\mathrm{m}$.

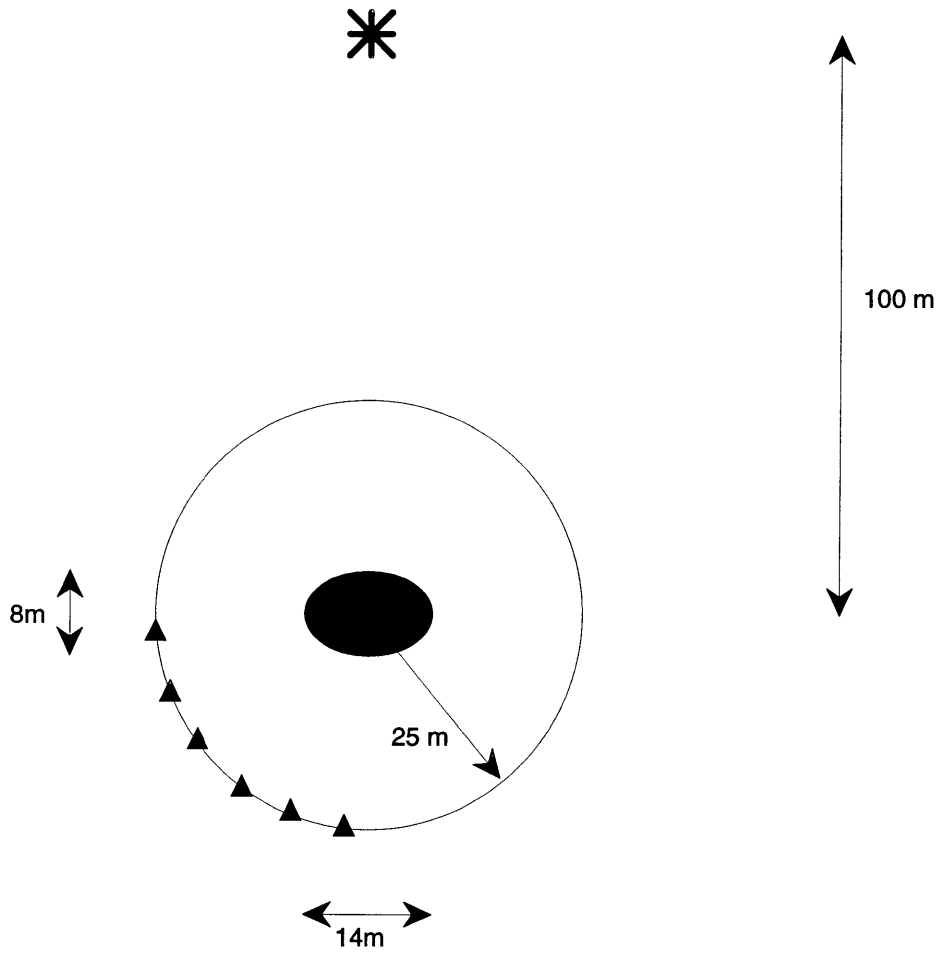

Figure C-1: Schematic of the geometry used to test (C.1). An elliptical cavity is illuminated by a P-wave. The tractions are measured along the ellipse to establish the convergence of (C.1). Also, the components of the displacement as a function of the order N are measured on the circle around the cavity. Triangles symbolize geophones. The star denotes the source.

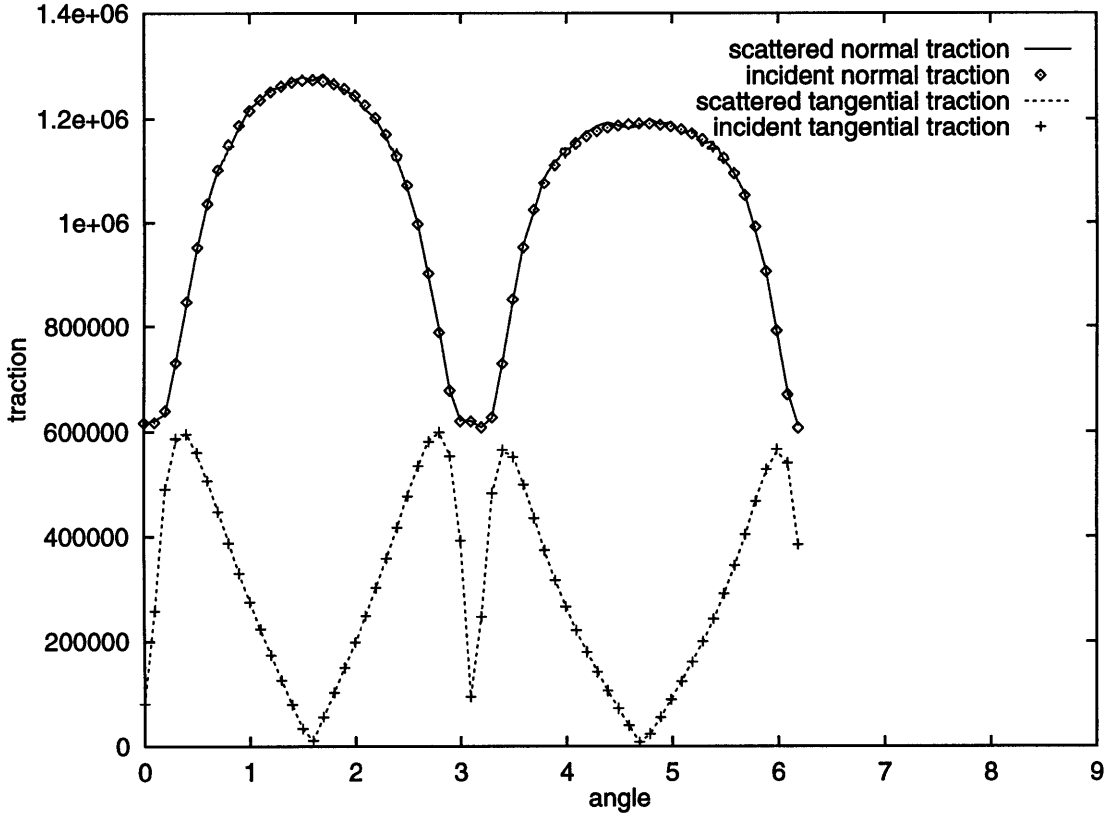

Figure C-2: Normal and tangential components of the traction for the incident field and the induced scattered field evaluated along the elliptical cavity. The semi-axes are 7 m and 4 m. The wavelength of the incident field is 340 m.

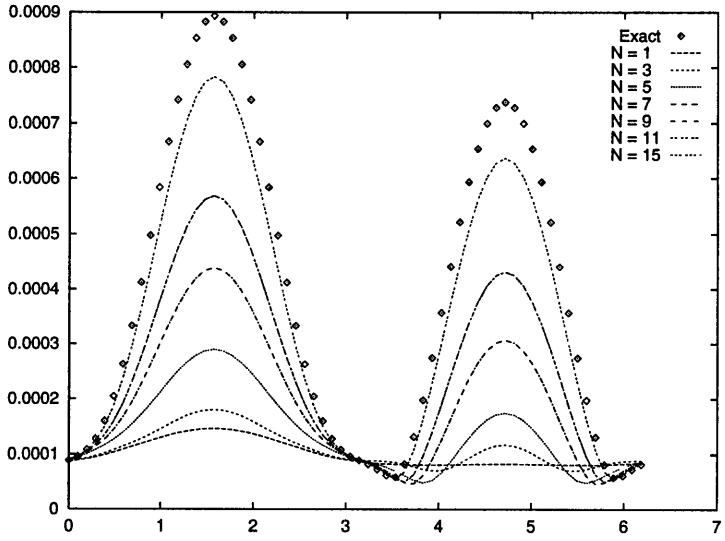

Figure C-3: The x-component of the displacement at a distance of 25 m from the center of the elliptical cavity. Shown is the displacement as a function of the order N in equation (C.1). The exact solution ($N = 41$) satisfies the boundary conditions perfectly as shown in Figure C-2.

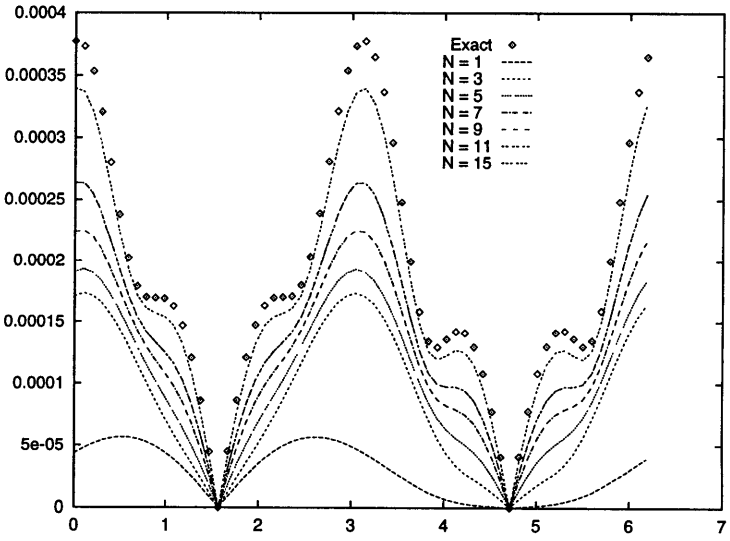

Figure C-4: The z-component of the displacement at a distance of 25 m from the center of the elliptical cavity. Shown is the displacement as a function of the order N in equation (C.1). The exact solution ($N = 41$) satisfies the boundary conditions perfectly as shown in Figure C-2.

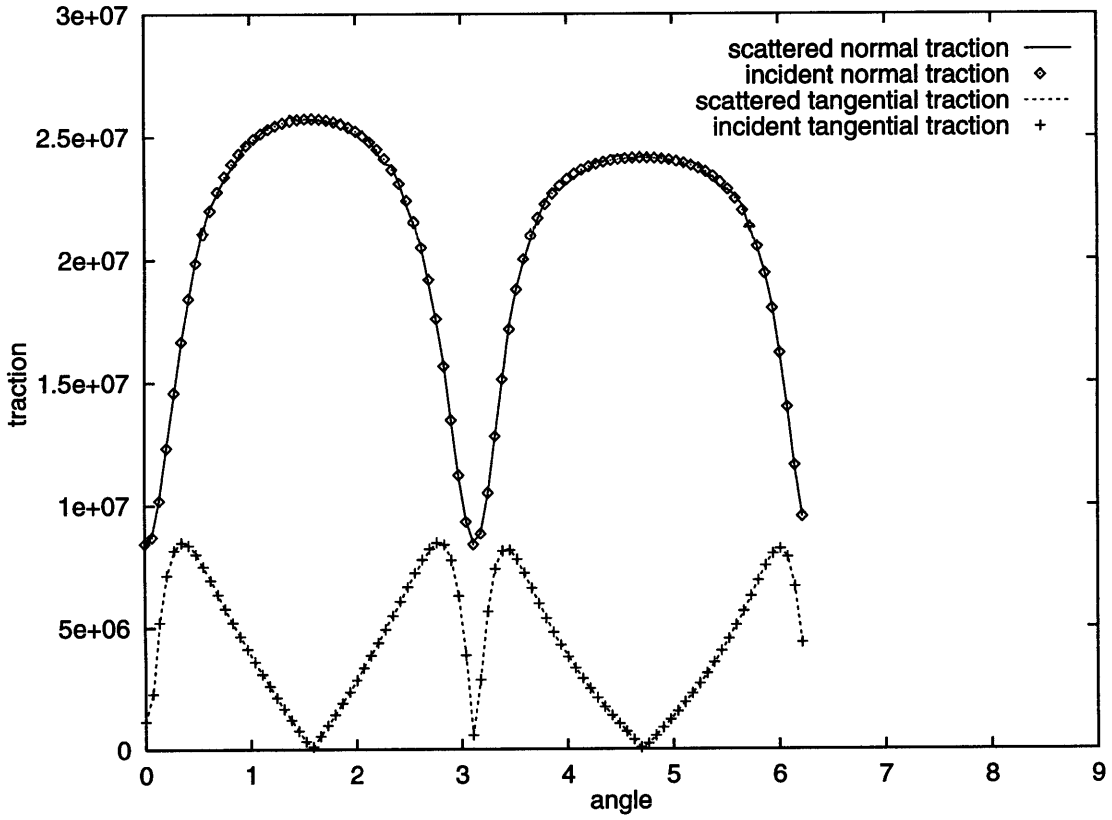

Figure C-5: Normal and tangential components of the traction for the incident field and the induced scattered field evaluated along the elliptical cavity. The semi-axes are 7 m and 4 m. The wavelength of the incident field is 45 m.

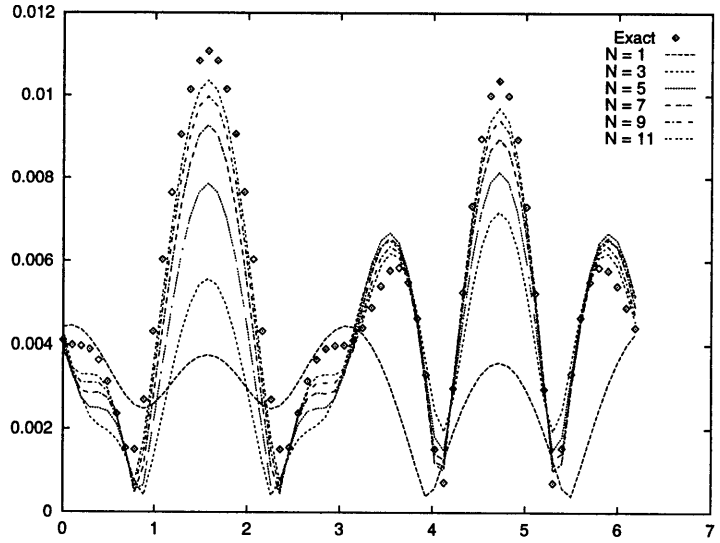

Figure C-6: The x-component of the displacement at a distance of 25 m from the center of the elliptical cavity. Shown is the displacement as a function of the order N in equation (C.1). The exact solution ($N = 41$) satisfies the boundary conditions perfectly as shown in Figure C-5.

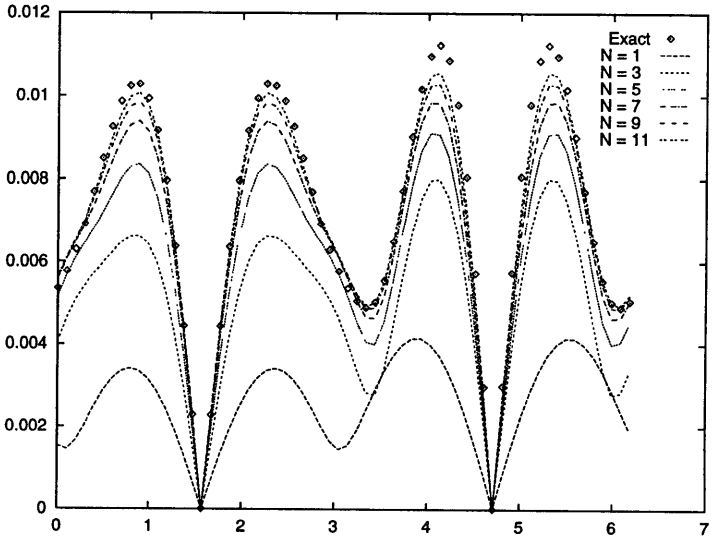

Figure C-7: The z-component of the displacement at a distance of 25 m from the center of the elliptical cavity. Shown is the displacement as a function of the order N in equation (C.1). The exact solution ($N = 41$) satisfies the boundary conditions perfectly as shown in Figure C-5.

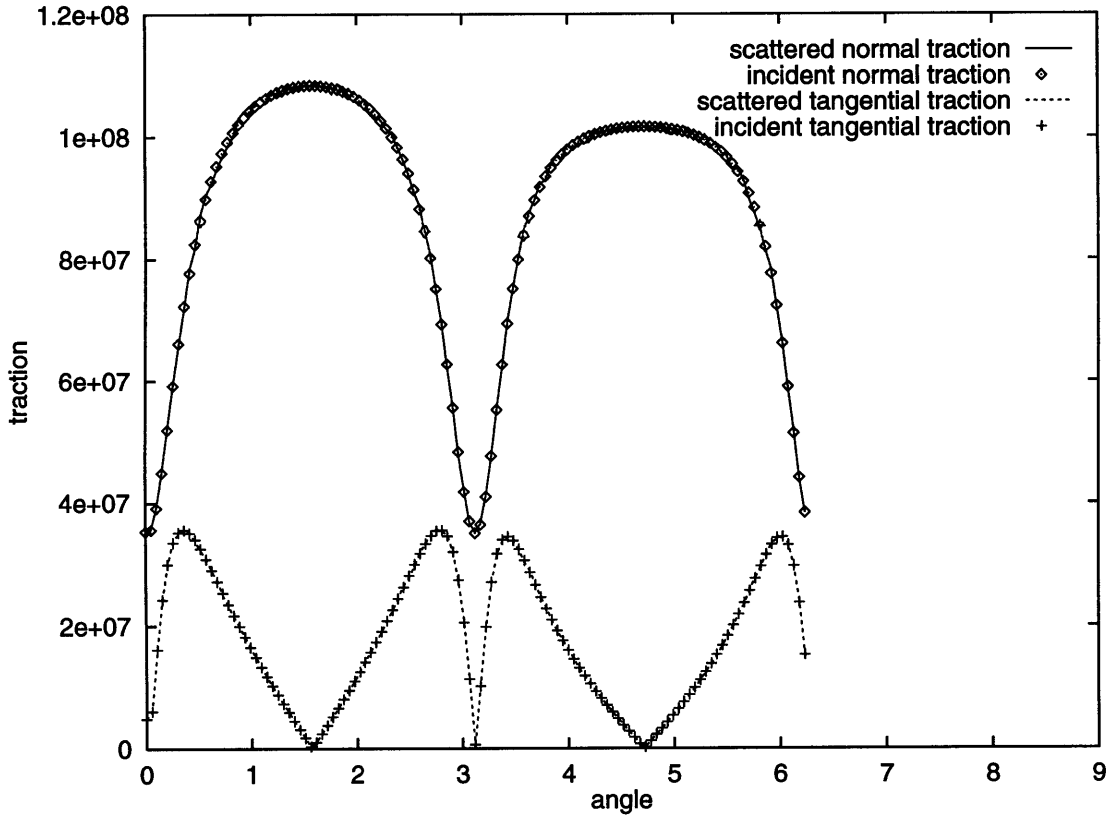

Figure C-8: Normal and tangential components of the traction for the incident field and the induced scattered field evaluated along the elliptical cavity. The semi-axes are 7 m and 4 m. The wavelength of the incident field is 17 m.

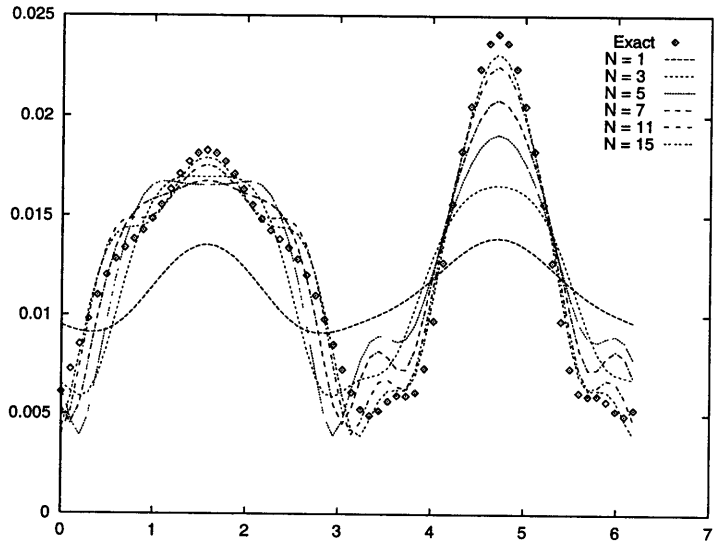

Figure C-9: The x-component of the displacement at a distance of 25 m from the center of the elliptical cavity. Shown is the displacement as a function of the order N in equation (C.1). The exact solution ($N = 41$) satisfies the boundary conditions perfectly as shown in Figure C-8.

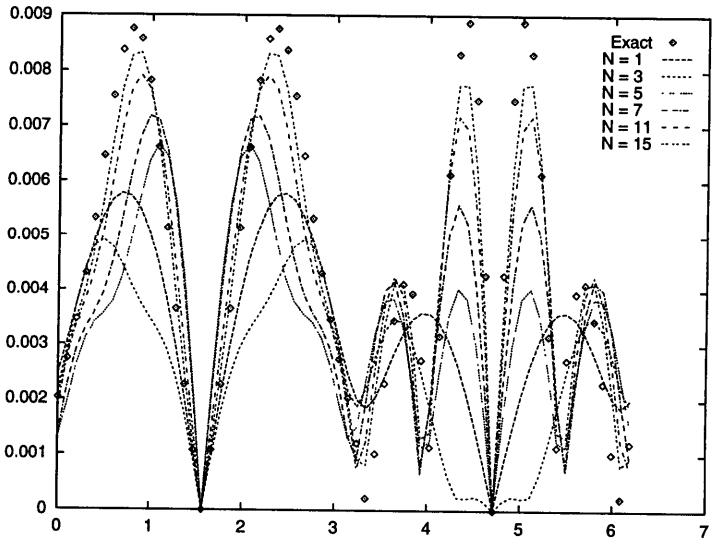

Figure C-10: The z-component of the displacement at a distance of 25 m from the center of the elliptical cavity. Shown is the displacement as a function of the order N in equation (C.1). The exact solution ($N = 41$) satisfies the boundary conditions perfectly as shown in Figure C-8.

Appendix D

Formulations for Displacement, Stress and Strain

D.1 Displacement, Stress and Strain in Cartesian Coordinates

Displacement as function of the scalar potentials Φ and Ψ:

$$u_x = \frac{\partial \Phi}{\partial x} - \frac{\partial \Psi}{\partial z} \tag{D.1a}$$

$$u_z = \frac{\partial \Phi}{\partial z} + \frac{\partial \Psi}{\partial x} \tag{D.1b}$$

Strain as function of the scalar potentials Φ and Ψ:

$$\epsilon_{xx} = \frac{\partial^2 \Phi}{\partial x} - \frac{\partial^2 \Psi}{\partial x \partial z} \tag{D.2a}$$

$$\epsilon_{zz} = \frac{\partial^2 \Phi}{\partial z^2} + \frac{\partial^2 \Psi}{\partial x \partial z} \tag{D.2b}$$

$$\epsilon_{xz} = \frac{1}{2}\left[2\frac{\partial^2 \Phi}{\partial x \partial z} + \frac{\partial^2 \Psi}{\partial x^2} - \frac{\partial^2 \Psi}{\partial z^2}\right] \tag{D.2c}$$

Stress as function of the scalar potentials Φ and Ψ:

$$\sigma_{xx} = \lambda\nabla^2\Phi + 2\mu\left[\frac{\partial^2\Phi}{\partial x^2} - \frac{\partial^2\Psi}{\partial x\partial z}\right] \tag{D.3a}$$

$$\sigma_z = \lambda\nabla^2\Phi + 2\mu\left[\frac{\partial^2\Phi}{\partial z^2} + \frac{\partial^2\Psi}{\partial x\partial z}\right] \tag{D.3b}$$

$$\sigma_{xz} = \mu\left[2\frac{\partial^2\Phi}{\partial x\partial z} + \frac{\partial^2\Psi}{\partial x^2} - \frac{\partial^2\Psi}{\partial z^2}\right] \tag{D.3c}$$

The potentials are substituted by Cartesian wave functions:

$$\Phi = e^{i(k_x x + k_z z)} \tag{D.4a}$$

$$\Psi = e^{i(l_x x + l_z z)} \tag{D.4b}$$

Displacement $\mathbf{u}$ due to $e^{i(k_x x + k_z z)}$:

$$\begin{pmatrix} u_x \\ u_z \end{pmatrix} = i \begin{pmatrix} k_x \\ k_z \end{pmatrix} e^{i(k_x x + k_z z)} \tag{D.5}$$

Displacement $\mathbf{u}$ due to $\Psi = e^{i(l_x x + l_z z)}$:

$$\begin{pmatrix} u_x \\ u_z \end{pmatrix} = i \begin{pmatrix} -l_z \\ l_x \end{pmatrix} e^{i(l_x x + l_z z)} \tag{D.6}$$

Stress $\boldsymbol{\sigma}$ due to $\Phi = e^{i(k_x x + k_z z)}$:

$$\begin{pmatrix} \sigma_{xx} & \sigma_{xz} \\ \sigma_{zx} & \sigma_{zz} \end{pmatrix} = \begin{pmatrix} a_{31} & a_{32} \\ a_{32} & a_{33} \end{pmatrix} e^{i(k_x x + k_z z)} \tag{D.7a}$$

$$a_{31} = -\left[\lambda k^2 + 2\mu k_x^2\right] \tag{D.7b}$$

$$a_{32} = -2\mu k_x k_z \tag{D.7c}$$

$$a_{33} = -\left[\lambda k^2 + 2\mu k_z^2\right] \tag{D.7d}$$

Stress σ due to $\Psi = e^{i(l_x x + l_z z)}$:

$$\begin{pmatrix} \sigma_{xx} & \sigma_{xz} \\ \sigma_{zx} & \sigma_{zz} \end{pmatrix} = 2\mu \begin{pmatrix} a_{41} & a_{42} \\ a_{42} & a_{43} \end{pmatrix} e^{i(l_x x + l_z z)} \tag{D.8a}$$

$$a_{41} = l_x\, l_z \tag{D.8b}$$

$$a_{42} = \frac{1}{2}\left[l_z^2 - l_x^2\right] \tag{D.8c}$$

$$a_{43} = -l_x\, l_z \tag{D.8d}$$

D.2 Displacement, Stress and Strain in Cylindrical Coordinates

Displacement as function of the scalar potentials Φ and Ψ:

$$u_r = \frac{\partial \Phi}{\partial r} + \frac{1}{r}\frac{\partial \Psi}{\partial \varphi} \tag{D.9a}$$

$$u_\varphi = \frac{1}{r}\frac{\partial \Phi}{\partial \varphi} - \frac{\partial \Psi}{\partial r} \tag{D.9b}$$

Strain as functions of the scalar potentials Φ and Ψ:

$$\epsilon_{rr} = \frac{\partial \Phi}{\partial r} + \frac{1}{r}\frac{\partial \Psi}{\partial \varphi} \tag{D.10a}$$

$$\epsilon_{\varphi\varphi} = \frac{1}{r}\left(\frac{\partial^2 \Phi}{\partial \varphi^2} - \frac{\partial^2 \Psi}{\partial r \partial \varphi}\right) + \frac{\partial \Phi}{\partial r} + \frac{\partial \Psi}{\partial \varphi} \tag{D.10b}$$

$$\epsilon_{r\varphi} = \frac{1}{2}\left[\frac{1}{r}\frac{\partial^2 \Phi}{\partial r^2} + \frac{1}{r}\left(\frac{1}{r}\frac{\partial \Psi}{\partial \varphi}\right) + \frac{\partial}{\partial r}\left(\frac{1}{r}\frac{\partial \Phi}{\partial \varphi}\right) - \frac{\partial^2 \Psi}{\partial r^2} - \frac{1}{r^2}\frac{\partial \Phi}{\partial \varphi} + \frac{1}{r}\frac{\partial \Psi}{\partial r}\right] \tag{D.10c}$$

Stress as function of the scalar potentials Φ and Ψ:

$$\sigma_{rr} = \lambda \nabla^2 \Phi + 2\mu\left[\frac{\partial^2 \Phi}{\partial r^2} + \frac{\partial}{\partial r}\left(\frac{1}{r}\frac{\partial \Psi}{\partial \varphi}\right)\right] \tag{D.11a}$$

$$\sigma_{\varphi\varphi} = \lambda \nabla^2 \Phi + 2\mu\left[\frac{1}{r}\left(\frac{\partial \Phi}{\partial r} + \frac{1}{r}\frac{\partial^2 \Phi}{\partial \varphi^2}\right) + \frac{1}{r}\left(\frac{1}{r}\frac{\partial \Psi}{\partial \varphi} - \frac{\partial^2 \Psi}{\partial r \partial \varphi}\right)\right] \tag{D.11b}$$

$$\sigma_{r\varphi} = 2\mu\left[\frac{1}{r}\frac{\partial^2 \Phi}{\partial r \partial \varphi} - \frac{1}{r^2}\frac{\partial \Phi}{\partial \varphi} + \frac{1}{2r^2}\frac{\partial^2 \Psi}{\partial \varphi^2} - \frac{r}{2}\frac{\partial}{\partial r}\left(\frac{1}{r}\frac{\partial \Psi}{\partial r}\right)\right] \tag{D.11c}$$

The potentials are substituted by cylindrical wave functions of order $|m| = |n|$:

$$\Phi = Z_m(kr)e^{in\varphi} \tag{D.12a}$$

$$\Psi = Z_m(lr)e^{in\varphi} \tag{D.12b}$$

where Z_m is any of $J_m, Y_m, H_m^{(1)}, H_m^{(2)}$, or a linear combination thereof.

Displacement $\mathbf{u}$ due to $\Phi = Z_m(kr)e^{in\varphi}$:

$$\begin{pmatrix} u_r \\ u_\varphi \end{pmatrix} = \frac{1}{r} \begin{pmatrix} a_{11} \\ a_{12} \end{pmatrix} e^{in\varphi} \tag{D.13a}$$

$$a_{11} = mZ_m(kr) - rkZ_{m+1}(kr) \tag{D.13b}$$

$$a_{12} = inZ_m(kr) \tag{D.13c}$$

Displacement $\mathbf{u}$ due to $\Psi = Z_m(lr)e^{in\varphi}$:

$$\begin{pmatrix} u_r \\ u_\varphi \end{pmatrix} = \frac{1}{r} \begin{pmatrix} a_{21} \\ a_{22} \end{pmatrix} e^{in\varphi} \tag{D.14a}$$

$$a_{21} = inZ_m(lr) \tag{D.14b}$$

$$a_{22} = rlZ_{m+1}(lr) - mZ_m(lr) \tag{D.14c}$$

Stress $\boldsymbol{\sigma}$ due to $\Phi = Z_m(kr)e^{in\varphi}$:

$$\begin{pmatrix} \sigma_{rr} & \sigma_{r\varphi} \\ \sigma_{\varphi r} & \sigma_{\varphi\varphi} \end{pmatrix} = \frac{1}{r^2} \begin{pmatrix} a_{31} & a_{32} \\ a_{32} & a_{33} \end{pmatrix} e^{in\varphi} \tag{D.15a}$$

$$a_{31} = -\lambda r^2 k^2 Z_m(kr) + 2\mu \left[\left(n^2 - m - r^2k^2\right) Z_m(kr) + rkZ_{m+1}(kr) \right] \tag{D.15b}$$

$$a_{32} = 2\mu in \left[(m-1) Z_m(kr) - rkZ_{m+1}(kr) \right] \tag{D.15c}$$

$$a_{33} = -\lambda r^2 k^2 Z_m(kr) + 2\mu \left[\left(m - n^2\right) Z_m(kr) - rkZ_{m+1}(kr) \right] \tag{D.15d}$$

Stress σ due to $\Psi = Z_m(lr)e^{in\varphi}$:

$$\begin{pmatrix} \sigma_{rr} & \sigma_{r\varphi} \\ \sigma_{\varphi r} & \sigma_{\varphi\varphi} \end{pmatrix} = \frac{2\mu}{r^2} \begin{pmatrix} a_{41} & a_{42} \\ a_{42} & a_{43} \end{pmatrix} e^{in\varphi} \tag{D.16a}$$

$$a_{41} = in\left[(m-1)\,Z_m(lr) - rlZ_{m+1}(lr)\right] \tag{D.16b}$$

$$a_{42} = \left[-\left(n^2 - m - \frac{r^2l^2}{2}\right) Z_m(lr) - rlZ_{m+1}(lr)\right] \tag{D.16c}$$

$$a_{43} = -in\left[(m-1)\,Z_m(lr) - rlZ_{m+1}(lr)\right] \tag{D.16d}$$

Bibliography

Abramowitz, M. and Stegun, I. A., editors (1964). *Handbook of Mathematical Functions*. Dover, New York.

Aki, K. (1982). Scattering and attenuation. *Bulletin of the Seismological Society of America*, **72**(6), S319–S330.

Aki, K. and Larner, K. L. (1970). Surface motion of a layered medium having an irregular interface due to incident plane SH-waves. *Journal of Geophysical Research*, **75**, 933–954.

Aki, K. and Richards, P. G. (1980). *Quantitative Seismology: Theory and Methods*, volume 1+2. Freeman, San Francisco.

Aki, K. and Wu, R. S., editors (1988). *Scattering and Attenuation of Seismic Waves*, volume 1-3 of *Pure and Applied Geophysics 128 (1/2), 131(4), 132(1/2)*. Birkhauser Verlag, Basel, Boston.

Amos, D. E. (1986). ALGORITHM 644: a portable package for Bessel functions of a complex argument and nonnegative order. *ACM Transactions on Mathematical Software*, **12**(3), 265–273.

Ballisti, R. and Hafner, C. (1983). The multiple multipole method in electro- and magnetostatic problems. *IEEE Transactions on Magnetics*, **19**(6), 2367–2370.

Bayer, G. and Niederdränk, T. (1993). Weak localization of acoustic waves in strongly scattering media. *Physical Review Letters*, **70**(25), 3884–3887.

Ben-Menahem, A. and Singh, S. J. (1981). *Seismic Waves and Sources*. Springer, New York.

Bender, C. M. and Orszag, S. A. (1978). *Advanced Mathematical Methods for Scientists and Engineers*. McGraw-Hill, Inc., New York.

Bleinstein, N. and Handelsman, R. A. (1986). *Asymptotic Expansions of Integrals*. Dover, New York.

Blonk, B. and Herman, G. C. (1994). Inverse scattering of surface waves: A new look at surface consistency. *Geophysics*, **59**(6), 963–972.

Blonk, B., Herman, G. C., and Drijkoningen, G. G. (1995). An elastodynamic inverse scattering method for removing scattered surface waves from field data. *Geophysics*, **60**(6), 1887–1905.

Bloom, A. L. (1978). *Geomorphology*. Prentice-Hall, Englewood Cliffs, NJ.

Boag, A. and Mittra, R. (1994). Complex multipole beam approach to electromagnetic scattering problems. *IEEE Transactions on Antennas and Propagation*, **42**(3), 366–372.

Boag, A., Leviatan, Y., and Boag, A. (1988). Analysis of acoustic scattering from fluid cylinders using a multifilament source model. *Journal of the Acoustical Society of America*, **83**, 1–8.

Bögli, A. (1980). *Karst Hydrology and Physical Speleology*. Springer, New York.

Bomholt, L. (1994). Coupling the generalized multipole technique and the finite element method. *Applied Computational Electromagnetics Society Journal*, **9**(3), 63–68.

Born, M. and Wolf, E. (1980). *Principles of Optics*. Pergamon Press, Oxford, U.K., 6th edition.

Boström, A. (1980a). Scattering by a smooth elastic obstacle. *Journal of the Acoustical Society of America*, **67**(6), 1904–1912.

Boström, A. (1980b). Scattering of stationary acoustic waves by an elastic obstacle immersed in a fluid. *Journal of the Acoustical Society of America*, **67**(2), 390–398.

Bouchon, M. (1993). A numerical simulation of the acoustic and elastic wavefields radiated by a source on a fluid-filled borehole embedded in a layered medium. *Geophysics*, **58**(4), 475–481.

Bouchon, M. and Aki, K. (1977). Discrete wavenumber representation of seismic-source wave fields. *Bulletin of the Seismological Society of America*, **67**(2), 259–277.

Bowman, J. J., Senior, T. B. A., and Uselenghi, P. L. E., editors (1969). *Electromagnetic and Acoustic Scattering by Simple Shapes*. North-Holland Publishing Company, Amsterdam.

Bracewell, R. N. (1986). *The Fourier Transform and its Applications*. McGraw-Hill, New York, 2nd edition.

Brebbia, C. A. and Dominguez, J., editors (1989). *Boundary Elements, an Introductory Course*. McGraw-Hill, New York.

Brigham, E. O. (1988). *The Fast Fourier Transform and its Applications*. Prentice Hall, Englewood Cliffs, NJ, 2nd edition.

Campillo, M. (1987). Modelling of SH-wave propagation in an irregularly layered medium – application to seismic profiles near a dome. *Geophysical Prospecting*, **35**, 236–249.

Červený, V. and Pšenčík, I. (1984). Gaussian beams in elastic 2-D laterally varying layered structures. *Geophysical Journal of the Royal Astronomical Society*, **78**, 65–91.

Červený, V., Molotkov, I. A., and Pšenčík, I. (1977). *Ray Methods in Seismology*. University Karbva, Praha.

Chang, C. L. (1990). A least-squares finite element method for the Helmholtz equation. *Computer Methods in Applied Mechanics and Engineering*, **83**, 1–7.

Cheng, N., Zhu, Z., Cheng, C. H., and Toksoz, M. N. (1994). Experimental and finite difference modelling of borehole Mach waves. *Geophysical Prospecting*, **42**(4), 303–319.

Chew, W. (1989). An N^2 algorithm for the multiple scattering solution of N scatterers. *Microwave and Optical Technology Letters*, **2**(11), 380–383.

Chew, W. C. (1988). A quick way to approximate a Sommerfeld-Weyl-type integral. *IEEE Transactions on Antennas and Propagation*, **36**(11), 1654–1657.

Chew, W. C. (1990). *Waves and Fields in Inhomogeneous Media*. Van Nostrand Reinhold, New York.

Chew, W. C., Barone, S., Anderson, B., and Hennessy, C. (1984). Diffraction of axisymmetric waves in a borehole by bed boundary discontinuities. *Geophysics*, **49**(10), 1586–1595.

Chin, R. C., Hedstrom, G. W., and Thigoen, L. (1984). Matrix methods in synthetic seismograms. *Geophysical Journal of the Royal Astronomical Society*, **77**, 483–502.

Chu, K. R., Kou, C. S., Chen, J. M., and Tsai, Y. C. (1992). Spectral domain analysis of open cavities. *International Journal of Infrared and Millimeter Waves*, **13**(10), 1571.

Clark, S. P., editor (1966). *Handbook of Physical Constants*. Geological Society of America, New York.

Coifman, R., Rokhlin, V., and Wandzura, S. (1993). The fast multipole method for the wave equation: a pedestrian prescription. *IEEE Antennas and Propagation Magazine*, **35**(3), 7–12.

de Hoop, A. T. (1960). Modification of Cagniard's method for solving seismic pulse problems. *Applied Science Research*, **B8**, 349–356.

de Hoop, A. T. (1990). Reciprocity theorems for acoustic wave fields in fluid/solid configurations. *Journal of the Acoustical Society of America*, **87**(5), 1932–1937.

DeSanto, J. A. (1992). *Scalar Wave Theory*. Springer, New York.

Deschamps, G. A. (1971). Gaussian beams as a bundle of complex rays. *Electronics Letters*, **7**(23), 684–685.

Domenico, S. N. (1976). Effect of brine-gas mixture on velocity in an unconsolidated sand reservoir. *Geophysics*, **41**(5), 882–894.

Dong, W., Bouchon, M., and Toksoz, M. N. (1995). Borehole seismic-source radiation in layered isotropic and anisotropic media: boundary element modeling. *Geophysics*, **60**(3), 735–747.

Dongarra, J. J., Moler, C. B., Bunch, J. R., and Stewart, G. W. (1979). *LINPACK User's Guide*. Society for Industrial and Applied Mathematics, Philadelphia.

Dubus, B. (1994). Coupling finite element and boundary element methods on a mixed solid-fluid / fluid-fluid boundary for radiation or scattering problems. *Journal of the Acoustical Society of America*, **96**(6), 3792–3799.

Elsherbeni, A., Kaifez, D., and Zeng, S. (1991). Cirular sectoral waveguides. *IEEE Transactions on Antennas and Propagation*, **33**(6), 20–27.

Engheta, N. (1996). On fractional calculus and fractional multipoles in electromagnetism. *IEEE Transactions on Antennas and Propagation*, **44**(4), 554–566.

Eremin, Y. A. and Sveshnikov, A. G. (1993). The discrete source method for investigating three-dimensional electromagnetic scattering problems. *Electromagnetics*, **13**(1), 1–22.

Esmersoy, C. (1986). *The Backpropagated Field Approach to Multidimensional Velocity Inversion*. Ph.D. thesis, Massachusetts Institute of Technology, Cambridge, MA.

Everstine, G. C. and Au-Yang, M. K., editors (1984). *Advances in Fluid-Structure Interaction*. American Society of Mechanical Engineers, New York.

Everstine, G. C. and Henderson, F. M. (1990). Coupled finite element / boundary element approach for fluid-structure interaction. *Journal of the Acoustical Society of America*, **87**, 1938–1947.

Ewing, W. M., Jardetzky, W. S., and Press, F. (1957). *Elastic Waves in Layered Media*. McGraw-Hill, New York.

Favati, P., Lotti, G., and Romani, F. (1991a). ALGORITHM 691: improving QUADPACK automatic integration routines. *ACM Transactions on Mathematical Software*, **17**(2), 218–232.

Favati, P., Lotti, G., and Romani, F. (1991b). Interpolatory integration formulas for optimal composition. *ACM Transactions on Mathematical Software*, **17**(2), 207–217.

Fletcher, C. A. (1984). *Computational Galerkin Method*. Springer, New York.

Frankel, A. and Clayton, R. (1986). Finite difference simulations of seismic scattering: implications for the propagation of short-period seismic waves in the crust and models of crustal heterogeneity. *Journal of Geophysical Research*, **B 91**(6), 6465–6488.

Frisk, G. V. (1994). *Ocean and Seabed Acoustics*. Prentice Hall, Englewood Cliffs NJ.

Fyfe, K. R., Coyette, J. P., and van Vooren, P. A. (1991). Acoustic and elasto-acoustic analysis using finite element and boundary element methods. *Sound and Vibration*, **25**(12), 16–22.

Galerkin, B. G. (1915). Series solutions of some problems of elastic equilibrium of rods and plates. *Vestn. Inzh. Tech.*, **19**, 897–908. in Russian.

Gan, H., Levin, P. L., and Ludwig, R. (1993). Finite element formulation of acoustic scattering phenomena with absorbing boundary condition in the frequency domain. *Journal of the Acoustical Society of America*, **94**(3), 1651–1662.

George, A. and Heath, M. T. (1980). Solutions of sparse linear least squares problems using Givens rotations. *Linear algebra and its applications*, **34**, 69–83.

Gottlieb, D. and Orszag, S. A. (1977). *Numerical Analysis of Spectral Methods: Theory and Applications*. Society for Industrial and Applied Mathematics, Philadelphia.

Haartsen, M. W., Bouchon, M., and Toksöz, M. N. (1994). A study of seismic acoustic wave propagation through a laterally varying medium using the boundary-integral-equation-discrete wave-number method. *Journal of the Acoustical Society of America*, **96**, 3010–3021.

Habashy, T. M., Groom, R. W., and Spies, B. R. (1993). Beyond the Born and Rytov approximations: a nonlinear approach to electromagnetic scattering. *Journal of Geophysical Research*, **98**(B2), 1759–1775.

Hafner, C. (1980). *Beiträge zur Berechnung elektromagnetischer Wellen in zylindrischen Strukturen mit Hilfe des 'Point Matching' Verfahrens*. Ph.D. thesis, Eidgenössische Technische Hochschule, Zürich, Switzerland. Diss. ETH Nr. 6683.

Hafner, C. (1990). *The Generalized Multipole Technique for Computational Electromagnetics*. Artech House, Boston.

Hafner, C. (1993). On the design of numerical methods. *IEEE Antennas and Propagation Magazine*, **35**(4), 13–21.

Hafner, C. (1994). MMP-GC-PET: The parameter estimation technique applied to the MMP code with the method of conjugate gradients. *Applied Computational Electromagnetics Society Journal*, **9**(3), 28–38.

Hafner, C. and Ballisti, R. (1983). The multiple multipole method (MMP). *COMPEL – The International Journal for Computation and Mathematics in Electrical and Electronic Engineering*, **2**(1), 1–7.

Hafner, C. and Bomholt, L. H. (1993). *The 3D Electrodynamic Wave Simulator: 3D MMP Software and User's Guide*. John Wiley and Sons.

Hafner, C., Waldvogel, J., Mosig, J., Zheng, J., and Brand, Y. (1994). On combination of MMP with MoM. *Applied Computational Electromagnetics Society Journal*, **9**(3), 18–27.

Harrington, R. F. (1968). *Field Computations by Moment Methods*. Macmillan, New York.

Hestenes, M. R. and Stiefel, E. (1952). Methods of conjugate gradients for solving linear systems. *Journal of Research of the National Bureau of Standards*, **49**(6), 409–436.

Hildebrand, F. B. (1976). *Advanced Calculus for Applications*. Prentice Hall, Englewood Cliffs, NJ.

Hong, T. L. and Helmberger, D. V. (1978). Glorified optics and wave propagation in nonplanar structure. *Bulletin of the Seismological Society of America*, **68**, 2013–2032.

Hosken, J. W. (1988). Ricker wavelets in their various guises. *First Break*, **6**(1), 24–33.

Imhof, M. G. (1995). Multiple multipole expansions for acoustic scattering. *Journal of the Acoustical Society of America*, **97**(2), 754–763.

Jennings, J. N. (1985). *Karst Geomorphology*. Blackwell, New York, 2nd edition.

Jensen, F. B., Kuperman, W. A., Porter, M. B., and Schmidt, H. (1994). *Computational Ocean Acoustics*. American Institute of Physics, New York.

Jih, R. S., McLaughlin, K. L., and Der, Z. A. (1988). Free-boundary conditions of arbitrary topography in a two-dimensional explicit finite difference scheme. *Geophysics*, **53**(8), 1045–1055.

Junger, M. C. and Feit, D. (1986). *Sound, Structures, and their Interaction*. MIT Press, Cambridge, MA, 2nd edition.

Kelly, K. R., Ward, R. W., Treitel, S., and Alford, R. M. (1976). Synthetic seismograms: a finite difference approach. *Geophysics*, **41**(1), 2–27.

Kennett, B. L. (1983). *Seismic Wave Propagation in Stratified Media*. Cambridge University Press.

Kessel, R. T. (1996). *Scattering of Elastic Waves in Layered Media: a Boundary Integral - Normal Mode Method*. Ph.D. thesis, University of Victoria, Victoria, British Columbia, Canada.

Kettenbrink, E. C., editor (1983). *Structure and Stratigraphy of the Val Verde Basin–Devils River Uplift, Texas*. WTGS Publications 83–77. West Texas Geological Society, Midland, TX.

Kirkpatrick, T. R. (1985). Localization of acoustic waves. *Physical Review*, **B31**(9), 5746–5755.

Kong, J. A. (1990). *Electromagnetic Wave Theory*. John Wiley & Sons.

Kuo, J. T. (1995). Accurate quasi-TEM spectral domain analysis of single and multiple coupled microstrip lines of arbitrary metallization thickness. *IEEE Transactions on Microwave Theory and Techniques*, **43**(8), 1881.

Kuster, G. T. and Toksöz, M. N. (1974). Velocity and attenuation of seismic waves in two-phase media - part I - theoretical formulations. *Geophysics*, **39**(5), 587–606.

Lakhtakia, A. and Mulholland, G. W. (1993). On two numerical techniques for light scattering by dielectric agglomerated structures. *Journal of Research of the National Institute of Standards and Technology*, **98**(6), 699–716.

Lakhtakia, A., Varadan, V. K., and Varadan, V. V. (1984). Iterative extended boundary condition method for scattering by objects of high aspect ratio. *Journal of the Acoustical Society of America*, **76**(3), 906–912.

Lapwood, E. R. (1949). The disturbance due to a line source in a semi-infinite elastic medium. *Philosophical Transactions of the Royal Society of London*, **A242**(841), 63–100.

Laroche, T. M. and Viveiros, J. J., editor (1994). *Structure and Tectonics of the Big Bend Area and Southern Permian Basin, Texas*. WTGS Publications 94-95. West Texas Geological Society, Midland, TX.

Leuchtmann, P. and Bomholt, F. (1993). Field modeling with the MMP code. *IEEE Transactions on Electromagnetic Compatibility*, **35**(2), 170–176.

Lo, T. W. (1987). *Seismic Borehole Tomography*. Ph.D. thesis, Massachusetts Institute of Technology, Cambridge, MA.

Ludwig, A. (1989). A new technique for numerical electromagnetics. *IEEE Transactions on Antennas and Propagation*, **31**(1), 40–41.

Luke, C. J. and Martin, P. A. (1995). Fluid-solid interaction: acoustic scattering by a smooth elastic obstacle. *SIAM Journal on Applied Mathematics*, **55**(4), 904.

Marfurt, K. J. (1984). Accuracy of finite-difference and finite-element modeling of the scalar and elastic wave equations. *Geophysics*, **49**, 533–549.

Marfurt, K. J. and Shin, C. S. (1989). The future of iterative modelling in geophysical exploration. In E. Eisner, editor, *Supercomputers in seismic exploration*, volume 21 of *Handbook of Geophysical Exploration, Section 1: Seismic Exploration*, chapter 9, pages 203–251. Pergamon Press, Oxford, U.K.

Mathews, I. C. (1986). Numerical techniques for three-dimensional steady-state fluid-structure interaction. *Journal of the Acoustical Society of America*, **79**(5), 1317–1325.

Mavko, G. M. and Nur, A. (1979). Waves attenuation in partially saturated rocks. *Geophysics*, **44**(2), 161–178.

Mazzullo, S. J., editor (1978). *Tectonics and Paleozoic Facies of the Marathon Geosyncline, West Texas*. WTGS Publications 78–17. West Texas Geological Society, Midland, TX.

Mie, G. (1900). Elektrische Wellen an zwei parallelen Drähten. *Annalen der Physik*, **2**, 201–249.

Miles, J. W. (1960). Scattering of elastic waves by small heterogeneities. *Geophysics*, **25**, 642–648.

Morse, P. M. and Feshbach, H. (1953). *Methods of Theoretical Physics*. McGraw-Hill, New York.

Muijres, G. J. and Herman, G. C. (1994). Two-dimensional acoustic waves in cracked media. In *64th Annual Internat. Mtg., Soc. Expl. Geophys., Expanded Abstracts*, volume 94, pages 1310–1313.

Mukerji, T., Mavko, G., Mujica, D., and Lucet, N. (1995). Scale-dependent seismic velocity in heterogeneous media. *Geophysics*, **60**(4), 1222–1233.

Müller, G. (1985). The reflectivity method: a tutorial. *Journal of Geophysics*, **58**, 153–174.

Murphy, J. E. and Chin-Bing, S. A. (1989). A finite-element model for ocean acoustic propagation and scattering. *Journal of the Acoustical Society of America*, **86**(4), 1478–1483.

Murphy, J. E. and Chin-Bing, S. A. (1991). A seismo-acoustic finite element model for underwater acoustic propagation. In J. M. Hovem, M. D. Richardson, and R. D. Stoll, editors, *Shear Waves in Marine Sediments*, pages 463–470. Kluwer Academic Publishers, Boston.

Murphy, J. E., Li, G., Chin-Bing, S. A., and King, D. B. (1996). Multifilament source model for short-range underwater acoustic problems involving penetrable ocean bottoms. *Journal of the Acoustical Society of America*, **99**(2), 845–850.

Norris, A. N. (1990). Resonant acoustic scattering from solid targets. *Journal of the Acoustical Society of America*, **88**(1), 505–514.

Paillet, F. L. and Cheng, C. H., editors (1991). *Acoustic Waves in Boreholes*. CRC Press, Boca Raton.

Pao, Y. H. and Mow, C. C. (1973). *Diffraction of Elastic Waves and Dynamic Stress Concentrations*. Crane Russak, New York.

Papworth, T. J. (1985). Seismic exploration over basalt covered areas in the U.K. *First Break*, **3**(4), 20–32.

Peng, C. and Toksöz, M. N. (1994). An optimal absorbing boundary condition for finite difference modeling of acoustic and elastic wave propagation. *Journal of the Acoustical Society of America*, **95**(2), 733–745.

Peterson, B. and Ström, S. (1974). Matrix formulations of acoustic scattering from an arbitrary number of scatterers. *Journal of the Acoustical Society of America*, **50**, 771–780.

Piessens, R. (1983). *QUADPACK: a Subroutine Package for Automatic Integration*. Springer, Berlin ; New York.

Press, F. and Siever, R., editors (1986). *Earth*. W. H. Freeman and Company, New York, 4th edition.

Press, W. H., Flannery, B. P., Teukolsky, S. A., and Vetterling, W. T. (1988). *Numerical Recipes*. Cambridge Press, Cambridge, U.K.

Pritchett, W. C. (1990). Problems and answers in recording reflections from beneath karst or volcanic surfaces. In *60th Annual Internat. Mtg., Soc. Expl. Geophys., Expanded Abstracts*, volume 90, pages 922–925.

Pujol, J., Fuller, B. N., and Smithson, S. B. (1989). Interpretation of a vertical seismic profile conducted in the Columbia Plateau basalts. *Geophysics*, **54**(10), 1258–1266.

Rayleigh, L. (1871). On the scattering of light by small particles. *Philosophical Magazine*, **41**, 441.

Rice, R. J. (1977). *Fundamentals of Geomorphology*. Longman, New York.

Ricker, N. H., editor (1977). *Transient Waves in Visco-Elastic Media*. Elsevier Scientific Publishers, Amsterdam.

Robertsson, J. O. A., Holliger, K., Green, A. G., Pugin, A., and Iaco, R. D. (1996). Effects of near-surface waveguides on shallow high-resolution seismic refraction and reflection data. *Geophysical Research Letters*, **23**, 495–498.

Rokhlin, V. (1983). Solution of acoustic scattering problems by means of second kind integral equations. *Wave Motion*, **5**, 257–272.

Rokhlin, V. (1990). Rapid solution of integral equations of scattering theory in two dimensions. *Journal of Computational Physics*, **86**, 414–439.

Rosen, E. M., Canning, F. X., and Schuetz Couchman, L. (1995). A sparse integral equation method for acoustic scattering. *Journal of the Acoustical Society of America*, **98**(1), 599–610.

Roth, M. and Korn, M. (1993). Single scattering theory versus numerical modelling in two-dimensional media. *Geophysical Journal International*, **112**, 124–140.

Sanchez-Sesma, F. J. and Campillo, M. (1991). Diffraction of P, SV, and Rayleigh waves by topographic features: a boundary integral formulation. *Bulletin of the Seismological Society of America*, **81**(6), 2234–2253.

Schmidt, H. and Tango, G. (1986). Efficient global matrix approach to the computation of synthetic seismograms. *Geophysical Journal of the Royal Astronomical Society*, **84**, 331–359.

Schultz, C. A. and Toksöz, M. N. (1995). Reflections from a randomly grooved interface: ultrasonic modelling and finite-difference calculations. *Geophysical Prospecting*, **43**, 581–594.

Schuster, G. T. and Smith, L. C. (1985). A comparison among four direct boundary integral methods. *Journal of the Acoustical Society of America*, **77**(3), 850–864.

Schwarz, H. R. (1988). *Finite Element Methods*. Academic Press, San Diego, CA.

Schwarz, H. R. (1989). *Numerical Analysis*. Wiley, New York.

Shah, A. H., Wong, K. C., and Datta, S. K. (1983). Single and multiple scattering of elastic waves in two dimensions. *Journal of the Acoustical Society of America*, **74**(3), 1033–1043.

Shin, S. Y. and Felsen, L. B. (1977). Gaussian beam modes by multipoles with complex source points. *Journal of the Optical Society of America*, **67**(5), 699–700.

Smith, W. D. (1974). The application of finite element analysis to body wave propagation problem. *Geophysical Journal of the Royal Astronomical Society*, **42**, 747–768.

Sroka, J., Baggenstoss, H., and Ballisti, R. (1990). On the coupling of the generalized multipole technique with the finite element method. *IEEE Transactions on Magnetics*, **26**(2), 658–661.

Strang, G. (1988). *Linear Algebra and its Applications*. Harcourt, San Diego, CA, 3rd edition.

Su, J. H., Varadan, V. V., and Varadan, V. K. (1983). Finite element eigenfunction method (FEEM) for elastic (SH) wave scattering. *Journal of the Acoustical Society of America*, **73**(5), 1499–1504.

Tessmer, E., Kosloff, D., and Behle, A. (1992). Elastic wave propagation simulation in the presence of surface topography. *Geophysical Journal International*, **108**(2), 621–632.

Thompson, D. R., Rodi, W., and Toköz, M. N. (1994). Nonlinear seismic diffraction tomography using minimum structure constraints. *Journal of the Acoustical Society of America*, **95**(1), 324–330.

Toksöz, M. N., Johnston, D. H., and Timur, A. (1979). Attenuation of seismic waves in dry and saturated rocks: I. laboratory measurements. *Geophysics*, **44**(4), 681–690.

Vandenberghe, N., Poggiagliolmi, E., and Watts, G. (1986). Offset-dependent seismic amplitudes from karst limestone in nothern Belgium. *First Break*, **4**(5), 9–27.

Varadan, V. K. and Varadan, V. V., editors (1980). *Acoustic, Electromagnetic and Elastic Wave Scattering - Focus on the T-matrix approach*. Pergamon Press, New York.

Vekua, I. N. (1967). *New Methods for Solving Elliptic Equations*. North-Holland Publishing Co, Amsterdam.

Virieux, J. (1985). SH wave propagation in heterogeneous media: velocity-stress finite-difference method. *Geophysics*, **49**, 1933–1957.

Virieux, J. (1986). P-SV wave propagation in heterogeneous media: velocity-stress finite-difference method. *Geophysics*, **51**(4), 889–901.

Voigt, R. G., Gottlieb, D., and Hussaini, M. Y., editors (1984). *Spectral Methods for Partial Differential Equations*. Society for Industrial and Applied Mathematics, Philadelphia.

Wang, Y. M. and Chew, W. C. (1993). A recursive T-matrix approach for the solution of electromagnetic scattering by many spheres. *IEEE Transactions on Antennas and Propagation*, **41**(12), 1633–1639.

Waterman, P. C. (1969). New formulation of acoustic scattering. *Journal of the Acoustical Society of America*, **45**(6), 1417–1429.

Waterman, P. C. (1976). Matrix theory of elastic wave scattering. *Journal of the Acoustical Society of America*, **60**(3), 567–580.

Watson, G. N. (1944). *A Treatise on the Theory of Bessel Functions*. Cambridge University Press, Cambridge, U.K.

White, J. E. (1975). Computed seismic speeds and attenuation in rocks with partial gas saturation. *Geophysics*, **40**, 224–232.

Wilkinson, J. H. (1988). *The Algebraic Eigenvalue Problem*. Oxford University Press, Oxford, U.K.

Wong, H. L. (1982). Effect of surface topography on the diffraction of P, SV, and Rayleigh waves. *Bulletin of the Seismological Society of America*, **72**(4), 1167–1183.

Wu, R. S. and Aki, K. (1985). Elastic wave scattering by a random medium and small-scale inhomogeneities in the lithosphere. *Journal of Geophysical Research*, **90**, 10261–10273.

Zienkiewicz, O. C., editor (1977). *The Finite Element Method*. McGraw-Hill, New York.

Zienkiewicz, O. C., Kelly, D. W., and Bettess, O. (1977). The coupling of the finite element method and boundary solution procedures. *International Journal for Numerical Methods in Engineering*, **11**, 355–375.